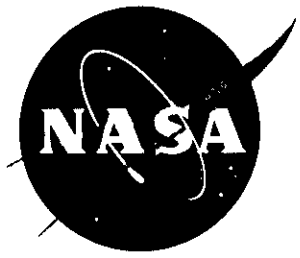

NASA Contractor Report 4671

The Acoustic Characteristics of Turbomachinery Cavities

M.J. Lucas, R. Noreen, L.D. Sutherland and J. Cole III, M. Jun[illegible]

Contract NAS8–37360
Prepared for Marshall Space Flight Center

May 1995

NASA Contractor Report 4671

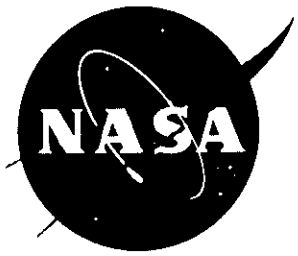

The Acoustic Characteristics of Turbomachinery Cavities

M.J. Lucas, R. Noreen, L.D. Sutherland
Wyle Laboratories

J. Cole III, M. Junger
Cambridge Acoustical Associates

National Aeronautics and Space Administration
Marshall Space Flight Center • MSFC, Alabama 35812

Prepared for Marshall Space Flight Center
under Contract NAS8–37360

May 1995

Preface

Internal fluid flows are subject not only to self-sustained oscillations of the purely hydrodynamic type but also to the coupling of the instability with the acoustic mode of the surrounding cavity. This situation is common to turbomachinery, since flow instabilities are confined within a flow path where the acoustic wavelength is typically smaller than the dimensions of the cavity and flow speeds are low enough to allow resonances. When acoustic coupling occurs, the fluctuations can become so severe in amplitude that it may induce structural failure of engine components. The potential for catastrophic failure makes identifying flow-induced noise and vibration sources a priority.

In view of the complexity of these types of flows, this report was written with the purpose of presenting many of the methods used to compute frequencies for self-sustained oscillations. The report also presents the engineering formulae needed to calculate the acoustic resonant modes for ducts and cavities. Although the report is not a replacement for more complex numerical or experimental modeling techniques, it is intended to be used on general types of flow configurations that are known to produce self-sustained oscillations. This report provides a complete collection of these models under one cover.

This report is divided into two parts. Part I (Chapters 2 through 6) presents many of the methods used to calculate acoustic resonances for internal flow paths inside turbomachinery for the conditions when the acoustic wavelength is much larger than the cavity dimensions (discrete resonator) and in which the wavelength is comparable to or smaller than the main flow path dimensions (distributed resonator). Part II (Chapters 7 through 11) shows how to compute the modes of instability for fluid oscillators that are self-sustained. These types of oscillations are termed instability-induced excitation (IIE) and include jets, wakes, and mixing layers. By combining Parts I and II, modes of flow instability and acoustic resonances can be calculated to determine the potential for coalescence between discrete or distributed resonators and instability-induced oscillators.

In addition to the report, FORTRAN 77 computer programs were developed to perform the calculations described in the report which go beyond what is reasonably expected from a hand-held calculator. To obtain copies of the programs, contact Tom Nesman at (205) 544-1546 or E-mail Tom.Nesman@msfc.nasa.gov.

ACKNOWLEDGMENTS

This work was funded under NASA–Marshall Space Flight Center Contract No. NAS8-37360. The authors are grateful to Messrs. Jess Jones and Tom Nesman of the NASA–Marshall Space Flight Center for their support and helpful suggestions during the preparation of this manuscript. The authors also wish to express there sincere gratitude to Prof. Donald Rockwell of Lehigh University and Dr. Eric Stusnick and Mr. Joseph Czech of Wyle Laboratories for their thorough review.

TABLE OF CONTENTS

TABLE OF CONTENTS (Continued)

TABLE OF CONTENTS (Continued)

TABLE OF CONTENTS (Continued)

TABLE OF CONTENTS (Continued)

TABLE OF CONTENTS (Continued)

LIST OF FIGURES

LIST OF FIGURES (Continued)

LIST OF FIGURES (Continued)

LIST OF FIGURES (Continued)

LIST OF FIGURES (Continued)

LIST OF TABLES

LIST OF TABLES (Continued)

SYMBOL	DEFINITION	FIRST REFERENCE
a	Bubble radius	Equation (4-52)
b	Cross-flow span of rectangular cascade system	Figure 6-1
b	Chord half-width	Table 7-1(f)
b	Shear layer thickness	Equation (8-4)
b_w	Jet half-width	Table 7-1(d)
c	Speed of sound	Equation (2-3)
c_a	Speed of sound inside a cavity	Equation (11-28)
c_c	Phase velocity in a capillary tube	Equation (4-26)
c_{eff}	Effective speed of sound	Equation (9-6)
c_{gnm}	Group velocity for mode nm	Equation (4-36a)
c_i	Imaginary part of complex sound speed	Equation (7-10)
c_L	Speed of liquid in a pipe	Equation (4-2a)
c_{nm}	Phase velocity for mode nm	Equation (4-34)
c_o	Speed of sound at 0° C	Equation (2-13)
c_o	Speed of sound in the absence of flow	Equation (5-2)
c_r	Real part of complex sound speed	Equation (7-10)
d	Acoustic boundary layer thickness	Equation (4-25a)
d	Diameter of cylinder	Figure 9-1
d'	Distance separating shear layers	Equation (9-3)
d_{fo}	Tube diameter at root of fin	Equation (9-14)
d_i	Inside tube diameter	Equation (9-10)
d_i	Inlet diameter to ring chamber	Figure 10-1
d_{if}	Tube inside diameter under fin section	Equation (9-14)
d_o	Helmholtz resonator neck diameter	Equation (2-66b)
d_o	Outside tube diameter	Equation (9-10)
d_o	Outlet diameter to ring chamber	Figure 10-1
d_T	Thermal boundary layer thickness	Equation (5-10a)
f_{an}	Anti-resonant frequency	Equation (4-12b)

SYMBOL	DEFINITION	FIRST REFERENCE
f_c	Vortex shedding frequency	Figure 9-7
f_i	Frequency of the i'th vortex merging	Equation (8-12)
f_m	Nyborg's stage number integer	Equation (11-15)
f_n	Natural frequency	Equation (2-12)
f_n	Shear layer mode	Table 8-1
f'_n	Stressed frequency	Equation (9-11)
f_{nm}	Cut-on frequency for mode nm	Equation (4-33b)
f_p	Preferred mode or column mode	Table 8-2
f_{rn}	Resonant frequency	Equation (4-12a)
f_{tb}	Turbulent buffeting frequency	Equation (9-5)
g	Acceleration due to gravity	Equation (7-1)
g	Tube layout parameter	Figure 9-6
h	Wall thickness	Equation (2-24)
h	Amplitude of shear layer	Equation (7-5)
h	Minimum jet thickness constant	Equation (9-8)
h	Complex amplitude of fluctuating part of h	Equation (7-9a)
k	Wave number	Equation (2-16)
k^+	Wave number of plane wave propagating with flow	Equation (5-3)
k^-	Wave number of plane wave propagating against flow	Equation (5-3)
k_c	Convected wave number	Equation (3-80)
k_i	Wave number of incident wave	Equation (3-80)
k_L	Wave number with flow and losses	Equation (3-87)
k_r	Real part of wave number	Equation (11-34)
k_R	Wave number of reflected wave	Equation (3-81)
k_v	Velocity ratio, shear layer velocity/free-stream velocity	Equation (11-27)
l	Apparent length scale	Equation (11-1)
m	Mass	Figure 2-1
m	Velocity ratio	Equation (8-3)

SYMBOL	DEFINITION	FIRST REFERENCE
n	Stage of oscillation	Equation (11-1)
p	Pressure	Equation (2-1)
p^+	Pressure of plane wave propagating with flow	Equation (5-5)
p^-	Pressure of plane wave propagating against flow	Equation (5-5)
p_i	Incident pressure wave	Equation (2-44)
p_R	Reflected pressure wave	Equation (2-47a)
p_{rms}	Root-mean-square pressure	Equation (3-14)
p_T	Transmitted pressure wave	Equation (2-47b)
q	Magnitude of velocity vector	Equation (7-1)
r	Radial distance coordinate	Equation (4-31)
r	Temperature recovery factor	Equation (11-29)
$r(\omega_o)$	Bubble resonance spectrum	Equation (4-62)
r_s	Radius of cylindrical shell, pipe, or capillary tube	Equation (2-24)
s	Pitch spacing of rectangular cascade system	Figure 6-1
t	Time	Equation (7-2)
u	Acoustic particle velocity	Equation (3-1)
u	Horizontal component of fluid velocity	Equation (7-2)
u^+	Particle speed of plane wave propagating with flow	Equation (5-5)
u^-	Particle speed of plane wave propagating against flow	Equation (5-5)
u_o	Acoustic particle velocity at x=0	Equation (5-16)
u_{rms}	Root-mean-square particle velocity	Equation (3-14)
v	Vertical component of fluid velocity	Equation (7-2)
v_i	Mass velocity of ith pipe element	Equation (3-26)
w	Radial displacement	Equation (2-26)
x	Horizontal corrdinate	Equation (2-16)
x'	Non-dimensional linear coordinate (= x/L)	Equation (6-3)

SYMBOL	DEFINITION	FIRST REFERENCE
x_s	Source region of pipe wall	Equation (5-8a)
x_u	Imaginary part of specific acoustic impedance	Equation (4-37)
y	Vertical coordinate	Equation (7-1)
z_u	Specific (or characteristic) acoustic impedance	Equation (3-1)
z_{uo}	Specific acoustic impedance at x=0	Equation (4-9)
z_{up}	Specific acoustic impedance of a plane wave	Equation (3-2)
A	Attenuation in dead zone	Equation (4-71)
A	Tube cross-sectional area	Equation (9-11)
A	Complex amplitude of Ø(y)	Equation (7-9)
A_c	Cross-sectional area of cavity	Figure 2-1
A_l	Loss factor	Equation (3-86)
A_o	Cross-sectional area of orifice	Figure 2-1
A_p	Cross-sectional area of pipe	Equation (2-45)
B	Adiabatic bulk modulus	Equation (2-1)
B_c	Bulk modulus for air bubble	Equation (4-53)
B_{eff}	Effective bulk modulus	Equation (2-32)
B_L	Bulk modulus of liquid	Equation (2-31)
B_s	Bulk modulus of shell	Equation (2-29)
B_s	Bulk modulus for bubble swarm	Equation (4-51)
C	Chord dimension of rectangular cascade system	Figure 6-1
C_b	Base pressure coefficient	Equation (9-1)
D	Depth of simple axisymmetric cavity	Table 1-2
D	Frequency constant	Equation (9-9)
D	Diameter of vortex whistle	Equation (10-1)
D_j	Diameter of jet	Table 8-2
D_p	Diameter of pipe	Equation (5-10a)

SYMBOL	DEFINITION	FIRST REFERENCE
E	Young's modulus	Equation (2-25)
E	Modulus of elasticity of tube material	Equation (9-9)
F	Force	Equation (2-5)
F_i	Residual error terms	Equation (6-11)
G_i	Resonance parameter, inline tube array	Equation (9-6)
G_s	Resonance parameter, staggered tube array	Equation (9-7)
I	Section moment of inertia	Equation (9-9)
I^+	Acoustic intensity of plane wave propagating with flow	Equation (5-6)
I^-	Acoustic intensity of plane wave propagating against flow	Equation (5-6)
J_n	Cylindrical Bessel function	Equation (4-31)
K	Spring constant, stiffness	Figure 2-1
K	Base pressure parameter	Equation (9-3)
L	Length of simple axisymmetric cavity	Table 1-2
L	Length of straight pipe section	Figure 3-3
L	Downstream tube length	Figure 10-1
L_c	Cavity depth of Helmholtz resonator	Figure 2-1
L_{eff}	Effective length	Figure 2-1
L_i	Incident acoustic power level	Equation (3-10)
L_o	Neck length of Helmholtz resonator	Figure 2-1
L_t	Transmitted acoustic power level	Equation (3-10)
M	Mach number of flow past cavity	Table 1-2
M	Entrained mass per unit area	Equation (4-55)
M_e	Mach number of flow at pipe exit	Figure 5-4
N	Number of cavities per unit volume	Equation (4-62)
P	Pressure amplitude of standing wave	Equation (6-10)
P	Axial load, negative if compressed, positive if tensile	Equation (9-11)

SYMBOL	DEFINITION	FIRST REFERENCE
P^+	Amplitude of upstream wave	Equation (5-9)
P^-	Amplitude of downstream wave	Equation (5-9)
P_b	Base pressure, the pressure at the back of the plate	Equation (9-1)
P_H	Amplitude of pressure in Helmholtz resonator	Equation (2-48b)
P_I	Amplitude of incident pressure wave	Equation (2-44)
P_{nm}	Modal amplitudes	Equation (4-31)
P_R	Amplitude of reflected pressure wave	Equation (2-47a)
P_T	Amplitude of transmitted pressure wave	Equation (2-47b)
P_1	Pressure entering vortex whistle	Equation (10-1)
P_2	Pressure exiting vortex whistle	Equation (10-1)
P_∞	Pressure in the undisturbed flow	Equation (9-1)
P_∞	Ambient pressure	Equation (2-2)
Q	Quality factor with acoustic and viscous losses	Table 2-1
Q_a	Acoustic quality factor	Equation (2-38)
$\dot{Q}_H$	Volume velocity in Helmholtz resonator	Equation (2-48d)
$\dot{Q}_I$	Volume velocity of incident pressure wave	Equation (2-45)
$\dot{Q}_R$	Volume velocity of reflected pressure wave	Equation (2-47a)
$\dot{Q}_T$	Volume velocity of reflected pressure wave	Equation (2-47b)
R	Dashpot resistance	Figure 2-1
R	Correlation function	Equation (2-58)
R	Real part of complex impedance	Equation (3-18)
R_a	Acoustic resistance	Equation (2-36)
Re	Reynolds number	Figure 8-2
Re*	Universal Reynolds number, based on d' and Us	Equation (9-4)
R_s	Viscous surface resistance	Equation (2-42)
R_v	Viscous resistance	Equation (2-41)

SYMBOL	DEFINITION	FIRST REFERENCE
S_i	Elements of state vector	Equation (3-63)
S_l	Tube layout parameter	Figure 9-6
St	Strouhal number	Equation (7-32)
S_t	Tube layout parameter	Figure 9-6
St*	Universal Strouhal number, based on d' and Us	Equation (9-4)
T	Temperature	Equation (2-11)
T_{ij}	Elements of transfer matrix	Equation (3-58)
TL	Transmission loss	Equation (2-53)
TL_{sp}	Transmission loss of a straight pipe	Equation (3-76)
U	Free-stream flow speed	Table 1-2
U_c	Convective velocity	Equation (2-65c)
U_c	Speed of fluid in cavity	Table 1-2
U_{group}	Group velocity	Equation (7-34)
U_m	Mean velocity at jet exit	Table 8-1
U_o	Axial exit velocity from ring chamber	Figure 10-1
U_s	Stream velocity	Equation (9-2)
U_1	Jet velocity	Equation (8-3)
U_2	Free stream velocity	Equation (8-3)
U_∞	Free-stream velocity	Equation (9-2)
V	Volume	Equation (2-1)
V_c	Volume of cavity	Figure 2-1
V_n	Velocity component normal to interface	Equation (7-6)
V_θ	Fluid anguliar velocity at swirl generator exit	Equation (10-2)
W	Acoustic power	Equation (3-14)
W_e	Effectivee weight of the tube per unit length	Equation (9-9)
W_i	Incident acoustic power	Equation (3-9)
W_{ref}	Reference acoustic power	Equation (3-11)
W_t	Transmitted acoustic power	Equation (3-9)

SYMBOL	DEFINITION	FIRST REFERENCE
X	Imaginary part of complex impedance	Equation (3-18)
X	Length of the potential core of a jet	Table 8-2
X_i	Distance from trailing edge to i'th vortex	Equation (8-12)
Y_1 , Y_2	Distance separating shear layer	Equation (8-9)
Z_H	Acoustic impedance of Helmholtz resonator	Equation (2-46b)
Z_m ,Z	Acoustic impedance based on mass velocity	Equation (3-5)
Z_{mp} , ζ	Acoustic impedance of plane wave based on mass velocity	Equation (3-6)
Z_p	Acoustic impedance of pipe	Equation (2-46a)
Z_v	Acoustic impedance based on volume velocity	Equation (3-3)
Z_{vp}	Acoustic impedance of plane wave based on volume velocity	Equation (3-4)

GREEK SYMBOLS

α	Volume fraction	Equation (4-50)
α	Wave number	Equation (7-9)
α	Empirical constant	Equation (11-27)
α_c	Classical attenuation in a pipe	Equation (5-10b)
α_d	Attenuation per diameter of pipe	Equation (4-27)
α_{flow}	Attenuation due to mean flow in a pipe	Equation (5-20)
α_{nm}	Radial wave number	Equation (4-31)
α_t	Transmission coefficient	Equation (3-9)
α_T	Coefficient of thermal diffusivity	Equation (5-10)
α_{turb}	Attenuation due to turbulence in a pipe	Equation (5-12)
β	Complex angular frequency	Equation (7-11)
βi	Eigenvalues of Helmholtz equation	Equation (6-9b)
βi	Complex part of complex angular frequency	Equation (7-11)
βr	Real part of complex angular frequency	Equation (7-11)
γ	Ratio of specific heats	Equation (2-2)

SYMBOL	DEFINITION	FIRST REFERENCE
γ_{nm}	Axial wave number	Equation (4-31)
Γ	Circulation	Equation (10-3)
δ	Fluid particle displacement	Equation (2-4)
δ	Damping constant	Equation (4-58)
ΔL_i	Length of entrained fluid within cavity	Figure 2-1
ΔL_o	Length of entrained fluid outside cavity	Figure 2-1
ΔV	Volume change in cavity	Equation (2-1)
δ_c	Displacement at open end of cavity	Equation (2-17a)
ϵ	Strain	Equation (2-25)
ξ	Increment in the x direction	Equation (2-58)
ζ_c	Impedance with flow and no losses	Equation (3-82)
ζ_L	Impedance with flow and losses	Equation (3-90)
η	Increment in the y direction	Equation (2-58)
η	Acoustic source displacement	Equation (5-10a)
θ	Momentum thickness	Equation (7-28)
θ_c	Coincidence cone vertex angle	Equation (4-49)
λ	Wavelength	Equation (2-7)
λ_1	Wavelength for upstream traveling wave	Equation (11-24)
λ_2	Wavelength for downstream traveling wave	Equation (11-24)
μ	Absolute viscosity	Equation (2-42)
μ_{eff}	Effective viscosity in a gas-filled tube	Equation (4-29)
ν	Kinematic viscosity	Equation (7-17)
ρ	Density	Equation (2-3)
ρ_c	Devsity of vapor	Equation (4-50)
ρ_L	Density of liquid	Equation (4-50)
ρ_o	Density at 0° C. and atmospheric pressure	Equation (2-11)

SYMBOL	DEFINITION	FIRST REFERENCE
σ	Stress	Equation (2-24)
σ	Solidity ratio	Equation (9-6)
τ	Increment in time	Equation (2-58)
τ	Ratio of shear layer thickness to free-stream coordinate	Equation (8-4)
ϕ	Circumferential angle coordinate	Equation (4-31)
ϕ	Velocity potential	Equation (7-1)
ϕ	Complex amplitude of velocity potential	Equation (7-9)
Φ	Complex amplitude of stream function	Equation (7-25)
Φ_i	Imaginary part of $\Phi(y)$	Equation (7-31)
Φ_r	Real part of $\Phi(y)$	Equation (7-31)
ψ_f	Friction factor for turbulent flow	Equation (5-12)
ψ	Complex stream function	Equation (7-25)
ω	Angular frequency	Equation (2-16)
ω_a	Antiresonance frequency	Equation (4-60)
ω_i	Imaginary part of complex angular frequency	Equation (5-19)
ω_o	Natural frequency of bubble	Equation (4-56)
ω_r	Real part of complex angular frequency	Equation (5-19)

CHAPTER 1

IDENTIFICATION AND CLASSIFICATION OF FLOW-INDUCED SOURCES INSIDE TURBOMACHINERY

Although the concept of flow-induced vibration may be well known, it is often difficult to identify an excitation source inside turbomachinery when the need arises. The difficulty in excitation source identification is due to the flow complexities and the bewildering number of geometric features that are found inside turbomachinery. To complicate matters further, engineers are often faced with having to identify possible sources of excitation with limited information on the details of the flow's thermo- and hydro-dynamic environment.

This report has been prepared to alleviate some of the difficulties with identifying potential sources of excitation inside turbomachinery. The report presents in consistent notation and format, the formulae, charts, and tables that are needed to determine the frequencies for self-sustained oscillations. The report is organized according to the basic acoustic and flow configurations common to turbomachinery. With each configuration, solutions to predict the preferred frequency of oscillation are provided using the latest analytical and empirical techniques found in the literature.

Section 1.1 introduces the basic source excitation mechanisms. Section 1.2 identifies the parts of the turbomachine which have a potential for excitation, and Section 1.3 classifies the excitation sources and presents the structure and organization for the rest of the report.

1.1 Basic Source Excitation Mechanisms

The first step in the process of identifying sources of excitation is to establish a classification scheme so that the distinction between each of the model categories is clearly stated. This shall be done using the source and classification scheme originally devised by Naudascher and Rockwell. The scheme begins by distinguishing three basic categories of mechanism.

- Extraneously Induced Excitation (EIE) – Generated by pulsations in the flow or pressure that is not part of the vibrating system. The source of excitation is independent of body movement or any instability that may arise from vortex shedding. An example EIE might be a pump surge that produces a strong pressure spike that in turn induces a force on downstream engine components.

- Instability-Induced Excitation (IIE) – Caused by an instability in the flow. Often times the instability is brought on by the very same structure that is endangered by the vibrations. These instabilities are simply a result of an inflection point in the mean velocity profile. Many flow configurations give rise to this type of flow. Some examples are jets, wakes, and mixing layers. The feature common to all of these is the existence of a shear layer.

- Movement-Induced Excitation (MIE) – An exciting force that is brought about through the vibration of a body. When there is body movement there is a phase relationship between the body displacement and the fluid force produced from the body displacement. At certain values of phase the flow will induce forces that will enhance the body movement, causing the body to undergo self-sustained oscillation. Common examples of MIE are couple mode flutter and galloping.

Any one of these three basic excitation mechanisms can be further subdivided. For example, the IIEs have three basic subdivisions; these are: fluid-dynamic, fluid-resonator, and body-resonator. Fluid-dynamic is the category of oscillators that is dependent on the dynamics of the flow alone and is not coupled to any other forcing mechanism. Fluid-resonator and body-resonator are two other categories of oscillators where the fluid flow is modulated by either the dynamics of the resonator or the movement of a body. In the case of the fluid-resonator, a clearly identifiable acoustic mode or modes must be excited by the action of a shear layer.

In practice there are many situations where these basic mechanisms may appear in any combination inside turbomachinery. Such coalescence of excitation mechanism is prone to highly amplified fluctuations and can lead to structural failure. Being able to identify the basic mechanisms is one of the main tasks when analyzing a vibration problem.

1.2 Source Identification

In this section, a search is made of all the possible excitation sources having geometric configurations that lend themselves to handbook treatment. Such a survey of source geometries defines the types, shapes, and range of flow conditions for which analytical models are suitable, and precludes modeling all types of excitation models and resonators that are not likely to occur inside turbomachinery. To accomplish this task, a list of vibration sources is first developed. Next, the sources are organized into a logical framework so as to define the appropriate models and establish the range of flow and acoustic conditions that might be expected.

Consider as an example the High-Pressure Fuel Turbo-Pump (HPFTP). This pump is one of four pumps on the Space Shuttle Main Engine (SSME). The space shuttle orbiter vehicle propulsion system has a total of three main engines. An engineering drawing of the HPFTP is shown in Figure 1-1. Included in the figure are the thermodynamic properties at selected locations along the flow path. The engines are presently throttled over a thrust range of 60 to 109 percent of the design thrust. The values reported here are for conditions at the full power level of 109 percent.

Liquid hydrogen from the low-pressure fuel pump enters the HPFTP at a pressure of 240 psia. After passing through the first impeller stage the hydrogen changes its phase to vapor and remains vapor through the remainder of the pump. At the pump exit, the hydrogen gas is used to cool the main combustion chamber nozzle, drive the turbine in the Low-Pressure Fuel Turbo-Pump (LPFTP), and is mixed with oxygen in the preburners of the High-Pressure Fuel and Oxygen Turbo-Pumps. The HPFTP preburner (not shown in the figure) produces hot gases that drive the turbine, that in turn drives the pump.

Using Figure 1-1 a search is made of all possible excitation sources. In Table 1-1 are listed some of the major cavities that are capable of maintaining a standing acoustic wave. Listed in the table are the major engine components and beside each component is the expected Mach number and frequency range. The frequencies reported here are for the quarter wavelength mode. Note that in most instances the Mach number is less than 0.2.

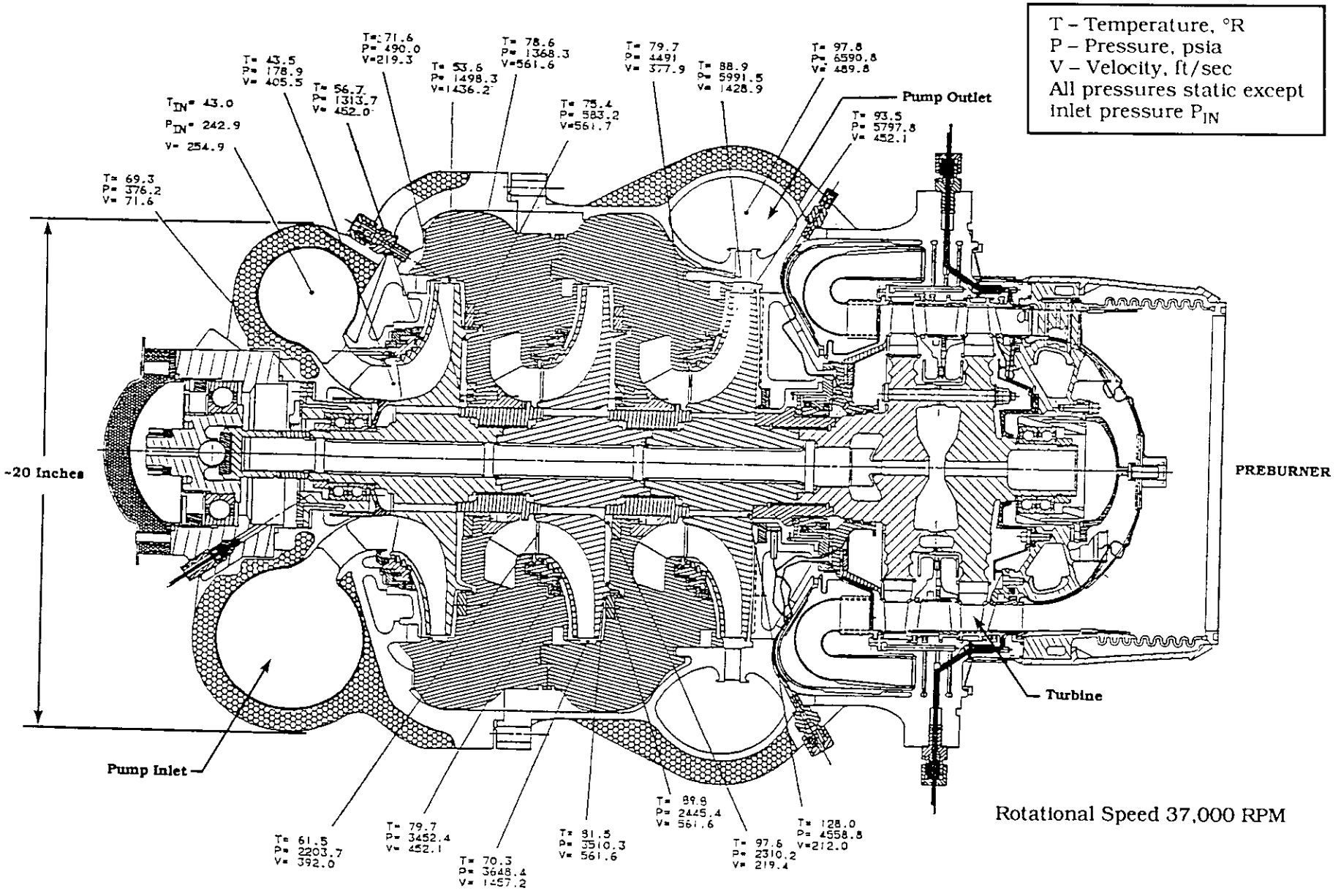

Figure 1-1. High-Pressure Fuel Turbo-Pump (HPFTP).
Conditions reported at Full Power Level, 109 Percent Power.

Table 1-1

Cavities Capable of Acoustic Standing Waves

	Basic Volumes	Engine Components	Mach Number	Frequency Range (One-Quarter Wave)
Axisymmetric	**Circular Torus** 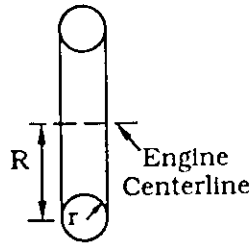	Pump Inlet and Exit Chambers Turbine Inlet and Exit Chambers	0.02 to 0.22 0.03 to 0.22	C: 322 to 587 Hz C: 280 to 839 Hz
	Irregular Torus $\Delta r > L$ $\Delta r \sim L$ 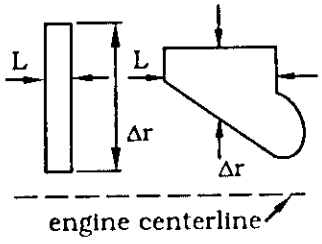	• Impeller Balance Cavity • Lubrication and/or Cooling Cavity • Combustion Chamber	<0.08 <0.21 0.12	C: 330 to 764 Hz R: 2500 to 11,000 Hz C: 296 to 1286 Hz R: 2500 to 20,000 Hz C: 790 Hz A: 2770 Hz
Non-Axisymmetric	**Drilling** 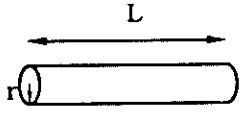	• Lubrication Ports • Bearing Slinger Drillings	<0.25 0.12	A: 2700 to 6900 Hz A: 47,780 Hz
	Duct 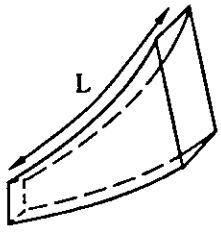	• Impeller • Diffuser • Combustion Chamber	<0.35 <0.1 <0.6	A: 1500 to 2600 Hz A: 1700 to 3200 Hz A: 2700 to 5000 Hz

C – Centrifugal Mode; R – Radial Mode; A – Axial Mode

Figure 1-2 further illustrates the range of resonance frequencies for selected engine components. The vertical scale is a logarithmic frequency scale. The components highlighted beside the scale indicate the first wavelength resonance mode. The figure is divided into two parts: on the left side of the figure are engine components that experience quarter wavelength modes in the radial and axial directions; on the right side are the engine components that experience circumferential standing waves. Longer wavelengths with frequencies below 2000 Hz are the product of circumferential acoustic waves, while shorter acoustic wavelengths are traceable to radial and axial resonance modes.

Continuing the search for excitation sources, Table 1-2 is another example of how sources may be classified. Shown in Table 1-2 are the results of a survey for cavities having dimensions smaller than the acoustic wavelengths. Four types of cavities are identified. The first two cavities, denoted as the cavities without branch pipes, are relatively simple configurations that can be modeled using a handbook. For example, the first cavity resembles the classical Rossiter cavity and might be analyzed using one of a number of models for flows over rectangular cavities. The second cavity is a Helmholtz resonator. Engineering data and formulae are readily available for these types of resonators.

The cavities appearing in the third and fourth rows are sufficiently more complicated; the existence of the branch pipe makes it nearly impossible to identify general handbook methodologies in the literature. In this situation, and many more like it, handbook methodologies are unavailable and the only appropriate measure is to use a computer modeling or a testing approach.

1.3 Source Classification

If one were to continue the search for sources through other parts of the SSME, it would be quickly discovered that the engine spans a wide range of flow conditions (liquid, vapor, and two-phase) and there are more possible flow situations than there are models. This statement is true in general for turbomachinery and is not limited to a particular engine such as the SSME which was chosen for this example exercise. Generally speaking, the following conclusions can be made about turbomachinery: the Reynolds numbers are typically greater than 10,000, the Mach number less than 0.2, and most frequencies of any significance are

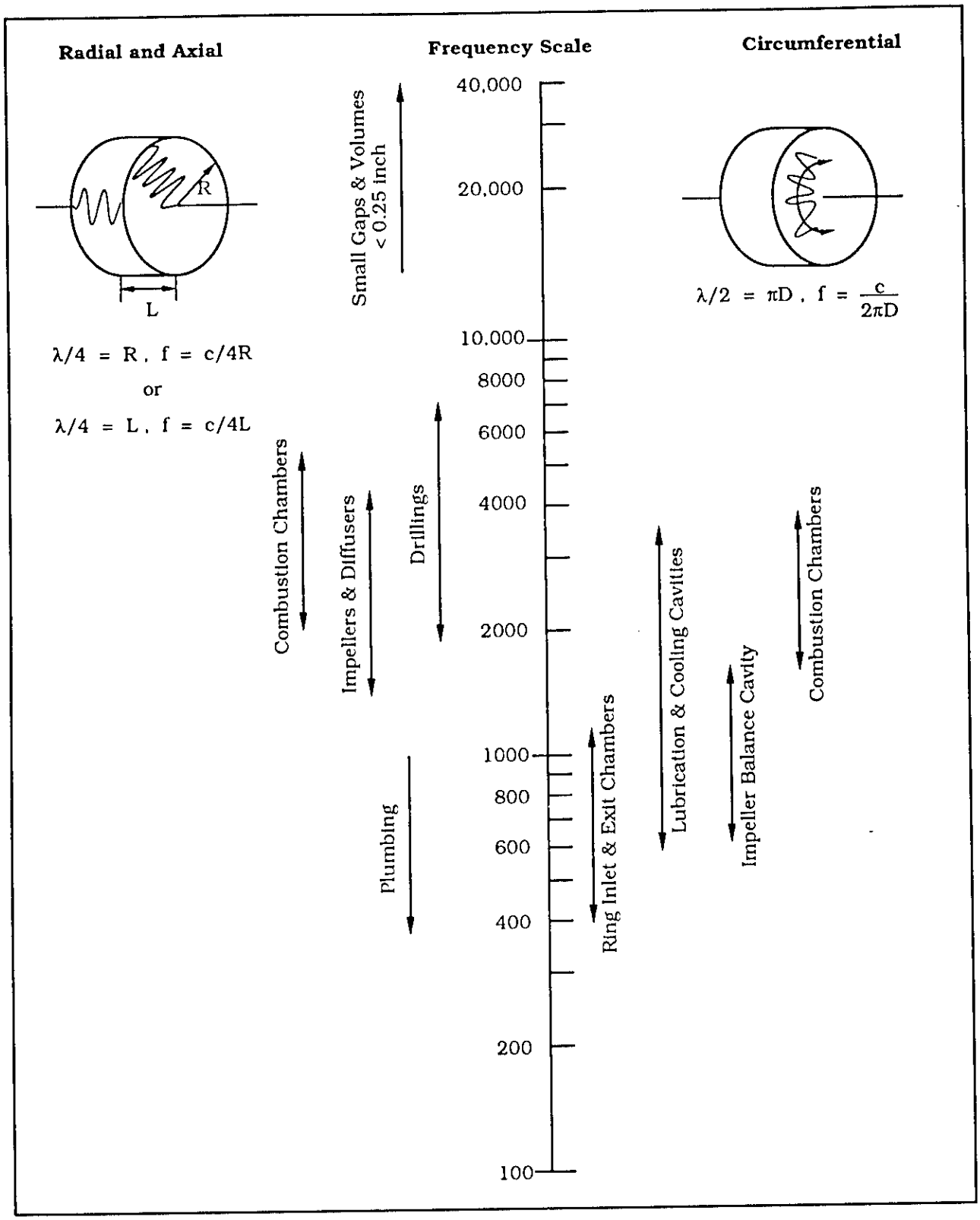

Figure 1-2. Range of Resonance Frequencies Found Inside Turbomachinery.

Table 1-2

Selected Cavities Inside Turbomachinery

	Basic Cavity	Variation of Basic Cavity	Significant Parameters	Approximate Range of Dimensions
Cavity Without Branch Pipe	**Simple Axisymmetric Cavity** 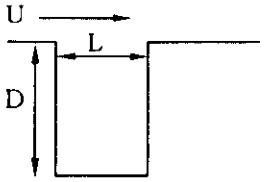	Bellows 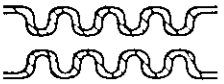 Sliding Expansion Joint  Turbine Blade Tip Seal 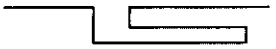	U = Free-stream velocity L = Cavity length D = Cavity depth M = Mach number	L/D ≤ 1 M < 0.15
	Non-Axisymmetric Helmholtz Resonator 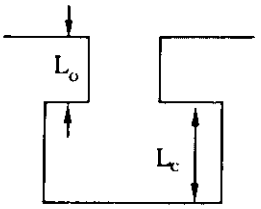	Combustion Chamber Resonator 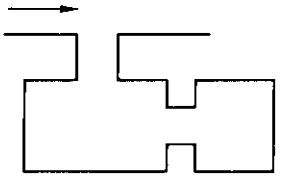	L_o = Neck length L_c = Cavity depth A_o = Orifice cross-sectional area A_c = Cavity cross-sectional area	L_o < 0.2 inch L_c < 0.5 inch A_o / A_c < 0.1
Cavity With Branch Pipe	**Simple Axisymmetric Cavity With Exit Flowing Fluid** 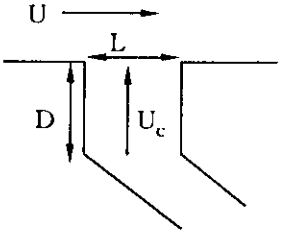	Lubrication and Cooling Port 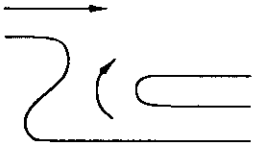	U = Free-stream velocity U_c = Cavity velocity L = Cavity length D = Cavity depth M = Mach number	L/D ≤ 1 M < 0.2 U_c / U < 1.5
	Simple Axisymmetric Cavity With Entrained Flowing Fluid 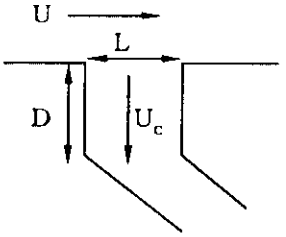	Lubrication and Cooling Port 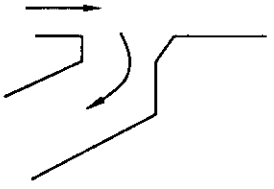	U = Free-stream velocity U_c = Cavity velocity L = Cavity length D = Cavity depth M = Mach number	L/D ≤ 0.5 M < 0.4 U / U_c < 0.1

below 5000 Hz. Furthermore, most sources of vibration concern in turbomachinery will be traceable to IIEs of the fluid-dynamic and fluid-resonator type. Based on this premise, all the models appearing in the handbook assume the basic mechanism as an Instability-Induced Excitation.

Also, given that the flows are internal, it is highly possible that an IIE may become coupled with an acoustic wave. To deal with this issue, the first part of the handbook (Chapters 2 through 6) presents a number of methods used to calculate acoustic resonances inside internal flow paths.

The second portion of the handbook (Chapters 7 through 11) reviews models that pertain to IIE. Included in the handbook are frequency prediction formulae for jets, wakes, and mixing layers. Also discussed at great length are aspects dealing with leading edge interactions. The models are organized according to the basic categories of shear layer flows and those having leading edge interactions.

Shown in Tables 1-3 and 1-4 are the acoustic and flow models considered in this handbook. The models appearing in these chapters were selected based upon results of the previous survey. In Table 1-3, the table is divided into two parts: discrete resonators - having a cavity small in terms of the acoustic wavelength, and distributed resonators - having cavity length measuring several acoustic wavelengths and a transverse dimension typically small in terms of the acoustic wavelength. In Table 1-4, the top row shows the basic flow configurations; below each configuration is shown the basic model acting with an acoustic resonator. These two tables are keyed to chapters in the handbook.

Table 1-3

Acoustic Resonator Models

	DISCRETE RESONATOR	DISTRIBUTED RESONATOR
PRINCIPLES	Acoustic Wavelength >> Characteristic Length Scale 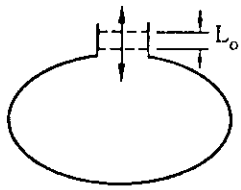	Acoustic Wavelength ≤ Characteristic Length Scale 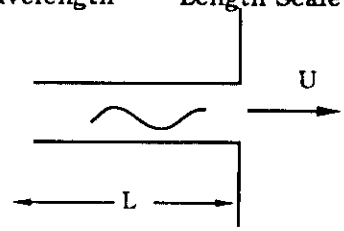
ACOUSTIC MODELS	CHAPTER 2 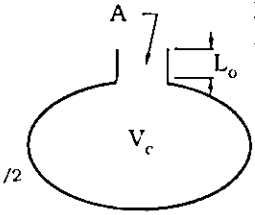 Ideal Helmholtz Resonator $\lambda >> L_o$ $\lambda >> A_o^{1/2}$ $\lambda >> V_c^{1/3}$	CHAPTER 4 $\lambda \leq L_1$, or L_2 , or L_3 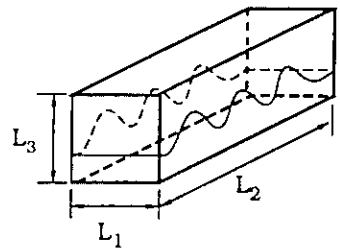 No Mean Flow
	CHAPTER 2 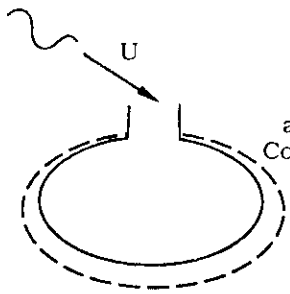 Skew and/or Compliant	CHAPTER 5 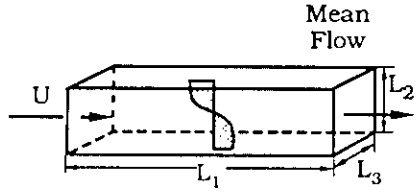 $\lambda \leq L_1$, or L_2 , or L_3
	CHAPTER 3 Filters 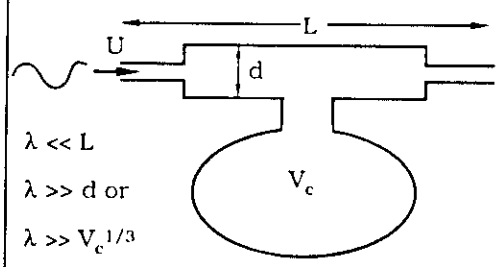 $\lambda << L$ $\lambda >> d$ or $\lambda >> V_c^{1/3}$	CHAPTER 6 Cascades 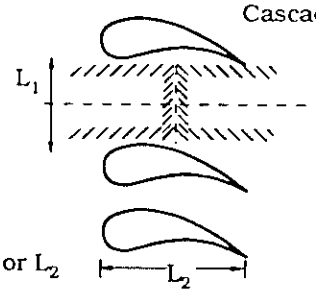 $\lambda \leq L_1$ or L_2

Table 1-4

Instability-Induced Excitation Models.

BASIC EXCITATION MECHANISMS	BASIC FLOW MODELS					
	CHAPTER 7 Mixing Layer	CHAPTER 8 Jets	CHAPTER 9 Wakes	CHAPTER 10 Swirling Flows	CHAPTER 11 Impinging Shear Layers	
					Jet Tones	Cavities
Fluid Dynamic Instability	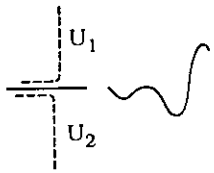	Planar: 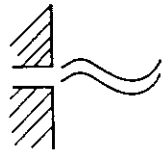 Axisymmetric: 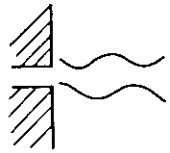	Single:  Multiple: 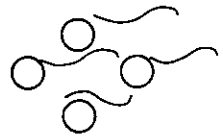	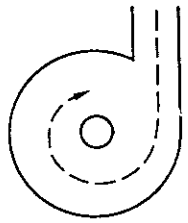	Hole Tone: 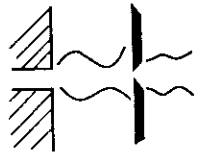 Edge Tone: 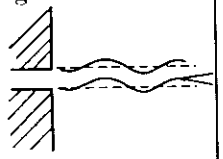	Shallow 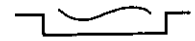 to Deep 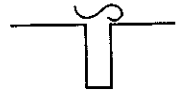
Fluid Dynamic Instability Coupled With Acoustic Resonators	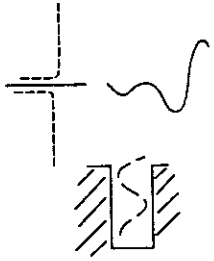	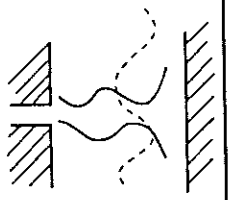	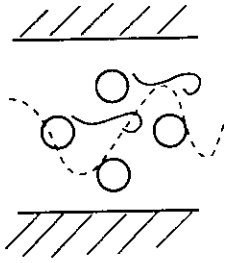	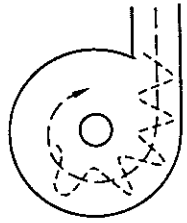	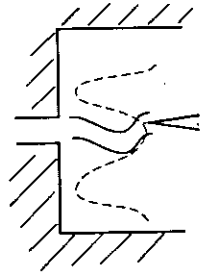	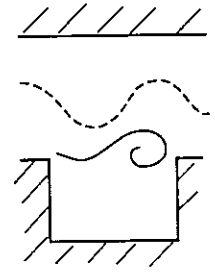

PART I

ACOUSTIC RESONATOR MODELING

CHAPTER 2

CAVITY RESONATORS

by Miguel C. Junger
Cambridge Acoustical Associates

The basic forms of cavity resonators are (a) resonators with cavities small in terms of acoustic wavelengths; (b) elongated cavities, e.g., pipes, which display a length measuring several acoustic wavelengths and transverse dimensions typically small in terms of acoustic wavelengths; and (c) fluid-filled spaces whose three dimensions measure several wavelengths. The mechanical analog of (a) is the simple mass–spring oscillator. The mechanical analog of (b) is a waveguide, *viz*, a column measuring several compressional wavelengths. The mechanical analog of (c) is a multi-modal, three-dimensional structure.

Systems of type (c), which are typically dealt with by means of statistical techniques, *viz*, room acoustics, are not relevant to turbomachine acoustics. In covering type (a) and (b) systems, we shall rely as much as possible on the familiar field of structural vibration.

Sections 2.1 and 2.2 introduces the basic mathematical models. Section 2.3 considers the situation when the resonator is filled with a liquid and the boundaries of the resonator are no longer rigid. Section 2.4 describes the resonator characteristics when a damping material is inserted into the orifice. Section 2.5 considers the Helmholtz resonator as a side branch. Sections 2.6 and 2.7 describe the effects of a high-incident pressure and turbulent flows incident on the mouth of the resonator.

2.1 The Helmholtz Resonator Reactance and Natural Frequency

2.1.1 The Mechanical–Acoustical Analog

A Helmholtz resonator's cavity is the equivalent of the spring of a simple oscillator. Figure 2-1 presents a sketch of a Helmholtz-type cavity and its spring-mass equivalent. The resonator's spring constant, K, is determined by the compliance of the fluid-filled cavity and of its boundaries.

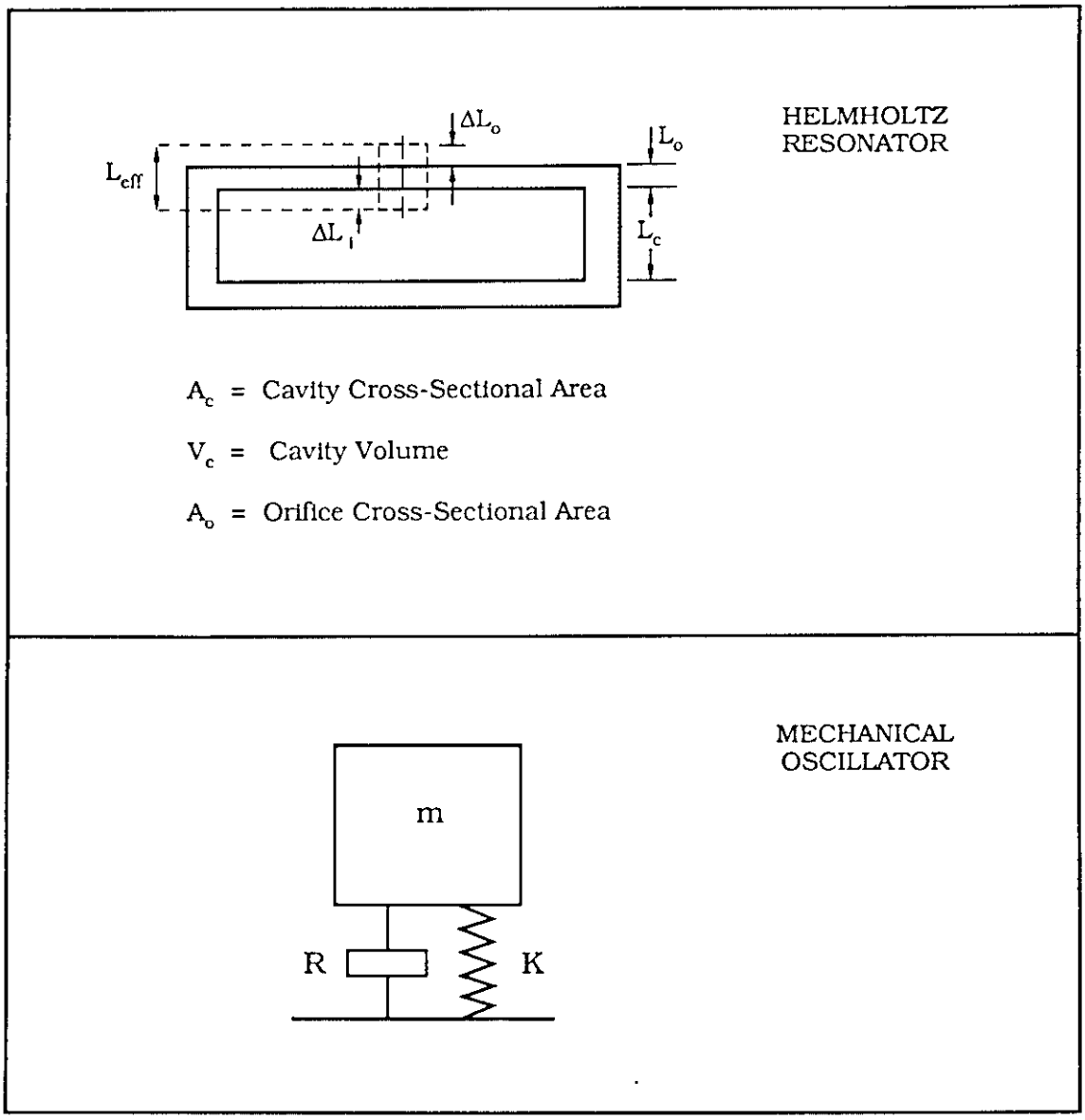

Figure 2-1. The Helmholtz Resonator and Its Mechanical Analog, the Simple Oscillator.

The equivalent of the oscillator mass, m, is the fluid mass in the resonator neck plus the entrained fluid mass. The latter can be envisioned as the reactive radiating loading on two virtual pistons forming the boundaries between the neck and, respectively, the cavity and exterior space. Even if the neck length L_o (see Figure 2-1) is small, the sloshing of fluid through the orifice as the cavity is alternatively compressed and decompressed entrains a mass of fluid corresponding to a volume $A_o \Delta L$ of fluid, where A_o is the orifice cross-sectional area and ΔL is the sum of the lengths of the entrained fluid outside the cavity, ΔL_o, and the entrained fluid within the cavity, ΔL_i.

The analog of the dashpot resistance in the mechanical system, R, is the sum of two components: the acoustic resistance R_a associated with sound radiation by the above-mentioned outward-facing virtual piston and the viscous resistance R_v embodying frictional losses. In airborne noise control applications, the latter resistance is deliberately enhanced, e.g., by inserting a fiberglass plug in the neck.

In this connection it is noted that Helmholtz resonators, which are now used to absorb noise, particularly narrowband noise such as associated with transformers, had been used traditionally in churches and theaters to render the space more reverberant. The name of the 19th century physicist Helmholtz was attached to the resonator not because he invented it but because he was the first to analyze it. It is this reverberation-enhancing performance of the Helmholtz resonator which is a potential problem in turbomachinery.

2.1.2 The Natural Frequency of the Helmholtz Resonator

The adiabatic bulk modulus (B) of a fluid – whether gas or liquid – relates the volume strain ($\Delta V/V$) of the adiabatically compressed fluid to the applied pressure. The applied pressure can be expressed as

$$p = -B \Delta V/V . \tag{2-1}$$

For a gas, B is a function of the ambient pressure P_∞,

$$B = \gamma P_\infty , \tag{2-2}$$

where γ is the ratio of the specific heats at, respectively, constant pressure and constant volume. The ratio γ, which is 1.40 for air under normal atmospheric conditions, is a function of pressure and, to a lesser extent, of temperature.[1] For 100 atm and -79°C $\gamma_{air} = 2.20$. The bulk modulus for a liquid and a gas is commonly expressed as

$$B = \rho c^2 , \tag{2-3}$$

where ρ is density and c sound speed. The bulk modulus of a liquid is far less sensitive to pressure and temperature.

Applying Equation (2-2) to the resonator,

$$\frac{\Delta V}{V} = - \frac{A_o \delta}{L_c A_c} , \tag{2-4}$$

where A_o and A_c are, respectively, the cross-sectional areas of the orifice and of the cavity, L_c is the cavity depth, and δ is the displacement of the virtual piston defining the boundary between the orifice and exterior space. The force acting on the piston is

$$F = A_o p . \tag{2-5}$$

Combining Equations (2-1), (2-4), and (2-5), one formulates the effective stiffness

$$\begin{aligned} K &= \frac{F}{\delta} \\ &= \frac{B A_o^2}{L_c A_c} \\ &= B A_o^2 / V_c , \end{aligned} \tag{2-6}$$

where $V_c = L_c A_c$ is the cavity volume.

As already mentioned, the mass is the mass in the orifice neck (with length L_o) augmented by the entrained mass of the virtual pistons forming the interface between the neck and, respectively, the exterior space (length ΔL_o) and the cavity (length ΔL_i). For openings small in terms of the cavity's cross-sectional area as well as of the wavelength squared, the entrained mass is that of a baffled piston with lengths[2]

$$\Delta L_o = \Delta L_i = 0.850\,(A_o/\pi)^{1/2}\,; \quad A_o \ll A_c,\ \lambda^2$$

$$= 0.48\,A_o^{1/2}. \tag{2-7}$$

This asymptotic small-orifice result is insensitive to cross-section geometry. As the orifice area increases, ΔL_i decreases, as seen from a graph in Figure 2-2 computed by Ingard.[3] An approximate expression for these curves is

$$\Delta L_i \cong 0.48\,A_o^{1/2}\,\left[1 - 1.25\,(A_o/A_c)^{1/2}\right]. \tag{2-8}$$

If the orifice opens outward through an extended boundary, the expression for ΔL_o in Equation (2-7) holds irrespective of A_o/A_c provided $A_o \ll \lambda^2$. Assuming this to be the case, the effective resonator mass is

$$m = \rho\,A_o\,L_{eff}, \tag{2-9}$$

where L_{eff} is the effective neck length shown in Figure 2-1 and is

$$L_{eff} = L_o + \Delta L_o + \Delta L_i$$

$$= L_o + 0.48\,A_o^{1/2}\,\left[2 - 1.25\,(A_o/A_c)^{1/2}\right]. \tag{2-10}$$

The density ρ of a gas is given by

$$\rho = \frac{\rho_o\,P_\infty}{(T/273)}, \tag{2-11}$$

where ρ_o is the density at 0°C (273°K) and atmospheric pressure (1.23×10^{-3} g/cm^3 for air), P_∞ is the pressure of the gas in atmospheres, and T is the temperature in degrees Kelvin.[4] The density of liquid is relatively insensitive to pressure and temperature.[5]

Substituting the above results for stiffness and mass, the familiar expression for the natural frequency of a simple oscillator is

$$f_n = \frac{1}{2\pi}\left(\frac{K}{m}\right)^{1/2}$$

$$= \frac{1}{2\pi}\left(\frac{B\,A_o}{\rho\,V_c\,L_{eff}}\right)^{1/2}. \tag{2-12a}$$

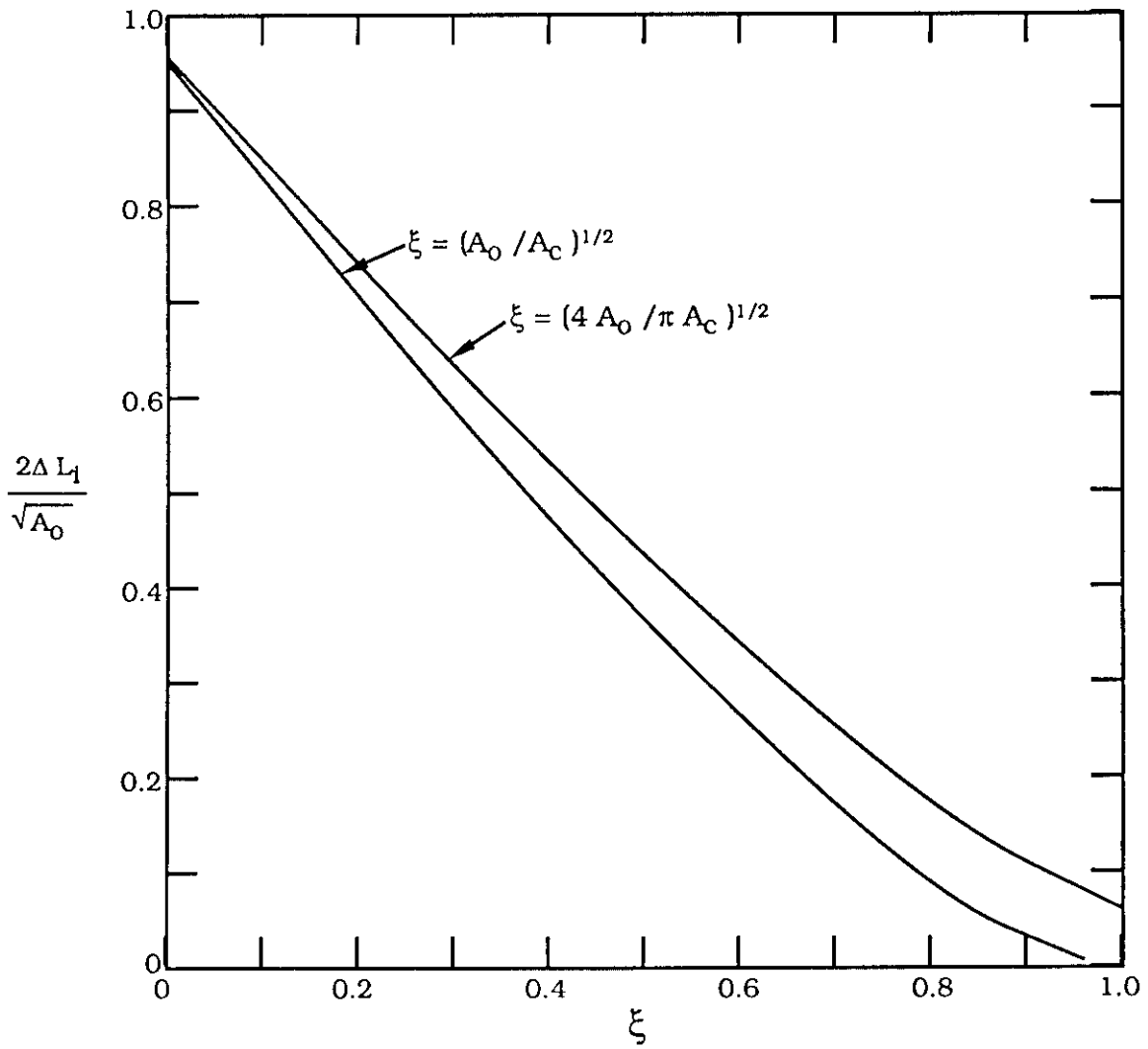

Figure 2-2. The Mass End Correction ΔL_i. (Reproduced from Ingard.[3])

Since $B = \rho c^2$, the term $(B/\rho)^{1/2}$ can be replaced with c so that

$$f_n = \frac{c}{2\pi} \left(\frac{A_o}{V_c L_{eff}} \right)^{1/2} . \qquad (2\text{-}12b)$$

Recalling that gasses have a density and bulk modulus which depend strongly on pressure and temperature, one would expect the same to hold for the sound velocity and consequently for f_n . Referring to Equations (2-2) and (2-11), one notes that the pressure cancels out, the sound velocity and hence f_n are only dependent on temperature

$$c(T) = c_o [T/273]^{1/2} , \qquad (2\text{-}13)$$

where c_o is the sound speed at 273°K (3.31×10^4 cm/s for air), and T is in degrees Kelvin. Consequently,

$$f_n(T) = \frac{c_o}{2\pi} \left(\frac{A_o T/273}{V_c L_{eff}} \right)^{1/2} . \qquad (2\text{-}14a)$$

Example Calculation

To illustrate the above result, consider an air-filled resonator with $L_o/\Delta L_o \ll 1$ and $A_o/A_c \ll 1$. In view of the latter inequality, Equation (2-10) applies, and

$$L_{eff} \cong 0.96\, A_o^{1/2} \cong A_o^{1/2} . \qquad (2\text{-}14b)$$

The natural frequency now becomes

$$f_n = \frac{3.31 \times 10^4}{2\pi} \left(\frac{A_o^{1/2} T/273}{V_c} \right)^{1/2} . \qquad (2\text{-}15)$$

As an example, at a temperature of $T = 293$°K, an orifice cross-sectional area $A_o = 10$ cm^2 , and a cavity volume $V_c = 1000$ cm^3 , the natural frequency computed with Equation (2-15) is 307 Hz.

2.2 Range of Validity of the Helmholtz Resonator Theory

The range of validity of the mathematical model of the cavity as a spring will be explored as it is applied to waveguides. A waveguide of length L_c terminated by a rigid boundary displays a standing wave pressure field of the form

$$p(x) = P \cos [k (x - L_c)] , \tag{2-16}$$

where $k = \omega/c$ = wavenumber and $\omega = 2\pi f$ is the angular frequency. The corresponding displacement δ_c at the open end of the cavity (x = 0) is given by Euler's equation specialized to harmonic motions whereby $\ddot{\delta}_c = -\omega^2 \delta_c$, or

$$\begin{aligned} \delta_c &= \frac{1}{\rho \omega^2} \frac{\partial p}{\partial x} \Bigg|_{x=0} \\ &= \frac{P k}{\rho \omega^2} \sin (k L_c) \\ &= \frac{P}{\rho c^2 k} \sin (k L_c). \end{aligned} \tag{2-17a}$$

Preserving a constant volume velocity, the corresponding particle displacement in the resonator neck is

$$\delta = \frac{A_c}{A_o} \delta_c . \tag{2-17b}$$

The pressure is also continuous at x = 0. Consequently, the effective stiffness at the neck–cavity interface is

$$\begin{aligned} K &= \frac{A_o p}{\delta} \\ &= \frac{A_o^2}{A_c} \frac{p}{\delta_c} \\ &= \frac{A_o^2}{A_c} \rho c^2 k \cot (k L_c). \end{aligned} \tag{2-18}$$

Noting that

$$\cot (x) = \frac{1}{x}\left(1 - \frac{x^2}{3} \ldots\right). \tag{2-19}$$

The low-frequency limit of the stiffness, for which $k^2 L_c^2/3 \ll 1$, is

$$K = \frac{A_0^2}{A_c} \frac{\rho c^2}{L_c}. \tag{2-20}$$

This inequality can now be used to formulate the restriction that resonator dimensions must satisfy to make the elementary theory applicable. The wave-number at the Helmholtz resonance is obtained from Equation (2-12b):

$$\begin{aligned} k^2 &= \frac{\omega^2}{c^2} = \frac{4\pi^2 f_n^2}{c^2} \\ &= \frac{A_0}{V_c L_{eff}} \\ &= \frac{A_0}{A_c L_c L_{eff}}. \end{aligned} \tag{2-21}$$

The inequality in Equation (2-20) now becomes

$$\frac{A_0}{3A_c} \frac{L_c}{L_{eff}} \ll 1, \tag{2-22}$$

which is the restriction that resonator dimensions must satisfy to make the elementary theory applicable.

Example Calculation

Using the numerical example selected in Section 2.1.2, the restriction becomes

$$\frac{A_0^{1/2} L_c^2}{3V_c} \cong 10^{-3} L_c^2 \ll 1.$$

The inequality implies

$$L_c \ll 31 \text{ cm}$$

and

$$A_c = \frac{V_c}{L_c} \gg 32 \text{ cm}^2. \tag{2-23}$$

A wave acoustic theory of the Helmholtz resonator which does not place limitations on cavity dimensions, and which yields somewhat more accurate expressions for the natural frequencies, was formulated by Bigg.[6] In view of the uncertainties brought on by dependence of the sound velocity on temperature as well as the presence of impurities, the more refined theory need not be introduced here.

2.3 The Liquid-Filled Cavity Resonator

For gas-filled cavities, the compressibility of the fluid in the cavity short-circuits the compliance of the boundary, except for unusually high static pressures. Boundaries were therefore considered rigid in the preceding sections. Because of the large bulk modulus of liquids, the boundary compliance cannot be ignored in this section.

The effective bulk modulus of a body of liquid in an elastic boundary is obtained by combining the compliances of the two media. The bulk modulus of the liquid is of course ρc^2, as it is for gases but, as already mentioned, it is comparatively insensitive to pressure and temperature. To illustrate the calculation of the effective bulk modulus, consider a cylindrical shell of diameter $2r_s$, length L_c, and wall thickness h. The desired insight can be gained from an elementary mathematical model of the cylindrical boundary whereby the radial expansion is assumed uniform, the axial expansion of the cavity being ignored. The hoop stress is computed from simple static equilibrium considerations

$$\sigma = p r_s / h . \tag{2-24}$$

The hoop strain is

$$\epsilon = \frac{\sigma}{E} = \frac{p\, r_s}{E\, h}, \tag{2-25}$$

where E is the Young's modulus. From simple geometric considerations, the hoop strain can also be related to the uniform radial displacement w where

$$\begin{aligned} w &= \epsilon r_s \\ &= \frac{p\, r_s^2}{E\, h} . \end{aligned} \tag{2-26}$$

The volume strain is

$$\begin{aligned} \frac{\Delta V}{V} &= \frac{2\pi\, r_s\, L_c\, w}{\pi\, r_s^2\, L_c} \\ &= \frac{2w}{r_s} . \end{aligned} \tag{2-27}$$

Substituting Equation (2-26),

$$\frac{\Delta V}{V} = \frac{2\,p\,r_s}{Eh}. \tag{2-28}$$

Consequently, the bulk modulus of the shell, B_s computed from Equation (2-1) (with a sign reversal because the pressure acts outward on the boundary, while the definition in Equation (2-1) assumes an inward-acting pressure), is

$$B_s = \frac{Eh}{2\,r_s}. \tag{2-29}$$

A slightly different expression would have been obtained had the axial strain been taken into account. The reader can, as an exercise, compute the effective bulk modulus contribution of various shells by referring to familiar handbooks.[7] The effective volume change which determines the cavity stiffness at the neck–cavity interface is obtained by adding the compression of the liquid and the expansion of the boundary

$$\frac{\Delta V}{V} = -p\left(\frac{1}{\rho c^2} + \frac{2\,r_s}{Eh}\right). \tag{2-30}$$

This can be generalized to arbitrary boundary geometries

$$\frac{\Delta V}{V} = -p\,(B_L^{-1} + B_s^{-1}), \tag{2-31}$$

where B_L is the bulk modulus of the liquid. The effective bulk modulus is therefore

$$\begin{aligned} B_{eff} &= \left(B_L^{-1} + B_s^{-1}\right)^{-1} \\ &= B_L\left(1 + \frac{B_L}{B_s}\right)^{-1}. \end{aligned} \tag{2-32}$$

Referring to electric circuit theory, the two bulk moduli are seen to add in parallel. Clearly, if the shell is quite flexible, the compressibility of the liquid is short-circuited.

Example Calculation

As a realistic example, consider a cylindrical steel shell ($E = 2.1 \times 10^{12}$ μ bar) containing water ($B_L = 2.2 \times 10^{10}$ μ bar), the thickness-to-radius ratio being $h/r_s = 1/50$. The ratio of the two bulk moduli is

$$\frac{B_L}{B_s} = \frac{2\rho c^2 r_s}{E h}$$

$$= 1.04. \qquad (2\text{-}33)$$

The effective bulk modulus, Equation (2-32), therefore becomes

$$B_{eff} = \frac{2.2 \times 10^{10}}{(1 + 1.04)}$$

$$= 1.1 \times 10^{10} \text{ μ bar}. \qquad (2\text{-}34)$$

This can now be substituted in Equation (2-12). Retaining resonator dimensions assumed earlier, the natural frequency of the liquid-filled resonator is

$$f_n = \frac{1}{2\pi} \left(\frac{B A_o^{1/2} r_s}{0.96 \rho V} \right)^{1/2}$$

$$= 958 \text{ Hz}. \qquad (2\text{-}35)$$

Even though the natural frequency is considerably higher than for the air-filled cavity, the inequality underlying the Helmholtz mathematical model is readily satisfied because the sound velocity is correspondingly larger. In other words, the cavity dimension rather than the acoustic fluid determines whether the Helmholtz model is valid. This is apparent from the inequality in Equation (2-22) which does not contain any of the acoustic fluid parameters. The above calculation does contain other approximations, the kinetic energy not only of the shell wall but also of the radial motion of the liquid in the cavity having been ignored. This is, however, small compared to the kinetic energy of the liquid sloshing through the orifice for the small ratio A_o/A_c assumed here.

It is interesting to note that this result could have been obtained directly from Equation (2-12) had the Korteweg-Lamb correction been applied to the sound velocity in an elastic pipe.[8] The Korteweg-Lamb correction will be discussed further in Section 4.1.

2.4 Helmholtz Resonator Damping

So far only the reactive portion of the resonator impedance has been analyzed. When resonators are used for the purpose of sound absorption, screens or fiberglass are inserted in the orifice to enhance sound dissipation, the maximum absorption cross-section being achieved when the acoustic and frictional resistance are matched. As long as $A_o \ll \lambda^2$, the acoustic resistance depends primarily on the orifice area A_o and only mildly on its shape. Therefore, results strictly applicable to circular orifices whose acoustic resistance is[2]

$$R_a = 2\pi\rho f^2 A_o^2/c, \tag{2-36}$$

are only considered. Referring to Equation (2-12), the acoustic resistance at resonance ($f = f_n$) becomes

$$R_a = \frac{\rho c A_o^3}{2\pi V_c L_{eff}}$$

$$= \frac{\rho c A_o^{5/2}}{2\pi V_c}, \tag{2-37}$$

where use has been made of Equation (2-14b).

The corresponding acoustic quality factor, which is a measure of the sharpness of the resonance of the Helmholtz resonator, is

$$Q_a = \frac{(K m)^{1/2}}{R_a}. \tag{2-38}$$

Combining Equations (2-6), (2-9), and (2-37),

$$Q_a = 2\pi \left(\frac{V_c L_{eff}^3}{A_o^3}\right)^{1/2}. \tag{2-39a}$$

For the numerical example selected earlier, for which $L_{eff} \equiv A_o^{1/2}$, the quality factor becomes

$$Q_a = 2\pi \left(V_c/A_o^{3/2}\right)^{1/2}$$

$$= 2\pi \left(10^3/10^{3/2}\right)^{1/2} = 35. \tag{2-39b}$$

It is noteworthy that the fluid parameters drop out, and that the quality factor is therefore independent of pressure and temperature. This, of course, does not follow for the resistance, Equation (2-37), which is proportional to ρc, since

$$\rho c = \rho_o c_o P \left(\frac{273}{T}\right)^{1/2}, \tag{2-40}$$

where $\rho_o c_o = 42.8\ \mu$ bar/cm/sec for air, P is in atmospheres, and T is in degrees Kelvin.

Additional damping is provided by fluid viscosity and to a much lesser extent by heat conduction. For air in the absence of a screen, the viscous resistance is typically small compared to the acoustic resistance. In our notation, the viscous resistance is

$$R_v = 2 R_s A_o \left(\frac{L_o}{r_s} + 2\right), \tag{2-41}$$

(Reference 3, Equation (11), where θ_e, the viscous end correction, is taken equal to $4 R_s/\rho c$, rather than the theoretical result $2 R_s/\rho c$, to account for experimental results also reported in Reference 3). The viscous surface resistance in terms of the viscosity μ is

$$R_s = (\pi \mu \rho f)^{1/2}. \tag{2-42}$$

Normalizing to the acoustic resistance, the resistance ratio at resonance is

$$\frac{R_v}{R_a} = \pi \left(\frac{L_o}{r_s} + 2\right) \left(\frac{8\mu}{\rho c}\right)^{1/2} \left(\frac{V_c^3 L_{eff}^3}{A_o^7}\right)^{1/4}$$

$$\equiv 2\pi \left(\frac{8\mu}{\rho c}\right)^{1/2} \frac{V_c^{3/4}}{A_o^{11/8}}, \quad L_o \equiv 0 \tag{2-43a}$$

where use has been made of Equations (2-12b) and (2-14b). The relevant parameters for air and water are tabulated in Table 2-1, as are the results of the resistance calculations for the resonator parameters used in earlier examples. The resultant Q accounting both for acoustical and viscous losses is

$$Q = Q_a \left[1 + \frac{R_v}{R_a}\right]^{-1} \tag{2-43b}$$

and also tabulated in Table 2-1. Even though the application of Equations (2-41) and (2-42) to water is a crude approximation, it adequately shows that, in the absence of an energy-absorbing device such as a screen, the resistance is mostly associated with the radiation resistance for the Helmholtz resonator parameters selected.

Table 2-1

Examples of Resistance Calculations for the Air and the Water-Filled Resonator

Parameter		Air (T = 293°K)	Water
Symbol	**Units**		
μ	μbar s	1.81×10^{-4}	0.01
ρ	g/cm^3	1.21×10^{-3}	1.0
μ/ρ	cm^2/s	0.15	0.01
c	cm/s	3.43×10^4	1.48×10^5
f_n	Hz	307	958
$\frac{R_v}{R_a}$	dimensionless [see Eq. (2-43)a]	0.27	0.034
Q_a	dimensionless [see Eq. (2-39b)]	35	35
Q	dimensionless [see Eq. (2-43b)]	28	34

2.5 The Helmholtz Resonator as a Side Branch

Although sound propagation in pipes will be studied in detail in Sections 3, 4, and 5, this section considers an elementary low-frequency situation of an incident plane sound wave propagating in a pipe. The purpose of this example is to demonstrate an application of the Helmholtz model and its electrical circuit analog to determine transmission loss as a function of frequency. Neglecting pipe wall compliance, the pressure propagates at the speed of sound in the fluid in the form of

$$p_i(x) = P_i \exp(ikx). \tag{2-44}$$

Since the pipe cross-sectional area, A_p, generally differs from A_o, it is desirable to introduce volume velocity. The volume velocity of the incident wave is

$$\dot{Q}_i = \frac{A_p P_i}{\rho c}. \tag{2-45}$$

The acoustic impedance in units of pressure per volume velocity is

$$Z_p = \frac{\rho c}{A_p}. \tag{2-46a}$$

That of the Helmholtz resonator is

$$\begin{aligned} Z_H &= \frac{i}{A_o^2}\left(\frac{K}{\omega} - \omega M\right) + \frac{R_a}{A_o^2}\left(1 + \frac{R_v}{R_a}\right) \\ &= \frac{iK}{2\pi f A_o^2}\left[\left(1 - \frac{i}{Q}\frac{f}{f_n}\right) - \frac{f^2}{f_n^2}\right]. \end{aligned} \tag{2-46b}$$

The reflected pressure can now be computed. The impedance at the pipe resonator junction is represented by a shunt circuit in Figure 2-3, where the Helmholtz resonator is short-circuiting energy flow into the downstream portion of the pipe. Using the subscripts R and T to identify the reflected and transmitted pressure, respectively,

$$\begin{aligned} p_R(x) &= P_R \exp(-ikx), \\ \dot{Q}_R &= -\frac{P_R A_p}{\rho c}, \end{aligned} \tag{2-47a}$$

$$\begin{aligned} p_T(x) &= P_T \exp(ikx), \\ \dot{Q}_T &= \frac{P_T A_p}{\rho c}. \end{aligned} \tag{2-47b}$$

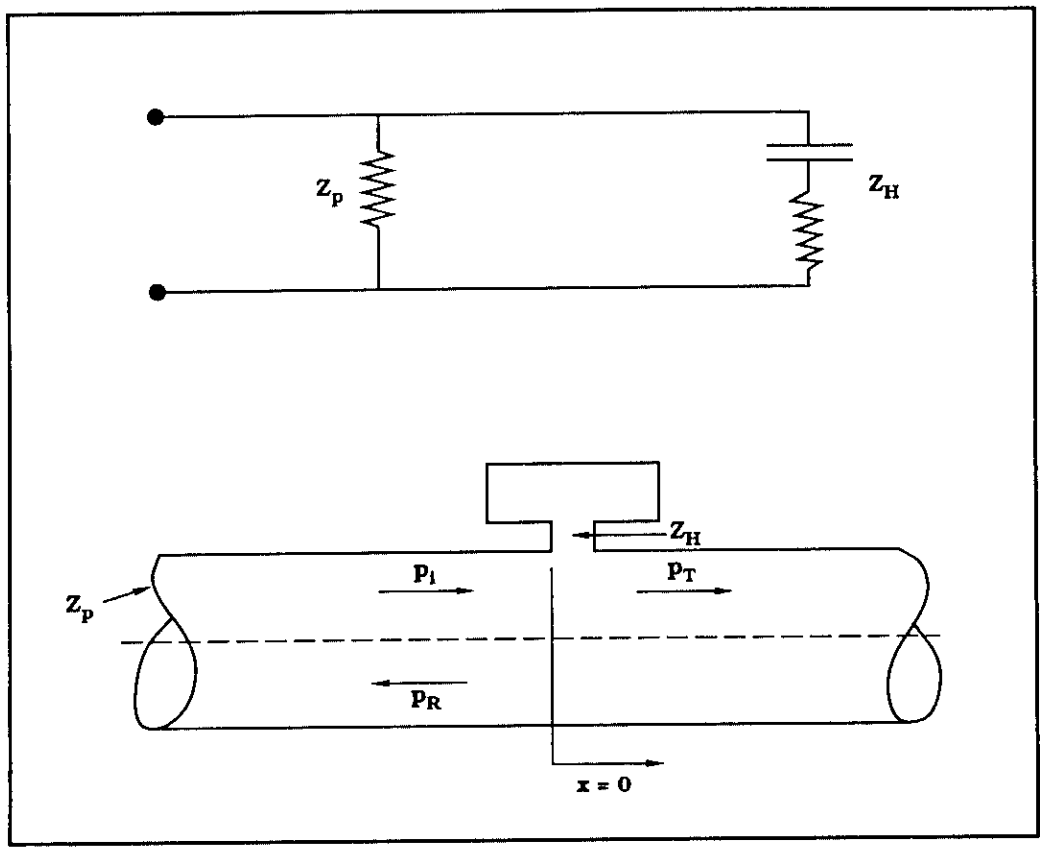

Figure 2-3. The Analog Circuit of a Pipe Provided With a Side Branch in the Form of a Helmholtz Resonator.

[Z_p = pipe impedance, Equation (2-46a).
Z_H = resonator impedance, Equation (2-46b).]

Continuity of pressure and of volume velocity at $x = 0$ requires that

$$P_R + P_I = P_T , \tag{2-48a}$$

$$= P_H , \tag{2-48b}$$

$$\dot{Q}_I + \dot{Q}_R = \dot{Q}_T + \dot{Q}_H , \tag{2-48c}$$

$$\dot{Q}_H = \frac{P_H}{Z_H} , \tag{2-48d}$$

where the subscript H identifies the Helmholtz resonator. Substituting Equations (2-45), (2-47a), (2-47b), and (2-48d) for the volume velocities, and using Equations (2-46a) and (2-48b), Equation (2-48c) becomes

$$\frac{P_I}{Z_p} - \frac{P_R}{Z_p} = P_T\left(\frac{1}{Z_p} + \frac{1}{Z_H}\right). \tag{2-49}$$

Consequently, the impedance just upstream of the resonator is (Figure 2-3)

$$Z = \left(Z_p^{-1} + Z_H^{-1}\right)^{-1} . \tag{2-50}$$

The simultaneous equations, Equations (2-48a) and (2-49), can now be solved for the reflected and transmitted pressure ratios:

$$\frac{P_T}{P_I} = \left(1 + \frac{Z_p}{2\,Z_H}\right)^{-1} ,$$

$$\frac{P_R}{P_I} = -\left(\frac{2\,Z_H}{Z_p} + 1\right)^{-1} . \tag{2-51}$$

At the Helmholtz resonance, the resonator impedance, Equation (2-46b), reduces, with the application of Equations (2-12a) and (2-35), to

$$Z_H = \frac{R_a}{A_o^2}\left(1 + \frac{R_v}{R_a}\right) \quad , \quad f = f_n . \tag{2-52}$$

At resonance, the resonator short-circuits the transmission of acoustic energy, i.e., $\left|P_R/P_I\right|$ approaches unity and $\left|P_T/P_I\right| \cong 0$. The resonator effectively simulates a pressure release termination. The transmission loss is

$$TL = -20 \log_{10} \frac{P_T}{P_I}$$

$$= 20 \log_{10}\left(1 + \frac{\rho\, c\, A_o^2}{2\, A_p\, R_a}\right) \quad , \quad f = f_n . \tag{2-53}$$

Example Calculation

For the resonator parameters used earlier, and selecting a pipe whose cross-sectional area $A_p = 10\,A_o$,

$$\frac{2\,A_p\,R_a}{\rho\,c\,A_o^2} = \frac{A_p\,A_o^{1/2}}{\pi\,V_c}\left(1 + \frac{R_v}{R_a}\right) \quad , \quad f = f_n ,$$

$$= 0.127 \text{ for the air-filled resonator, and}$$

$$= 0.101 \text{ for the water-filled resonator.} \qquad (2\text{-}54)$$

Substituting these results in Equation (2-53), one computes a transmission loss of 19.0 dB for the air-filled resonator and of 20.7 dB for the water-filled resonator at their respective resonances. Sufficiently far from resonance, Z_H is large compared to Z_p and the resonator does not short-circuit the downstream pipe impedance. Substituting Z_H, Equation (2-46b) in lieu of R_a/A_o^2 in Equation (2-53), the transmission loss at low frequencies becomes

$$TL = 10\log_{10}\left[1 + \left(\frac{\rho\,c\,A_o^2\,\pi\,f}{A_p\,K}\right)^2\right]$$

$$= 10\log_{10}\left[1 + \left(\frac{\pi\,f\,V}{c\,A_p}\right)^2\right] \qquad f^2 \ll f_n^2$$

$$\cong 0 \quad \text{as} \quad f \to 0 \qquad (2\text{-}55)$$

and, at high frequencies, the transmission loss becomes

$$TL = 10\log_{10}\left[1 + \left(\frac{\rho\,c\,A_o^2}{4\,\pi\,f\,A_p\,M}\right)^2\right] \qquad f^2 \gg f_n^2$$

$$= 10\log_{10}\left[1 + \left(\frac{c\,A_o}{4\,\pi\,f\,A_p\,L_{eff}}\right)^2\right]$$

$$\cong 0 \quad \text{as} \quad f/f_n \to \infty . \qquad (2\text{-}56)$$

These trends are plotted schematically in Figure 2-4.

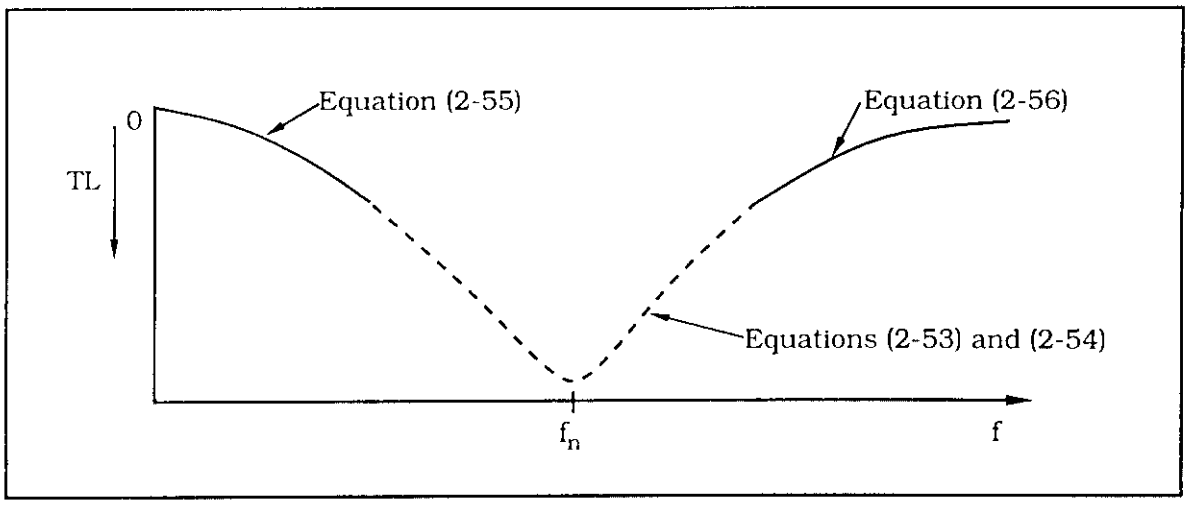

Figure 2-4. Schematic Plot of the Transmission Loss Provided by a Side Branch in the Form of a Helmholtz Resonator.

2.6 High Incident Pressure Amplitude on a Helmholtz Resonator

The basic discussion of Helmholtz resonators above assumes that the resonator is excited in a quiescent acoustic medium. The more likely situation in turbomachinery is one in which a cavity resonator is excited by a grazing flow across the orifice. The presence of the flow alters both the reactance (i.e., effective end correction) as well as the resistance of the resonator, thus shifting the resonance frequency and its quality factor. Unfortunately, the ability to predict these shifts has only been determined for a few geometries and flow ranges. The following is a brief summary of pertinent literature and results in this area.

A problem related to grazing flow past a Helmholtz resonator – namely, the non-linear dependence of the resistance of an orifice on large incident pressure amplitude – is treated by Ingard.[9,10] Here the non-linearity is due to flow separation and the formation of a jet on the downstream side of the orifice. This flow switches from side to side through an excitation period as sketched in Figure 2-5. Measurements made in the orifice show a distortion in the velocity curves with increasing sound pressure level and a gradual change in phase between the pressure and velocity. When the incident pressure amplitude exceeds a transition point, where pressure and velocity in the orifice begin to become distorted, the non-linear resistance of the orifice is approximately $\rho\, u^2$, where u is the acoustic velocity in the orifice.

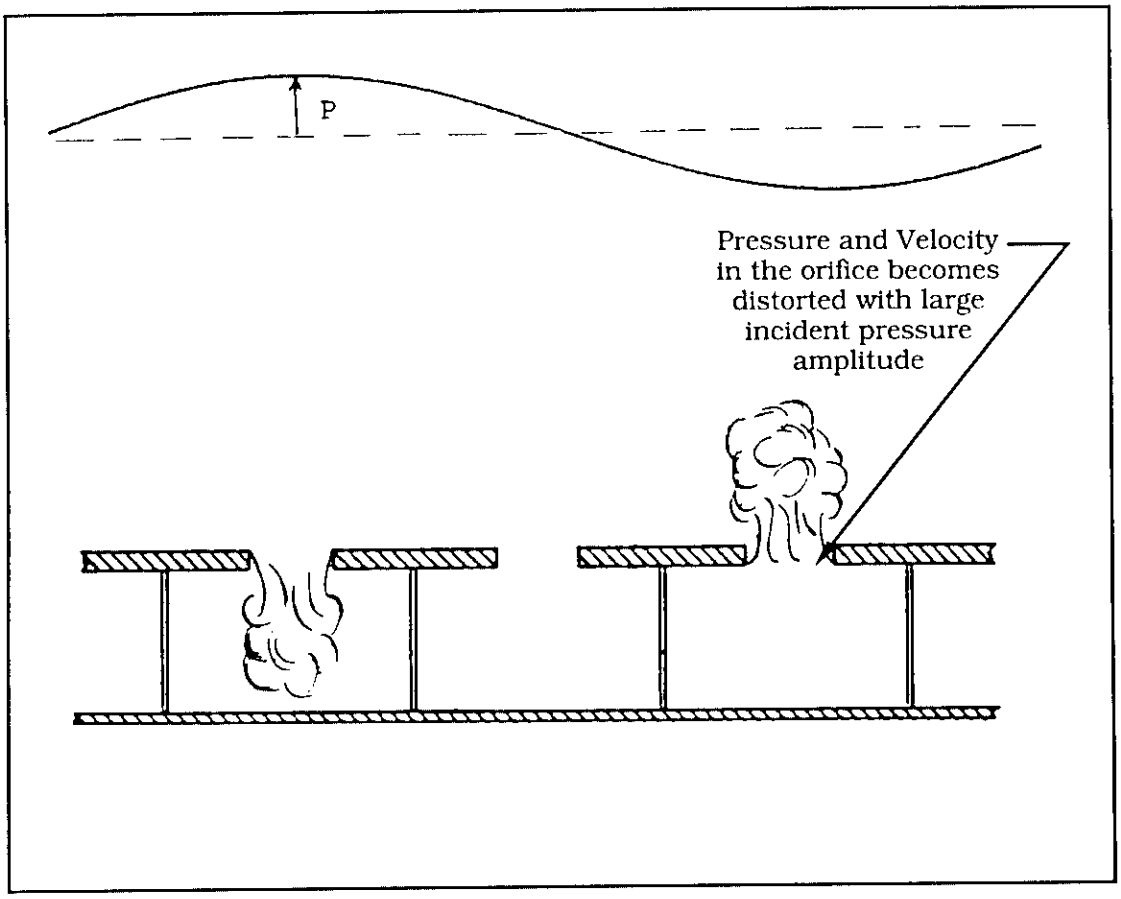

Figure 2-5. Schematic of Non-Linear Flow Separation and Jet Formation Through a Period of Excitation. (The source of this excitation is a large incident pressure amplitude.)

Ingard[10] provides a computational procedure to determine the transmission loss for a high-amplitude incident pressure field. The procedure requires knowledge of the angle of incidence and pressure amplitude of the wave front. Both parameters are difficult if not impossible to determine inside turbomachinery. An approximation made is to apply the end correction in Equation (2-10) only once. This will reflect the lack of added mass on the jet side of the orifice. Equation (2-10) then becomes

$$\begin{aligned} L_{eff} &= L_o + \Delta L_o \\ &= L_o + 0.48\, A_o^{1/2}. \end{aligned} \tag{2-57}$$

The effect of steady (i.e., "DC bias") flow through the orifice is discussed in Reference 9 where it is concluded that the dependence of orifice resistance on flow speed is similar to the non-linear dependence on unsteady orifice flow speed. The effect of a grazing turbulent flow on a resonator duct lining is briefly discussed in Reference 10. Turbulent pressure fluctuations are viewed as causing a slowly fluctuating bias flow in the orifice similar to the steady flow discussed above with corresponding resistance and reactance effects.

An analytical model of a circular cylindrical Helmholtz resonator in the wall of a duct carrying low subsonic flow is given by Howe in Reference 11. The duct and the cavity communicate through a slit orifice. Howe's explanation for the increased resistance of a resonator with a "DC bias" flow is that the vorticity generated by an incident acoustic pressure fluctuation is swept downstream by the flow carrying a portion of the acoustic energy with it. Explicit expressions are derived for the impedance of the cavity as seen by an incident plane wave in the flow duct. Consistent with the results of Ingard, Howe finds that the cavity resonance shifts to higher frequency (i.e., smaller end correction) as the flow Mach number increases. The magnitude of the shift, however, depends on the dimensions of the cavity, duct, and orifice slit.

Two other references are an experimental study of Helmholtz resonator excitation by an external flow over a glider fuselage in flight[12] and a semi-empirical study of the effects of grazing flow over an array of resonators.[13] Both studies confirm the reduction in end correction with flow Mach number.

2.7 Excitation of Resonators by Turbulence

Sound radiation by turbulence-excited Helmholtz resonators will be discussed. Subsection 2.7.1 provides a description of the turbulent boundary layer; Subsection 2.7.2 describes the response of a Helmholtz resonator to a turbulent boundary layer; and Subsection 2.7.3 deals with the acoustic response of cavities of constant cross-section, i.e., those devoid of the Helmholtz resonator neck.

2.7.1 Description of the Turbulent Boundary Layer

A concise description of the boundary turbulence in terms of cross-spectral density and correlation length is adequate, particularly because the much debated, controversial low-wavenumber portion of the spectrum associated with direct sound radiation from the boundary layer proper, is not specifically relevant to sound radiation by Helmholtz resonators and cavities. A more detailed discussion including a review of various models of the low-frequency spectrum is found in Reference 14. A recent comparison of various mathematical models is available in Reference 15.

The randomly fluctuating surface pressures exerted on the boundary by the turbulent boundary layer are expressed in terms of the mean-square value $\langle p^2 \rangle$ of the pressure and of the correlation function R as

$$\langle p(x, y, t)\ p(x+\xi,\ y+\eta,\ t+\tau) \rangle = \langle p^2 \rangle\ R(\xi, \eta, \tau)\,. \qquad (2\text{-}58)$$

Here x and y are, respectively, the coordinate in the direction parallel and normal to the flow velocity, ξ and η are their respective increments. In a fully developed turbulent boundary layer, the correlation function does not depend on the location (x, y) but only on the separation (ξ, η) between two points. The mean square pressure is in the nature of a Bernoulli pressure, being proportional to $\rho\, U^2$, where ρ is density and U is flow velocity.

The cross-spectral density is the Fourier transform in time of Equation (2-58)

$$\tilde{p}(\xi, \eta; \omega) = \frac{\langle p^2 \rangle}{2\pi} \int_{-\infty}^{\infty} R(\xi, \eta, \tau)\ \exp(i\omega\tau)\, d\tau \qquad (2\text{-}59)$$

$$= \tilde{p}(\omega)\, T(\xi, \eta; \omega).$$

The spectrum density

$$\tilde{p}(\omega) = \frac{\langle p^2 \rangle}{2\pi} \int_{-\infty}^{\infty} R(0, 0, \tau) \exp(i\omega\tau)\, d\tau \tag{2-60}$$

can be approximated in terms of the boundary layer thickness δ as

$$\tilde{p}(\omega) \cong \frac{5 \times 10^{-7}\ \rho^2\ U^3\ \delta}{1 + (\omega\delta/4\pi U)^3} . \tag{2-61}$$

In Reference 13a, for fully developed turbulence in a pipe or duct, 2δ equals the conduit's transverse dimension. The second factor in Equation (2-59) is the normalized cross-spectral density

$$T(\xi, \eta; \omega) = \frac{\langle p^2 \rangle}{\tilde{p}(\omega)} R(\xi, \eta, \tau) \tag{2-62}$$

which can be approximated as the product of the ξ- and η-dependent cross-spectral densities

$$T(\xi, \eta; \omega) \cong T(\xi, 0; \omega)\ T(0, \eta; \omega) . \tag{2-63}$$

The two factors in Equation (2-63) are formulated in terms of the corresponding Strouhal numbers

$$S_\xi = \frac{\omega \xi}{U_c}$$

and

$$S_\eta = \frac{\omega \eta}{U_c} \tag{2-64}$$

where U_c is the convection velocity. The ratio U_c / U varies with eddy wave-number and Reynolds number. A representative value for this ratio is 0.6 (Reference 14, page 744). The two factors in Equation (2-63) can now be expressed as

$$T(\xi, 0; \omega) = \exp(-0.11\ |S_\xi|) \cos S_\xi$$

$$T(0, \eta; \omega) = \exp(-0.60\ |S_\eta|) . \tag{2-65a}$$

The latter factor indicates rapid monotonic decay in the direction normal to the flow direction. The former decays slowly in an oscillatory manner, in the direction of the flow.

One can define a correlation length in terms of the limits of S_ξ associated with a change in sign of the cross-spectral density:

$$-\frac{\pi}{2} < S_\xi < \frac{\pi}{2}. \tag{2-65b}$$

This Strouhal number range can be expressed in a physically more meaningful manner by introducing an unconventional parameter not found in the literature, e.g., the convection wavelength

$$\lambda_c = \frac{U_c}{f}. \tag{2-65c}$$

The inequality in Equation (2-65b) now becomes

$$-\frac{\lambda_c}{4} < \xi < \frac{\lambda_c}{4}. \tag{2-65d}$$

A meaningful correlation length, ξ , can therefore be defined as equivalent to $\lambda_c/2$.

2.7.2 Helmholtz Resonator Response to the Turbulent Boundary Layer

The natural frequency of the resonator, Equation (2-12), is altered by mean flow which modifies the entrained mass as well as the radiation resistance, as summarized in Section 2.6 and in References 9, 10, 11, 15, and 16. The experimental study which specifically addresses the response of Helmholtz resonators[12] concludes that in most cases the outside end correction is wiped out by mean flow, shifting the natural frequency upward, a conclusion consistent with that of the other experimental studies. Reference 12 does, however, conclude that in some cases the outside end correction remains unchanged or is even increased by mean flow. Obviously, additional studies are required to reconcile apparently conflicting experimental results. The resistive component of the acoustic impedance of the resonator neck increases with flow velocity.

The experimental study in Reference 12 indicates a strong response when

$$\frac{2 d_o f_n}{U_c} \cong 1 \tag{2-66a}$$

or

$$d_o \cong \lambda_c / 2 \tag{2-66b}$$

where d_o is the Helmholtz resonator neck diameter and f_n is either the Helmholtz resonance frequency, Equation (2-12), or the fundamental standing wave or organ pipe resonance. For the latter, the effective cavity neck length, L_{eff}, measures one acoustic half-wavelength, so the natural frequency would be

$$f_n \cong \frac{c}{2 L_{eff}} \tag{2-67a}$$

or

$$L_{eff} \cong \lambda / 2 . \tag{2-67b}$$

Once again, the convection wavelength defined in Equation (2-65c) can be introduced to express the condition for strong coupling, Equation (2-66), in a physically insightful manner if

$$d_o \cong \lambda_c / 2 . \tag{2-68}$$

The result in Equation (2-66) is based on a limited number of experiments encompassing three values of d_o / δ (between 1/4 and 1/2), and a single ratio $\delta / L \cong 6$ where L is the resonator neck length (0.32 cm). The boundary layer thickness δ is 2 cm. The free-stream velocity U is 30 m/s and air is the acoustic fluid. The results are summarized in dimensionless form in Figure 2-6. The pressure enhancement at resonance is of the order of 30 dB. The peak in Figure 2-6 occurs for

$$\omega d_o / u_* \cong 40 , \tag{2-69a}$$

where the friction velocity u_* is defined and related to U_c in the caption of that figure. Expressing u_* in terms of the convection velocity U_c

$$\begin{aligned} \omega d_o / U_c &= (2 d_o f / U_c) \pi \\ &\cong 2\pi / \lambda_c \\ &\cong 40/15. \end{aligned} \tag{2-69b}$$

This is consistent with Equation (2-66) since $(40/15\pi)$ is of a first order of magnitude.

It is useful to interpret these experimental results in terms of the standard mathematical model of the turbulent boundary layer presented in Subsection 2.7.1.

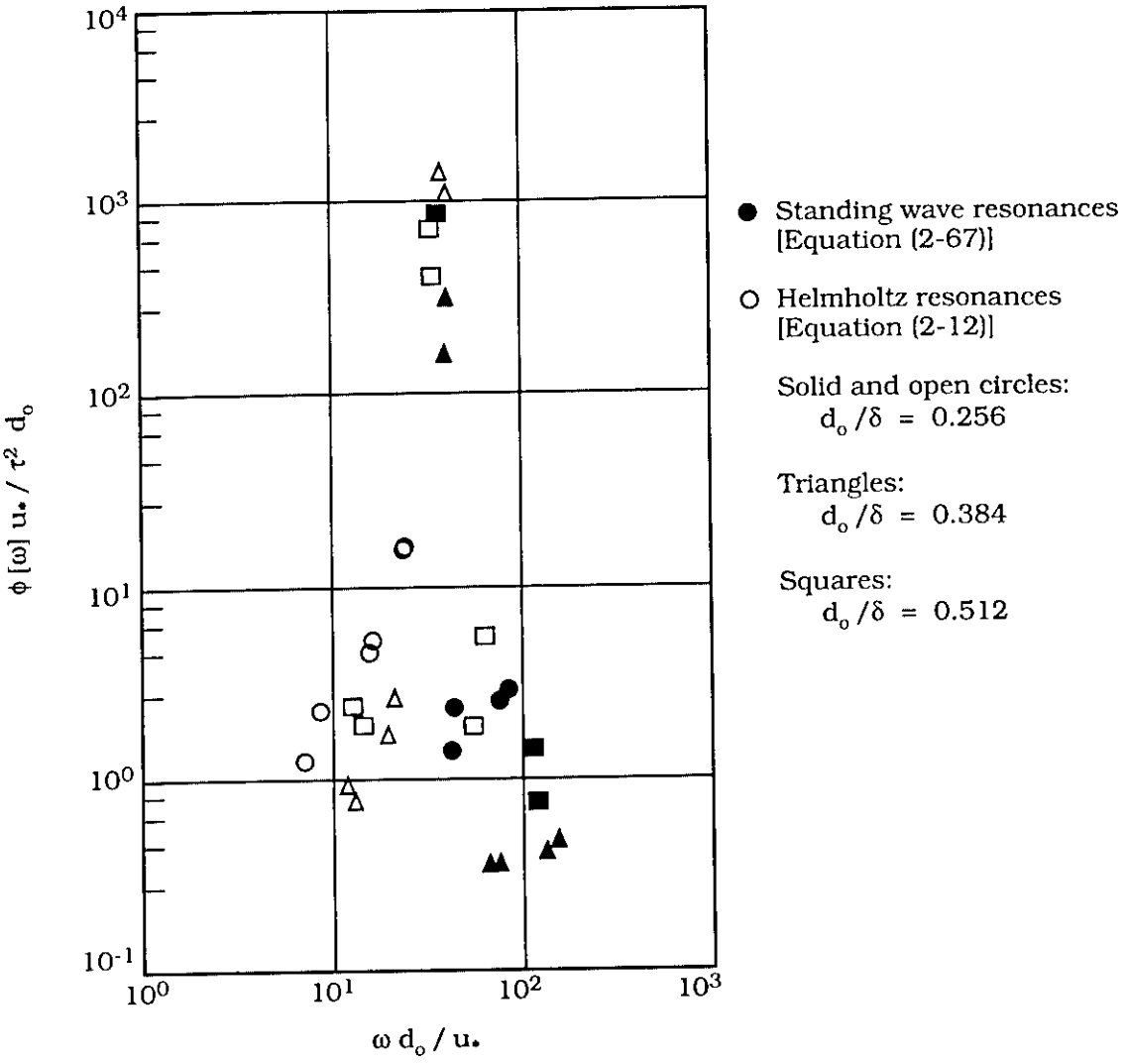

$\phi(\omega)$ = mean square pressure spectral density

τ = wall shear stress

u_* = friction velocity = $(\tau/\rho)^{1/2} \cong U_c/15$ for relevant test parameters

Figure 2-6. Strouhal Number Correlation of Strong Helmholtz Resonator Excitation. (Reproduced from Panton and Miller.[12])

Relating the resonator neck diameter d_o to ξ, the resonance condition in Equation (2-66) is equivalent to a Strouhal number spanning the range of $-\pi/2$ to $\pi/2$, i.e., to a neck diameter d_o across which the cross-spectral density remains positive. This is consistent with the results formulated in Equations (2-65b,c,d).

Strong coupling between the turbulent boundary layer and the resonator occurs when the resonator neck measures one convection half-wavelength, Equation (2-65d). When the corresponding frequency coincides with either the Helmholtz resonance frequency, Equation (2-12), or the organ pipe fundamental natural frequency, Equation (2-67), the resonance peaks of the pressure spectrum displayed in Figure 2-6 takes place. Clearly, referring to Equation (2-66), the Helmholtz resonance being characterized by the smaller of the two resonance natural frequencies is excited at a lower convection velocity than the organ pipe resonance.

2.7.3 Turbulence Excitation of Cavities of Uniform Cross-Section

The response of cavities of uniform cross-section displays two types of resonance. The primary one is the depth resonance. Insightful results were obtained for a cavity in the form of a rectangular parallelepiped one of whose six faces was left open to air flow in a wind tunnel.[17] With the goal of approximating two-dimensional flow conditions, the dimension perpendicular to the direction was large compared to the gap width b parallel to flow. As anticipated, an organ pipe depth resonance is observed when the depth d of the cavity is much larger than its width b:

$$\left.\begin{aligned} \frac{d}{\lambda} &\cong \frac{1}{4} \\ f_n &\cong \frac{c}{4d} \end{aligned}\right\} \frac{b}{d} \ll 1 \qquad (2\text{-}70)$$

For this situation, the end correction is negligible. For aspect ratios b/d which are not negligible, resonances are observed at a lower frequency (see Figure 2-7)

$$f_n = \frac{c}{4d}\left[1 + 0.65\left(\frac{b}{d}\right)^{3/4}\right]^{-1}. \qquad (2\text{-}71)$$

Multiple resonances are observed for some values of b/d. These groups of peaks correspond to roughly constant Strouhal numbers. The cause of these multiple

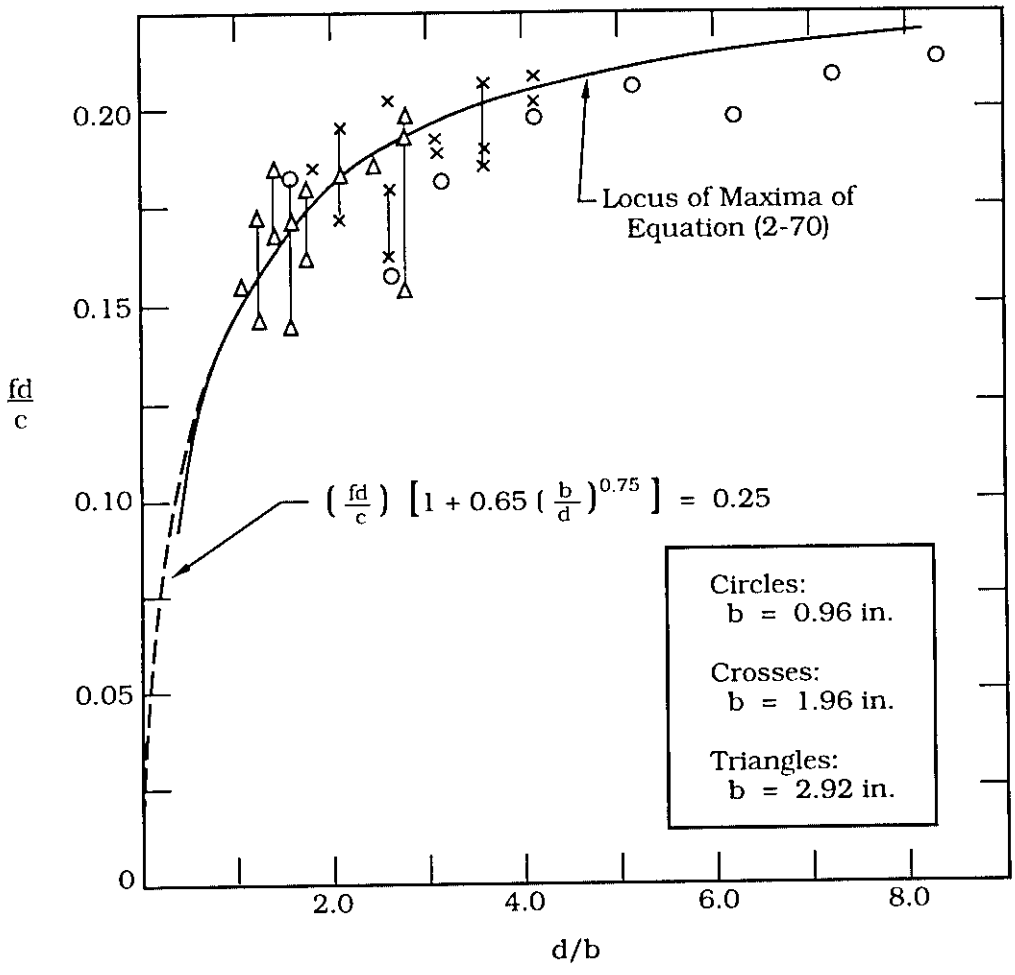

Figure 2-7. Plot of Cavity Depth d Normalized to Wavelength ($\lambda = c/f$) versus Ratio of Depth d Normalized to Cavity Width b in the Direction of Flow. (Reproduced from East.[17])

resonances is not explained by existing theory, which associates depth mode resonances with maxima of the expression

$$\frac{p}{p_f} = \left\{ (R \sin kd)^2 + (X \sin kd - \cos kd)^2 \right\}^{-1/2}. \qquad (2\text{-}72)$$

In Equation (2-72), p and p_f are, respectively, the RMS pressure amplitude at the cavity base and mouth, and k is the wavenumber $2\pi/\lambda$. R and X are complicated functions tabulated in Reference 17. As anticipated from the impedance components of the acoustically compact piston radiator for $k^2 b^2 << 1$, R varies approximately as $(kb)^2$ while X grows linearly with kb. R and X are therefore in the nature of the resistive and reactive components of the impedance ratio. Consequently, for small kb, where the cosine is much larger than the R and X terms, the pressure ratio displays a maximum for the first root of $\cos kd$, which corresponds to Equation (2-70). The theoretical basis of depth mode resonances, which is seen to be in satisfactory agreement with measurements, can be found in a paper by Plumblee *et al.*[18]

Equation (2-72) does not involve either the flow velocity or the convection velocity. Consequently, one would anticipate resonances at any flow velocity. This, however, is not the case. The reason is that the velocity must be such that the Strouhal number

$$S_\xi = \frac{\omega b}{U} \qquad (2\text{-}73)$$

is compatible with the shear layer feedback mechanism. The empirical Strouhal number proposed by Rossiter[19] is

$$S_\xi = 2\pi \frac{(m - 1/4)(U_c/U)}{1 + M(U_c/U)}, \quad m = 1, 2 \qquad (2\text{-}74a)$$

$$\left.\begin{aligned} &\cong (3\pi/2)\, U_c/U, && m = 1 \\ &= (7\pi/2)\, U_c/U, && m = 2 \end{aligned}\right\} \; M << 1 \qquad (2\text{-}74b,\ 2\text{-}74c)$$

where M is the Mach number. Equating Equations (2-74b) and (2-74c) to Equation (2-73), one obtains two convection velocities:

$$\left.\begin{aligned} U_c &= \frac{4fb}{3}, && m = 1 \\ U_c &= \frac{4fb}{7}, && m = 2 \end{aligned}\right\} \; M << 1 \qquad (2\text{-}75)$$

Rossiter showed that under resonant conditions, the shear layer develops into a series of eddies having the same rotational direction, effectively like one-half of a Karman vortex street. Strouhal numbers compatible with experimentally observed resonances are plotted in Figure 2-8. These resonances require that the frequency of which Equation (2-72) displays a maximum satisfy Equation (2-74). These twin requirements explain why depth resonance, Equation (2-72), is possible only at discrete velocities. For $b/d < 1$ and $M < 0.18$, the principal cavity pressure resonances observed occur in the fundamental depth mode with $m = 1$ and 2. For small Mach numbers, and small values of b/d, these requirements are satisfied by convection velocities obtained by substituting the fundamental depth resonance frequency, Equations (2-70), in Equations (2-75):

$$\left.\begin{aligned} U_c &= \frac{c\,b}{3d}, \quad m = 1 \\ U_c &= \frac{c\,b}{7d}, \quad m = 2 \end{aligned}\right\} \; M,\ b/d \ll 1, \quad f = c/4d \qquad (2\text{-}76)$$

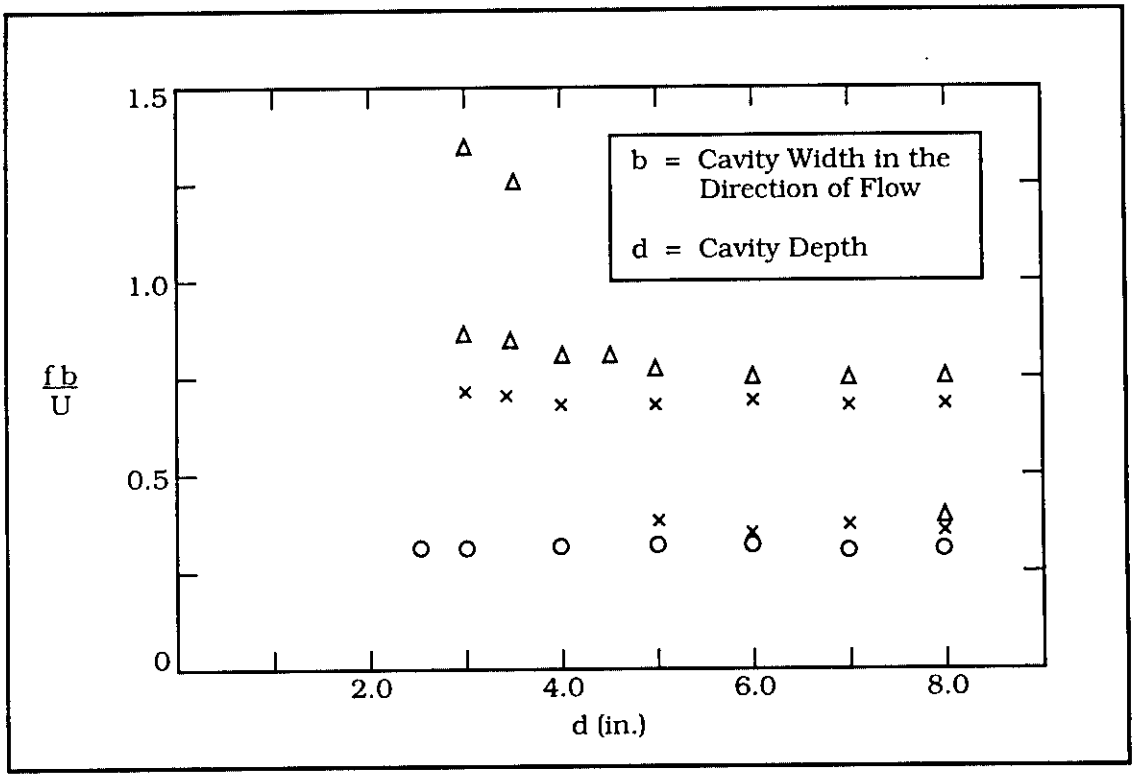

Figure 2-8. Plot of Strouhal Number Versus Cavity Depth for Resonant Conditions. (Reproduced from East.[17])

REFERENCES FOR CHAPTER 2

1. *American Institute of Physics (AIP) Handbook*, McGraw-Hill, New York, 1957, p. 3-59.

2. See for example, Beranek, L.L., *Acoustics*, McGraw Hill, New York, 1954, p. 124.

3. Ingard, U., "On the Theory and Design of Acoustic Resonators," *J. Acoust. Soc. Am.*, *25*, 1953, 1037-1061.

4. See *AIP*, *op.cit.* pp.3-56 *et seq.*

5. *Ibid.* pp. 3-69 *et seq.*

6. G.R. Bigg, "The Three-Dimensional Cavity Resonator," *J. Sound Vib.*, *85*, 1982, 85-103.

7. See for example, Roark, P.J., *Formulas for Stress and Strain*, 4th ed., McGraw-Hill, New York, 1965), pp. 298-299.

8. Lamb, H., *The Dynamic Theory of Sound*, 2nd ed., Dover Publications, New York, 1960, pp. 176-177.

9. Ingard, U., and Ising, H., "Acoustic Non-linearity of an Orifice," *J. Acoust. Soc. Am.*, *42*, 1967, 6-17.

10. Ingard, U., "Absorption Characteristics of Nonlinear Acoustic Resonators," *J. Acoust. Soc. Am.*, *44*, 1968, 1155-1156.

11. Howe, M.S., "The Influence of Grazing Flow on the Acoustic Impedance of a Cylindrical Wall Cavity," *J. Sound Vib.*, *67*, 1979, 533-544.

12. Panton, R.L., and Miller, J.M., "Excitation of a Helmholtz Resonator by a Turbulent Boundary Layer," *J. Acoust. Soc. Am.*, *58*, 1975, 800-806.

13. Groeneweg, J.F., "Current Understanding of Helmholtz Resonator Arrays as Duct Boundary Conditions," Basic Aerodynamic Noise Research, NASA SP-207, 1969, 357-368.

14. Blake, W.K., *Aero-Hydroacoustics for Ships*, David Taylor Naval Ship Research & Development Center, 1984, Chapter 7.

15. Howe, M.S., "Surface Pressure and Sound Produced by Turbulent Flow Over Smooth and Rough Walls", *J. Acoust. Soc. Am.*, *90*, 1041-1047, 1991.

16. Ronneberger, D., "The Acoustical Impedance of Holes in the Walls of Flow Ducts", *J. Sound Vib.*, *24*, 113-150, 1972.

17. East, L.F., "Aerodynamically Induced Resonance in Rectangular Cavities", *J. Sound Vib.*, *3*, 277-287, 1966.

18. Plumblee, H.E., Gibson, J.S., and Lassiter, L.W., "A Theoretical and Experimental Investigation of the Acoustic Response of Cavities in an Aerodynamic Flow", Wright-Patterson Air Force Base WADD TR-61-75, 1962.

19. Rossiter, J.E., "Wind Tunnel Experiments on the Flow Over Rectangular Cavities at Subsonic and Transonic Speeds", RAE Tech. Report 64037, 1964.

CHAPTER 3

ACOUSTIC FILTERS AND NETWORKS

by Robert Noreen
Wyle Laboratories

Turbomachinery pipe systems containing propagating acoustic waves are not simply constant area straight pipes with uniform pressure and temperature. Rather, the pipes contain changes in cross-sectional area, pressure, and temperature, and often have openings in a wall that lead to a cavity. Generally these pipe changes create a change in the acoustic impedance of the pipe and thus create a reflected acoustic wave. Interference between the incident and the reflected waves then causes a decrease in the energy transmitted along the pipe, i.e., the impedance change causes a pipe transmission loss.

Since the change in acoustic impedance for most changes in pipe conditions is a function of frequency, the transmission loss corresponding to this impedance change is also a function of frequency. Thus an impedance change is an acoustic filter, passing acoustic energy at some frequencies while blocking this energy at other frequencies. Pipe systems often contain many changes in area or conditions, resulting in multiple impedance changes with differing frequency relationships, and thus may be considered as a type of filter network.

The pipe elements described in the previous chapter are either acoustic filters themselves, when considered as single pipe elements, or can be easily combined with other elements to make a filter. A cavity on one side of a pipe can form a Helmholtz resonator, and then would be an acoustic filter as shown previously in Figure 2-3. A change in pipe cross-sectional area creates reflections and, if separated some distance from another pipe impedance change, will create a pipe transmission loss that is a function of both frequency and the distance between the pipe changes – another example of an acoustic filter.

Combinations of these relatively simple elements can produce a complex pipe system with many impedance changes having widely varying transmission loss versus frequency characteristics. Many of the pipe systems within turbomachinery can be modeled as combinations of these individual simple elements. This chapter will show how to calculate the acoustic performance of a pipe system consisting of combinations of simple elements by using a transfer

matrix technique. Section 3.1 defines pipe acoustic impedance and transmission loss. Section 3.2 presents calculation methods and examples for simple networks containing only a few elements. Section 3.3 presents the transfer matrix method for analyzing acoustic pipe systems containing any number of elements, i.e., a network, and gives example calculations. Section 3.4 gives a brief description of how the transfer matrix method is used to model pipe systems with mean flow and energy losses with an example that includes mean flow.

3.1 Pipe Acoustic Impedance and Transmission Loss

3.1.1 Pipe Acoustic Impedance

The specific or characteristic (both terms are used) acoustic impedance of the gas or medium supporting the propagation of an acoustic wave is a characteristic of the medium and has a single definition

$$z_u = p/u \tag{3-1}$$

where z_u = specific acoustic impedance,
p = acoustic pressure, and
u = acoustic particle velocity.

For acoustic pressure variations small enough to be considered isentropic, the specific impedance for plane wave propagation in a stationary medium is

$$z_{up} = \rho\, c \tag{3-2}$$

where z_{up} = specific acoustic impedance of a plane wave,
ρ = ambient density, and
c = speed of sound.

The acoustic impedance of a pipe can have several definitions – all of which can be useful – and the most convenient definition to use will depend upon the specifics of the particular problem. The most common definition is probably that used earlier in Equation (2-46a) and by Kinsler and Frey,[1] which is based upon the acoustic volume velocity in the pipe, $A_p\, u$

$$Z_v = \frac{p}{A_p\, u} = \frac{z_u}{A_p} \tag{3-3}$$

where Z_v = acoustic impedance of pipe, based on volume velocity, and
A_p = cross-sectional area of pipe.

For a plane wave in a stationary medium, this acoustic impedance becomes

$$Z_{vp} = \frac{\rho c}{A_p} . \tag{3-4}$$

Since both the density and speed of sound are functions of temperature, for actual calculations on problems in which the pipe temperature can vary it is generally more convenient to define a pipe impedance based on the acoustic mass velocity in the pipe, $\rho A_p u$ as

$$Z_m = \frac{p}{\rho A_p u} = \frac{z_u}{\rho A_p} \equiv Z. \tag{3-5}$$

For a plane wave in a stationary medium, this becomes

$$Z_{mp} = \frac{\rho c}{\rho A_p} = \frac{c}{A_p} \equiv \zeta. \tag{3-6}$$

This is the definition of pipe impedance that will be used in this chapter, and follows Munjal.[2] To simplify notation in later sections, Z_m will be denoted by Z and Z_{mp} will be denoted by ζ. These impedance definitions are summarized in Table 3-1.

Table 3-1

Definitions of Acoustic Impedance Used in Text

Parameter	General	Plane Wave
Specific acoustic impedance	$z_u = \frac{p}{u}$	$z_p = \rho c$
Acoustic impedance based on acoustic volume flow, $A_p u$	$Z_v = \frac{p}{A_p u} = \frac{z_u}{A_p}$	$Z_{vp} = \frac{\rho c}{A_p}$
Acoustic impedance based on acoustic mass flow, $\rho A_p u$	$Z_m = \frac{p}{\rho A_p u} = \frac{z_u}{\rho A_p} \equiv Z$	$Z_{mp} = \frac{\rho c}{\rho A_p} = \frac{c}{A_p} \equiv \zeta$

The expressions for impedance given above assumed a single wave propagating in the positive direction. Most pipe problems will involve two waves – an incident wave propagating in the positive direction and a reflected wave propagating in the negative direction. Using the basic wave equations for a pipe containing incident and reflected waves it can be shown that

$$\begin{aligned} \textit{Incident Wave:}\ & p_i(x,t)/u = \rho c\ , \\ \textit{Reflected Wave:}\ & p_R(x,t)/u = -\rho c\ , \end{aligned} \tag{3-7}$$

where the subscript "i" designates the incident wave amplitude and the subscript "R" designates the reflected wave amplitude. Using these relationships, the impedance of a pipe containing both waves is

$$Z = \zeta \frac{P_i + P_R}{P_i - P_R}. \tag{3-8}$$

3.1.2 Pipe Transmission Loss

The acoustic performance of a pipe is generally measured by the amount of acoustic power reflected or transmitted by the pipe, usually in terms of the amount of power initially incident on the pipe. The transmission coefficient is simply the ratio of transmitted to incident power

$$\alpha_t = W_t/W_i \tag{3-9}$$

where α_t = transmission coefficient,
W_i = incident acoustic power, and
W_t = transmitted acoustic power.

The transmission loss, TL, of a pipe or pipe element is

$$TL = L_i - L_t \tag{3-10}$$

where L_i = incident acoustic power level, and
L_t = transmitted acoustic power level.

The power level is

$$L = 10 \log_{10} (W/W_{ref})\ , \tag{3-11}$$

where W_{ref}, the reference power level, is generally 1 picowatt. The transmission loss of a pipe is thus

$$TL = 10 \log_{10} (W_i/W_t) \tag{3-12}$$

or

$$TL = -10 \log_{10} (\alpha_t) \, . \tag{3-13}$$

This definition of transmission loss provides positive values for the usual situation of transmitted power being less than incident power.

The acoustic power of a propagating wave in a pipe is related to the acoustic pressure and particle velocity by

$$W = \frac{p_{rms} \, u_{rms}}{2} A_p \tag{3-14}$$

where the subscript "rms" designates the root-mean-square value of the acoustic variable.

Combining this with the impedance from Equations (3-5) and (3-6) and assuming a plane wave,

$$W = \frac{(p_{rms})^2}{2 \rho \zeta} \tag{3-15}$$

For a pipe having known inlet and outlet areas, a fluid with known temperatures and densities, the transmission loss is

$$TL = 10 \log_{10} \left\{ \left[\frac{\zeta_t}{\zeta_i} \right] \left[\frac{\rho_t}{\rho_i} \right] \left[\frac{(p_{rms})_i}{(p_{rms})_t} \right]^2 \right\} \tag{3-16}$$

and the transmission coefficient is

$$\alpha_t = \left[\frac{\zeta_i}{\zeta_t} \right] \left[\frac{\rho_i}{\rho_t} \right] \left[\frac{(p_{rms})_t}{(p_{rms})_i} \right]^2 \tag{3-17}$$

where p_{rms} = rms magnitude of the acoustic pressure,

$( )_i$ = indicates the incident wave, and

$( )_t$ = indicates the transmitted wave.

Thus, given the pipe areas and temperatures, a determination of the rms magnitudes of the incident and transmitted acoustic pressures will provide both the transmission coefficient and the transmission loss of the pipe.

3.2 Calculation Methods for Simple Networks

In Sections 3.2.1 and 3.2.2, the transmission loss of two simple pipe configurations is derived using the "classical" method of filter network evaluation which, simply stated, is to write down the equations which describe the configuration or network and solve them for TL. Section 3.2.3 then provides a brief generalization and discussion of the approach. The methods shown in this section can be found in nearly any standard text on acoustics, with this section generally following Reference 1, except for the use of acoustic mass velocity instead of acoustic volume velocity.

3.2.1 Single-Element Configuration

The acoustic impedance, Z, of an element is a complex number, which can be written in the form

$$Z = R + iX, \tag{3-18}$$

where R is the real part and X is the imaginary part.

For a section of pipe containing a single side branch as shown in Figure 3-1,

$$p_1 = A_1 e^{i(\omega t - kx)} + B_1 e^{i(\omega t + kx)}, \tag{3-19}$$

$$p_2 = A_2 e^{i(\omega t)}, \tag{3-20}$$

$$p_3 = A_3 e^{i(\omega t - kx)} + B_3 e^{i(\omega t + kx)}, \tag{3-21}$$

where $\omega = 2\pi f$, t is time, and k is wave number.

The "As" are complex constants setting the magnitude and phase of the incident waves and the "Bs" are complex constants for the reflected waves. If the cross-section dimensions of the pipe and the branch opening are assumed to be small compared to the wavelengths of the frequencies of interest, then

$$p_3 = p_2 = p_1 .$$

If it is also assumed that the branch is at the origin of the coordinate system and that there is an anechoic termination downstream, meaning the pipe is either infinitely long or otherwise terminates without creating any reflections, then $x = 0$, $B_1 = 0$, and

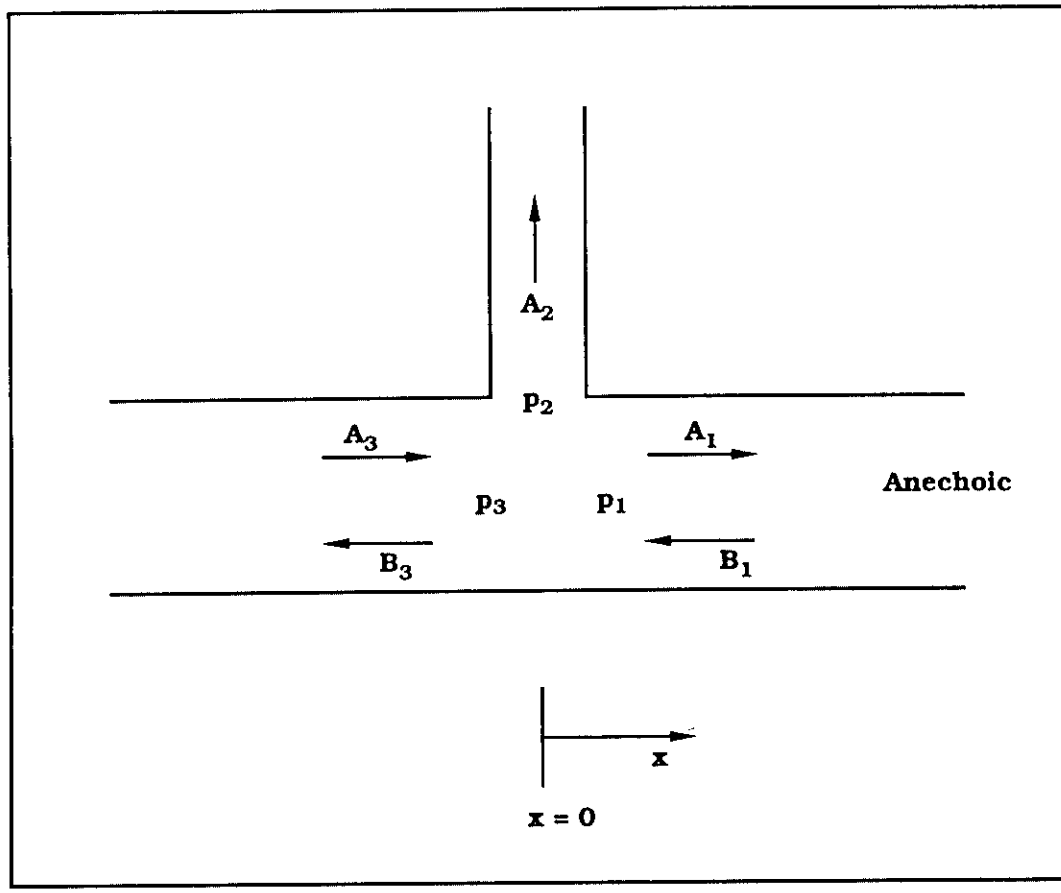

Figure 3-1. Single-Element Configuration.

$$A_3\ e^{i\omega t} + B_3\ e^{i\omega t} = A_2\ e^{i\omega t} = A_1\ e^{i\omega t}$$

$$A_3 + B_3 = A_2 = A_1 \tag{3-22}$$

The impedances for the pipe sections are

$$Z_3 = \frac{p_3}{v_3} = \zeta_3\left(\frac{A_3 + B_3}{A_3 - B_3}\right), \tag{3-23}$$

$$Z_2 = \frac{p_2}{v_2}, \tag{3-24}$$

$$Z_1 = \frac{p_1}{v_1} = \frac{A_1}{v_1} = \zeta_1, \tag{3-25}$$

where the v's are the mass velocities of the corresponding pipe elements.

The incident mass flow is conserved, so

$$v_3 = v_2 + v_1 \tag{3-26}$$

or, since the pressures at 1, 2, and 3 are equal, it follows that

$$\frac{1}{Z_3} = \frac{1}{Z_2} + \frac{1}{Z_1} \tag{3-27}$$

so that

$$\left(\frac{1}{\zeta_3}\right)\left(\frac{A_3 - B_3}{A_3 + B_3}\right) = \frac{1}{Z_2} + \frac{1}{\zeta_1} \tag{3-28}$$

Assuming there are no temperature changes within the pipe and that the upstream and downstream pipe areas are equal, $\zeta_3 = \zeta_1 \equiv \zeta$, then Equation (3-28) can be rewritten as

$$\left(\frac{1}{\zeta}\right)\left(\frac{A_3 - B_3}{A_3 + B_3}\right) = \frac{1}{Z_2} + \frac{1}{\zeta} \tag{3-29}$$

This can be rearranged to solve for the reflected pressure in terms of the incident pressure,

$$B_3 = -A_3\left(\frac{\zeta}{2Z_2 + \zeta}\right) \tag{3-30}$$

Using Equation (3-22) to eliminate B_3, one obtains

$$\frac{A_3}{A_1} = \frac{Z_2 + (\zeta/2)}{Z_2} \tag{3-31}$$

Using $Z_2 = R + iX$, the transmission loss is

$$TL = 10 \log_{10} \left(\frac{A_3}{A_1} \right)^2_{rms} = 10 \log_{10} \left\{ \frac{[R + (\zeta/2)]^2 + X^2}{R^2 + X^2} \right\} \qquad (3\text{-}32)$$

Example Calculation

As an example, a Helmholtz resonator can be selected for the branch element. Assuming no acoustic energy is lost in the neck of the resonator, the real and imaginary parts of the branch impedance z_2 are

$$R = 0 ,$$

$$X = \frac{\omega L_{eff}}{A_o} - \frac{c^2}{\omega V_c} \qquad (3\text{-}33)$$

where, as in Figure 2-1,

L_{eff} = effective length of resonator neck = $L_o + \Delta L_o + \Delta L_i$; use Equation (2-7) for ΔL_o and ΔL_i ;

A_o = cross-sectional area of resonator neck; and

V_c = Volume of resonator cavity.

Figure 3-2 shows the transmission loss calculated by Equation (3-32) for the following gas and resonator characteristics:

c = 1,670 ft/sec,

A_p = 3.41 10^{-4} ft^2 (1/4-inch diameter),

A_o = 3.41 10^{-4} ft^2 (1/4-inch diameter),

V_c = 2.89 10^{-3} ft^3 (5 in^3), and

L_{eff} = 0.026 ft (0.1 inch physical length + 2 (0.85) $(A_o/\pi)^{1/2}$).

As shown in Figure 3-2, the transmission loss rises to a large peak at 565 Hz, the resonant frequency of this resonator, then decreases uniformly with increasing frequency.

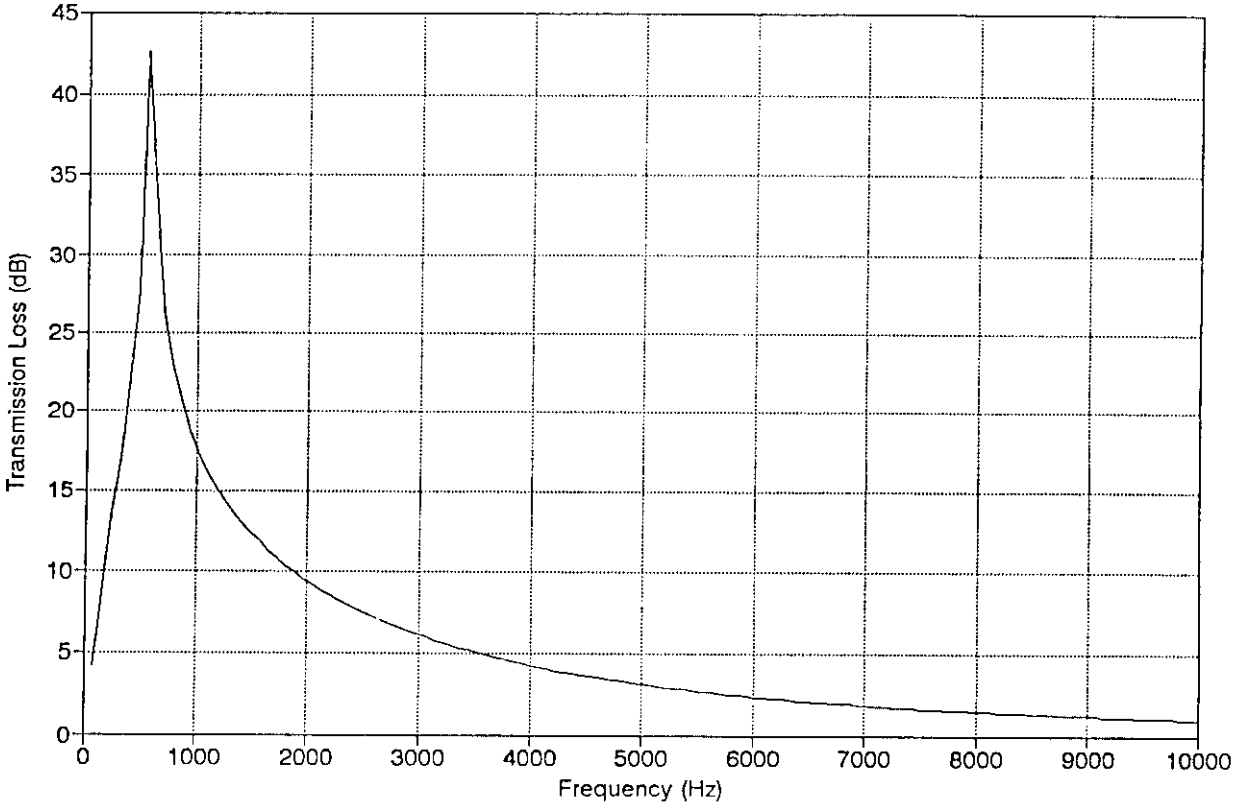

Figure 3-2. Transmission Loss for a Single-Element Configuration – Helmholtz Resonator Branch From a Pipe With One Ancehoic Termination.

3.2.2 Three-Element Configuration

Figure 3-3 shows a pipe configuration containing three elements: a Helmholtz resonator, a section of straight pipe of length L, and then a sudden contraction to a pipe with an anechoic termination. The pressures and velocities in each of the five locations are

$$p_5 = A_5 + B_5 , \tag{3-34}$$

$$v_5 = \frac{1}{\zeta_5}(A_5 - B_5), \tag{3-35}$$

$$p_4 = A_4 , \tag{3-36}$$

$$v_4 = \frac{A_4}{Z_4} , \tag{3-37}$$

$$p_3 = A_3 + B_3 , \tag{3-38}$$

$$v_3 = \frac{1}{\zeta_3}(A_3 - B_3), \tag{3-39}$$

$$p_2 = A_3 e^{-ikL} + B_3 e^{ikL} , \tag{3-40}$$

$$v_2 = \frac{1}{\zeta_2}(A_3 e^{-ikL} - B_3 e^{ikL}) , \tag{3-41}$$

$$p_1 = A_1 , \tag{3-42}$$

$$v_1 = \frac{A_1}{\zeta_1} . \tag{3-43}$$

Again assuming that the pipe cross-section dimensions are small compared to a wavelength,

$$p_5 = p_4 , \tag{3-44}$$

$$p_4 = p_3 , \tag{3-45}$$

$$p_2 = p_1 . \tag{3-46}$$

and using continuity of mass flow,

$$v_5 = v_4 + v_3 , \tag{3-47}$$

$$v_2 = v_1 . \tag{3-48}$$

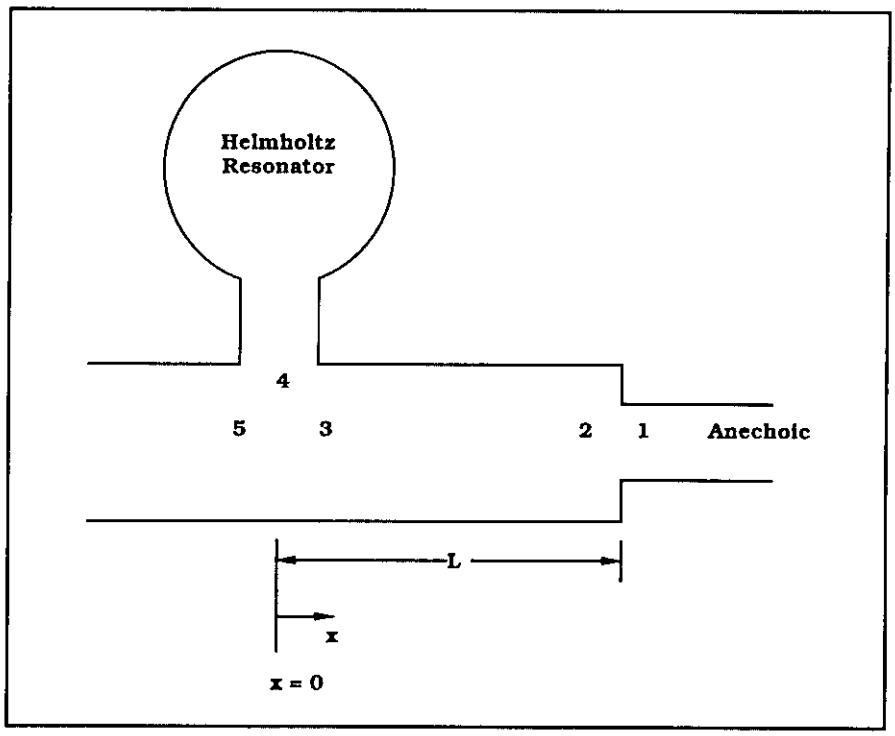

Figure 3-3. Three-Element Configuration.

Equations (3-34) through (3-48) are a set of 15 equations containing 16 unknowns if the impedances, the ζ and Z terms, are known. If either the incident pressure, A_5, is known or if only the ratio of A_5/A_1 is desired, the number of unknowns is reduced to 15 and the system can be solved. Assuming a frequently occurring configuration where the pipe area and temperature are constant from location 5 to 2, then

$$\zeta_5 = \zeta_3 = \zeta_2 \equiv \zeta \tag{3-49}$$

and the form of the solution is simplified.

Beginning at the downstream end of the pipe, Equations (3-38) through (3-43), (3-46), and (3-48) can be used to obtain A_3 and B_3 in terms of A_1,

$$A_3 = A_1 e^{ikL}\left(\frac{\zeta_1 + \zeta}{2\zeta_1}\right), \tag{3-50}$$

$$B_3 = A_1 e^{-ikL}\left(\frac{\zeta_1 - \zeta}{2\zeta_1}\right). \tag{3-51}$$

Equations (3-34), (3-38), (3-44), and (3-45) give

$$B_5 = (A_3 + B_3) - A_5 \tag{3-52}$$

and as in the previous section, Equations (3-34) through (3-39), (3-44), (3-45), and (3-47) can be combined

$$\frac{1}{Z_5} = \frac{1}{Z_4} + \frac{1}{Z_3}, \tag{3-53}$$

$$\left(\frac{1}{\zeta}\right)\left(\frac{A_5 - B_5}{A_5 + B_5}\right) = \frac{1}{Z_4} + \left(\frac{1}{\zeta}\right)\left(\frac{A_3 - B_3}{A_3 + B_3}\right). \tag{3-54}$$

Now Equation (3-52) can be substituted into Equation (3-54) to obtain A_5 in terms of A_3 and B_3, then Equations (3-50) and (3-51) substituted for A_3 and B_3, and finally the resulting expression solved for A_5/A_1. Again using R and X for the real and imaginary parts of this ratio,

$$A_5/A_1 = R + iX \tag{3-55}$$

where $$R = \left(\frac{1}{2}\right)\left|\left(1 + \frac{\zeta}{\zeta_1}\right)\cos(kL) + \left(\frac{\zeta^2}{\zeta_1 |Z_4|}\right)\sin(kL)\right|,$$

$$X = \left(\frac{1}{2}\right)\left|\left(1 + \frac{\zeta}{\zeta_1}\right)\sin(kL) - \left(\frac{\zeta}{|Z_4|}\right)\cos(kL)\right|,$$

and $|\ |$ = indicates the magnitude of a complex number.

The transmission loss in terms of R and X is

$$TL = 10 \log_{10}(R^2 + X^2). \tag{3-56}$$

Figure 3-4 shows values of transmission loss for the sample three-element pipe configuration based on the same Helmholtz resonator geometry used for Figure 3-2 combined with a 6-inch-long straight section of 1/4-inch-diameter pipe then reducing to 1/8-inch diameter with an anechoic termination. The transmission loss peak from the resonator is obvious at 565 Hz in Figure 3-4 and, comparing to Figure 3-2, the cyclic variation of transmission loss caused by the straight pipe section with an impedance change at each end has been combined with the resonator transmission loss. The peak and minimum values of the cyclic attenuation repeat at a frequency interval of about 1670 Hz, the frequency where the length of the straight section corresponds to a half wavelength.

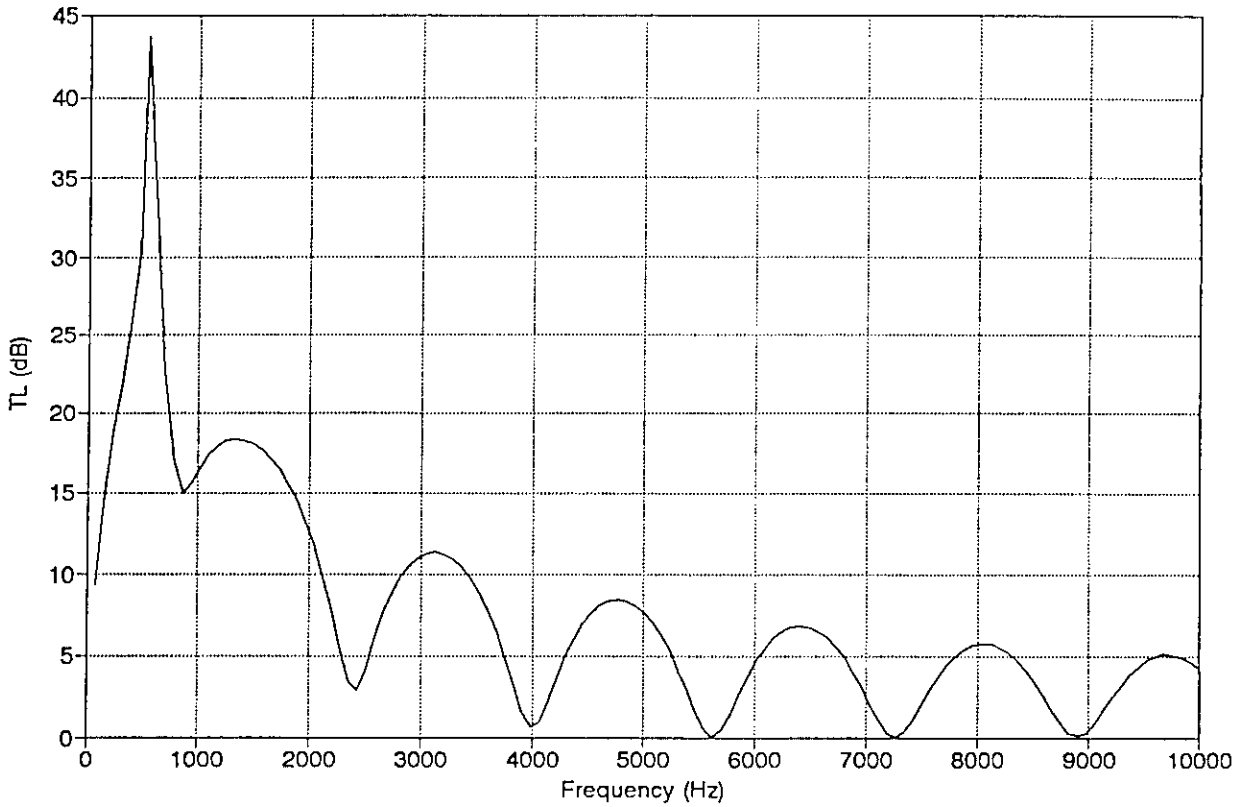

Figure 3-4. Transmission Loss for a Three-Element Configuration.

3.2.3 Discussion

As shown in the previous sections, the method presented for determining the performance of simple pipe configurations, networks, is based upon setting up the system of equations that defines the acoustic pressure and velocity relationships within the pipe then solving for the desired performance characteristic. The examples presented only solved for the pipe transmission loss, but the transmission coefficient is merely the inverse of the same ratio presented as a fraction instead of a level, and the reflection coefficient can be determined by using the same techniques but solving for a different pressure ratio.

Four basic concepts are used in determining the system of equations. First, the pipe impedance, ζ, relates pressures and velocities in constant area pipe sections. Second, the assumption of plane wave propagation and wavelengths large compared to pipe cross-section dimensions provides simplified relationships between acoustic pressures in regions connecting elements. Third, mass flow continuity provides relationships between velocities at various points in the pipe. Finally, independently determined expressions for the acoustic impedance provide pressure and velocity relationships for more complex elements.

Since acoustic impedance functions exist for many common pipe elements and many seemingly complex pipe systems are simply combinations of a few basic impedance changes with varying geometries, this method can be applied to complex pipe configurations. As with the three-element example in Section 3.2.2, one simply starts at one end of the pipe and writes the equations relating the acoustic pressures and velocities for each section using pipe or element impedances as required. Continuity and plane wave propagation are then used to relate velocities and pressures between sections.

This approach is clearly analogous to that used for determining the performance of an AC electrical circuit. Detailed analysis of the analogies shows that they are so accurate that much of the terminology and methods for acoustic analysis are derived from electrical circuit analysis. Acoustic pressures are analogous to electrical voltages and the acoustic mass, or volume velocity is analogous to electrical current. Impedance is the ratio of pressure to velocity in acoustical analysis and the ratio of voltage to current in electrical analysis. Table 3-2 shows the quantities and units for the various parameters of this electroacoustic analogy. Further discussion can be found in nearly any standard acoustics textbook.

Table 3-2

Major Variables for Electro-Acoustic Analogy

ACOUSTICAL			ELECTRICAL	
Variable	**Units**		**Variable**	**Units SI**
	English	**SI**		
Pressure	lb/ft^2	Pascal	Potential	Volt
Mass Velocity	slug/sec	kg/sec	Current	Amp
Duct Impedance	$(ft \cdot sec)^{-1}$	$(m \cdot sec)^{-1}$	Impedance	Ohm

Just as in electrical filter network analysis, even though this classical method will work on an arbitrary pipe configuration or network, significant difficulties arise when trying to apply the method to a network with more than a very small number of elements. The basic approach and methods are straightforward, but actual calculations very rapidly become quite laborious as the number of elements increases. The example with only three elements involved a system of 15 equations and unknowns.

Standard computer routines could be used to obtain the solutions of large systems of equations, but a system of equations corresponds to only a single pipe configuration. If a simple change is made to the configuration by just adding or deleting an element, or perhaps rearranging elements, a new set of equations must be established. This classical method is useful in providing an understanding of pipe system analysis and performance, but is clearly not efficient for performance calculations involving actual multi-element configurations. The transfer matrix method presented in the next sections provides a means of easily calculating the characteristics of pipes containing any number of elements in any sequence.

3.3 Transfer Matrix Analysis

The transfer matrix method of network analysis was originally developed for electrical networks and its application to acoustical networks derives from the analogy between electrical and acoustical analyses. This method is also called the transmission matrix or four-pole parameter method and strictly applies to a network of any number of impedance changes but with a single source and a single termination. The transfer matrix method can be useful in the analysis of networks with multiple terminations if the network can be divided into single source/ termination portions with the other branches represented by impedances that are either known or can be evaluated. The presentation and terminology used in this subsection generally follows Munjal.[2]

3.3.1 The Transfer Matrix Method

Figure 3-5 shows a schematic representation of a portion of a pipe containing an impedance change represented by T_n. The upstream acoustic pressure is p_n, the upstream acoustic mass velocity is v_n; p_{n-1} and v_{n-1} are the downstream acoustic pressure and mass velocity, respectively. Since we have assumed small acoustic variables, they are linearly related and we can define a matrix $[T_n]$ such that

$$\begin{bmatrix} p_n \\ v_n \end{bmatrix} = \begin{bmatrix} (T_n)_{11} & (T_n)_{12} \\ (T_n)_{21} & (T_n)_{22} \end{bmatrix} \begin{bmatrix} p_{n-1} \\ v_{n-1} \end{bmatrix}. \tag{3-57}$$

The transfer matrix $[T_n]$ relates the upstream and downstream state variables p and v in terms of the state vectors $[p_n , v_n]$ and $[p_{n-1} , v_{n-1}]$. From the definition of $[T_n]$ its individual terms are

$$(T_n)_{11} = \left.\frac{p_n}{p_{n-1}}\right|_{v_{n-1}=0}, \qquad (T_n)_{12} = \left.\frac{p_n}{v_{n-1}}\right|_{p_{n-1}=0},$$

$$(T_n)_{21} = \left.\frac{v_n}{p_{n-1}}\right|_{v_{n-1}=0}, \qquad (T_n)_{22} = \left.\frac{v_n}{v_{n-1}}\right|_{p_{n-1}=0}. \tag{3-58}$$

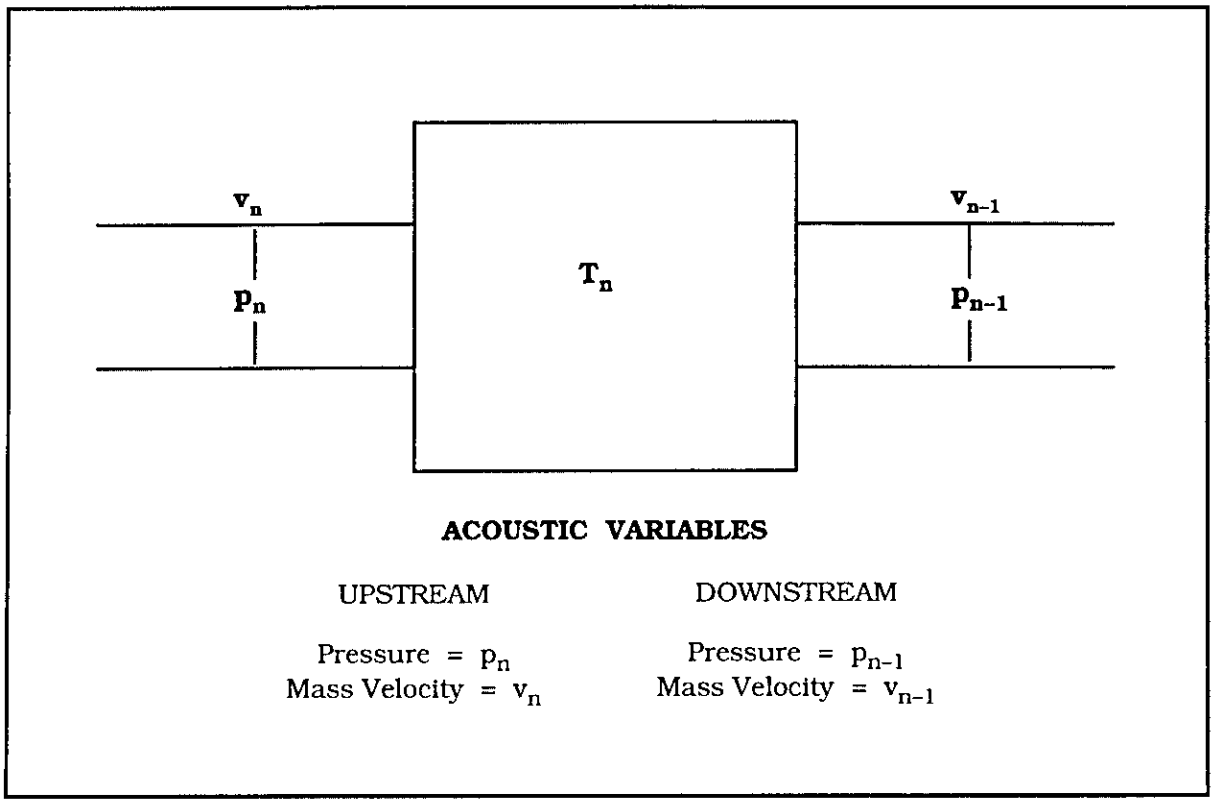

Figure 3-5. Schematic Representation of a Single-Element Pipe Impedance Change, T_n .

If the pipe contains another linear element, T_{n-1}, one can write

$$\begin{bmatrix} p_{n-1} \\ v_{n-1} \end{bmatrix} = \begin{bmatrix} (T_{n-1})_{11} & (T_{n-1})_{12} \\ (T_{n-1})_{21} & (T_{n-1})_{22} \end{bmatrix} \begin{bmatrix} p_{n-2} \\ v_{n-2} \end{bmatrix} \tag{3-59}$$

or

$$\begin{bmatrix} p_n \\ v_n \end{bmatrix} = [T_n]\,[T_{n-1}] \begin{bmatrix} p_{n-2} \\ v_{n-2} \end{bmatrix}. \tag{3-60}$$

This can be generalized to yield

$$[S_n] = [T_n]\,[T_{n-1}] \ldots [T_2]\,[T_1]\,[S_0] \tag{3-61}$$

$$[S_n] = [T_t]\,[S_0]\,, \tag{3-62}$$

where $[T_t] = [T_n]\,[T_{n-1}] \ldots [T_2]\,[T_1]$ is the "total" transfer matrix,

$$[S_n] = \begin{bmatrix} p_n \\ v_n \end{bmatrix} \tag{3-63}$$

is the generalized state vector for the upstream or source end of the pipe, and

$$[S_0] = \begin{bmatrix} p_0 \\ v_0 \end{bmatrix} \tag{3-64}$$

is the generalized state vector for the downstream or termination end of the pipe.

The transmission loss for this pipe can be calculated from

$$TL = 10 \log_{10} \left[\left(\frac{\zeta_0}{\zeta_n} \right) T_{term}^2 \right], \tag{3-65}$$

where $T_{term} = \frac{1}{2} \left| T_{11} + \frac{T_{12}}{\zeta_0} + \zeta_n T_{21} + \left(\frac{\zeta_n}{\zeta_0} \right) T_{22} \right|$ and $|\ |$ indicates the magnitude of a complex number.

This transfer matrix approach allows calculating the acoustic performance of a pipe with multiple elements by forming a transfer matrix for each individual element and then successively multiplying by a cumulative total matrix. This process avoids the need to set up and solve a large system of simultaneous equations.

The definition of the transfer matrix terms shows that they are related to the impedance of the pipe element and two limiting cases for lumped impedances will provide examples. For a purely "in-line" impedance, Z_i, which alters acoustic pressure but not velocity,

$$[T_i] = \begin{bmatrix} 1 & Z_i \\ 0 & 1 \end{bmatrix} \tag{3-66}$$

or for a purely "shunt" impedance, Z_s, which alters acoustic velocity but not pressure,

$$[T_s] = \begin{bmatrix} 1 & 0 \\ 1/Z_s & 1 \end{bmatrix}. \tag{3-67}$$

Using these and the definitions of the element terms, one can develop generalized transfer matrices for individual elements such as a straight pipe, Helmholtz resonator, or many others.[2]

The equations for the matrix elements will be functions of frequency and include flow and geometry terms. A relatively simple computer model can then be constructed with separate subprograms that evaluate the transfer matrix terms of each element type, multiplies an accumulating total transfer matrix by the element matrix, successively proceeds to the next element repeating the evaluation of matrix terms and multiplication, and finally calculates the overall transmission loss. Since the transfer matrix terms are functions of frequency, all portions of the computer model would loop through a frequency range to provide transmission loss as a function of frequency.

3.3.2 Transfer Matrices for Typical Elements

This section presents transfer matrices for three pipe elements that are found in turbomachinery: a straight pipe section, a side-branch Helmholtz resonator, and a simple "wide mouth" side-branch cavity. Matrices for many other elements can be found in Reference 2, but the three elements given here represent many of the turbomachinery pipe impedance changes.

3.3.2.1 *Straight-Pipe Section*

The transfer matrix terms for a section of straight pipe of length L and pipe impedance ζ are

$$T_{11} = \cos(kL), \qquad T_{12} = i\,\zeta \sin(kL),$$
$$T_{21} = \frac{i}{\zeta} \sin(kL), \qquad T_{22} = \cos(kL). \tag{3-68}$$

Note that because the state variable v is a mass flow, the straight-pipe matrix contains the pipe cross-sectional area within the impedance ζ. This area would not appear in transfer matrix terms for a straight pipe which are based on a state variable of simply u, or $\rho c u$. This also means that separate transfer matrices for sudden expansions or contractions of the pipe are not required when acoustic mass flow is used as a state variable; the mass flow does not change even if the pipe area does. Sudden area changes are reflected in the changes in pipe impedance ζ used in the elements on either side of the area change. A sudden contraction with sections of straight pipe both upstream and downstream would be modeled as just two separate lengths of pipe with different areas and this area difference would be included in the individual ζ's of the two pipes.

3.3.2.2 *Helmholtz Resonator*

The Helmholtz resonator is a "side-branch" pipe element providing a "shunt" impedance, so its transfer matrix would have the general form of

$$\begin{bmatrix} 1 & 0 \\ 1/Z & 1 \end{bmatrix},$$

where Z is the impedance of the Helmholtz resonator. Again using $Z = R + iX$ and assuming no energy is lost in the neck of the resonator,

$$R = 0,$$
$$X = \frac{\omega L_{eff}}{A_o} - \frac{c^2}{\omega V_c},$$

where the Helmholtz parameters have the same definitions as given in Equation (3-33). The individual matrix terms are then

$$T_{11} = 1 , \qquad T_{12} = 0 ,$$
$$T_{21} = \frac{-i}{X} , \qquad T_{22} = 1 . \tag{3-69}$$

3.3.2.3 *Simple Cavity*

The simple cavity described by this matrix is shown schematically in Figure 3-6 and is a cavity with constant cross-sectional area, A_c , along its depth and a depth, L_c , that is long compared to wavelengths of interest. This type of cavity is another side-branch (shunt) element, but without a neck and having a large depth; it is not a Helmholtz resonator. Again, the general side-branch form will be

$$\begin{bmatrix} 1 & 0 \\ 1/Z_c & 1 \end{bmatrix}$$

but now Z_c will be that for a length of straight pipe terminated at one end with a rigid cap. The impedance, based upon acoustic mass velocity derived from Reference 2, is

$$Z_c = -i \zeta_c \cot (k L_c) . \tag{3-70}$$

Substituting this expression into the general form:

$$T_{11} = 1 , \qquad T_{12} = 0 ,$$
$$T_{21} = \frac{i}{\zeta_c} \tan (k L_c) , \qquad T_{22} = 1 . \tag{3-71}$$

3.3.3 Example Calculations Using Transfer Matrices

This section shows the solution of the same example problems solved in Sections 3.2.1 and 3.2.2 using the transfer matrix method rather than the classical method.

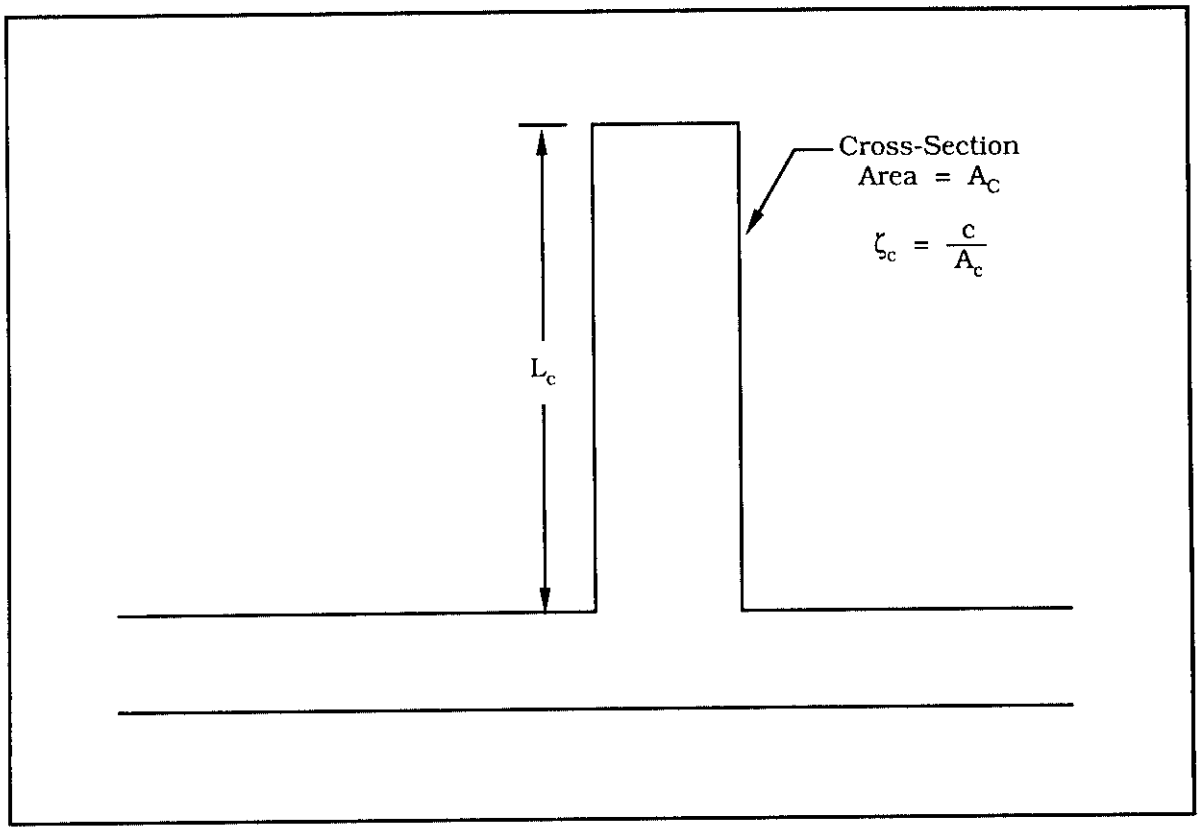

Figure 3-6. Schematic of Cavity Side Branch.

3.3.3.1 *Single-Element Configuration*

In analyzing a pipe with only a single element, there is only one transfer matrix to set up. Since the example selected in Section 3.2.1 is a Helmholtz resonator, the single matrix is given by Equation (3-69). Using Equation (3-65) one can obtain the expression for the transmission loss of this single resonator element

$$TL = 10 \log_{10}\left\{ (1) \left[\frac{1}{2} \left| (1) + \left(\frac{0}{\zeta}\right) + \left(\frac{-i\zeta}{X}\right) + (1) \right| \right]^2 \right\}$$

or

$$TL = 10 \log_{10}\left\{ \frac{1}{4} \left[4 + \left(\frac{\zeta}{X}\right)^2 \right] \right\}, \qquad (3\text{-}72)$$

which is equal to Equation (3-32) when $R = 0$, so the transmission loss determined by the transfer matrix method with the same element dimensions given in Section 3.2.1 is exactly that shown in Figure 3-2.

Demonstrating the advantages of the transfer matrix method requires considering a pipe system with multiple elements as is done in Section 3.3.3.2.

3.3.3.2 *Three-Element Configuration*

The three-element pipe configuration solved in Section 3.2.2 consisted of a Helmholtz resonator, a straight-pipe section, and a sudden contraction to an anechoic termination. This example will use the same physical parameters. The general transfer matrix method is to form the first matrix, form the second matrix, multiply them to a current total, form the third matrix, multiply the total and the third, then evaluate the transmission loss. This example presents a special case, ending with an anechoically terminated sudden contraction.

The first matrix, $[T_3]$, is again the Helmholtz resonator matrix

$$\begin{aligned} (T_3)_{11} &= 1, & (T_3)_{12} &= 0, \\ (T_3)_{21} &= -\frac{i}{X}, & (T_3)_{22} &= 1, \end{aligned} \qquad (3\text{-}73)$$

where X is given by Equation (3-33).

The second matrix, $[T_2]$, is that for a straight section with a length, L, of 6 inches

$$(T_2)_{11} = \cos(k\,L), \qquad (T_2)_{12} = i\,\zeta_2 \sin(k\,L),$$
$$(T_2)_{21} = \frac{i}{\zeta_2}\sin(k\,L), \qquad (T_2)_{22} = \cos(k\,L). \tag{3-74}$$

Their product, $[T_3]\ [T_2]$, is

$$(T_{32})_{11} = \cos(k\,L),$$
$$(T_{32})_{12} = i\,\zeta_2 \sin(k\,L),$$
$$(T_{32})_{21} = \frac{-i}{X}\cos(k\,L) + \frac{i}{\zeta_2}\sin(k\,L), \tag{3-75}$$
$$(T_{32})_{22} = \frac{\zeta_2}{X}\sin(k\,L) + \cos(k\,L).$$

The third element is an anechoically terminated sudden contraction, which could be modeled as an added straight pipe with the new diameter and arbitrary length using Equation (3-68). Calculating the transmission loss of a section of straight pipe,

$$(TL)_{sp} = 10\log_{10}\left[\frac{2\cos^2(kL) + 2\sin^2(kL)}{2}\right] = 0 \tag{3-76}$$

which is why the selection of length would be arbitrary if the sudden contraction were modeled this way. Since the models presented here do not consider any viscous losses or losses through the pipe walls, there are no power losses in a straight pipe section, only phase changes.

The other way to "model" the sudden contraction element is to simply consider the new smaller diameter as defining the last pipe impedance in the expression for transmission loss, which then becomes

$$TL = 10\log_{10}\left\{\left(\frac{\zeta_3}{\zeta_1}\right)\left|\frac{1}{2}\left[(T_{32})_{11} + \frac{(T_{32})_{12}}{\zeta_1} + \zeta_3\,(T_{32})_{21} + \frac{\zeta_3}{\zeta_1}\,(T_{32})_{22}\right]\right|^2\right\}, \tag{3-77}$$

where ζ_3 is the impedance for the initial 1/4-inch-diameter pipe section, ζ_1 the impedance of the 1/8-inch-diameter section, and the matrix terms are those from

the product of the two other elements given in Equation (3-75). If the substitution of these equations into Equation (3-77) is made and the resulting expression simplified, it reduces to the results given by Equation (3-56). Thus the transmission loss predicted by the transfer matrix method is exactly the same as shown in Figure 3-4 for the classical method.

3.4 Mean Flow and Energy Loss

The transfer matrix method can be applied to pipe systems with mean flow and energy losses by formulating the appropriate relationships for the transfer matrix terms and including the effects of convection. For a pipe with no losses but mean flow in the positive direction, there are separate wavenumbers for the incident and reflected waves

$$k_I = \frac{\omega}{c+U}, \tag{3-78}$$

$$k_R = \frac{\omega}{c-U}, \tag{3-79}$$

where U is the mean flow velocity, the subscript "i" again indicates the positive or incident direction, and the subscript "R" indicates the negative or reflected direction. Introducing the Mach number, M , and a convected wavenumber, k_c

$$k_I = k_c (1 - M), \tag{3-80}$$

$$k_R = k_c (1 + M), \tag{3-81}$$

where $M = \frac{U}{c}$,

$$k_c = \frac{\omega}{c(1-M^2)}.$$

With these relationships and the basic wave equations, the resulting pipe impedance is the same as for a pipe without flow, that is

$$(\zeta_c)_I = \zeta_I = \frac{c}{A_p}, \tag{3-82}$$

$$(\zeta_c)_R = \zeta_R = -\frac{c}{A_p}, \tag{3-83}$$

where ζ = pipe impedance with no flow and

ζ_c = pipe impedance with flow and no losses.

Since the pipe contains a mean flow, the acoustic waves will be convected with that flow, and the pipe transmission loss of interest will be for the convected acoustic power. The relation between the convected and stationary acoustic variables can be expressed in transfer matrix form as

$$\begin{bmatrix} p_c \\ v_c \end{bmatrix} = \begin{bmatrix} 1 & M\zeta \\ \frac{M}{\zeta} & 1 \end{bmatrix} \begin{bmatrix} p \\ v \end{bmatrix}. \tag{3-84}$$

If the energy losses in the pipe are considered, the expressions for wave number are again modified. Following Reference 2, where both viscous and boundary layer losses are considered,

$$k_I = \frac{k - i A_I}{1 + M}, \tag{3-85}$$

$$k_R = \frac{k - i A_I}{1 - M}, \tag{3-86}$$

where $k = \frac{\omega}{c}$, and

A_I = combined loss factor.

k_L can be defined as

$$k_L = \frac{k - i A_I}{1 - M^2} \tag{3-87}$$

so that

$$k_I = k_L (1 - M), \tag{3-88}$$

$$k_R = k_L (1 + M). \tag{3-89}$$

However, if the energy losses in the pipe are considered, the impedance of the pipe is no longer equal to the stationary impedance. The impedance for the positive or incident wave for a pipe containing mean flow and losses becomes

$$\zeta_L = \zeta\left(1 - \frac{i A_I}{k}\right), \tag{3-90}$$

where ζ is the stationary impedance, c/A_p. The equation relating the stationary acoustic variables at either end of a section of straight pipe becomes

$$\begin{bmatrix} p_n \\ v_n \end{bmatrix} = \exp(-i M k_L L) \begin{bmatrix} \cos(k_L L) & i \zeta_L \sin(k_L L) \\ \frac{1}{\zeta} \sin(k_L L) & \cos(k_L L) \end{bmatrix} \begin{bmatrix} p_{n-1} \\ v_{n-1} \end{bmatrix}. \tag{3-91}$$

Equation (3-84) and its inverse are used to obtain the desired relationship between the convected variables

$$\begin{bmatrix} (p_c)_n \\ (v_c)_n \end{bmatrix} = \frac{\exp(-i M k_L L)}{1 - M^2} \begin{bmatrix} 1 & M\zeta \\ \frac{M}{\zeta} & 1 \end{bmatrix} \times \begin{bmatrix} \cos(k_L L) & i\zeta_L \sin(k_L L) \\ \frac{i}{\zeta_L} \sin(k_L L) & \cos(k_L L) \end{bmatrix} \times \begin{bmatrix} 1 & M\zeta \\ -\frac{M}{\zeta} & 1 \end{bmatrix} \begin{bmatrix} (p_c)_{n-1} \\ (v_c)_{n-1} \end{bmatrix}. \quad (3\text{-}92)$$

This general procedure can also be applied to other forms of losses such as acoustically absorbing pipe walls. If there are no losses in the pipe, then

$$\zeta_L = \zeta_c = \zeta \quad (3\text{-}93)$$

and Equation (3-92) reduces to

$$\begin{bmatrix} (p_c)_n \\ (v_c)_n \end{bmatrix} = \exp(-i M k_c L) \begin{bmatrix} \cos(k_c L) & i\zeta \sin(k_c L) \\ \frac{i}{\zeta} \sin(k_c L) & \cos(k_c L) \end{bmatrix} \begin{bmatrix} (p_c)_{n-1} \\ (v_c)_{n-1} \end{bmatrix}, \quad (3\text{-}94)$$

a relatively simple expression for the convected acoustic variables, very similar to Equation (3-68). Since the viscous or boundary layer losses in most pipe systems with solid walls are extremely small, they can often be neglected and only the effects of mean flow considered with the resulting simplification of relationships.

Figure 3-7 shows the results of calculations using the transfer matrix resulting from Equation (3-94) for the straight section of the three-element sample problem of Sections 3.2.2 and 3.3.3.2 with and without a mean flow velocity of 250 ft/sec (M = 0.15). For this particular example, the primary effect of adding flow is to decrease the period of the cyclic variation at frequencies above 100 Hz, similar to the results for a lengthened straight section between the Helmholtz resonator and the contraction.

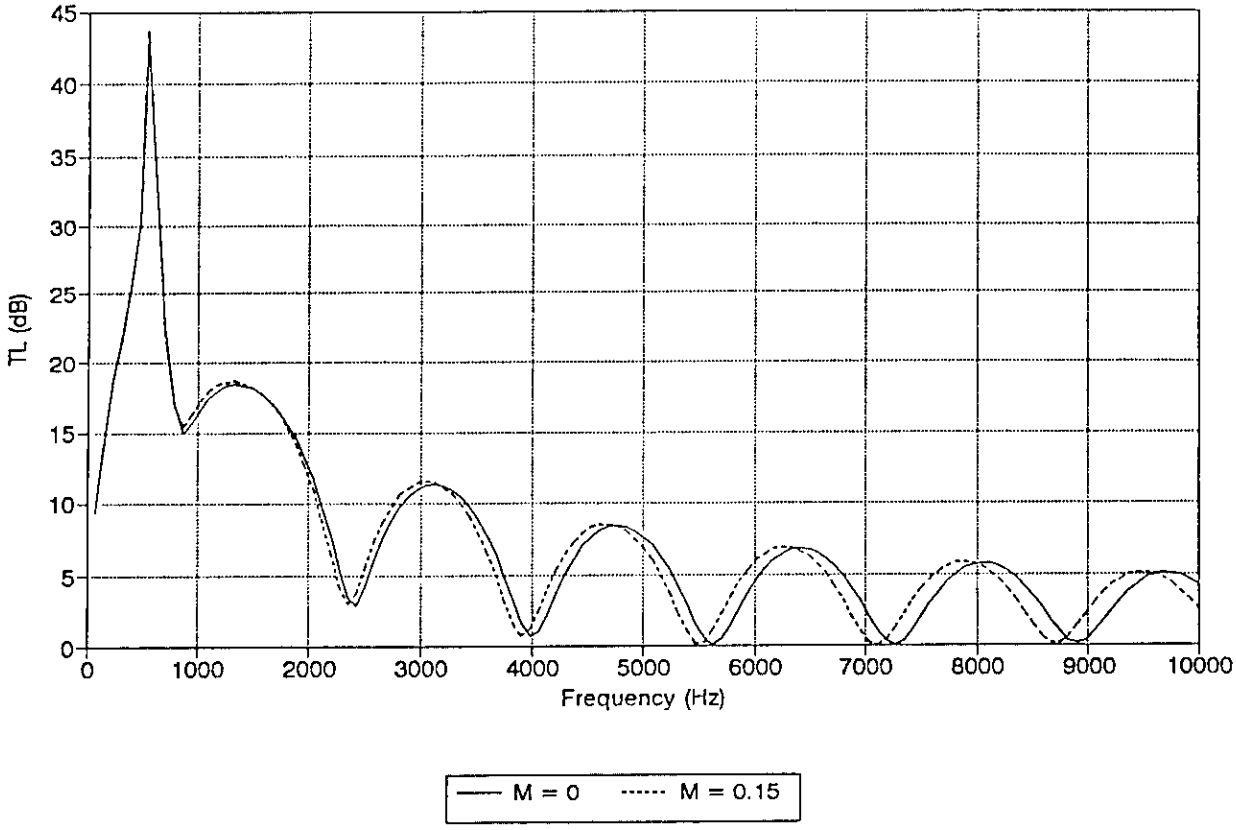

Figure 3-7. Transmission Loss for Three-Element Pipe Configuration With and Without Flow.

REFERENCES FOR CHAPTER 3

1. Kinsler, L.E., Frey, A.R., Coppens, A.B., and Sanders, J.V., *Fundamentals of Acoustics*, John Wiley & Sons, New York, 1982.

2. Munjal, M.L., *Acoustics of Ducts and Mufflers*, John Wiley & Sons, New York, 1987.

CHAPTER 4

SOUND PROPAGATION IN PIPES WITH NO MEAN FLOW

by Miguel C. Junger
Cambridge Acoustical Associates

This chapter deals with the situation in which one of three dimensions of the fluid-filled space is large or at least comparable to the acoustic wavelength. Sections 4.1 through 4.4 consider the most important situation where the pipe diameter measures less than one-half wavelength. In Sections 4.2 and 4.3, standing wave resonance and anti-resonance frequencies are formulated. Section 4.4 considers the special situation in turbomachinery where a T-tube junction is used to model the engine inlet and exit chambers. Section 4.5 examines the situation where the pipe diameter is small enough to allow viscous stresses to play a predominant role. Section 4.6 considers the short-wavelength range, where higher order modes characterized by cut-on frequencies begin to propagate. In Section 4.8, the sound speed and wave number for two-phase medium is derived.

4.1 The Quasi-Planar Wave

Consider an infinite plane wave propagating in the x-direction:

$$\begin{aligned} \textit{Incident Wave:} \quad & p_i(x,t) = P_i\, e^{i(\omega t - kx)}, \\ \textit{Reflected Wave:} \quad & p_r(x,t) = P_r\, e^{i(\omega t + kx)}. \end{aligned} \tag{4-1}$$

Now envision a rigid pipe aligned with the x-axis, i.e., with the direction of propagation. Clearly, the pipe being normal to the plane wave front does not disturb its propagation. Consequently, sound will propagate inside the pipe with the sound velocity of the infinite plane wave. It will be shown later that, even in a rigid pipe, waves can propagate with a speed other than the speed of sound. However, these latter modes of propagation require that the pipe diameter exceed approximately one-half wavelength (more precisely, 0.57λ).

When the pipe contains a liquid, the pipe wall compliance cannot be ignored compared to that of the liquid. The volume strain of the liquid column in an elastic duct is again given by Equation (2-31); the phase velocity, c, now dips below the velocity of the liquid, c_L:

$$c = \left(\frac{B_{eff}}{\rho}\right)^{1/2}$$

$$= \left[\left(B_L^{-1} + B_s^{-1}\right)\rho\right]^{-1/2}$$

$$= c_L\left[1 + (B_L/B_s)\right]^{-1/2}, \qquad (4\text{-}2a)$$

where $c_L = \left(\frac{B_L}{\rho}\right)^{1/2}$.

This is specialized to circular pipes of radius r_s by introducing Equation (2-33)

$$\frac{c}{c_L} = \left[1 + \frac{2B_L r_s}{Eh}\right]^{-1/2} \qquad (4\text{-}2b)$$

$$\cong 1 - \frac{B_L r_s}{Eh}, \qquad \left(\frac{B_L r_s}{Eh}\right)^2 \ll 1. \qquad (4\text{-}2c)$$

This is the Korteweg-Lamb correction[1] which was previously mentioned in Section 2.3.

For example, for water ($B_L = 2.25 \times 10^{10}$ μ bar) in a glass tube ($E = 6.03 \times 10^{11}$ μ bar), with a wall thickness-to-radius ratio of 1/10, $c/c_L = 0.76$. Note that the wave is no longer plane, since the displacement of liquid particles adjoining the wall displays a substantial radial component. In fact, only the particles located on the pipe axis undergo a strictly axial displacement. The pressure does not, however, display a phase reversal over the pipe cross-section. This type of mode is therefore called *quasi-planar*.

4.2 Standing Waves: Resonances and Anti-Resonances in Pipes With Rigid Terminations

Now consider a pipe of finite length L. If the pipe is terminated by a rigid plug, the axial particle velocity must vanish at $x = L$. It is recalled from basic fluid mechanics that Euler's law relates the fluid particle acceleration $\ddot{\delta}$ to the pressure gradient

$$\ddot{\delta} = \frac{\partial u}{\partial t} = -\frac{1}{\rho}\frac{\partial p}{\partial x}. \qquad (4\text{-}3a)$$

For harmonic time dependence, the corresponding velocity and displacement are

$$u = -\frac{i}{\rho\omega}\frac{\partial p}{\partial x}$$

$$= -\frac{i}{\rho c k}\frac{\partial p}{\partial x} ,$$

$$\delta = \frac{1}{\rho c^2 k^2}\frac{\partial p}{\partial x} . \qquad (4\text{-}3b)$$

Consequently, for the rigid termination ($\delta = 0$), the pressure must satisfy the boundary condition

$$\frac{\partial p}{\partial x} = 0 , \qquad x = L . \qquad (4\text{-}4)$$

The pressure in the fluid column can be formulated as the superposition of an incident wave traveling in the positive x-direction, e.g., Equation (4-1), and a reflected pressure traveling in the negative x-direction

$$p(x) = P_I e^{-ikx} + P_R e^{ikx} , \qquad (4\text{-}5)$$

where the $\exp(-i\omega t)$ has been suppressed to simplify the notation.

The pressure gradient at the termination is

$$\frac{\partial p}{\partial x} = ik\left[-P_I e^{-ikL} + P_R e^{ikL}\right] , \qquad (4\text{-}6)$$

For a rigid termination, the derivative satisfying Equation (4-4) requires that

$$P_R = P_I e^{-2ikL} , \qquad (4\text{-}7)$$

The resultant pressure, Equation (4-5), now becomes

$$p(x) = P_I\left[e^{-ikx} + e^{(ikx - 2ikL)}\right]$$

$$= P_I e^{-ikL}\left[e^{(ikL - ikx)} + e^{(ikx - ikL)}\right]$$

$$= 2 P_I e^{-ikL} \cos k(L - x) . \qquad (4\text{-}8)$$

This is a standing wave. The specific acoustic impedance at the drive point, $x = 0$, is

$$\begin{aligned} z_u &= \frac{p}{u}\Big|_{x=0} \\ &= i\rho c k \frac{p}{\partial p/\partial x}\Big|_{x=0} \\ &= i\rho c \cot(kL) \\ &\equiv \frac{i\rho c^2}{\omega L} \quad , \qquad k^2 L^2 \ll 1 . \end{aligned} \tag{4-9}$$

Consequently, like the resonator cavity, the liquid column in the closed cavity acts as a spring when the pipe length is small in terms of wavelengths. This impedance vanishes when $kL = \pi/2$, $3\pi/2$, . . ., or

$$L = \frac{\lambda}{4}(2n + 1) \quad , \quad n = 0, 1, 2, \cdots . \tag{4-10}$$

This is readily envisioned for the fundamental resonance (Figure 4-1a). At $x = 0$, the pressure is zero and the velocity, in terms of the Reynolds number

$$\begin{aligned} \mathrm{Re}\,[u(o)] &= \frac{2P_i}{\rho c}\,|\sin k(x - L)|_{x=0} \\ &= \frac{2P_i}{\rho c}\sin kL \end{aligned} \tag{4-11}$$

peaks when $L = \lambda/4$. Natural resonant frequencies corresponding to Equation (4-10) are

$$f_{rn} = \frac{(2n + 1)c}{4L} . \tag{4-12a}$$

These results apply to both gas- and liquid-filled pipes provided one uses Equation (4-2) for the sound speed (c) of the latter.

The pipe also displays anti-resonances whereby the drive point impedance is infinite. Referring to Equation (4-9) this occurs when (Figure 4-1b)

$$\begin{aligned} kL &= n\pi , \\ f_{an} &= \frac{nc}{2L} \quad , \qquad n = 1, 2, \ldots \end{aligned} \tag{4-12b}$$

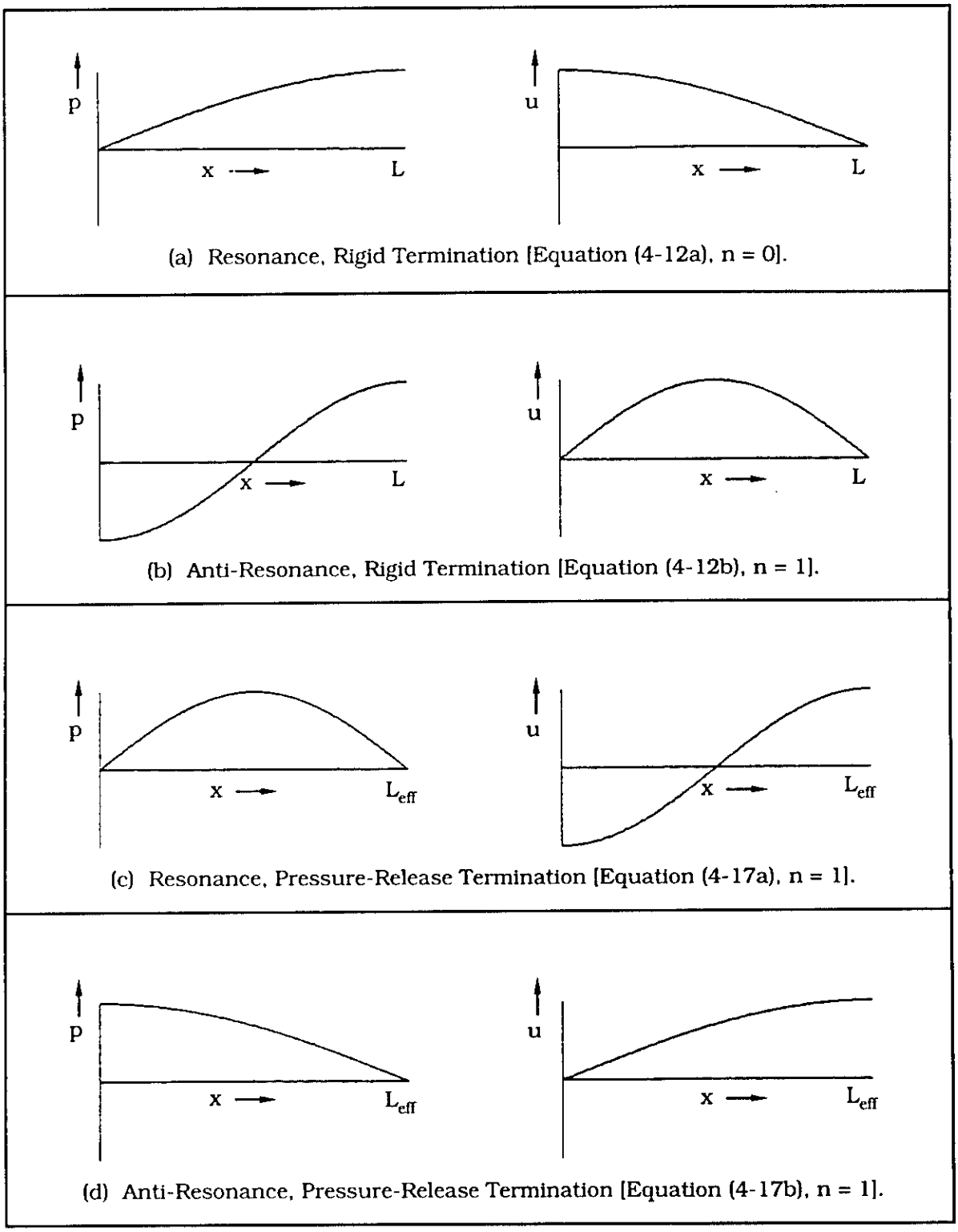

Figure 4-1. Pressure, p, and Axial Fluid Particle Velocity, u, for Fundamental Resonance (a, c) and anti-resonance (b, d), at end L having rigid (a, b) or pressure-release (c, d) termination.

4.3 Standing Waves in Open-Ended Pipes

Consider a "pressure release" termination, i.e., a boundary condition which requires that the pressure at $x = L$ vanish. For a liquid-filled pipe, this is readily approximated by an open-ended stand pipe. For either a gas- or liquid-filled pipe, this boundary condition is also approximated by a pipe opening into a space filled with the same acoustic fluid provided $A_p << \lambda^2$. The interface between the fluid column and the adjoining extended column is simulated by a virtual piston. The piston impedance embodies a resistive component R_a representing sound radiation, Equation (2-36), and a reactive component associated with the entrained mass $-i\omega\rho\, A_p\, \Delta L_o$, where ΔL_o is the same end correction as for the Helmholtz resonator, Equation (2-7) ($\Delta L_o = 0.48\, A_p^{1/2}$). Consequently, for $A_p << \lambda^2$, the impedance ratio at the open end of a pipe is

$$\frac{z_u}{\rho c\, A_p} = -i\, k \Delta L_o + \frac{k^2 A_p}{2\pi}, \qquad x = L$$

$$= 2\pi \left(-i\, 0.48\, \frac{A_p^{1/2}}{\lambda} + \frac{A_p}{\lambda^2} \right). \tag{4-13}$$

The resistance ratio can be neglected in the long wavelength limit. The entrained mass is not negligible, but can be accounted for by substituting an equivalent length L_{eff}, a procedure already familiar from the analysis of the Helmholtz resonator

$$L_{eff} = L + \Delta L_o$$

$$= L + 0.48\, A_p^{1/2}. \tag{4-14}$$

In what follows, $L_{eff} = L$ is used when dealing with a water-filled, open-ended stand pipe, while L_{eff} is given by Equation (4-14) when dealing with a pipe opening into a space filled with the same acoustic fluid. The "pressure-release" boundary condition, $p(L_{eff}) = 0$, is satisfied by Equation (4-5) when

$$P_R = -P_I\, e^{(-2ik\, L_{eff})}$$

The standing wave field therefore becomes

$$\begin{aligned} p(x) &= P_i \left[e^{(-ikx)} - e^{(ikx - 2ik L_{eff})} \right] \\ &= P_i \, e^{(-ik L_{eff})} \left[e^{(ik L_{eff} - ikx)} - e^{(ikx - ik L_{eff})} \right] \\ &= 2i \, P_i \, e^{(-ik L_{eff})} \sin (k L_{eff} - kx) \, . \end{aligned} \tag{4-15}$$

The drive point impedance is computed as in Equation (4-9). However, the present calculation is approximate in that the radiation resistance in Equation (4-13) is ignored compared to the reactance. This approximation is valid if $k A_p^{1/2} \ll 1$, an assumption inherent in Equation (4-13)

$$\begin{aligned} Im(z_{uo}) &= -\rho c \tan (k L_{eff}) \\ &\cong -\rho \omega L_{eff} \, , \qquad k^2 L_{eff}^2 \ll 1 \, . \end{aligned} \tag{4-16}$$

Consequently, as anticipated, the column of water displays the impedance of a solid slug of fluid when its length is short in terms of wavelength.

The open pipe displays a resonance when

$$k L_{eff} = n\pi \, , \qquad n = 1, 2, \ldots$$

i.e., at frequencies

$$f_n = \frac{nc}{2 L_{eff}} \, , \qquad n = 1, 2, \ldots \tag{4-17a}$$

This situation is illustrated in Figure 4-1c. The open pipe displays an anti-resonance when (Figure 4-1d)

$$k L_{eff} = \frac{(2n + 1)\pi}{2} \, , \qquad n = 1, 2, \ldots$$

$$f_{an} = \frac{(2n + 1) c}{4 L_{eff}} \, . \tag{4-17b}$$

Consequently, the natural frequencies of the open-ended pipe corresponds to the anti-resonance frequencies of the closed pipe, and vice versa.

4.4 T-Tube Junction

Consider the acoustic resonance frequency for a "T-tube" junction (Figure 4-2). This problem has immediate practical application in turbomachinery because of its resemblance to an engine's inlet and exit volute. The engine inlet and exit chambers are each formed by wrapping the two branches of the top of a symmetrical T-tube around a cylinder and joining both ends together.

The general solution to the T-tube junction may be derived using the techniques described in Chapters 2 and 3. The interested reader who wishes to examine the details of this solution should see the paper by Merkli.[2]

The general solution is rather involved; however, after a few simplifying assumptions it reduces to

$$-2\,i\,\frac{1}{\rho\,\zeta}\,\tan(k\,L) = \frac{1 + i\,(1/\rho\,\zeta)\,(Z_v)_c\,\tan(k\,l)}{(Z_v)_c + i\,\rho\,\zeta\,\tan(k\,l)}, \qquad (4\text{-}18)$$

where $\zeta = c/A_p$, and $(Z_v)_c$ is the acoustic impedance based upon acoustic volume velocity at the c end of the pipe (see Figure 4-2). This solution assumes that all three pipes of the T-tube have the same cross-sectional area and that the ends a and b are closed.

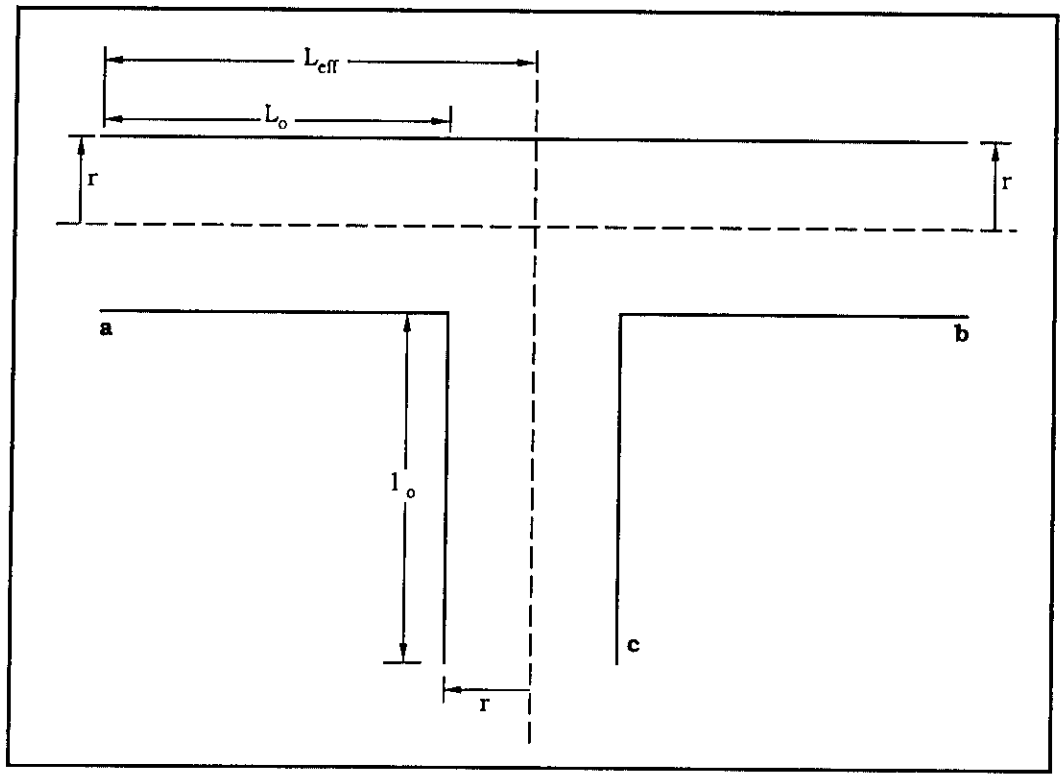

Figure 4-2. T-Tube Junction.

In Chapter 3 the resonance frequencies were derived for a pipe section with a single side branch. In this derivation it was assumed that the tubes were long in comparison to the radius, making it unnecessary to consider the effective length due to the junction. When the tubes are short, as in the case of an engine inlet and exit chamber, corrections must be applied to the tube lengths. Merkli[2] shows that when the pipe cross-sectional areas of all three branches of the T-tube are the same, then

$$\begin{aligned} L_{eff} &= L_o + \Delta L_1 + \Delta L_2 \ , \\ l_{eff} &= l_o + \Delta l_1 + \Delta l_2 \ , \end{aligned} \tag{4-19}$$

where

$$\begin{aligned} \Delta L_1 &= \Delta l_1 = r\left(1 - \frac{8}{3\pi}\right) , \\ \Delta L_2 &= \frac{16\,r}{3\,\pi}\,\frac{L_o}{2L_o + l_o} \ , \\ \Delta l_2 &= \frac{16\,r}{3\,\pi}\,\frac{l_o}{2L_o + l_o} \ , \end{aligned} \tag{4-20}$$

where L_o and l_o are the lengths of the purely cylindrical parts of the T-tube as shown in Figure 4-2.

The general solution, Equation (4-18), can be solved for several special cases:

1. The top of the T-tube junction is a special solution in which a standing wave is confined to the top of the T with a pressure node at the junction. Consequently, the length of the stem has no effect on the resonance at the top of the junction. The effective length becomes

$$L_{eff} = L_o + r \tag{4-21}$$

and the resonance frequencies are determined using Equation (4-12a) where the L appearing in that equation is the effective length.

2. A closed end at c is a special solution for which $(Z_v)_c = \infty$. For this condition, Equation (4-18) reduces to

$$3 \sin\left[\frac{\omega}{c}(L_{eff} + l_{eff})\right] + \sin\left[\frac{\omega}{c}(L_{eff} - l_{eff})\right] = 0. \tag{4-22}$$

This transcendental equation gives the resonances of the T-tube.

3. An open end at c is a special solution for which $(Z_v)_c = 0$. This is the condition that applies in most turbomachinery applications. For this condition, Equation (4-18) reduces to

$$3 \cos\left[\frac{\omega}{c}(L_{eff} + l_{eff})\right] - \cos\left[\frac{\omega}{c}(L_{eff} - l_{eff})\right] = 0. \qquad (4\text{-}23)$$

In this situation, the end correction, Δl_1, given in Equation (4-20), must be modified to account for the open end at c. In Section 4.3 it was shown that the end correction is $0.48\, A_p^{1/2}$, so that Δl_1 in Equation (4-20) becomes

$$\Delta l_1 = r\left(1 - \frac{8}{3\pi}\right) + 0.48\, A_p^{1/2}. \qquad (4\text{-}24)$$

Finally, when solving for the acoustic resonances in a T-tube junction, whether it be open or closed at c, resonance frequencies given by Equation (4-12a) at the top of the T are found together with the resonance frequencies given by Equations (4-22) or (4-23).

4.5 Capillary Tubes

The situations considered so far apply when the pipe diameter measures a fraction of a wavelength. Before turning to the short-wavelength range in Section 4.6, we consider, in this seciton, the extreme long-wave limit where the pipe radius is comparable to the viscous boundary layer thickness. The equations governing this situation will be presented in a manner appealing to the intuition of the fluid mechanics rather than being rigorously derived from basic principles. The reader who wishes to explore the matter in greater detail is referred to Rayleigh's[3] classical work.

Let us first consider the acoustic boundary layer thicknesses on a flat plate. Rayleigh[3] (page 317, Equation (5)) shows that this thickness is

$$d = \left(\frac{\mu}{\pi \rho f}\right)^{1/2}, \qquad (4\text{-}25a)$$

where μ is the viscosity. Referring to Table 2-1, one computes

$$d = \frac{0.22}{f^{1/2}} \quad \text{cm} \quad \text{for air} \quad \text{and}$$

$$d = \frac{0.056}{f^{1/2}} \quad \text{cm} \quad \text{for water}. \qquad (4\text{-}25b)$$

The propagation and attenuation of sound in capillary tubes can be compactly expressed in terms of this boundary layer thickness. Sound propagates at a lower velocity in a capillary tube than in a pipe where $2\,r_s \gg d$. The effective phase velocity c_c in the capillary tube is

$$c_c = c_L \left(1 - \frac{d}{2\,r_s}\right) , \qquad 2\,r_s \ll \lambda . \tag{4-26}$$

This wave is markedly attenuated compared to sound propagating in an extended medium. The attenuation per diameter can be expressed in terms of the boundary layer thickness:

$$\alpha_d = \frac{54\,d}{\lambda} \text{ dB/diam.} , \tag{4-27}$$

where λ is the acoustic wavelength in the extended medium. Referring to the second of Equations (4-25b), and substituting $c = 1.48 \times 10^5$ cm/s, the attenuation per diameter in a water-filled capillary tube becomes

$$\alpha_d = 2.0 \times 10^{-5}\ f^{1/2} \text{ dB/diam.} \quad \text{[water-filled capillary]} , \tag{4-28}$$

where f is in Hz and the diameter is in cm. Consequently, for $f = 1000$ Hz, a 0.4 cm tube diameter, and a 1 m tube length, the total attenuation is

$$2 \times 10^{-5} \times 1000^{1/2} \times 100/0.4 = 0.16 \text{ dB.}$$

While this is a modest figure indeed, the attenuation in an extended body of sea water, owing to viscosity as well as to other factors is a mere 10^{-5} to 10^{-4} dB/m at this frequency.[4] If only viscosity were accounted for in computing attenuation, the latter figure would be three orders of magnitude smaller.

In gas-filled tubes, the effective viscosity μ_{eff} is markedly increased by heat conduction. For air at room temperature, the effective viscosity required to yield the observed attenuation is

$$\mu_{eff} = 1.93\,\mu . \tag{4-29}$$

Consequently, for air the effective boundary layer thickness to be used in Equation (4-27) is $1.93^{1/2}$ larger than the one indicated in the first of Equations (4-25b). Substituting $c = 3.43 \times 10^4$ cm/sec into Equation (4-27), the resulting attenuation per diameter is

$$\alpha_d = 4.8 \times 10^{-4}\ f^{1/2} \text{ dB/diam.} \quad \text{[air-filled capillary]} , \tag{4-30}$$

where f is in Hz and the diameter is in cm. For the same tube dimensions as before, one achieves an attenuation of 3.8 dB at 1 kHz.

4.6 Modal Propagation in Gas-Filled Pipes

So far, we have limited the discussion to wavelengths measuring more than two pipe diameters, i.e., to quasi-planar waves displaying no phase reversal over the pipe cross-section and consequently no nodal diameters or circles. For the quasi-planar mode, the pressure field could be approximated by the solution to the one-dimensional wave equation, modified where necessary to account for boundary elasticity. For pipe diameters commensurate with the wavelength, the pressure field must be formulated as the solution of the three-dimensional wave equation in cylindrical coordinates, the pressure distribution over the pipe cross-section now becoming a function of the radial dimension r and of the circumferential angle ϕ. As in the case of the capillary tube, we shall not derive the solution rigorously from basic principles but start from an intuitively reasonable basis. The interested reader can find a self-contained and detailed development in Reference 5.

The three-dimensional pressure field in an effectively infinitely long pipe of radius r_s is described by a summation of orthogonal waveguide-type modes whose radial dependence is formulated in terms of Bessel functions $J_n(\alpha_{nm} r/r_s)$

$$p(r,z,\phi) = \sum_{n,m} P_{nm} J_n(\alpha_{nm} r/r_s) \cos(n\phi) \exp(i \gamma_{nm} x). \qquad (4\text{-}31)$$

The modal amplitudes P_{nm} can be computed in terms of the source distribution which gives rise to the pressure field. The number of modal circles is m, that of modal diameters n. If the pressure field does not admit a plane of symmetry, $\sin(n\phi)$ terms must be added. The radial wavenumbers α_{nm}/r_s are determined by the boundary condition at the inside pipe wall. Each mode separately must match the pipe wall specific acoustic impedance, which will be considered here to be locally reacting

$$z_n = \frac{p}{\dot{\delta}} = \frac{p}{u} \quad , \qquad r = r_s$$

$$= \frac{i \rho c k p}{\partial p/\partial r}$$

$$= \frac{i \rho c k r_s J_n(\alpha_{nm})}{\alpha_{nm} J'_n(\alpha_{nm})} \, . \qquad (4\text{-}32a)$$

In this section, where we restrict ourselves to gas-filled pipes, the wall impedances can be taken to be infinite. The boundary condition therefore becomes

$$J'_n\ (\alpha_{nm}) = 0\,. \tag{4-32b}$$

For Equation (4-31) to be a solution of the wave equation, the axial wavenumber (γ_{nm}) must be related to the radial wavenumber (α_{nm}/r_s) and the acoustic wavenumber k as follows

$$\gamma_{nm} = [k^2 - (\alpha_{nm}/r_s)^2]^{1/2}\,. \tag{4-33a}$$

Consequently the axial wavenumber is imaginary, i.e., the mode decays exponentially if $k\,r_s < \alpha_{nm}$. The cut-on frequency, where the mode begins to propagate, therefore is

$$f_{nm} = \frac{c\ \alpha_{nm}}{2\pi\ r_s}\,. \tag{4-33b}$$

The modal phase velocity in the propagating range is

$$c_{nm} = \frac{2\pi f}{\gamma_{nm}}\,, \quad f > f_{nm}$$

$$= c\left[1 - \left(\frac{\alpha_{nm}}{k\ r_s}\right)^2\right]^{-1/2}\,. \tag{4-34}$$

The phase velocity decreases monotonically from infinity at the cut-on frequency to the sound velocity at high frequencies (Figure 4-3).

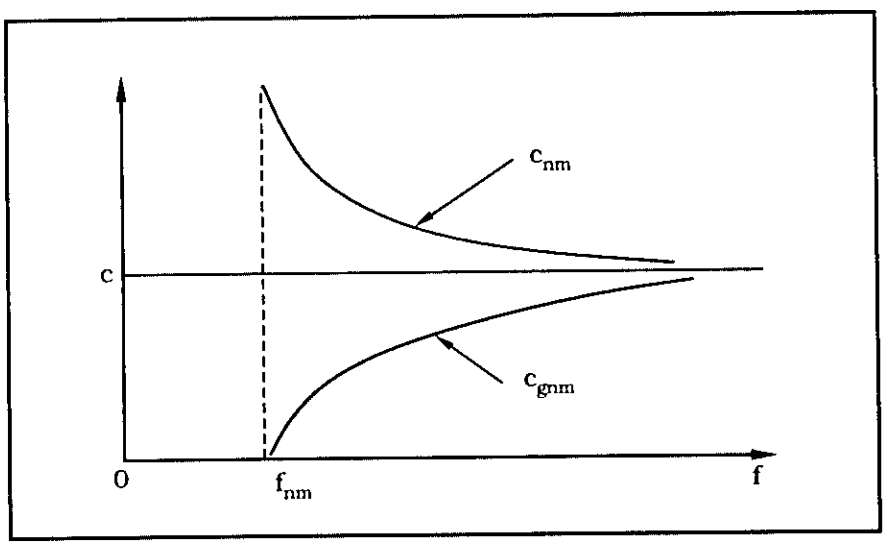

Figure 4-3. Schematic Dispersion Curves for the Phase Velocity c_{nm}, Equation (4-34), and the Group Velocity c_{gnm}, Equation (4-36b), in a Rigid Pipe, the Cut-On Frequency Being Given in Equation (4-33b).

For the effectively rigid boundary representative of gas-filled pipes, Equation (4-32b), the fundamental planar mode has, as expected, a zero cut-on frequency, since $J'_0(0) = 0$. Consequently, $c_{oo} = c$ at all frequencies, as anticipated in Section 4.1. The higher modes are all non-propagating in the low-frequency range, since they display a finite cut-on frequency. The lowest of these corresponds to mode $n = 1$, $m = 0$, a mode displaying one nodal diameter and no nodal circle, for which $\alpha_{10} = 1.8$. Its cut-on frequency is therefore

$$f_{10} = \frac{1.8c}{2\pi r_s}. \tag{4-35}$$

For a 4-inch (10 cm)-diameter water-filled pipe, this yields $f_{10} = 4.2$ kHz. As a radially oriented dipole located on the pipe axis does not excite the planar mode, such a source does not generate a propagating wave below 4.2 kHz for the parameters selected in this example.

While the phase velocity diverges at the cut-on frequency, the modal *group velocity* c_{gnm}, i.e., the velocity at which energy associated with a wave packet travels, cannot exceed the sound velocity c. The group velocity is computed from the dispersion relation[6]

$$c_{gnm} = \frac{d\omega}{d\,\gamma_{nm}}. \tag{4-36a}$$

Since the planar wave is non-dispersive ($\gamma_{oo} = k$), both the group and the phase velocity equal the sound velocity c. For all other modes, the phase velocity is dispersive and therefore differs from the group velocity. Elementary though laborious calculations which the reader might want to check as an exercise yield the group velocity

$$c_{gnm} = c\left(1 - \frac{\alpha_{nm}^2}{k^2 r_s^2}\right)^{1/2}, \qquad k r_s > \alpha_{nm}, \quad f > f_{nm}. \tag{4-36b}$$

Consequently, as the frequency approaches the cut-on frequency from above, the group velocity tends to zero. In the high-frequency limit, it tends to the sound velocity in the extended fluid medium (Figure 4-3).

4.7 Wave Mode Propagation in Fluid-Filled Non-Rigid Waveguides

The specific impedance of unlined pipes is typically reactive, i.e.,

$$z_u \cong i\, x_u \,. \tag{4-37}$$

Referring to Equation (4-32a), the boundary condition can be expressed as

$$\frac{x_u}{\rho\, c\, k\, r_s} = F_n(\alpha) \tag{4-38a}$$

where

$$F_n(\alpha) = \frac{J_n(\alpha)}{\alpha\, J'_n(\alpha)} \,. \tag{4-38b}$$

This function is plotted for axisymmetric ($n = 0$) modes in Figure 4-4. It is apparent that an infinite reactance, $|F_o| = \infty$, calls for $\alpha = 0$, i.e., a zero cut-on frequency, and, since $J_o(0) \equiv 1$, a strictly planar wave, as anticipated in the previous section.

Recall that, in our notation, a negative reactance indicates a mass-controlled pipe wall. The branches labelled $-F_o(\alpha)$ correspond to this situation. The stiffness-controlled pipe, i.e., $x_u > 0$, cannot be matched by Bessel functions of real argument, but requires imaginary arguments, i.e., $\alpha = i|\alpha|$. This gives rise to the curve labelled $F_o(i|\alpha|)$ in Figure 4-4. The corresponding phase velocity is obtained from Equation (4-34) where $-\alpha^2 = |\alpha^2|$. The phase velocity is less than the sound velocity in the extended medium as already anticipated from the Korteweg-Lamb approximation

$$c_{oo} = c\left[1 + \left(\frac{|\alpha_{oo}|}{k\, r_s}\right)^2\right]^{-1/2} \,. \tag{4-39}$$

The low-frequency reactance of a cylindrical shell was already formulated in connection with Helmholtz resonators

$$x_u = \frac{Eh}{\omega\, r_s^2} = \frac{Eh}{ck\, r_s^2} \,, \quad f^2 \ll f_o^2 \tag{4-40a}$$

where f_o is the breathing mode resonance frequency

$$f_o = \frac{c_b}{2\pi\, r_s} \,, \tag{4-40b}$$

where c_b is the compressional wave velocity in the pipe wall ($\cong 5.4 \times 10^5$ cm/s in steel). The corresponding dimensionless frequency is

$$(k\, r_s)_o = \frac{c_b}{c} \,.$$

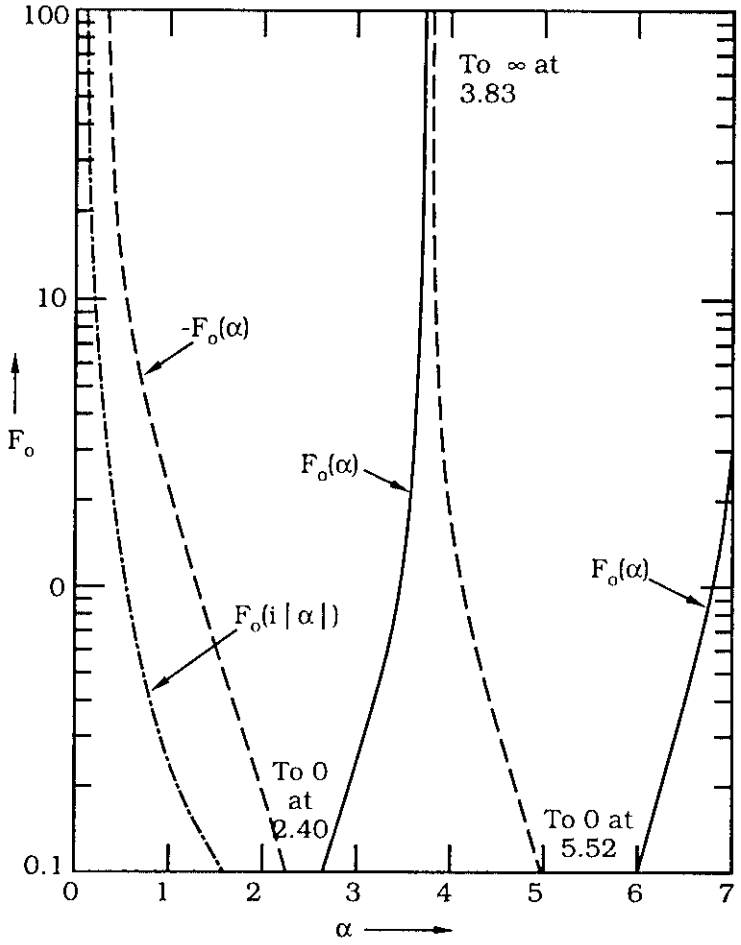

Figure 4-4. Plot of the Bessel Function Ratio Relating the Radial Wavenumber α/r_s to the Pipe Wall Reactance, for the Axisymmetric Modes, $F_o(\alpha)$, Equation (4-39). The negative values of F_o correspond to mass-controlled pipe wall reactances. (Reproduced from Junger and Feit.[5])

Substituting this result in Equation (4-38a), one obtains the boundary condition in terms of the pipe parameters

$$\frac{Eh}{\rho c^2 k^2 r_s^3} = F_o(i|\alpha|). \tag{4-41}$$

Consider the low-frequency limit $k^2 r_s^2 \ll 1$, where $F_o(i|\alpha|)$ is large, its small-argument asymptotic form being

$$F_o(i|\alpha|) \equiv 2|\alpha|^{-2}, \qquad |\alpha|^2 \ll 1. \tag{4-42}$$

Combining Equations (4-41) and (4-42),

$$(|\alpha|)/k r_s)^2 = 2\rho c^2 r_s/Eh, \qquad k^2 r_s^2, |\alpha|^2 \ll 1. \tag{4-43}$$

When this is substituted in Equation (4-39), one retrieves the Korteweg-Lamb correction, Equation (4-2), where $B_L = \rho c^2$.

At higher frequencies, the pipe wall inertia forces reduce the stiffness-controlled reactance. However, flexural rigidity, which is proportional to $(h^2/12 r_s^2)\, \partial^4 \delta/\partial z^4$, keeps the reactance stiffness-controlled even above the ring resonance. The boundary condition now becomes[6]

$$\frac{x_u}{\rho c k r_s} = \frac{Eh}{\rho c^2 k^2 r_s^3}\left[1 - \left(\frac{k r_s c}{c_b}\right)^2 + \frac{h^2}{12 r_s^2}\gamma_{om}^4 r_s^4\right]. \tag{4-44}$$

Setting this quantity equal to $F_o(i|\alpha|)$, one solves for the frequency-dependent value of $|\alpha|$, and hence for the phase velocity in Equation (4-39). The results are in fair agreement with phase velocity measurements as shown in Figure 4-5.

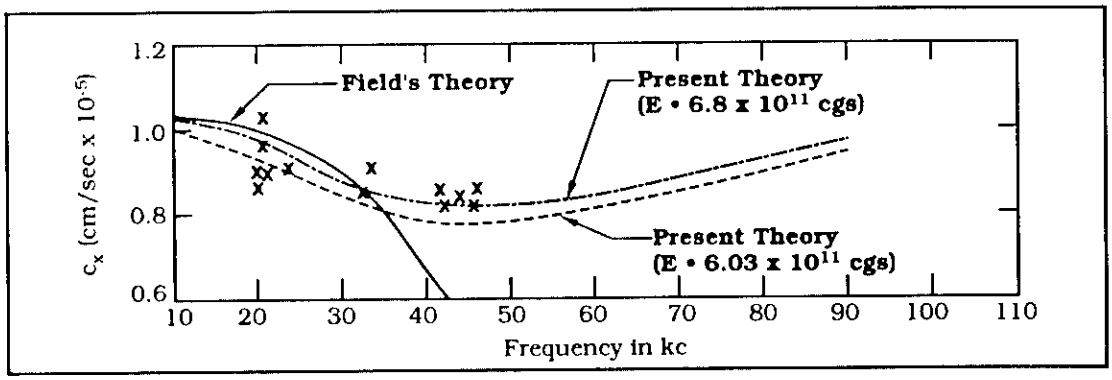

Figure 4-5. Dispersion Curve for the Quasi-Planar Wave in a Liquid (Naphtha) Column in a Glass Tube: h = 0.14 cm, $2r_s$ = 3.04 cm, ρ_s = 2.6, c = 1.21 x 10^5 cm/s, ρ = 0.74 g/cm^3. (Reproduced from Junger.[7]) Dashed Curves Equation (4-44) for the wall reactance, and Equation (4-39) with $\alpha = i|a|$ (see Figure 4-4). Solid line is the same, but ignores the flexural term in Equation (4-44). (Reproduced from Field and Boyle.[8]) Crosses: experimental points from Reference 8.

The stiffness component of a soft rubber hose does not embody the flexural term which prevents the pipe wall from becoming mass-controlled. The hose therefore presents a mass-like impedance above its ring resonance. Sufficiently far above that resonance, the membrane-stiffness can also be dropped, the wall reactance being effectively that of the mass per unit area of hose wall

$$\frac{x_w}{\rho c k r_s} \cong -\frac{\rho_s h}{\rho r_s} = F_o(\alpha) , \qquad f^2 >> f_o^2 . \tag{4-45}$$

An experimental study was performed on a soft rubber hose in air[9] (ρ_s/ρ = 6.5 x 10^2, h/r_s = 0.043). The resulting value of α obtained from the lower $-F(\alpha)$ branch in Figure 4-4, or from the asymptotic small $-\alpha$ relation

$$F_o(\alpha) \cong -\frac{2}{\alpha^2} , \qquad \alpha^2 << 1 \tag{4-46}$$

is

$$\alpha \cong \left(\frac{2}{(\rho_s/\rho)(h/r_s)}\right)^{1/2} = 0.27. \tag{4-47}$$

The phase velocity is obtained from Equation (4-34)

$$\frac{c_{01}}{c} \cong \left[1 - \left(\frac{0.27}{k r_s}\right)^2\right]^{-1/2} . \tag{4-48}$$

This dispersion curve is plotted in Figure 4-6 together with experimental points. The velocity ratio was computed from the coincidence cone vertex angle, θ_c, of the distribution-in-angle of the sound field radiated as a supersonic line array, by the hose coupled to a small loudspeaker

$$\frac{c_{01}}{c} = \frac{1}{\sin\theta_c} , \tag{4-49}$$

where θ_c is measured from the hose axis. A physical interpretation of the enhancement of the effective sound velocity is that the hose responds out of phase with the pressure exerted by air in the hose, thereby reducing the effective compliance of the air within a mass-controlled boundary.

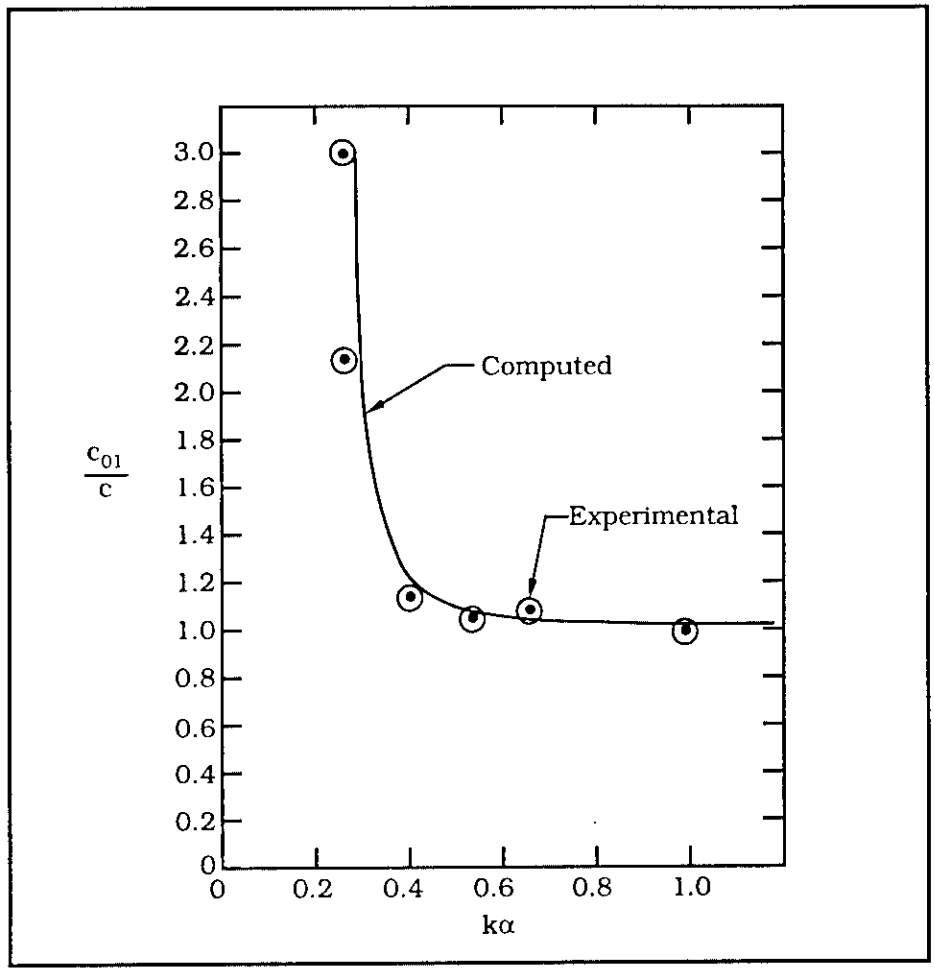

Figure 4-6. Phase Velocity in a Rubber Hose Whose Reactance is Mass-Controlled. (Reproduced from Junger.[9])

4.8 Sound Propagation in Two-Phase Systems

Sound propagation in a boiling liquid, or in a liquid containing gas bubbles, shares a fundamental feature with sound propagating in a liquid contained in an elastic pipe or duct (Section 4.1). The reciprocal of the effective bulk modulus B_{eff} is the resultant of the compliance of the liquid B_L^{-1}, and of another component, i.e., the elastic waveguide boundary in the former situation, and the compliance B_s^{-1} of the bubble swarm in the present case. This mathematical model applies as long as individual gas bubbles or vapor pockets are small in terms of the liquid-borne sound wavelength. Furthermore, the situation where gas or vapor has risen under the effect of buoyancy to form a continuous layer above the liquid is not considered either. This latter situation does not, of course, arise in a boiling liquid where the vapor bubbles collapse before they coalesce, or in a zero-gravity environment. The next subsection reviews the thermodynamics of a two-phase medium. Subsection 4.8.2 derives the sound velocity in various frequency ranges. Subsection 4.8.3 deals with resonances in pipes containing a two-phase medium.

4.8.1 Thermodynamics of a Two-Phase Media

The thermodynamic state of pure substances such as hydrogen and oxygen is defined by two independent thermodynamic properties. The term "state" is used to denote the phase (i.e., solid, liquid, vapor) and the pressure, temperature, etc., at which the substance remains in equilibrium. For conditions experienced in turbomachinery, such as in the SSME, both substances can exist in liquid and vapor phases through parts of the system. As described in the following subsection (4.8.2), the sound speed in the substance, being proportional to the square root of the bulk modulus, varies substantially between liquid and vapor phases. Furthermore, the sound speed in two-phase mixtures that exist during boiling or condensation is extremely sensitive to the fractional content of vapor (i.e., the quality) in the mixture.

Thermodynamic states consisting of liquid–vapor mixtures can exist between the triple point and the critical point. The triple point is a single state at which the three phases exist in equilibrium. For oxygen the triple point temperature and pressure are 97°R and 1.06 psia, while for hydrogen they are 24°R and 0.022 psia. The highest temperature and pressure that a liquid–vapor mixture can exist in equilibrium is denoted as the critical point. The critical

point temperature and pressure for oxygen and hydrogen, respectively, are 278°R, 735 psia, and 60°R, 188 psia.

Although all three phases can exist at pressures higher than the critical pressure, there is no liquid phase at temperatures above the critical temperature. Consequently, liquid–vapor mixtures can only exist between the triple and critical point temperatures (97°–278°R for oxygen, 24°–60°R for hydrogen). Within this range, the pressure at which such mixtures can exist is the saturation pressure (i.e., the pressure at which boiling or condensation occurs) at the prescribed temperature. The thermodynamic saturation properties (e.g., pressure and temperature) for both substances are tabulated in chemical handbooks.[10] Pressure and temperature are not independent properties in saturated states. Rather, either one of these properties along with the quality of the mixture (i.e., the mass of vapor per total mixture mass) define the state.

In normal operation of the SSME, hydrogen changes phase after leaving the high-pressure turbopump as it acquires heat in cooling the nozzle and combustion chamber. Oxygen flows to the combustion chamber as a liquid; however, a portion of the oxygen flow from the high-pressure turbopump is converted to vapor in the Pogo suppression system. Except for these areas, both substances are either liquid or vapor under normal operating conditions.

4.8.2 Sound Velocity in Two-Phase Media

If α is the volume fraction of vapor or gas, the effective density of the medium is

$$\begin{aligned} \rho &= \alpha \rho_c + (1 - \alpha) \rho_L \\ &\cong (1 - \alpha) \rho_L \quad , \qquad \alpha \rho c \ll \rho_L \end{aligned} \tag{4-50}$$

where the subscripts L and c refer, respectively, to the liquid and to the vapor or gas forming the cavities or bubbles. The sound velocity is formulated as in Equation (4-2a):

$$\begin{aligned} c &= \left(B_{eff}^{-1} \rho\right)^{-1/2} \\ &= \left\{ \left[(1 - \alpha) B_L^{-1} + B_s^{-1} \right] \rho \right\}^{-1/2} , \end{aligned} \tag{4-51}$$

where B_s^{-1} is the compliance contributed by the bubble swarm.

This compliance component is the product of the fractional volume of vapor or gas and of the effective compliance B_c^{-1} of individual vapor-filled cavities or gas bubbles. Since the cavities are acoustically compact, sound pressure acts uniformly over their entire surface, resulting in a spherically symmetric "breathing mode" response. The cavity volume and the volume change associated with this response are, respectively

$$V = \frac{4\pi a^3}{3}, \qquad \Delta V = 4\pi a^2 w, \tag{4-52}$$

where a = cavity radius, and
w = radial response.

From the definition of bulk modulus,

$$B_c = -p / (\Delta V/V) = -p / (3w/a). \tag{4-53}$$

For air bubbles, $B_c = 1.4P_\infty$, where P_∞ is the static pressure. The spring stiffness K per unit surface area is

$$K = 3 B_c / a. \tag{4-54}$$

Assuming that the bubble swarm is sparse enough to avoid overlap of the nearfield of neighboring cavities, the entrained mass per unit area is[11,12]

$$M = \rho_L a. \tag{4-55}$$

The resultant entrained mass of the breathing mode of the entire cavity, $4\pi a^2 M$, therefore equals three times the mass of the displaced volume of liquid. The natural frequency for air bubbles in water is

$$\omega_o = (K / M)^{1/2} = (3 B_c / \rho_L)^{1/2} / a = 2.0 \times 10^{-3} (P_\infty/\text{atm}) / (a/\text{cm}) \quad (\text{rad/sec}),$$

$$k_L a = (3 B_c / B_L)^{1/2} = 1.4 \times 10^{-2} P_\infty / \text{atm} \quad (\text{dimensionless}). \tag{4-56}$$

The compliance of individual cavities is enhanced by resonance effects, each bubble responding in its breathing mode as a single-degree-of-freedom oscillator of natural frequency ω_o. For cavities of uniform size, i.e., of identical natural frequency ω_o, the compliance B_s^{-1} of the bubble swarm takes the simple form

$$B_s^{-1} = \frac{\alpha}{B_c}\left(1 - \frac{\omega^2}{\omega_o^2} - \frac{i\,\omega\,\delta}{\omega_o}\right)^{-1} \qquad (4\text{-}57)$$

$$\cong \frac{\alpha}{B_c} \quad , \quad \omega^2 << \omega_o^2$$

where the damping constant δ has viscous, thermodynamic, and acoustic radiation components[13] (Figure 4-7). As resonance is approached, B_s^{-1} becomes very large and imaginary

$$B_s^{-1} = i\,\alpha / B_c\,\delta \quad , \quad \omega = \omega_o \quad . \qquad (4\text{-}58)$$

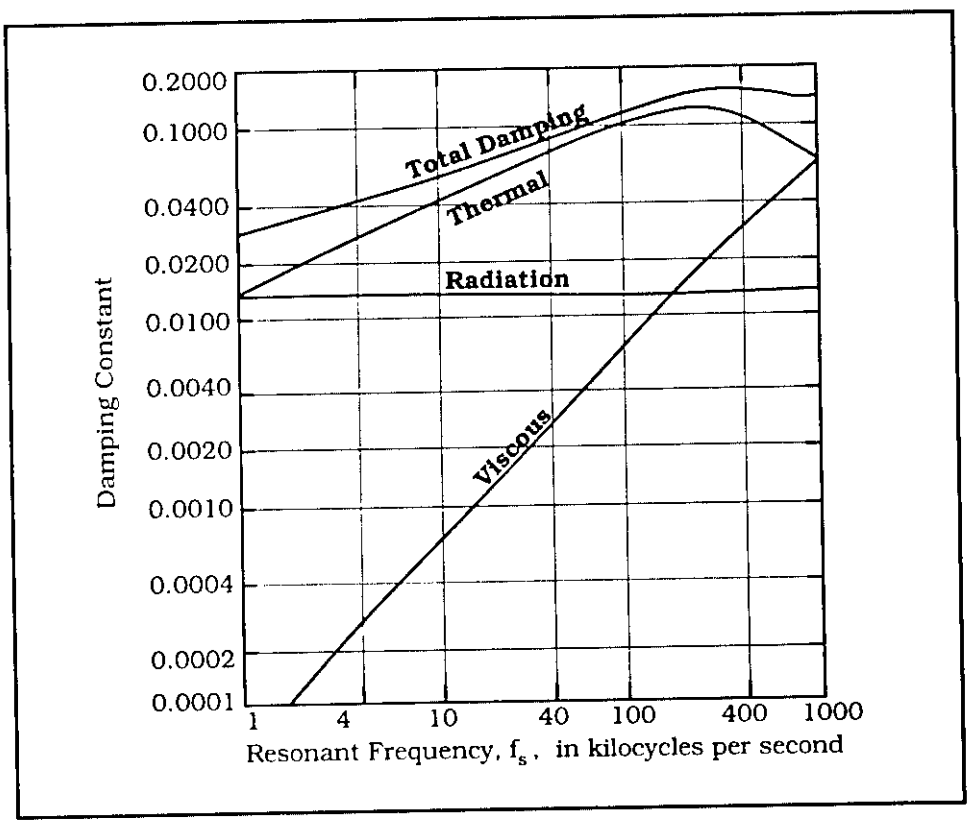

Figure 4-7. Theoretical Thermal, Radiation, Viscous, and Total Damping Constants for Resonant Air Bubbles in Water. (Reproduced from Devin.[13]) To relate this to bubble size, see Equation (4-56). The radiation damping constant is $k_L a$. The damping constant equals the reciprocal of the resonance quality factor.

Above the resonance region, B_s^{-1} has a negative real component

$$\mathrm{Re}\left(B_s^{-1}\right) \equiv -\frac{\alpha\,\omega_o^2}{\omega^2 B_c}$$

$$= -\frac{3\alpha}{\omega^2 a^2 \rho_L}$$

$$= -\frac{3\alpha}{k_L^2 a = B_L} \quad . \tag{4-59}$$

When this is substituted in Equation (4-51), the real component of the compliance is negative in the frequency range $\omega_o < \omega < \omega_a$, where ω_a is the anti-resonance frequency at which the real components of the two compliances cancel

$$\mathrm{Re}\,(B_s^{-1}) = -B_L^{-1}$$

$$\omega_a = \frac{1}{a}\left[\frac{3\alpha B_L}{(1-\alpha)\,\rho_L}\right]^{1/2}$$

$$= \frac{1}{a}\left(\frac{3\alpha}{1-\alpha}\right)^{1/2} c_L$$

$$= \omega_o\left[\frac{\alpha B_L}{(1-\alpha)\,B_c}\right]^{1/2} . \tag{4-60}$$

The latter expression will be used in formulating wavenumbers. Since wave motion requires an elastic restoring force, i.e., a positive bulk modulus, the frequency range $\omega_o < \omega < \omega_a$ constitutes a dead zone where pressure is attenuated exponentially with distance. This will be discussed further in the subsection on wavenumbers. At higher frequencies, $\omega > \omega_a$, wave motion resumes. The three frequency ranges are clearly revealed by experimental dispersion curves[14] (Figure 4-8). Substituting the parameter values corresponding to this test, ($B_c \equiv 1.4 \times 10^6$ μ bar, $\rho_L = 1\,\mathrm{g/cm^3}$, $a = 0.21$ cm, $\alpha = 5.3 \times 10^{-3}$) Equation (4-56) yields the breathing mode natural frequency $\omega_o / 2\pi = 9.8$ kHz and Equation (4-60) the anti-resonance frequency 87 kHz. Equation (4-57) yields a low-frequency reciprocal bulk modulus

$$B_s^{-1} \approx B_{eff}^{-1} = \alpha/\gamma P = 3.8 \times 10^{-9}\ \mu\,\mathrm{bar}^{-1}, \quad \omega^2 \ll w_o^2 . \tag{4-61}$$

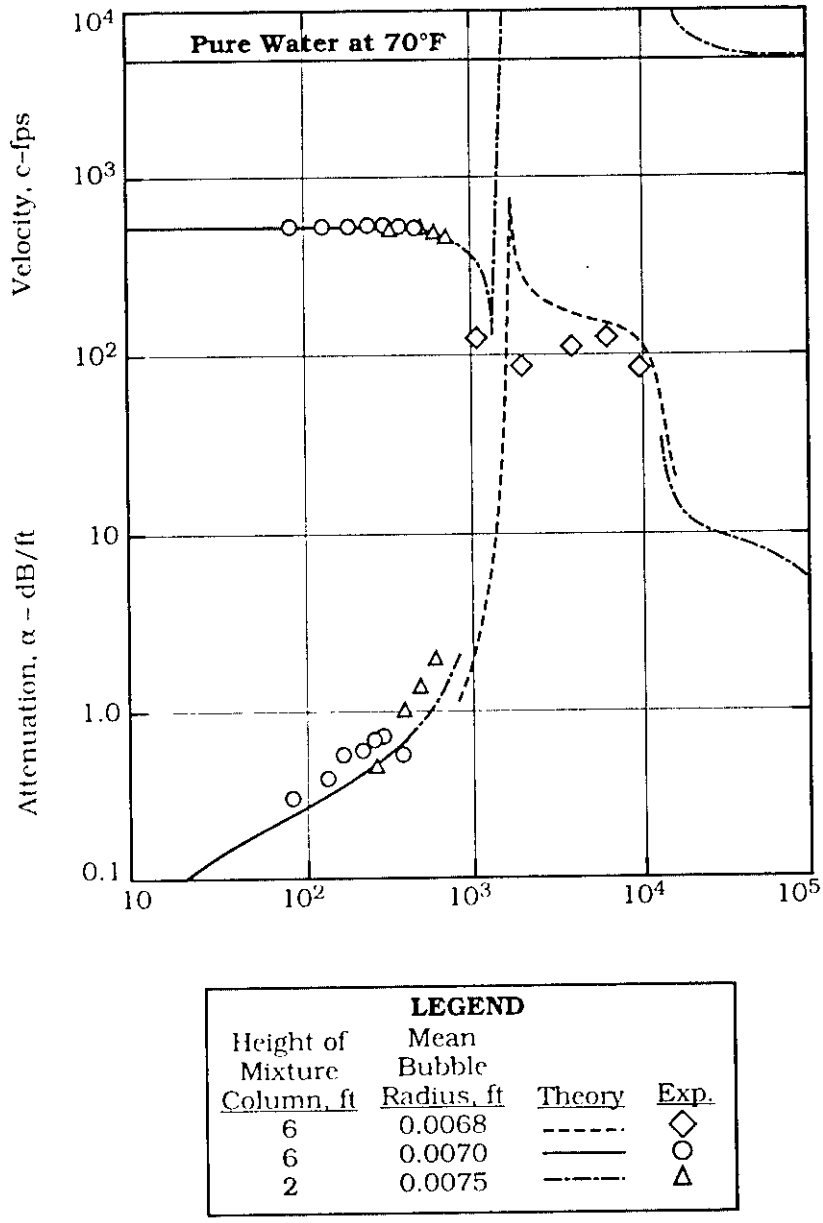

Figure 4-8. Comparison of the Theoretically Predicted Phase Velocity and Attenuation of a Sound Wave in a Bubble Swarm With Measurements. [Reproduced from Silberman[14] who used the theory developed by Spitzer, L., Jr., NDRC Report No. 6-1-sr20-918 (1943) and Carstensen, E.L., and Foldy, L.L., summarized in *Physics of Sound in the Sea*, Wildt, R. (Ed.), "Acoustic Properties of Wakes", National Research Council NSRDC Summary Report (Washington, D.C., 1946).]

The low-frequency sound velocity obtained from Equation (4-57) is $c = 1.6 \times 10^4$ cm/sec = 530 ft/sec. The results generated with the simple theory developed above are seen to be in adequate agreement with measurements. The attenuation will be evaluated in the last subsection which deals with wavenumbers.

A more realistic situation than cavities of uniform size is a bubble swarm encompassing a random distribution of bubble radii, extending from a_2 to a_1. The bubble resonance spectrum is defined as

$$r(\omega_o) \equiv dN / d\omega_o , \tag{4-62}$$

where N is the number of cavities per unit volume. The spectrum $r(\omega_o)$ is the number of these bubbles whose natural frequency falls within a bandwidth of 1 rad/sec. The spectrum r has units time/Length^3. Referring to Equation (4-56), this can be formulated in terms of the cavity radius

$$\frac{dN}{da} = \frac{dN}{d\omega_o} \frac{d\omega_o}{da} \tag{4-63}$$

or

$$\frac{dN}{da} da = r(\omega_o)\, d\omega_o .$$

This cavity size spectrum determines the fractional volume of cavities

$$\alpha = \frac{4\pi}{3} \int_{a_2}^{a_1} \frac{dN}{da} a^3 da . \tag{4-64}$$

Introducing the bubble natural frequency, Equation (4-56), to express a^3

$$a^3 = \frac{1}{\omega_o^3} \left(\frac{3B_c}{\rho_L} \right)^{3/2} , \tag{4-65}$$

and substituting Equations (4-57) and (4-65) in Equation (4-64), one obtains an expression for the fractional volume in terms of ω_o

$$\alpha = 22 \left(\frac{B_c}{\rho_L} \right)^{3/2} \int_{\omega_1}^{\omega_2} \frac{r(\omega_o)\, d\omega_o}{\omega_o^3} . \tag{4-66}$$

This can be expressed concisely in terms of the general moment of the number spectrum, defined as[15]

$$\left\langle \omega_o^{-r} \right\rangle = \frac{1}{N} \int_{\omega_1}^{\omega_2} \omega_o^{-r} \, r(\omega_o) \, d\omega_o \, . \tag{4-67}$$

Consequently, Equation (4-66) now becomes

$$\begin{aligned} \alpha &= 22 \left(\frac{B_c}{\rho_L} \right)^{3/2} N \left\langle \omega_o^{-3} \right\rangle \\ &= 3.6 \times 10^{10} \, (P_\infty/\text{atm})^{3/2} \; N \left\langle w_o^{-3} \right\rangle \quad \text{for air bubbles in water.} \end{aligned} \tag{4-68}$$

The sound velocity in Equation (4-51) can now be expressed explicitly for statistical bubble size distributions. Since the density depends only on the fractional volume of bubbles rather than on their size distribution and frequency, it is convenient to formulate the results in terms of the reciprocal of the effective bulk modulus. Referring to Equation (4-57) for the effect of resonance amplification:

$$\begin{aligned} B_{eff}^{-1} &= (\rho \, c^2)^{-1} \\ &= \frac{1-\alpha}{B_L} + 4\pi \left(\frac{3B_c}{\rho_L^3} \right)^{1/2} \int_{\omega_1}^{\omega_2} \frac{r(\omega_o) \, d\omega_o}{\omega_o \left(\omega_o^2 - \omega^2 - i\omega \, \omega_o \, \delta \right)} \\ &\cong \frac{1-\alpha}{B_L} + \frac{\alpha}{B_c} \, , \qquad \omega^2 \ll \omega_1^2 \\ &\cong -\frac{i 2\pi^2 r(\omega_o)}{\rho_L \, \omega^2} \left(\frac{3B_c}{\rho_L} \right)^{1/2} \, , \qquad \omega_1 < \omega_o < \omega_2 \\ &\cong \frac{1-\alpha}{B_L} \, , \qquad \omega^2 \gg \omega_a^2 \, . \end{aligned} \tag{4-69}$$

Finally, the anti-resonance frequency for a random distribution of bubble sizes is

$$\omega_a = \left(\frac{\alpha B_L}{(1-\alpha) B_c} \right)^{1/2} \left[\frac{\left\langle \omega_o^{-1} \right\rangle}{\left\langle \omega_o^{-3} \right\rangle} \right]^{1/2} \, , \qquad \omega_a^2 \gg \omega_2^2 \, . \tag{4-70}$$

4.8.3 Pipe Resonances and Dead-Zone Attenuation in Two-Phase Systems

The solution developed in Section 4.1 formally holds for two-phase system, it only being necessary to substitute the sound velocity, c, in Equation (4-51), and the wavenumber $k = \omega/c$ corresponding to the compliances in Equation (4-69). An organ pipe-type resonance is only possible in the range where the compliance is predominantly real, i.e., in the low-frequency range, $\omega < \omega_o$ and the high-frequency range, $\omega > \omega_a$. Consequently, resonances are not observed in the dead zone $\omega_o \leq \omega \leq \omega_a$, where sound is attenuated exponentially. The values of the normalized real and imaginary component of the wavenumber of a two-phase medium are summarized in Table 4-1 for a two-phase medium endowed with cavities of uniform size. Extension to statistical cavity size distribution is straightforward but cumbersome. The results will not be formulated here. As already mentioned, meaningful resonances can only occur when $k_r \gg k_i$, i.e., when k_r is independent of the damping constant δ. For these situations, rigid pipe terminations correspond to the roots of $\cot(k_r L)$, Equation (4-9), and open-ended pipe terminations to the zeroes of $\tan(k_r L_{eff})$, Equation (4-16). In other words, the resonance frequencies obtained for the liquid-filled pipes (Equation (4-12a) for the rigidly terminated pipe, Equation (4-17a) for the open-ended pipe) are multiplied by the appropriate ratio K_L/k_r, Table 4-1.

The attenuation in the dead zone, $\omega_o < \omega < \omega_a$ is

$$A = 8.68\, k_i \text{ dB/unit distance.} \tag{4-71}$$

Referring to Table 4-1 and to Equation (4-60), this becomes

$$\begin{aligned} A &= 8.68\,(1-\alpha)\,\frac{\omega_a}{c_L} \\ &= 8.68\,[\,3\alpha\,(1-\alpha)\,]^{1/2}/a\,. \end{aligned} \tag{4-72}$$

For the values of the parameters in Figure 4-8, e.g., $\alpha = 5.3 \times 10^{-3}$, $a = 7 \times 10^{-3}$ ft, this yields 160 dB/ft. This result is only in mediocre agreement with the measured attenuation of approximately 100 dB/ft. However, the predicted attenuation is so large that one anticipates some short-circuiting of the fluid-borne path by the structureborne path in the tube wall.

Table 4-1

Asymptotic Expressions for the Complex Wavenumber ($k_r + i\,k_i$)
of Sound Propagating Through a Swarm of Single-Size Gas-Filled or Vaporous Cavities

Frequency Range	$\frac{k_r}{k_L}$	$\frac{k_i}{k_L}$	**Bubble Behavior**	**Propagation Characteristics**
$\omega^2 << \omega^2_o$, $\omega^2_o << \omega^2_a$, $\delta << 1$	$(1-\alpha)\,\frac{\omega_a}{\omega_o}$	$\frac{k_r}{k_L}\,\frac{\omega\delta}{2\,\omega_o}$	Cavity compressibility short-circuits compressibility of liquid, bubble size irrelevant.	Slow, non-dispersive negligibly attenuated waves.
$\omega = \omega_o$	$\frac{1-a}{(2\delta)^{1/2}}\,\frac{\omega_a}{\omega_o}$	$\frac{k_r}{k_L}$	Resistance-controlled cavity admittance short-circuits compressibility of liquid.	Very highly attenuated, slow waves.
$\omega^2_o << \omega^2$ $\omega^2 << \omega^2_a$	$\frac{k_i}{k_L}\,\frac{\omega_o\,\delta}{2\,\omega}$	$(1-\alpha)\,\frac{\omega_a}{\omega}$	Mass-controlled cavity admittance short-circuits compressibility of liquid.	Highly attenuated, fast waves; dead zone for $\delta = 0$.
$\omega = \omega_a$	$(1-\alpha)\left(\frac{\delta\,\omega_a}{2\,\omega_o}\right)^{1/2}$	$\frac{k_r}{k_L}$	Mass-controlled cavity admittance cancels compressibility of liquid.	High-pass cut-off frequency: attenuated, fast waves.
$\omega^2 >> \omega^2_a$	$(1-\alpha)$	$(1-\alpha)\,\frac{\omega_o\,\omega^2_a\,\delta}{2\,\omega^3}$	Compressibility of liquid short-circuits highly mass-loaded cavity pulsations.	Liquid-borne sound diffracts around effectively rigid cavities.

$$\frac{\omega_a}{\omega_o} = \left[\frac{\alpha\,B_L}{(1-\alpha)\,B_c}\right]^{1/2}$$

REFERENCES FOR CHAPTER 4

1. Lamb, H., *The Dynamic Theory of Sound*, 2nd Ed., Dover Publications, New York, 1960, pp. 176-177.

2. Merkli, P., "Acoustic Resonance Frequency for a T-Tube", *J. Applied Math. & Physics (ZAMP), 29*, 1978, 486-498.

3. Rayleigh, J.W.S., *Theory of Sound*, 2nd Ed., Dover Publications, 1945, Volume II, pp. 312-327.

4. Goodman, R.P., "Ocean Acoustics: The Remarkable Sea of Sound", *Proc. 12th Intern. Congress of Acoustics*, Plenary Session I, Toronto, Canada, 1986.

5. Junger, M.C., and Feit, D., *Sound Structures and Their Interaction*, 2nd Ed., MIT Press, 1986, "Sound Propagation in Fluid-Filled Elastic Pipes", 378-386.

6. Jeffries, H., and B.S., *Methods of Mathematical Physics*, 3rd Ed., Cambridge University Press, 1956, p. 512, where in their notation γ and κ are, respectively, equivalent to our ω and γ_{nm}.

7. Junger, M.C., "The Effect of a Surrounding Fluid on Pressure Waves in a Fluid-Filled Elastic Tube", *J. Appl. Mech., 22*, 1955, 227-231.

8. Field, G.S., and Boyle, R.W., "Dispersion and Selective Absorption in the Propagation of Ultrasound in Liquids Contained in Tubes", *Can. J. Research, 6*, 1932, 192-202.

9. Junger, M.C., "Sound Propagation in a Fluid-Filled Tube With Massive Wall Reactance", *J. Acoust. Soc. Am., 28*, 1956, 165-167.

10. Hendricks, R.C., Baron, A.K., and Peller, I.C., "GASP – A Computer Code for Calculating the Thermodynamic and Transport Properties for Ten Fluids: Parahydrogen, Helium, Neon, Methane, Nitrogen, Carbon Monoxide, Oxygen, Fluorine, Argon, and Carbon Dioxide", NASA TN D-7808, 1975.

11. Kinsler, L.E., and Frey, A.R., *Fundamentals of Acoustics*, 2nd Ed., Wiley, New York, 1962. See page 159, Equation 7.20, with $M = Im z/\omega$.

12. Junger and Feit, *op. cit.*, p. 162, Equation 6.32, with $r = 0$.

13. Devin, C., Jr., "Survey of Thermal, Radiation, and Viscous Damping of Pulsating Air Bubbles in Water", *J. Acoust. Soc. Am., 31*, 1654-1667, 1959.

14. Silberman, E., "Sound Velocity and Attenuation in Bubbly Mixtures Measured in Standing Wave Tubes, *J. Acoust. Soc. Am., 29*, 925-933, 1957.

15. Hoel, P.G., *Introduction to Mathematical Statistics*, Wiley, New York, 1947, p. 28.

CHAPTER 5

STANDING WAVE MODES IN PIPES AND DUCTS WITH MEAN FLOW

by John Cole III
Cambridge Acoustical Associates

The purpose of this chapter is to investigate the effect of flow on the acoustic resonance in turbomachinery piping systems. Sound propagation in pipes is influenced in a number of ways. Since various aspects of the flow affect sound propagation, Section 5.1.1 begins by reviewing the effect of a sound pressure propagating in a mean flow in the absence of the pipe. Wall effect and the attenuation due to turbulence are then considered in Sections 5.1.2 and 5.1.3. Section 5.2 considers the acoustic losses both in the interior and at the ends of a finite length pipe. This section shows that the presence of the flow in the pipe will reduce any amplification that may occur from axial resonance and the damping effect will increase with Mach number.

5.1 Flow Effects on Sound Propagation

5.1.1 Mean Flow Effects - Convection

In linear acoustics, sound is a small disturbance or perturbation that propagates through a fluid medium. If the fluid medium is flowing with a uniform speed U (i.e., constant in both space and time), sound is carried or convected along with the flow as it propagates. To a stationary observer (e.g., a wall-mounted pressure sensor), the effect of the flow is to give a directionally dependent sound propagation speed,

$$c(\theta) = c_o (1 + M \cos\theta) \qquad (5\text{-}1)$$

where c_o = the sound speed in the fluid medium in the absence of flow,

$M = U/c_o$ is the flow Mach number, and

θ = angle of propagation relative to the flow direction (i.e., $\theta = 0$ is the direction of the flow).

The propagation speed "with" the flow is $c_o(1 + M)$, that "against" the flow is $c_o(1 - M)$, and that "across" the flow is c_o. Note that, in the following discussion, we assume that c_o is the sound speed of the ambient medium, which when applied to pipes assumes that the pipe walls are rigid.

Because of the directionally dependent sound speed, the wavelength of a propagating sinusoidal disturbance having frequency f (measured in hertz) also depends on direction when measured by a stationary observer, that is,

$$\lambda(\theta) = c_o (1 + M \cos\theta)/f \tag{5-2}$$

We therefore express the sound pressure propagating as infinite plane waves in the downstream (i.e., with the flow) and the upstream (i.e., against the flow) directions respectively as:

$$\begin{aligned} p^+(x) &= p(\theta = 0, x) = P^+ e^{i(\omega t + k^+ x)}, \\ p^-(x) &= p(\theta = \pi, x) = P^- e^{i(\omega t - k^- x)}, \end{aligned} \tag{5-3}$$

where x increases in the flow direction,

$k^+ = \frac{\omega}{c_o} (1 + M)$, and

$k^- = \frac{\omega}{c_o} (1 - M)$.

These expressions represent waves propagating in the fundamental mode of a rigid-walled pipe carrying a uniform flow of an inviscid fluid (i.e., a fluid that can "slip" along the wall).

The acoustic pressure field satisfies the wave equation obtained by linearizing the equations of motion about the state of uniform flow.[1] Assuming flow in the positive x direction, this requires changing the time derivative to

$$\frac{\partial}{\partial t} \rightarrow \left(\frac{\partial}{\partial t} + U \frac{\partial}{\partial x} \right) \tag{5-4a}$$

and gives the following momentum equation

$$\rho \left(\frac{\partial}{\partial t} + U \frac{\partial}{\partial x} \right) u = - \frac{\partial p}{\partial x}. \tag{5-4b}$$

Substitution of the expressions for downstream and upstream propagating waves (Equation (5-3)) into the momentum equation (Equation (5-4(b)) provides the following relationships between pressure and particle velocity:

$$\begin{aligned} \frac{p^+}{u^+} &= \rho c, \\ \frac{p^-}{u^-} &= -\rho c; \end{aligned} \tag{5-5}$$

that is, the magnitude of the acoustic impedance of plane waves propagating in the moving medium is equal to the characteristic impedance of the medium. (The negative sign results from the assumption of positive velocity in the x direction.)

The root-mean-square acoustic intensity (i.e., energy per unit area) of waves propagating in a uniformly moving medium is given in Reference 2. The intensity of downstream and upstream propagating waves is

$$I^{+} = \frac{|p^{+}|^2}{\rho c} (1 + M)^2 ,$$
$$I^{-} = \frac{|p^{-}|^2}{\rho c} (1 - M)^2 . \qquad (5\text{-}6)$$

The "convective" wave equation that governs acoustic pressures measured by a stationary observer in a uniformly moving medium is obtained by substituting the convective time derivative (Equation (5-4a)) into the wave equation for a stationary acoustic medium

$$(1 - M^2) \frac{\partial^2 p}{\partial x^2} + \frac{\partial^2 p}{\partial y^2} + \frac{\partial^2 p}{\partial z^2} - \frac{2M}{c} \frac{\partial^2 p}{\partial x \partial t} - \frac{1}{c^2} \frac{\partial^2 p}{\partial t^2} = 0. \qquad (5\text{-}7)$$

Solutions for Equation (5-7) are obtained by specifying a source configuration at a boundary. Analytical solutions and measurements are given in Reference 3 for a source located in the wall of a pipe. In the absence of flow, the boundary conditions posed by such a source are well defined. For a source that vibrates with constant amplitude over a region of the wall, the same disturbance is applied to the fluid in the duct, that is,

$$\dot{w} (x_s, r_s) = \frac{\partial \eta}{\partial t} (x_s, r_s) \qquad (5\text{-}8a)$$

where $\dot{w}$ = the radial wall velocity,
x_s = the source region of the pipe wall,
r_s = the pipe radius, and
η = the source displacement.

The corresponding boundary condition in the presence of uniform flow requires interpretation and empirical correlation. Direct application of Equation (5-4a) to Equation (5-8a) gives the following result for the source velocity at the pipe wall in the presence of uniform flow:

$$\dot{w} (x_s, r_s) = \left(\frac{\partial}{\partial t} + U \frac{\partial}{\partial x} \right) \eta (x_s, r_s) \qquad (5\text{-}8b)$$

Effectively this assumes that the flow over the source region is laminar and that the normal velocity component merely displaces the streamlines. If, however, the flow in the source region is turbulent, the contributions to the spatial portion of the derivative in Equation (5-8b) are uncorrelated and therefore tend to cancel on average in this region. An approximate formulation of the boundary condition is then the same as that for the duct with no flow (i.e., Equation(5-8a)).

Application of the two boundary conditions results in different flow dependences of the acoustic pressures in the downstream and upstream directions. If we consider only the fundamental propagation mode in a pipe whose walls are rigid outside the source region, the ratios of downstream to upstream pressure amplitudes corresponding to Equations (5-8a) and (5-8b) are, respectively,[3]

$$\frac{P^-}{P^+} = \begin{cases} \dfrac{(1+M)}{(1-M)} & ; \quad \text{Turbulent Flow – Equation (5-10a)} \\ \dfrac{(1+M)^2}{(1-M)^2} & ; \quad \text{Laminar Flow – Equation (5-10b)} \end{cases} \tag{5-9}$$

It is noted that convection of the sound field by the flow causes the downstream pressure amplitude to be lower than the upstream amplitude. This seems to be at variance with "common observation" associated with outdoor sound propagation; however, as discussed in the next section, refraction, which often dominates outdoor propagation, tends to reduce pressure amplitudes "upwind".

Comparison of the predictions of Equation (5-9) with measurements is shown on Figure 5-1. The data are consistent with the "laminar" assumption at Mach numbers below 0.1 and show a transition to the "turbulent" result above a Mach number of approximately 0.2.

5.1.2 Wall Effects – Refraction

When discussing flows of real fluids in pipes, the presence of viscosity makes the assumption of uniform flow invalid, especially near the walls. In the simplest sense, the increase of flow velocity with distance with the wall means that the effective propagation speed of sound also varies with distance from the wall. Close to the wall where the flow speed is small (but outside the region of the acoustic boundary layer, discussed in Section 4.4.), the sound propagation speed is that of the fluid in the absence of flow. Near the centerline of the pipe, the

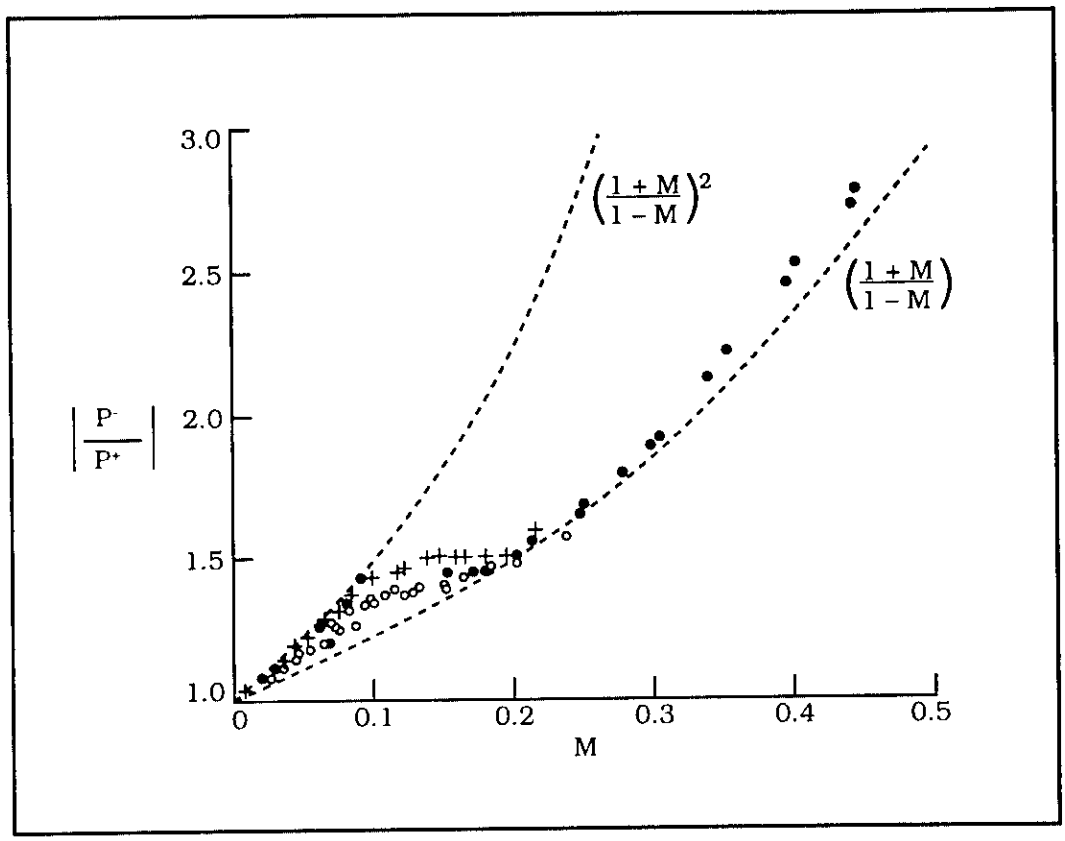

Figure 5-1. Mach Number Dependence of the Measured Ratio $\left|P^-/P^+\right|$ Between the Pressure Amplitudes Radiated in the Upstream and Downstream Directions.
(Reproduced from Ingard and Singhal.[3])

• – 1477 Hz; ∘ – 1000 Hz; + – 1000 Hz (different location in the duct)

effective sound propagation speed is given by Equation (5-1). When sound propagates with the flow, it therefore travels faster near the pipe center than it does near the wall. If a plane wave of sound were to propagate in such a flow field, it would tend to "bend" or be refracted towards the wall. Conversely, a plane wave propagating against the flow would propagate slower near the pipe center, and it would tend to be refracted away from the wall.

The importance of refraction in pipe flow is generally smaller at low frequency and for lower order propagation modes. There are no general analytical results available for estimating the effects of refraction on propagation within pipes. Results that do exist in the literature are obtained by numerical calculation for specific parameters. A primary effect of refraction is to alter the attenuation rate of waves propagating with and against the flow from those predicted using the uniform flow assumption.

5.1.3 Attenuation Due to Turbulent Flow

In the absence of flow, attenuation of sound propagating in the fundamental mode in a circular pipe having rigid walls is due to irreversible processes involving viscosity and heat conduction. This so-called "classical" attenuation which is due to linear processes is given by[4]

$$\alpha_c = 8.7\, \beta_v\, L\,, \quad \text{dB} \tag{5-10a}$$

where L = pipe length,

$\beta_v = k\,[d_v + (\gamma - 1)\, d_T]/D_p$,

$k = \omega/c_o$ = the acoustic wavenumber,

$d_v = \sqrt{2\nu/\omega}$ = the viscous boundary layer thickness,

$d_T = \sqrt{2\alpha_T/\omega}$ = the thermal boundary layer thickness,

α_T = the coefficient of thermal diffusivity,

γ = the ratio of heat capacities ($\gamma = c_p/c_v$), and

$D_p = 2\, r_s$ = the pipe diameter.

For gases this attenuation is generally small. As an example, the classical attenuation for air at standard temperature and pressure ($\nu = 0.23$ cm^2/s, $\alpha_T = 0.32$ cm^2/s) and a frequency of 1000 Hz is

$$\alpha_c \equiv 0.02\, L/D_p \qquad \text{dB}, \tag{5-10b}$$

or approximately 1 dB per 50 diameters of pipe length.

When there is mean flow in a pipe, other mechanisms are present that result in higher attenuation of sound. These mechanisms are viewed as being "non-linear" and result either from the interaction of large amplitude sound waves with the mean flow vorticity (i.e., dU/dy) or by the irreversible generation of turbulence in the pipe.

A simple phenomenological formulation for this attenuation is derived in Reference 5 by including in the momentum equation terms associated with the steady-state pressure drop due to the presence of turbulent pipe flow. The result is the following pair of complex-valued wavenumbers for propagation with and against the flow

$$\begin{aligned} k^+ &= \frac{\omega}{c_o(1+M)} + i\,\frac{A_l}{1+M}, \\ k^- &= \frac{\omega}{c_o(1-M)} - i\,\frac{A_l}{1-M}, \end{aligned} \tag{5-11}$$

where the loss factor $A_l = \beta_v + 2\,\psi_f\, M\,[1 + (R_c/2)\,(\partial \ln \psi_f/\partial R_c)]/D_p$ and ψ_f is the friction factor for turbulent flow at Reynolds number Re for steady pipe flow (i.e., $\Delta P/L = \psi_f\, \rho\, \bar{U}^2/2D_p$ where ΔP is the static pressure drop along length L of pipe). (Note that the friction factor for circular pipes ψ_f is four times larger than that defined in Reference 5 owing to the definition of equivalent diameter for ducts of arbitrary cross-section.)

This formulation is shown in Reference 5 to be in reasonable agreement with measurements. At high Reynolds numbers the friction factor becomes independent of Re, and the attenuation due to turbulence is given by

$$\alpha_{turb} \equiv 8.7\, A_l\, L = \frac{17\,\psi_f\, M}{(1 \pm M)}\,\frac{L}{D_p} \qquad \text{dB} \tag{5-12}$$

where the positive and negative signs refer respectively to downstream and upstream propagation. For relatively smooth pipes the friction factor is $\psi_f \equiv 0.02$, and the attenuation given by Equation (5-12) exceeds the classical attenuation for the conditions of Equation (5-10b) when $M > 0.06$.

5.2 Flow Effects on Resonances in Finite Pipe Lengths

5.2.1 Overview

The presence of flow in a pipe acts to reduce the amplification occurring at the axial (i.e., "organ pipe") resonances that are found in the absence of flow. This is observed in measurements of the sound pressure in a pipe shown on Figures 5-2(a) and 5-2(b). In Figure 5-2(a), the sound source is external to the pipe, and the results show decreasing resonance amplification with increasing flow Mach number. The source of noise in Figure 5-2(b) is the flow through a pipe having an unflanged sharp inlet and a flanged outlet. In this case the noise increases as the flow Mach number increases; however, pipe resonances which are apparent at M = 0.27 are nearly absent at M = 0.55.

Several factors contribute to the reduction of resonance amplification at high flow Mach numbers. As discussed previously, the disparity of spatial wave-numbers in the upstream and downstream directions means that there are fewer opportunities for purely constructive or destructive interference of waves in the pipe. Furthermore, additional attenuation mechanisms directly related to the flow are present. One of these discussed previously is the interaction of the sound wave with vorticity and turbulence within the pipe. Another dissipation mechanism is the interaction of the sound wave with vorticity generated by the flow entrance and exit. Although the basic physics of flow interaction with vorticity is understood, quantitative results for specific flow geometries remain empirical in nature. Available empirical results are therefore presented next, followed by analytical aspects.

5.2.2 Reflection Coefficient Measurements

The effect of flow on the pressure reflection coefficients (i.e., P^-/P^+, or the reciprocal) at unflanged pipe ends for propagation upstream and downstream from Reference 6 are shown on Figures 5-3(a) and 5-3(b). The dimensionless frequencies (i.e., $k\, r_s$) for these data range from 0.12 to 0.50 for the downstream data and 0.36 to 0.50 for the upstream data. Little dependence on flow Mach number is found for the downstream end (Figure 5-3b), while the reflection coefficient at the upstream end shows a reasonably strong Mach number dependence. The magnitude of the downstream and upstream reflection coefficients, respectively, is approximated by 1 and $[(1 - M)/(1 + M)]^{1.33}$.

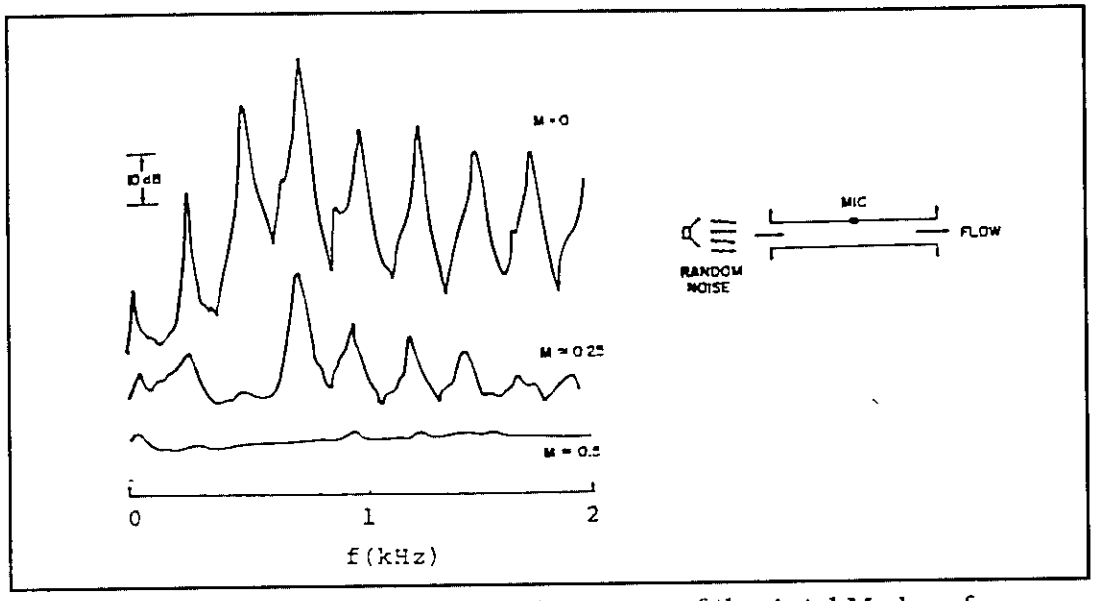

(a) Effect of Flow on the Frequency Response of the Axial Modes of an Open-Ended Duct to an External Random Noise Field.

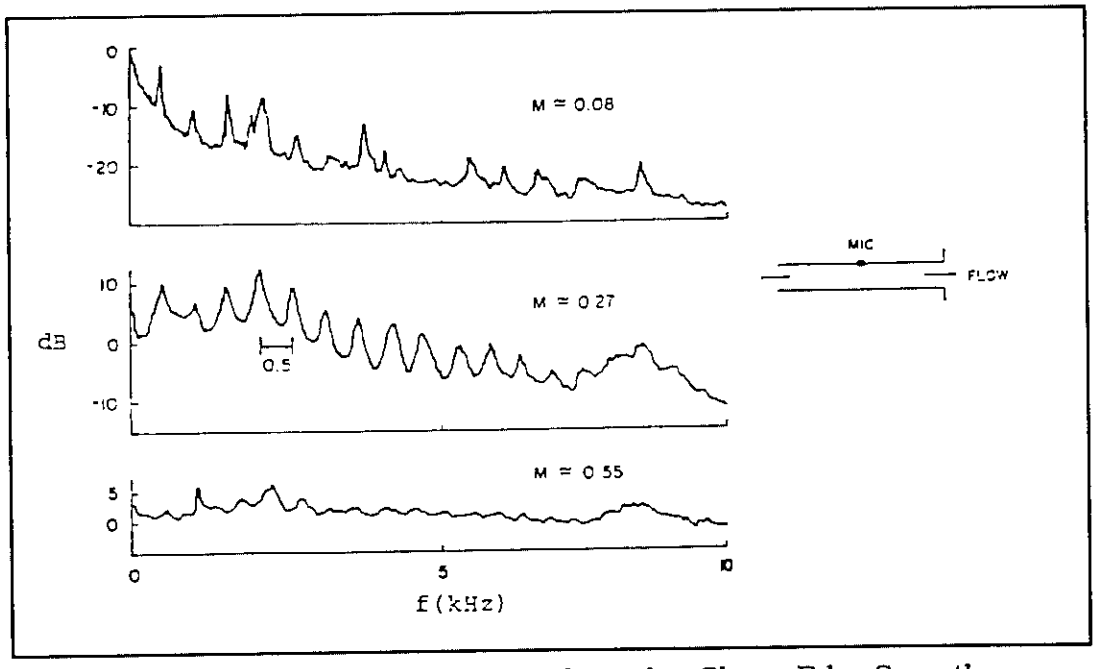

(b) Noise Spectra Produced by Flow Through a Sharp-Edge Smooth Circular Duct 12 Inches Long, With an Inner Diameter of 0.75 inch. The Entrance End is Unflanged and the Exit End Flanged.

Figure 5-2. Measurements of Sound Pressure in a Pipe. (Reproduced from Ingard and Singhal.[6])

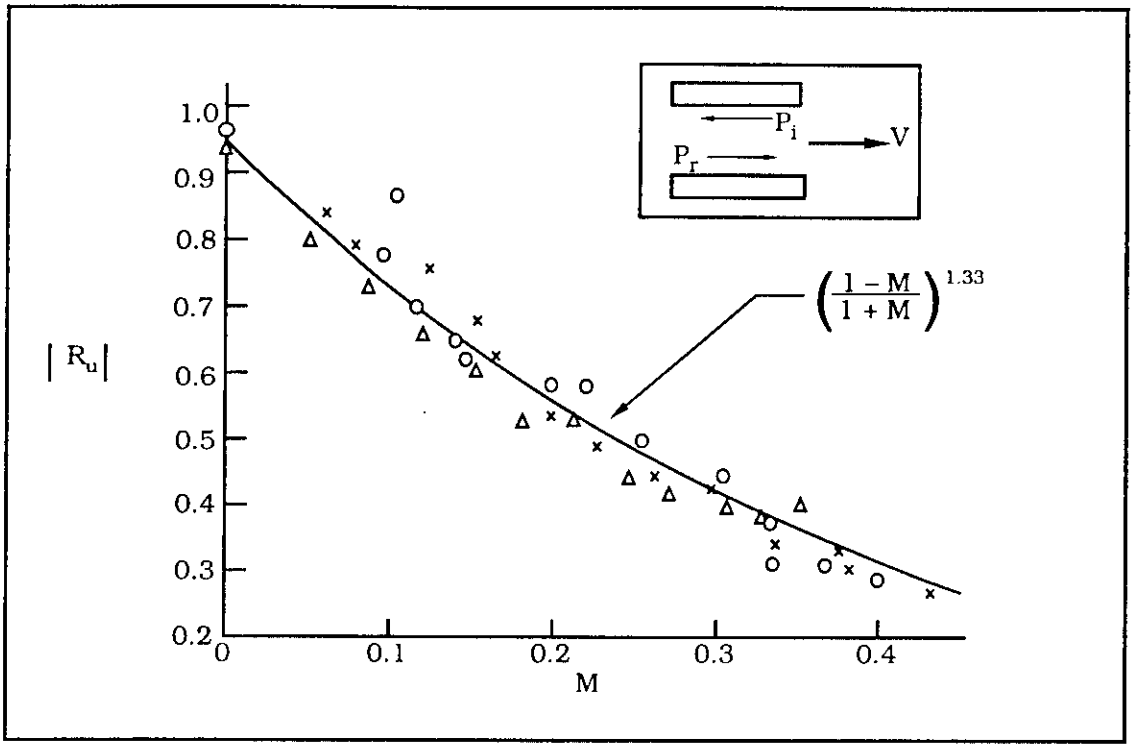

(a) Upstream End of the Duct.

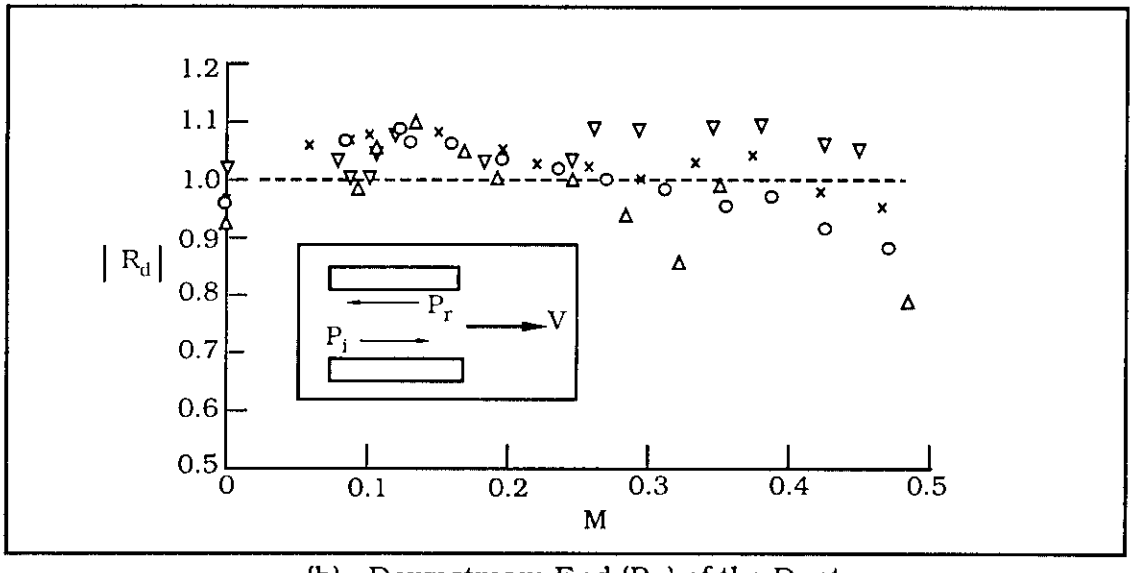

(b) Downstream End (R_d) of the Duct.

Figure 5-3. Measured Mach Number Dependence of the Magnitude of the Pressure Reflection Coefficients.
(Standing Wave Measurements: o – 1400 Hz; x – 1000 Hz; ∇ – 350 Hz.
Pulse Measurements: Δ – 1200 Hz.) (Reproduced from Ingard and Singhal.[6])

When flow is present, a pressure reflection coefficient of unity does not imply total reflection without absorption. The relationship between pressure reflection coefficient and acoustic intensity is obtained using Equation (5-6). By substituting the above results for pressure reflection coefficients, we obtain the following "energy" reflection coefficient at the downstream end

$$\frac{I^-}{I^+} = \left(\frac{P^-}{P^+}\right)^2 \left(\frac{1-M}{1+M}\right)^2 \cong \left(\frac{1-M}{1+M}\right)^2 . \qquad (5\text{-}13a)$$

At the upstream end the corresponding result is

$$\frac{I^+}{I^-} = \left(\frac{P^+}{P^-}\right)^2 \left(\frac{1+M}{1-M}\right)^2 \cong \left(\frac{1-M}{1+M}\right)^{0.66} . \qquad (5\text{-}13b)$$

Acoustic energy is therefore absorbed by reflection at both ends; however, more energy is dissipated at the downstream end. Although the measurements only extend up to M = 0.5, extrapolation of these dependences confirm that anechoic ends (i.e., no reflections) are obtained at sonic conditions (M = 1).

Flow restrictions at the downstream end of a pipe can be designed to provide anechoic termination. Results are shown on Figure 5-4 for flow restrictions in the form of a single nozzle and a perforated plate. The energy reflection coefficient has minima that approach zero when the exit flow Mach number (M_e) is approximately equal to the contraction ratio of the area (i.e., ratio of flow area of the restriction to that of the pipe, this ratio being 0.132 for the results of Figure 5-4). As indicated, this condition applies to low dimensionless frequency and relatively low Mach numbers.

5.2.3 Analytical Modeling

Alteration by a flow of the acoustic characteristics of flow in a pipe can be obtained using a simple analytical example, namely a pipe of length L carrying a uniform flow with Mach number M. A disturbance at the downstream end generates an equivalent plane wave velocity u_o in the pipe. The wave propagating upstream is assumed to reflect at the pipe end such that the pressure vanishes, this being equivalent to an open pipe termination at low frequency. The acoustic pressure field in the pipe is the sum of the waves propagating upstream and downstream, that is,

$$p(x) = P^+ e^{-ik^+ x} + P^- e^{-ik^- x} \qquad (5\text{-}14)$$

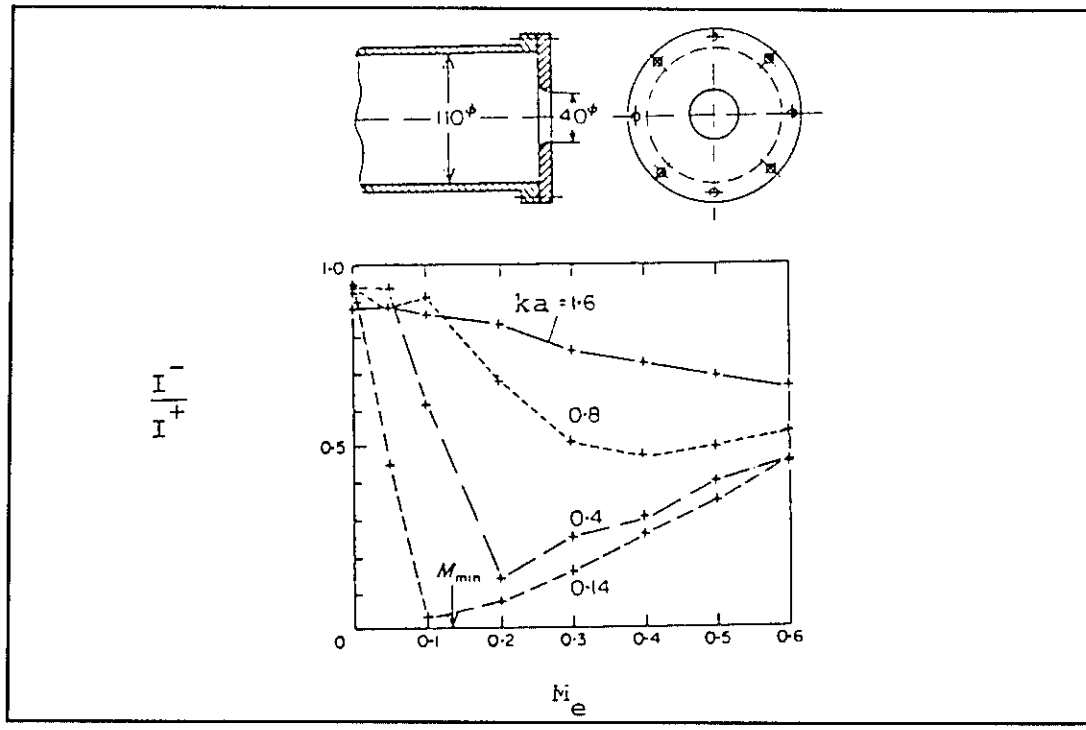

(a) Single Nozzle.

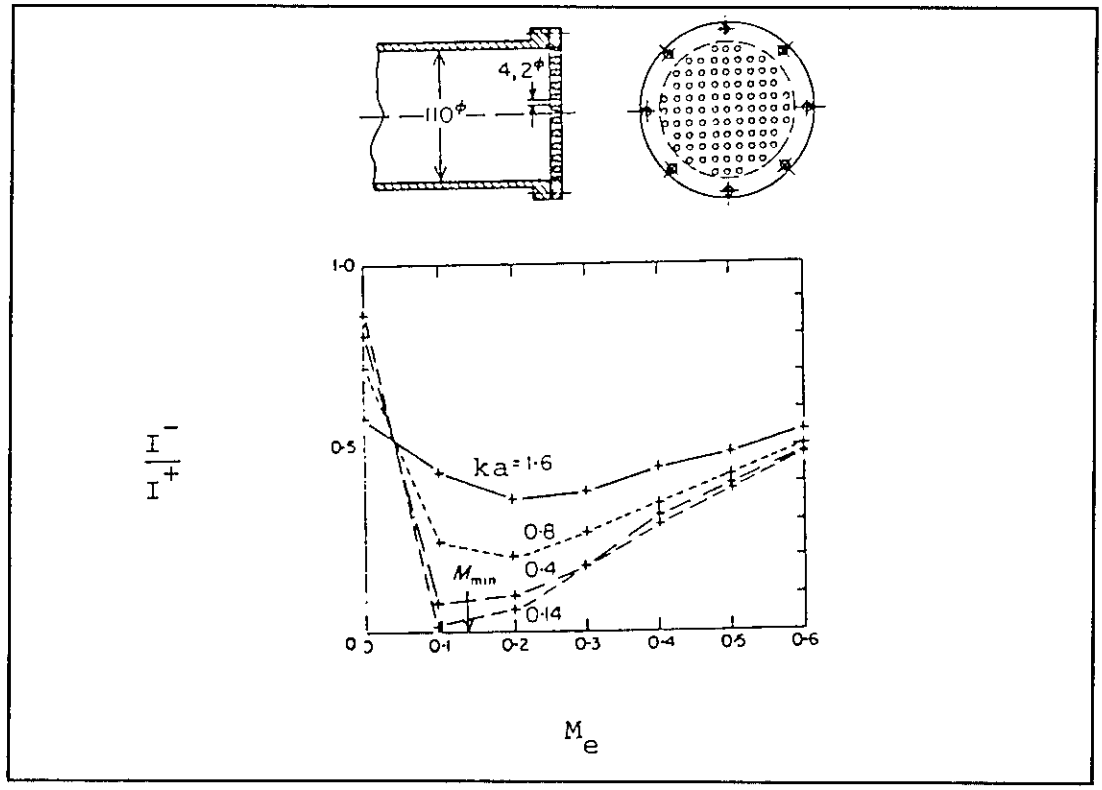

(b) Perforated Plate.

Figure 5-4. Sound Power Reflection Coefficient I^-/I^+ in the Tube Versus Jet Exit Mach Number (M_e) at Various Dimensionless Frequencies $k r_s$ for Two Exit Configurations. Area Contraction Ratio = 0.132. (Reproduced from Bechert.[8])

where k^+ and k^- are defined in Equation (5-3). We determine the amplitudes P^+ and P^- by requiring the particle velocity to be u_o at x = 0 and the total pressure to be zero at the other end. As discussed in Section 4.3, an end correction is applied to the physical length of the pipe to account for the entrained fluid outside the pipe. For circular pipes carrying flow, the end correction for an unflanged pipe is given by[6.7]

$$\Delta L_o = \frac{0.61\, k\, r_s}{1 - M^2} \,. \tag{5-15}$$

Using the effective length in the condition giving zero pressure, we obtain the following relationships for the amplitudes

$$\frac{P^+}{1+M} - \frac{P^-}{1-M} = \rho\, c\, u_o \,, \tag{5-16}$$

$$P^+ \, e^{i k^+ L_{eff}} + P^- \, e^{-i k^- L_{eff}} = 0.$$

These amplitudes are used to calculate the acoustic impedance at the source location (i.e., the ratio of pressure in the pipe to particle velocity at x = 0),

$$z_o = \left.\frac{p(x)}{u_o}\right|_{x=0} = \frac{-i\,\rho c\,(1-M^2)\sin k_c L_{eff}}{\cos k_c L_{eff} + i\, M \sin k_c L_{eff}} \,, \tag{5-17}$$

where $k_c = \dfrac{\omega}{c_o(1-M^2)}$ is the convected wavenumber.

In the absence of flow, the result given in Equation (4-14) is obtained in which the source impedance is infinite (anti-resonance) when the pipe measures an odd number of quarter wavelengths (i.e., the zeroes of cos kL) and zero (resonance) when the pipe measures an integer number of half wavelengths. The effect of uniform flow is to shift the location of the resonances and to eliminate the possibility of pure anti-resonance in that there are no longer real-valued frequencies that cause the denominator to vanish. Complex-valued frequency roots of the denominator can be found, but these are effectively damped in time.

When the source is located in the wall of the pipe and reflections from upstream and downstream ends are accounted for,[6] the function corresponding to the denominator of Equation (5-17) is

$$1 - R_u\, R_d\, e^{i(k^+ + k^-) L_{eff}} \,, \tag{5-18}$$

where the pressure reflection coefficients R_u and R_d are shown on Figure 5-3. Anti-resonances in the pipe are obtained at frequencies that are the roots of Equation (5-18). As discussed above, these roots or eigenvalues are complex-valued frequencies

$$\omega = \omega_r - i\,\omega_i \tag{5-19}$$

such that: $\exp(-i\omega t) = \exp(-i\omega_r t)\exp(-\omega_i t)$. The real and imaginary parts of these roots are given graphically on Figure 5-5 for various flow Mach numbers and turbulent flow friction factors (i.e., Equation (5-11) is used for the wavenumbers). Purely real roots giving zero particle velocity for a finite pressure are only obtained when flow is absent. When the Mach number is 0.4, a propagating signal at the eigenvalue in the absence of attenuation due to turbulence ($\psi_f = 0$) is attenuated by

$$\alpha_{flow} = 8.7\ \frac{\omega_i L_{eff}}{c_o} = 8.7\,(0.475) \cong 4 \quad dB \tag{5-20}$$

in the time, L_{eff}/c_o, taken to travel the length of the pipe. The value 0.475 is taken from Figure 5-5.

Analytical predictions of the absorption of sound through interaction with flow vorticity have been made for several configurations (see References 7 to 10). The physical understanding of this process is that dissipation is obtained when sound interacts with the mean flow field to generate vorticity which is then swept away by the flow. Tuning of this process to the flow and sound field results in the anechoic termination (i.e., zero power reflection coefficient) shown on Figure 5-4.

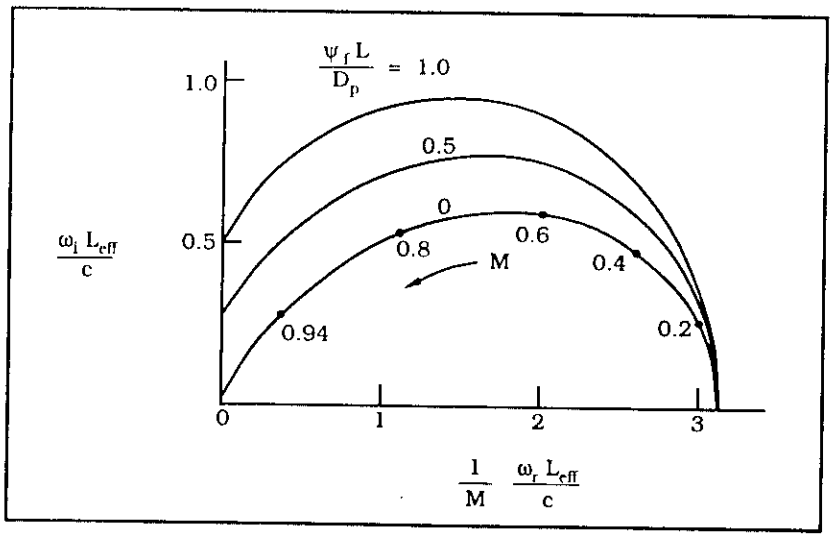

Figure 5-5. Mach Number Dependence of the (Complex) Eigenfrequency of the m'th Axial Acoustic Mode (m = 1, 2, . . .) of an Open-Ended Duct of Effective Length L_{eff} for Several Values of the Turbulent Pipe Flow Friction Factor, ψ_f. (Reproduced from Ingard and Singhal.[6])

REFERENCES FOR CHAPTER FIVE

1. Schlichting, H., *Boundary-Layer Theory*, 6th Ed., McGraw-Hill Book Co., New York, 1968, 560.

2. Morfey, C.L., "Sound Transmission and Generation in Ducts With Flow", *J. Sound Vib.*, *14*, 1971, 37-55.

3. Ingard, U., and Singhal, V.K., "Upstream and Downstream Sound Radiation Into a Moving Fluid", *J. Acoust. Soc. Am.*, *54* , 1973, 1343-1346.

4. Morse, P.M., and Ingard, K.U., *Theoretical Acoustics*, McGraw-Hill Book Company, New York, 1968, 519.

5. Ingard, U., and Singhal, V.K., "Sound Attenuation in Turbulent Pipe Flow", *J. Acoust. Soc. Am.*, *55* , 1974, 535-538.

6. Ingard, U., and Singhal, V.K., "Effect of Flow on the Acoustic Resonances of an Open-Ended Duct", *J. Acoust. Soc. Am.*, *58*, 1975, 788-793.

7. Mechel, F., *et al.*, "Akustische impedanz einer luftdurchstromten offnung", *Acustica*, *15*, 1965, 199-206.

8. Bechert, D.W., "Sound Absorption Caused by Vorticity Shedding, Demonstrated with a Jet Flow", *J. Sound Vib.*, *70*, 1980, 389-405.

9. Howe, M.S., "The Dissipation of Sound at an Edge", *J. Sound Vib.*, *70*, 1980, 407-411.

10. Howe, M.S., "Attenuation of Sound in a Low Mach Number Nozzle Flow", *J. Fluid Mech.*, *91*, 1979, 209-229.

CHAPTER 6

ACOUSTIC RESONANCES IN CASCADES

by Louis C. Sutherland
Consultant in Acoustics

Cascades are defined as an array of parallel or annular plates in the plane of flow of a gas or any compressible fluid – generally assumed to be subsonic. These surfaces introduce fixed boundaries which can give rise to acoustic resonances. The cascades can be considered as an idealized representation of stators in hydraulic pumps or bends, guide vanes in bends, intake ports, etc. In contrast to the well-known phenomenon of vortex shedding-induced vibration of structures placed in a fluid flow of effectively infinite extent, the introduction of boundaries within the fluid flow introduces a new element to this interaction of fluid flow and structures. That is, the acoustic resonances that occur within these bounded surfaces. It is often assumed that these acoustic resonances are, themselves, the source of the structural excitation that frequently accompanies them. In fact, Parker and Stoneman[1] have shown conclusively that the vortex shedding is still the primary source of flow-induced vibrations in the presence of cascades. However, the latter can have a strong influence on the strength of the resulting aero-acoustic excitation. Particularly significant for this handbook can be:

- The vibration of blades in axial-flow compressors and other turbo-machinery, and
- Noise and vibration from in-flow support spokes and corner vanes in piping systems.

This chapter addresses these acoustic resonances from two aspects: (1) the computation of their resonance frequencies and mode shapes, and (2) the general impact of these acoustic resonances on the related aeroacoustic environment and resulting structural responses. Emphasis is placed on the first aspect, which is not readily available in practical engineering terms suitable for problem solving. For the second aspect, only a brief review is attempted here since this topic has been thoroughly treated in the literature listed at the end of this chapter and has been well summarized in a recent review paper.[1]

6.1 Geometry of Cascades

A typical rectangular cascade system is shown in Figure 6-1. It is treated as an infinite stack of parallel plates with a cross-flow span b and a chord dimension C in the direction of flow separated by a pitch spacing s perpendicular to the flow. The acoustic resonances of primary concern involve only the chord-pitch plane and can thus be considered in terms of the acoustic resonance frequencies of two-dimensional cavities. These resonances (as well as the three-dimensional resonances which can occur) may also involve secondary interaction with structural resonances of the cascade plates themselves. They are excited by the fluctuating wakes shed by the flow at the trailing edge of the plates.

For cascade systems of the type shown in Figure 6-1, four characteristic types of acoustic modes can be defined. They are designated, after Parker,[2] as the α, β, γ, and δ modes which have the general modal pattern illustrated in Figure 6-2. The first two types of modes (α and β) have a pressure anti-node (region of high pressure) along the mid-pitch plane halfway between each pair of plates and are distinguished by either a pressure node (region of zero or minimum pressure) along the mid-chord plane (α mode) or an anti-node along this plane (β mode). The other two modes shown in Figure 6-2 have in common a pressure node along the mid-pitch plane but are distinguished by either a pressure node along the mid-chord plane (γ mode) or an anti-node along this plane (δ mode). The significance of these acoustic resonances is that, when they are excited by vortex shedding, the resulting acoustic pressures may cause unacceptably high vibration responses of adjacent structure or generate very high noise levels. This occurs when the acoustic resonances frequencies are close to the vortex shedding frequency, which varies with flow velocity. However, as will be illustrated later, the vortex shedding frequency itself may change significantly as the sound pressures of the acoustic field interact with the vortex shedding process.

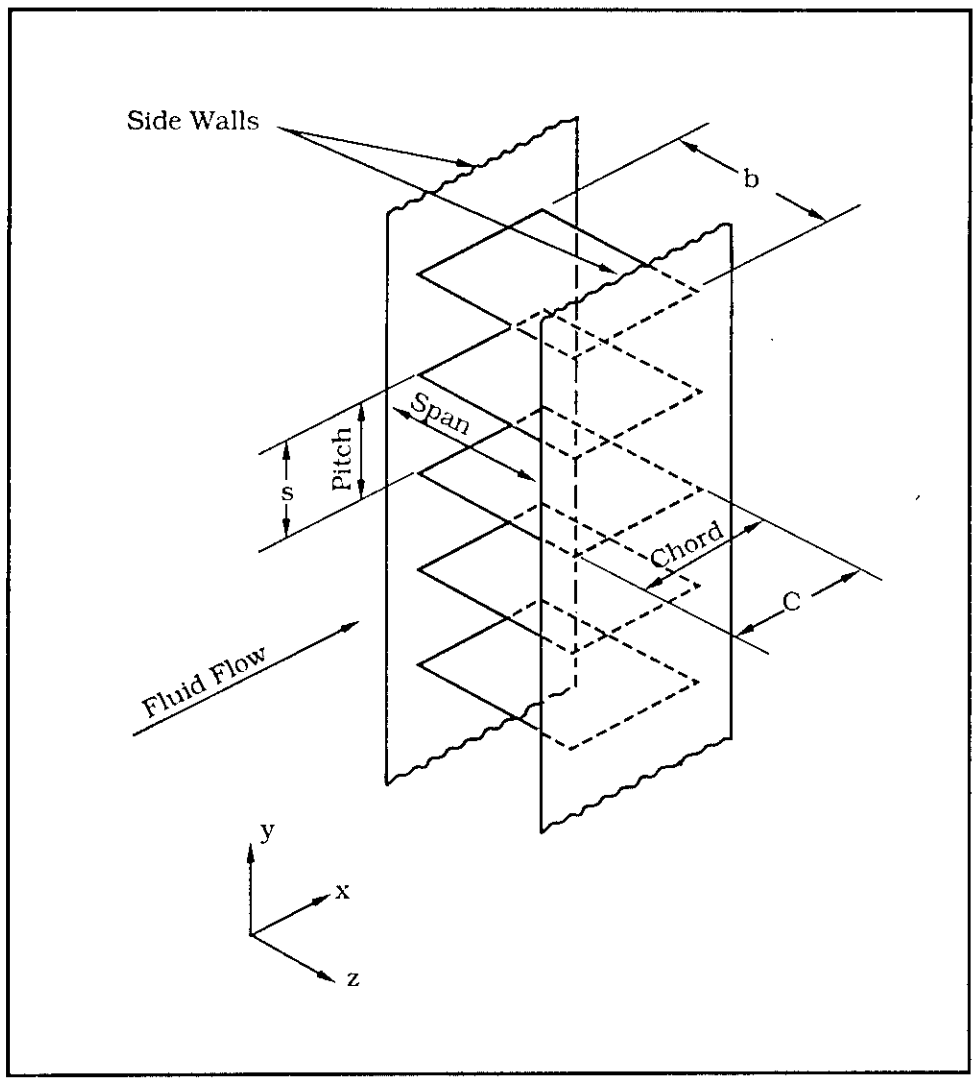

Figure 6-1. Illustration of Cascade System.
(Reproduced from Parker.[2])

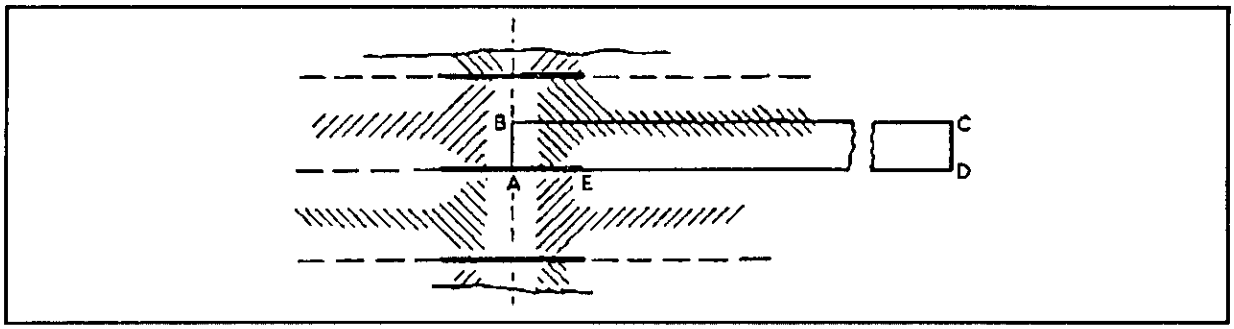

(a) Principal Two-Dimensional Modes – Node at Mid-Chord (Mode α).

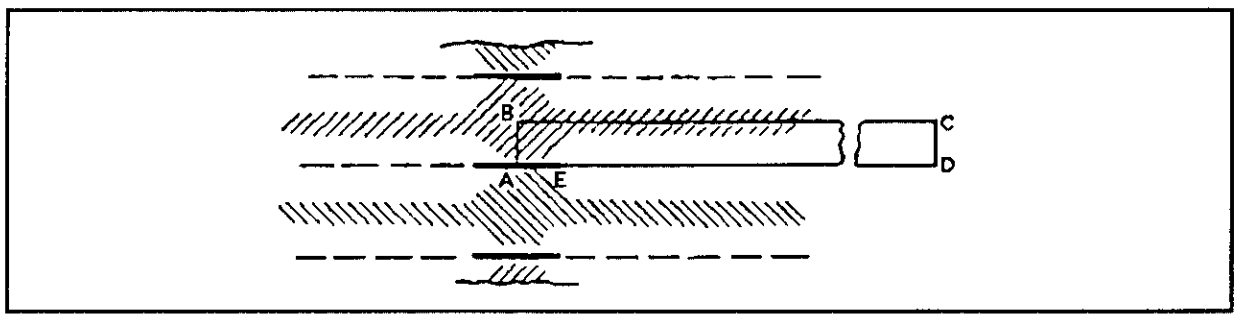

(b) Principal Two-Dimensional Modes – Anti-Node at Mid-Chord (Mode β).

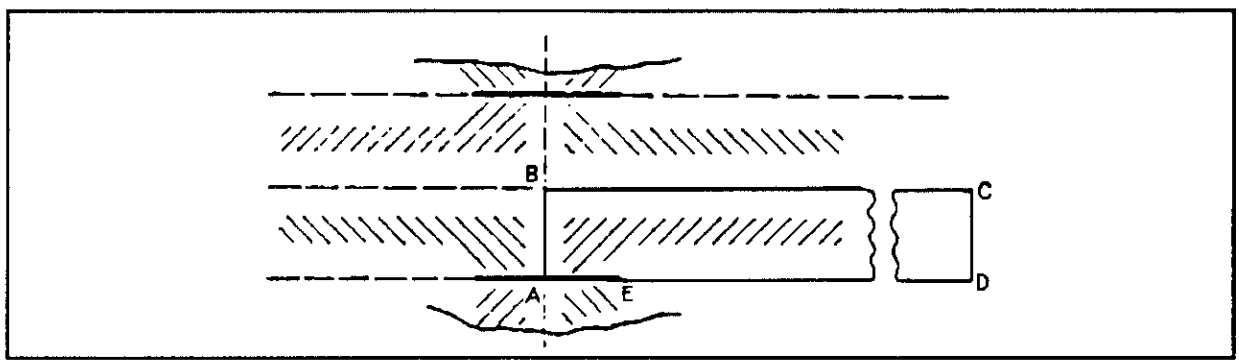

(c) Higher-Order Two-Dimensional Modes – (Mode γ).

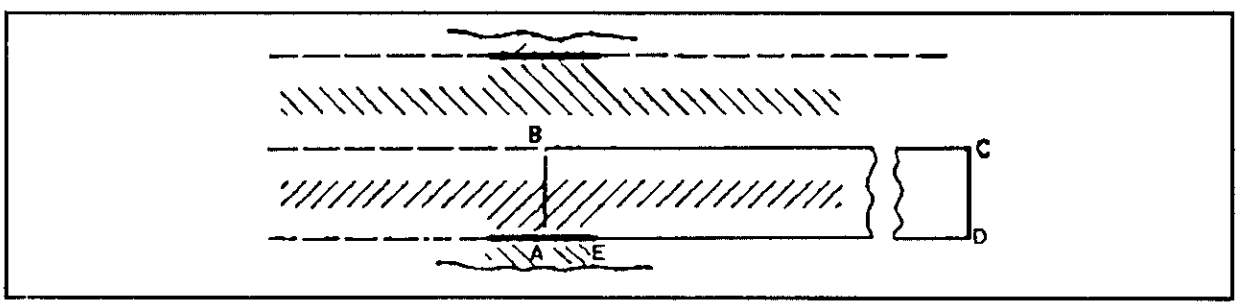

(d) Higher-Order Two-Dimensional Modes – Node at Mid-Chord (Mode δ).

—— Plates – – – Pressure Nodes / / / / Regions of High SPL Velocity Nodes

Figure 6-2. Mode Shapes for the Cascade System in Figure 6-1. (Reproduced from Parker.[2])

6.2 Relaxation Method

This section provides a method of determining the acoustic resonance frequency in cascades using a numerical "relaxation" method. The technique is able to compute resonance frequency and mode shapes for complex geometries, as in turbomachinery cascades.

The relaxation method was originally developed to solve mechanical stability problems in structural framework systems, "the method of systematic relaxation of constraints" (Allen[3]). The method provides a mathematically forgiving process for simultaneously solving a set of N linear equations in N unknowns. The relaxation process does not really operate on the equations themselves but uses them only to define "residual error terms" – analogous to the residual constraint forces applied to the framework – which are "relaxed" or gradually reduced to zero by a simple iterative process.

For example, assume the acoustic mode shape in a system is describ . by a set of N linear equations in X_j which can be expressed in the follow.ng form, where the indices i and j both go from 1 to N:

$$
\begin{array}{cc}
 & j \rightarrow \\
i & a_{11} X_1 + a_{12} X_2 + \ldots a_{1N} X_N = B_1 \\
\downarrow & a_{21} X_1 + a_{22} X_2 + \ldots a_{2N} X_N = B_2 \\
 & a_{N1} X_1 + a_{N2} X_2 + \ldots a_{NN} X_N = B_N
\end{array}
\qquad (6\text{-}1)
$$

The solution to this set of equations is reached when a specific set of values of X_j satisfies the above expressions. A solution to any one of the equations in the above set is also reached when there is no longer any residual error in the equality between the left and right sides of the equation. This is the key concept of the relaxation process.

That is, for this process, the same "solution" to Equation (6-1) is reached for the set of X_j for which all of the residual errors, F_i expressed in the following form, approach zero:

$$
\begin{array}{cc}
 & j \rightarrow \\
i & F_1 = a_{11} X_1 + a_{12} X_2 + \ldots a_{1N} X_N - B_1 \\
\downarrow & F_2 = a_{21} X_1 + a_{22} X_2 + \ldots a_{2N} X_N - B_2 \\
 & F_N = a_{N1} X_1 + a_{N2} X_2 + \ldots a_{NN} X_N - B_N
\end{array}
\qquad (6\text{-}2)
$$

In other words, when the correct values of X_j are substituted into Equation (6-1), the right and left sides of Equation (6-1) become equal. Correspondingly, in Equation (6-2), the values of the residual errors, F_i, approach zero when the values of X_j approach (within acceptable accuracy) the correct values for the mode shape that would have been obtained from the exact solution of Equation (6-1).

Basically, the relaxation process starts by breaking an acoustic cavity down into finite elements and approximating the applicable Helmholtz equation for the cavity by finite difference equations which also define a set of residual error terms, F_i. Then values are assumed for the unknowns, X_j, in these equations. Depending on which of the two basic versions of the relaxation method is employed, these initial values for the desired unknown mode shapes may, in general, be quite arbitrary, or may be very rough estimates of the actual mode shape. However, in either case, any initial values at the cavity boundaries must conform to applicable boundary conditions such as zero particle velocity at a rigid wall or zero pressure at an assumed pressure node.

Next, the residual error terms, F_i, from Equation (6-2) are computed and, from these, incremental changes δX_j to one or more of the assumed X_j values are computed. These increments are computed so as to reduce the magnitude of the residual errors. The new values of X_j, X_j (new) = X_j (initial) + δX_j, are then used to compute new values for the residual error terms. The process is repeated or iterated until the residual error terms, F_i, approach zero and the iterated values for the mode shape, X_j, stabilize. This final close approximation to the mode shape is then used to compute the desired resonance frequency.

Accuracies in mode shape of the order of 5 to 10 percent and roughly tenfold higher accuracies in resonance frequency are possible with a relatively small number of iterations readily carried out on a computer. The number of iterations will decrease as the initially estimated mode shape more closely approximates the correct value and will increase as the number, N, of variables increases, where N is equal to the number of two- or three-dimensional cells or elements used to describe the acoustic cavity or cascade system.

Several variations in the iterative relaxation process can be used:

- **Point Relaxation** – Iterative change in one element at a time (i.e., a change in one variable, say X_1) selected for change because it had the

highest residual error at the end of the previous iteration. The change in X_1 is computed so as to reduce the residual error F_1 to zero for the next iteration.

- **Block Relaxation** – Equal iterative changes in a block of elements (e.g., all N variables in a set of equations for the pressure in a cavity are changed by the same amount designed to reduce the total residual error (ΣF_i) to zero at the next iteration).
- **Group Relaxation** – Unequal iterative changes in a block of elements (e.g., all variables in a set of equations are changed simultaneously but by unequal amounts).
- **Multiplying Factors** – A single multiplier applied to all of the residual error terms, F_i, at the same time when the iteration process has reached the point where they are all non-zero but have the same relative proportion (i.e., $F_1 : F_2$, $F_1 : F_3$, etc.) that they have at the beginning of the iteration process. If the estimated values for X_j are all multiplied by this definable factor, a final solution is achieved in just one more iteration step.

In addition to these four variations for relaxation iteration defined by Allen,[3] a variation on point relaxation is useful for efficient computer implementation of the relaxation process.

- **Multiple Point Relaxation** – This consists of applying an incremental change to all points for which the previous residual error was equal to or greater than a specified fraction (25 percent has been found to be suitable) of the maximum residual error. That is, a defined incremental change (not the same for each point) is made to all points with a residual error within 25 to 100 percent of the maximum value. The incremental change made to each such point is the same as for a true single point relaxation, i.e., it will reduce the residual error to zero for that point in the next iteration, in the absence of changes to any other points.

For efficient computerized execution of the relaxation method, only the Point, Block, and Multiple Point relaxation techniques are appropriate. The other two variations require more complex judgment, not suitable for a simple computerized iteration program.

Consider, now, some of the key aspects involved in the application of the relaxation process to the determination of the fundamental acoustic resonance frequency and mode shape for a simple one-dimensional acoustic system. While these parameters can be readily defined by classical methods, for this example the relaxation method is applied to this case for illustration of these key concepts.

Consider the sound field inside a closed rigid tube of length L. The *spatial* variation in the sinusoidally varying (time-wise) pressure in the tube is found from the solution of an ordinary, second-order, differential equation, called the *Helmholtz equation.* If the axial position along the tube is expressed in a non-dimensional form as the ratio $x' = x/L$ of the x coordinate to the tube length L, the Helmholtz equation can be given by[4]

$$\frac{d^2 P(x')}{dx'^2} + (kL)^2 \, P(x') = 0 , \qquad (6\text{-}3)$$

where $k = 2\pi f/c$ is the wave number for a sinusoidal pressure wave with a frequency f and sound speed c.

Equation (6-3) is one form of a general class of equations which define eigenvalues or resonance frequencies of a linear (in this case, one-dimensional) system in terms of a set of normal modes. In this case, the acoustic pressure in the closed tube for one of these resonance frequencies, say the n'th, will have the general form

$$p_n(x', t) = P_n(x') \cos(2\pi f_n t) , \qquad (6\text{-}4)$$

where $P_n(x')$ is the, as yet undefined, mode shape for the n'th mode at point x' and f_n is the n'th resonance frequency, related to the corresponding wave number by $k_n = 2\pi f_n/c$. To determine this resonance frequency by the relaxation method, either one of two variations may be used: (1) the "Modal Intensification" method, or (2) the Rayleigh method. These variations, explained in more detail in Section 6.2.5, are summarized here with emphasis on the Modal Intensification method.

Consider, now in Section 6.2.1, the key element common to both of these approaches, the Rayleigh quotient, which is used to compute the resonance frequencies.

6.2.1 Rayleigh Quotient

The Rayleigh quotient can be developed, semi-empirically, by recognizing that a general solution to Equation (6-3) should apply at all values of x' within a system (e.g., all along the axis of the closed tube in our example). Thus integration of both parts of Equation (6-3) is implied. Further, assume that the magnitude of each term in Equation (6-3) at any position should be weighted by the magnitude of the pressure P(x') at that position. Applying these concepts, and solving the weighted integral version of Equation (6-3) for the eigenvalue $(kL)^2$, the Rayleigh quotient is given by[3]

$$(kL)^2 = - \frac{\int P(x') \left(d^2 P(x') / d x'^2 \right) dx'}{\int P^2 (x') \, dx'}, \qquad (6\text{-}5)$$

where it is understood that the integrations take place over all values of x' from one end of the tube to the other (i.e., x' = 0 to 1, where x' is non-dimensional).

The application of the Rayleigh quotient involves an intuitive guess at the expected mode shape, followed by an evaluation of Equation (6-5) to obtain an estimate of the eigenvalue. This method will yield the eigenvalue to a high degree of accuracy.

To apply Equation (6-5) to one of the following relaxation methods, it is first necessary to develop a finite difference approximation (FDA) to the second derivative of P(x') in the numerator of this equation. For the simple example used here of the closed end tube, this FDA is started by breaking the tube into a set of four equal segments, as illustrated in the following sketch. (Only four segments are used here, for the sake of simplicity.)

Dropping the prime from x' for convenience, the FDA to Equation (6-3) at the point x_i can be shown to be[3]

$$\frac{d^2 P(x_i)}{dx^2} \simeq \frac{P(x_{i-1}) + P(x_{i+1}) - 2 P(x_i)}{h^2}, \qquad (6\text{-}6)$$

where $P(x_i)$ are the values for the acoustic pressure P(x) along the x axis at positions x_{i-1}, x_i, and x_{i+1} spaced at equal intervals, h, as illustrated in the sketch, where i has the values 0 to 4. Equation (6-6) is simply the first term of a central difference approximation of the second derivative of P(x) with error of order h^2. The central difference approximation was derived from the sum of the Taylor series expansion of $P(x_i - h)$ and $P(x_i + h)$.

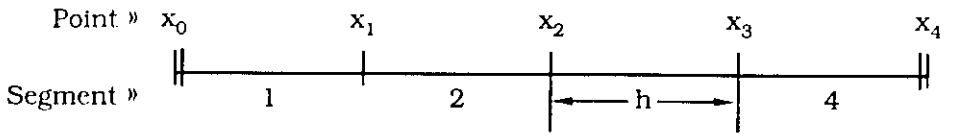

Applying this approximation for $d^2 P(x_i)/dx^2$, and replacing the continuous integral of Equation (6-5) with a summation over the finite elements, an equivalent form of Equation (6-5) suitable for numerical computation is

$$(kL)^2 = - \frac{-\sum_{i=0}^{4} P(x_i) \left[P(x_{i-1}) + P(x_{i+1}) - 2P(x_i) \right]}{h^2 \sum_{i=0}^{4} P^2(x_i)} . \qquad (6\text{-}7)$$

Note that, since the x-coordinates are actually expressed in non-dimensional form, the variable, h , is also non-dimensional and, in this case, is simply equal to 1/4, or the inverse of the number of segments into which the tube length has been divided.

6.2.2 Modal Intensification Method

For this method, the pressure at any point in the cavity is expressed as the sum of the pressures in the n normal modes for the cavity. This normal mode summation concept is then applied, with the aid of the relaxation process, to find the shape of the first normal mode of the system and then, with the aid of the Rayleigh quotient, to find the corresponding resonance frequency.

If desired, the method can be applied to find higher-order modes by utilizing the orthogonality property of normal modes and "sweeping out" the already determined first mode shape from the initially assumed mode shape for the second mode and so on for higher modes.[3] Modal Intensification is the principal method utilized for previous studies of acoustic resonances of cascades (e.g., Parker[2]). It has the advantage of always finding the lowest order mode and it is computationally simple to use because it requires only a succession of solutions to a set of linear algebraic equations.

6.2.3 Rayleigh Method

For this method, the Rayleigh quotient is first applied to estimate the fundamental resonance frequency (in terms of the non-dimensional parameter $((k_1 L)^2$) based on an initial rough estimate of the *approximate* fundamental mode

shape of the system. This first approximation to $(k_1 L)^2$ is then used to compute the residual errors for this initial estimate of the mode shape. From these values, refined estimates of the mode shape are derived. The process is then repeated until the resonance frequency and mode shape stabilize.

The Rayleigh method suffers by giving no indication which of the n modes of a solution is obtained. The method does not deliberately arrange computation of the modes so that the lowest order mode is always selected first. Another difficulty occurs when two of the eigenvalues are close together or nearly equal. Convergence to one of the modes may be practically impossible unless a sufficiently good first guess is made. The Modal Intensification method does not suffer from these defects, and is therefore the method of choice.

6.2.4 Implementation of the Modal Intensification Relaxation Method

This section contains a generalized application of the Modal Intensification relaxation method to a simple one-dimensional case. Section 6.2.5.1 provides a detailed example of the computation of the mode shape and resonance frequency of fluid in a pipe with closed ends.

As indicated earlier, this method assumes that the pressure P(x) at any position x can be expressed as the sum of the pressures in the normal modes, $P_1(x), P_2(x), \ldots, P_n(x)$, with resonance frequencies/eigenvalues represented, for convenience, by the non-dimensional eigenvalue $\beta_i = (k_i L)^2$. From this concept, it can be shown[3] that the Helmholtz equation takes the form (again dropping the prime from x')

$$\frac{d^2 P'(x)}{dx^2} + P(x) = 0 \qquad (6\text{-}8)$$

where

$$P'(x) = \frac{P_1(x)}{\beta_1} + \frac{P_2(x)}{\beta_2} + \ldots + \frac{P_n(x)}{\beta_n} \qquad (6\text{-}9a)$$

and the eigenvalues for the n modes have ascending values such that

$$\beta_1 < \beta_2 < \beta_3 < \ldots \beta_n . \qquad (6\text{-}9b)$$

The variable P' now becomes the unknown sum of the modal amplitudes to be found in terms of the presumed known total amplitude P(x). Equation (6-8) is solved for P'(x) by relaxation and this solution is substituted back into Equation (6-8) as a better estimate of P(x). This process is then repeated several

times. Given the relationships in Equation (6-9), the result is that this iteration process stabilizes on the amplitude of the lowest mode since, in the series $P_1(x)/\beta_1 + P_2(x)/\beta_2 + \ldots P_n(x)/\beta_n$, the first term for the fundamental mode will be "intensified" at each step in the iteration process.

Now, using Equation (6-6) to express Equation (6-8) in terms of an FDA for the point $i = 0$, the result is

$$\frac{P'(x_{-1}) + P'(x_1) - 2\,P'(x_0)}{h^2} + P(x_0) = 0. \qquad (6\text{-}10)$$

Since the actual amplitudes, $P'(x_i)$, of the normal modes are not of importance here, the value of h can be arbitrarily set equal to 1 at this point. Therefore the corresponding residual error term F_0, representing the equivalent of Equation (6-2) at the point $i = 0$, is

$$F_0 = [P'(x_{-1}) + P'(x_1) - 2\,P'(x_0)] + P(x_0). \qquad (6\text{-}11)$$

Similarly, the residual error term F_1, at the point $i = 1$ is

$$F_1 = [P'(x_0) + P'(x_2) - 2\,P'(x_1)] + P(x_1). \qquad (6\text{-}12)$$

It is immediately apparent from these two equations that a unit change in $P'(x_0)$ will change the residual error terms F_0 and F_1 by -2 and +1, respectively.

It is desirable, at this point, to define the boundary conditions applicable for a closed-end tube. The boundary condition for the first mode is a zero particle velocity at the ends of the tube. This is equivalent to saying that $dP(x)/dx = 0$ at each end of the tube. However, the finite difference approximation for this first derivative at a point x_i is simply

$$\frac{dP(x)}{dx} \approx \frac{P(x_{i+1}) - P(x_{i-1})}{2h} = 0. \qquad (6\text{-}13)$$

The boundary condition of zero particle velocity at x_i leads to

$$P(x_{i+1}) = P(x_{i-1}),$$

where $P(x_{i \pm 1})$ are the pressures on each side of the i'th point at positions separated by a total distance $2h$.

Thus the boundary condition at a rigid surface located at, say, $x = x_0$, is simulated, for calculation purposes in the relaxation process by establishing a

fictitious point on the other side of the boundary at x_{-1} which has the same pressure as at point x_{+1}. All that is necessary is to carry this point through the relaxation process solely for purposes of conveniently computing the residual error terms.

It is convenient to facilitate, conceptually, the computation of the residual error terms, as in Equation (6-12), by what is called an operations table. This is shown in Table 6-1, below, for the case of the simple closed-end tube divided into four segments. This shows the change in the value of F_i at each i'th point for a unit change in the pressure at this point only and for a unit change in pressure at all the points simultaneously.

Table 6-1

Operation Table for the Analysis of
Fundamental Acoustic Mode of Closed-End Pipe

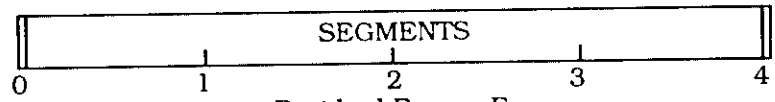

Residual Errors, F_i

δ P'(i)	F_{-1} *	F_0	F_1	F_2	F_3	F_4	F_5 *
P'(0) = 1	1	-2	1				
P'(0) = 1		1	-2	1			
P'(0) = 1			1	-2	1		
P'(0) = 1				1	-2	1	
P'(0) = 1					1	-2	1
All P'(i)**		-1	0	0	0	-1	

* Fictitious point outside ends of closed tube.
** Sum of F_i for $P'_i = 1$ at all points = -2.

6.2.5 Example Calculation of a String With Fixed Ends

6.2.5.1 *Modal Intensification Relaxation Method*

The Helmholtz equation for vibration of a string of linear mass density ρ, length L, under tension T is given by[4]

$$\frac{d^2\, w(x')}{dx'^2} + (kL)^2\, w(x') = 0, \qquad (6\text{-}14)$$

where the wave number $k = 2\pi f/c$, the speed of wave motion in the string $c = \sqrt{T/\rho}$, and $w(x')$ is the displacement of the string at a non-dimensional axial position $x' = x/L$ from a rest position. This can be transformed into the following form by applying the principle of construction of any vibration pattern for the string as the sum of its normal modes.[3] For this approach, a new variable w' is defined as the sum of these normal modes, each having an eigenvalue $\beta_n = (k_n L)^2$ where $\beta_1 < \beta_2 < \beta_3$, etc. Thus, if w is equal to $A_1 w_1 + A_2 w_2 + \ldots + A_n w_n$, where A_i is the modal amplitude of the i'th mode with shape w_i, Equation (6-14) could be written, dropping the prime from x', as

$$\frac{d^2 w'}{dx^2} + w = 0, \qquad (6\text{-}15)$$

where $w' = \frac{A_1 w_1}{\beta_1} + \frac{A_2 w_2}{\beta_2} + \ldots \frac{A_n w_n}{\beta_n}$.

Now, since $\beta_1 < \beta_2 < \beta_3$, etc., the first term of this series will be the largest for constant modal amplitude A_n, so that solving Equation (6-15) for w_1 for a *given* (estimated) value of w will provide an *intensified* estimate of the shape w_1 of the first mode of vibration of the string. Successive iterations of this solution for w_1 as an improved estimate for w finally produces an accurate estimate for the fundamental mode of vibration of the string.

To solve Equation (6-15) by this version of the relaxation method, it is first transformed by a finite difference approximation for the second derivative into the following form for the i'th point:

$$\frac{w'_{i-1} + w'_{i+1} - 2w'_i}{h^2} + w_i = 0, \qquad (6\text{-}16)$$

where h = the length of each finite segment into which the string is divided. For now, the value of h can be arbitrarily set to 1, since the absolute magnitude of the modal amplitude is not of interest.

Equation (6-16) is now solved for the unknown w' values using alternating block and point relaxation processes. Application of these processes to the determination of the mode shape and fundamental resonance frequency for vibration of a fixed-end string of length L is illustrated as follows. First, the string is broken into four finite segments as illustrated in the diagram below, where h = 1/4:

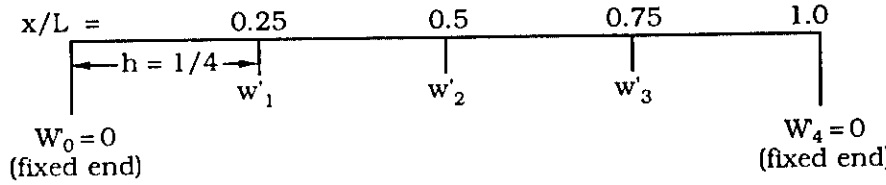

The displacements at the two end points are, of course, zero. Applying Equation (6-16) for each of the remaining three intermediate points (i = 1,2,3), the expressions for the residual error at these three points, are (with h set equal to 1):

$$F_1 = -2w'_1 + w'_2 + w_1 \qquad (6\text{-}17a)$$

$$F_2 = +w'_1 - 2w'_2 + w'_3 + w_2 \qquad (6\text{-}17b)$$

$$F_3 = w'_2 - 2w'_3 + w_3 . \qquad (6\text{-}17c)$$

It is helpful, when applying the relaxation process to define the following operations table which simply defines the change in the value of each of the residual error terms for a unit increase in each of the unknowns w'(i) one at a time (lines 1, 2, and 3, below) and (for application to block operations), all at the same time (line 4, below).

Table 6-2

Operations Table for the Analysis of
Fundamental; Displacement Modes of a Vibrating String

Line	$\delta w'_1$	Residual Errors, F(i)			
		F_1	F_2	F_3	
1	$w'_1 = 1$	-2	1	0	
2	$w'_2 = 1$	1	-2	1	
3	$w'_3 = 1$	0	1	-2	
4	$w'_1 = w'_2 = w'_3 = 1$	-1	0	-1	$\sum [F_1 (w'_1 = 1)] = -2$

In Table 6-2, the values -2, 1, and 0 appearing under F_1 are the coefficients to the W primes in Equation (6-17a). The value of w_i is arbitrarily assumed to be 100 initially and, for each step, the first values of w'_i, the modal component of w_i to be determined, are set to 0. As can be seen from Equation (6-17), the result is that the initial values of the residual error terms, F_i, are also equal to 100. The most efficient way to start the relaxation process is to first apply a block relaxation. This consists of applying a change, $\delta w'_i$, to each w_i, selected such that the *sum* of the resulting residual error terms is zero. It can be shown that this value of $\delta w'_i$ is given by:

$$\delta w'_i = \frac{-\sum (F_i)}{\sum F_i (w'_i = 1)} \qquad (6\text{-}18)$$

where F_i are the actual error terms for specified values of w'_i, and $F_i (w'_i = 1)$ are the error terms for a unit change in w'_i at each point.

From Table 6-2, $\delta w'_i$ is equal to $-(100 + 100 + 100)/(-1 + 0 - 1) = 150$. With this change to w'_i, new values for F_i are then calculated. As shown in Table 6-3, line 1d the sum of the residual error values of F_i (-50 + 100 - 50) is equal to 0.

For Step 2 of the relaxation process for this case, it is most efficient to simply apply a point relaxation operation. This method is usually reserved until the end of the solution in order to make small local adjustments. Point Relaxation amounts to adding a new increment $\delta w'_i$ to only the value of w'_i which had the largest residual error from the previous step. The magnitude of this change is found from the operations table and is set equal to the value necessary to make this (largest) residual error equal to 0. For value i = 2, which has the largest residual error at the end of the first part of Step 1, changing w'_2 by -100/(-2) = 50 will accomplish this. The other w'_is are not changed but the resulting new value for the residual errors are zero at point 2, as required, and, *by coincidence*, the residual error is also zero at the other two points at the end of Step 2.

Table 6-3

Relaxation Table Showing Steps 1 and 2 for
Displacement Modes of Vibrating String

Line	$F_i = w_i$ (initial)	i = 1	i = 2	i = 3	Initial Estimate for w_i
1a		100	100	100	
1b	$\delta w'_i$	150	150	150	BLOCK RELAXATION
1c	w'_i	150	150	150	[$\delta w'$ applied at all points]
1d	F'_i Eq. (6-17)	-50	100	-50	
2b	$\delta w'_i$	0	50	0	POINT RELAXATION
2c	w'_i	150	200	150	[$\delta w'$ applied only where previous F_i is max.]
2d	F'_i Eq. (6-17)	0	0	0	

The operations carried out in Table 6-3 are:

Line 1a Initially, assume $w_i = 100$ and $w'_i = 0$; hence, from Equation (6-17), $F_i = w_i$.

Line 1b $\delta w'_i$ computed from Equation (6-18), applied for block relaxation at all non-fixed points.

Line 1c $w'_i = w'_i$ (initial) + $\delta w'_i = 0 + \delta w'_i$.

Line 1d New values for F_i computed from Equation (6-17).

Line 2b $\delta w'_i$ computed again from Equation (6-18) with new values of F_i .

Line 2c $w_i = w'_i$(new) + $\delta w'_i$

Line 2d New values for F_i computed from Equation (6-17).

The new estimates of the modal amplitudes w'_i are now used to revise the initial value of w_i which starts another iteration loop carrying out these same series of steps.

Before proceeding to the next step, it is convenient to normalize the new values of w'_i and w_i to a maximum of 100 (see Table 6-4, line 3a). The entire process is now repeated, starting with a block relaxation change $\delta w'_i$ to all three points which is, from Equation (6-18), equal to -(75 + 100 + 75)/(-2) = 125. Again note that the initial value of w'_i is assumed equal to zero for the first iteration of each step, so the second estimate of w'_i (line 3c) is simply equal to $\delta w'_i$ on line 3b.

Table 6-4

Relaxation Table Showing Steps 3 and 4 for
Displacement Modes of Vibrating String

Line 3a	$F_i = w_i$ (initial)	i = 1	i = 2	i = 3	Initial Estimate for w_i
		75	100	75	
3b	$\delta w'_i$	125	125	125	BLOCK RELAXATION
3c	w'_i	125	125	125	↓
3d	F'_i	-50	100	-50	
4b	$\delta w'_i$	0	50	0	POINT RELAXATION
4c	w'_i	125	175	125	↓
4d	F'_i	0	0	0	

The same procedure repeated again gives the following result. Again, note that it is purely coincidence, for this simple case, that *all* of the values of F_i on line 4d are zero. Only the value for $i = 2$ is expected to be zero by application of the point relaxation at this point.

Table 6-5

Relaxation Table Showing Steps 5 and 6 for
Displacement Modes of Vibrating String

Line 5a	w_i (initial)	i = 1	i = 2	i = 3	Normalized From Line 4c
		71.43	100	71.43	
5b	$\delta w'_i$	121.4	121.4	121.4	BLOCK RELAXATION
5c	w'_i	121.4	121.4	121.4	↓
5d	F'_i	-46.4	100.0	-46.4	
6b	$\delta w'_i$	0	50.0	0	POINT RELAXATION
6c	w'_i	121.4	171.4	121.4	↓
6db	F'_i	0	0	0	

After three more identical iterations of the same process (see Tables 6-5 and 6-6), the resulting mode shape, expressed in a normalized form, is identical to five significant figures to the theoretical result given in Table 6-6. Note, however, that in this case, just two iterations are all that would be required to achieve an accuracy of about 1 percent in mode shape (i.e., compare the normalized mode

shape, 0:71.43:100:71.43:0 at the beginning of Step 5 with the exact values 0:70.711:100:70.711:0) for the first (sinusoidal) mode of a vibrating string. Thus a very accurate solution has been obtained for the fundamental mode shape w_1 of the string by this simple relaxation process.

Table 6-6

Relaxation Table Showing Steps 7 and 8 for Displacement Modes of Vibrating String

Line 7a	w_i (initial)	i = 1	i = 1	i = 1	
		70.7	100	70.7	
7b	$\delta w'_i$	120.7	120.7	120.7	BLOCK RELAXATION
7c	w'_i	120.7	120.7	120.7	↓
7d	F'_i	-50.0	100.0	-50	
8b	$\delta w'_i$	0	50.0	0	POINT RELAXATION
8c	w'_i	120.7	170.7	120.7	↓
8d	F'_i	0	0	0	

Table 6-7

Normalized Values From Line 8c and Exact Values

Line 9a	w'_i	i = 1	i = 1	i = 1	
		70.711	100	70.711	
Exact Values From Theory, $w'_i = 100 \sin(\pi x/L)$					
	w'_i	70.711	100	70.711	

All that remains is to define the fundamental resonance frequency from this relaxation process. From the Rayleigh quotient, the value of $(k_1 L)^2$ is given by[3]

$$(k_1 L)^2 = \frac{-\int w(x)\,(d^2 w(x)/dx^2)\,dx}{\int w^2(x)\,dx}, \qquad (6\text{-}19)$$

where it is understood that the integration takes place over all values of x from one end of the string to the other.

Using the finite difference approximation for the second derivative in the top integral and now using the true non-dimensional value of $h = 1/4$ (it was arbitrary when computing relative mode shapes)

$$(k_1 L)^2 = \frac{-\Sigma w_i (w_{i-1} + w_{i+1} - 2w_i)}{h^2 \Sigma w_i^2} . \qquad (6\text{-}20)$$

Applying this to the normalized values for w'_i at the end of Step 2, the result is

$$(k_1 L)^2 = \frac{-[71.43\,(100 - 2x71.43) + 100\,(71.43 + 71.43 - 2x100) + 71.43\,(100 - 2x71.43)]}{(1/4)^2[(71.43)^2 + (100)^2 + (71.43)^2]}$$

$$= 9.374$$

or $k_1 L = 3.062$, within 2.5 percent of the true value, π, for the fundamental mode of vibration of a fixed-fixed string.

In summary, with no knowledge whatsoever of the mode shape of the string except for the required boundary condition of zero displacement at the ends of the string (i.e., the initial guess was for a constant amplitude of 100) and using only the finite difference approximation to the Helmholtz equation for the vibration of the string, the mode shape for its fundamental frequency of vibration is easily computed by the Modal Intensification relaxation method. A close approximation to the resonance frequency is then computed from another finite difference approximation to the Rayleigh quotient. Note that if the more exact estimate of the mode shape had been used after Step 7, instead of two iterations of the relaxation process, then the calculated resonance frequency, from Equation (6-20) would have had a value for $k_1 L$ of 3.061, just slightly lower than the first estimate.

If the string had been broken into eight, instead of four, segments, the above process would have produced a value for $k_1 L$ of 3.12, within less than 1 percent of the true value π (Allen[3]). Thus, in general, improved estimates of the resonance frequency of a system require a finer breakdown into more elements – that is, accuracy for modal frequencies is more dependent upon a finer segmentation for the Rayleigh quotient than on the accuracy of the mode shape determined from the relaxation process.

This highly simplified demonstration of the application of the modal intensification relaxation method to find the fundamental mode shape and

resonance frequency of vibration of a string can be directly applied to the case of the acoustic resonance in an open-ended pipe. This analogy neglects the end correction of a virtual "acoustic" mass at the ends of the open pipe which accounts for sound radiation at the ends (Kinsler and Frey[4]). The string displacement w is replaced by the acoustic pressure, P, and the speed $c = \sqrt{T/\rho}$ of vibration waves in the string is replaced by the speed of sound $c = \sqrt{\gamma P_o/\rho}$, where γ is the ratio of specific heats, P_o is the atmospheric pressure, and ρ is the gas density. In all cases, the relaxation process is carried out by successive applications of the incremental changes, δw_i, defined by Equation (6-18), to one or more points in the system such that, in each case, the sum of the residual errors for all the points changed is zero.

6.2.5.2 *Rayleigh Relaxation Method*

For this method, the finite difference approximation to the Helmholtz equation can be written down directly without resort to any assumption about normal mode summation. The resulting Finite Difference approximation to Equation (6-14) at the i'th point is

$$[w_{i-1} + w_{i+1} - 2w_i] / h^2 + (kL)^2 w_i = 0 , \qquad (6\text{-}21)$$

where h equals the length of each segment of the string.

The corresponding expression for the residual error, F_i is, for the i'th point:

$$F_i = w_{i-1} + w_{i+1} - w_i [2 - (kLh)^2] w_i . \qquad (6\text{-}22)$$

Note that, unlike the modal intensification method, the residual error terms inherently include the eigenfrequency term $(kLh)^3$.

The Rayleigh relaxation method is carried out as follows:

1. An initial estimate is made of the values of w_i defining the shape of the fundamental mode.
2. A value for the quantity $(kLh)^3$ is calculated from the Rayleigh quotient, Equation (6-20), using these values of w_i.
3. A value for the residual error, F_i, at each point is calculated from Equation (6-22).

4. An incremental change δw_i is computed to initiate a block or point relaxation step. The value of δw_i is again found from Equation (6-18) and is equal to minus one times the total or maximum value of the residual errors terms for a block or point relaxation step, respectively, divided by the corresponding total value of the residual error for a unit change in w_i at the point(s) affected.

5. The value(s) of δw_i is then applied as a correction to the corresponding previous values of w_i to obtain a refined estimate of w_i.

6. This process is repeated from Step 2 through Step 5 until the computed eigenvalue (kL) and mode shape become stable, i.e., the change in these quantities between iterations is within the accepted accuracy criteria.

The process is illustrated as follows for the case of the string. Unlike the beginning of the modal intensification method where the initial mode shape was not critical, *now it may be necessary that the initial estimate of the mode shape be at least a reasonable, first-order approximation to the actual mode shape of the fundamental mode.* That is, the initial estimate should roughly indicate the general location of the maxima and must, of course, be consistent with the boundary or mode conditions such as a zero displacement at a boundary or at a known or assumed node point or line. For this case, an initial crude estimate of the mode shape is given by 0:60:100:60:0.

In Table 6-8, two different versions of the relaxation process are applied to illustrate the potential flexibility of the method. For the first approach, Equation (6-22) is used throughout for calculation of the residual error terms, F_i, and the change, δw_i, to be made to extinguish these errors using the block relaxation process. For the second variation, Equation (6-22) is only used to compute the error terms and a simplified version of Equation (6-18) is used to compute the change δw_i made to each point to minimize F_i using, initially, a block relaxation process and the point relaxation method thereafter. The simplification consists of setting (kLh) equal to zero when computing the change in F_i for a unit change in w_i (Allen[3]). For the sake of brevity, only the first two steps and the last step required to achieve good accuracy are shown for each of these two variations.

Table 6-8

Rayleigh Relaxation Table for First Mode of Fixed-Fixed String

(a) Using exact expression for F_i and δw_i for all (block relation) steps.

STEP X/L >>		1	2	3	$(kLh)^2$	Sum $[F_i]$	Sum $[F_i, w_i = 1]$	
0	F_i, $w_i = 1$, Eq.(6-22)#	-0.4	0.6	-0.4			-0.186	Type of Step
0	$w_i(0)$, Initial	60	100	60	0.6046			
0	F_i, Eq.(6-22)	16.3	-19.5	16.3		13.023		
1	δw_i, Eq.(6-18)	70.0	70.0	70.0				Block
1	$w_i(0) + \delta w_i$	130.0	170.0	130.0				
1	w_i (n) *	76.5	100.0	76.5	0.5901			
1	F_i , Eq.(6-22)	-7.8	12.0	-7.8		-3.678	-0.230	
2	δw_i, Eq.(6-18)	16.0	-16.0	16.0				Block
2	$w_i(1) + \delta w_i$	60.5	84.0	60.5				
2	w_i (n) *	72.0	100.0	72.0	0.5860			
2	F_i , Eq.(6-22)	-1.8	2.6	-1.8		-1.000	-0.2420	
•	•	•	•	•	•	•	•	•
•	•	•	•	•	•	•	•	•
4	δw_i, Eq.(6-18)	-0.22	-0.22	-0.22				Block
4	$w_i(3) + \delta w_i$	70.6	99.8	70.6				
4	w_i (n) *	70.7	100.0	70.7	0.5857			
4	F_i , Eq.(6-22)	-0	0.0	-0		-0.0001	-0.2426	

* Signifies value of w_i normalized to a maximum of 100. # Sum $[F_i]$ for $w_i = 1$.

(b) Using approximate expression for F_i for $w_i = 1$ plus use of point & block steps.

STEP X/L >>		1	2	3	$(kLh)^2$	Sum $[F_i]$	Sum $[F_i, w_i = 1]$	
0	F_i, $w_i = 1$, Eq.(6-22)#	-1.0	0.0	-1.0			-2##	Type of Step
0	$w_i(0)$, Initial	60	100	60	0.6046			
0	F_i, Eq.(6-22)	16.3	19.5	16.3		13.023		
1	δw_i, Eq.(6-18)	6.51	6.51	6.51				Block
1	$w_i(0) + \delta w_i$	66.5	106.5	66.5				
1	w_i (n) *	62.4	100.0	62.4	0.5966			
1	F_i , Eq.(6-22)	12.4	15.4	12.4		9.289	-2##	
2	δw_i, Eq.(6-18)**	0.0	-7.7	0.0				Point
2	$w_i(1) + \delta w_i$	62.4	92.3	62.4				
2	w'_i (n) *	67.7	100.0	67.7	0.5871			
2	F_i , Eq.(6-22)	4.4	-5.9	4.4		2.839	-2##	
•	•	•	•	•	•	•	•	•
•	•	•	•	•	•	•	•	•
6	δw_i, Eq.(6-18) **	0.0	-0.1	0.0				Point
6	$w_i(1) + \delta w_i$	70.6	99.9	70.6				
6	w'_i (n) *	70.7	100.0	70.7	0.5857			
6	F_i , Eq.(6-22)	0.0	-0.0	0.0		0.02090	-2##	

** Equation (6-18) applied only to point with maximum F_i from preceding step.

Sum $[F_i]$ for $w_i = 1$ and assuming $(kLh)^2 = 0$.

Note that for the Rayleigh relaxation method there is only one iteration per step, whereas for the modal intensification method, there can be several iterations of the mode shape for each step. (Only two, a block and a point relaxation, were used for the simple case treated earlier.) For either variation of the Rayleigh relaxation method, the final mode shape: 0:70.7:100:70.7:0 and the value of $(k_1L)^2 = [1/(1/4)^2]\ (0.5857) = 9.371$ is essentially the same as achieved earlier by the modal intensification method.

In Table 6-9, the sensitivity to the accuracy of the initial mode shape assumed is examined. The results are summarized for each version (a) and (b) used in the previous table, in terms of the initial mode shape, and the number of steps required to achieve a stable and accurate value. In some case, stability is achieved, but the result does not represent the desired mode, i.e., the relaxation process stabilizes on an invalid value of $(k_1Lh)^2$ for the first mode.

In general, however, it is found that a stable, valid result is reached by using the first version (a) of the Rayleigh relaxation method, which employed block relaxation at each step, only when the initial assumption of mode shape had the *correct trend in slope.* This occurred, for this simple example of the first mode of vibration of a string, when the change in assumed amplitude between either end point (= 0) and the next nearest point was *greater* than the change between adjacent points near the middle of the string.

In contrast, for the second version (b) of the Rayleigh relaxation method, which used only point relaxation after the first block relaxation step, and assumed that the change in the residual error, F_i, for unit change in w_i was simply -2 [equivalent to neglecting $(kLh)^2$ in Equation (6-22)], a valid, stable result was always obtained, regardless of the assumption about the initial mode shape. Thus this version of the Rayleigh relaxation method is similar to the Modal Intensification relaxation method in that it was not sensitive to initial mode shape. It has been found that this generalization still holds for more complex systems.

In all cases, as expected, fewer iteration steps were required when the initial estimate of mode shape was close to the final result.

Table 6-9

Sensitivity of Rayleigh Relaxation Method to Assumption for Initial Mode Shape of String

Relaxation Version From Table 1	**Assumed Mode Shape at Point Between Ends**			**No. of Iteration Steps**
	1	**2**	**3**	
(a)	0	100	0	*
	25	100	25	*
All BLOCK	50	100	50	*
Relaxation –	55	100	55	5
Correct Value	60	100	60	4
for F_i , δw_i	70	100	70	1
	80	100	80	3
	90	100	90	5
	100	100	100	*
(b)	0	100	0	7
	25	100	25	7
BLOCK + POINT	50	100	50	6
Relaxation –	60	100	60	6
Correct Value	70	100	70	3
for F_i but	80	100	80	6
$[F_i , w_i = 1] = -2$	90	100	90	6
or $[kLh]^2 = 0$	100	100	100	6

* Relaxation fails to reach valid or stable value.

6.2.6 Extensions to a Two-Dimensional System

In Figure 6-3, an area with dimensions L_x x L_y could be divided into N x M cells with dimensions h_x and h_y in the x- and y-directions, respectively. The area shown is, in fact, the finite-element network used by Parker[2] to represent a cascade system of an infinite stack of parallel plates with a cord dimension $C = 2L_x$ (in the x-direction), pitch spacing $s = 2L_y$ (in the y-direction), and cross-span width b . By taking advantage of the symmetry of the modes in the vertical x–y plan parallel to the flow for this system, it is only necessary to evaluate one quadrant of the area between any two plates. This quadrant is the rectangle ABCD noted on the figure made up of 51 cells (52 points) in the x-direction and four cells (five points) in the y-direction. Rectangle ABCD is the same rectangle appearing in Figure 6-2. In Figure 6-3, one set of additional points is required on each side of this rectangle to supply fictitious points, as discussed earlier, for defining pressure gradients along the area boundaries.

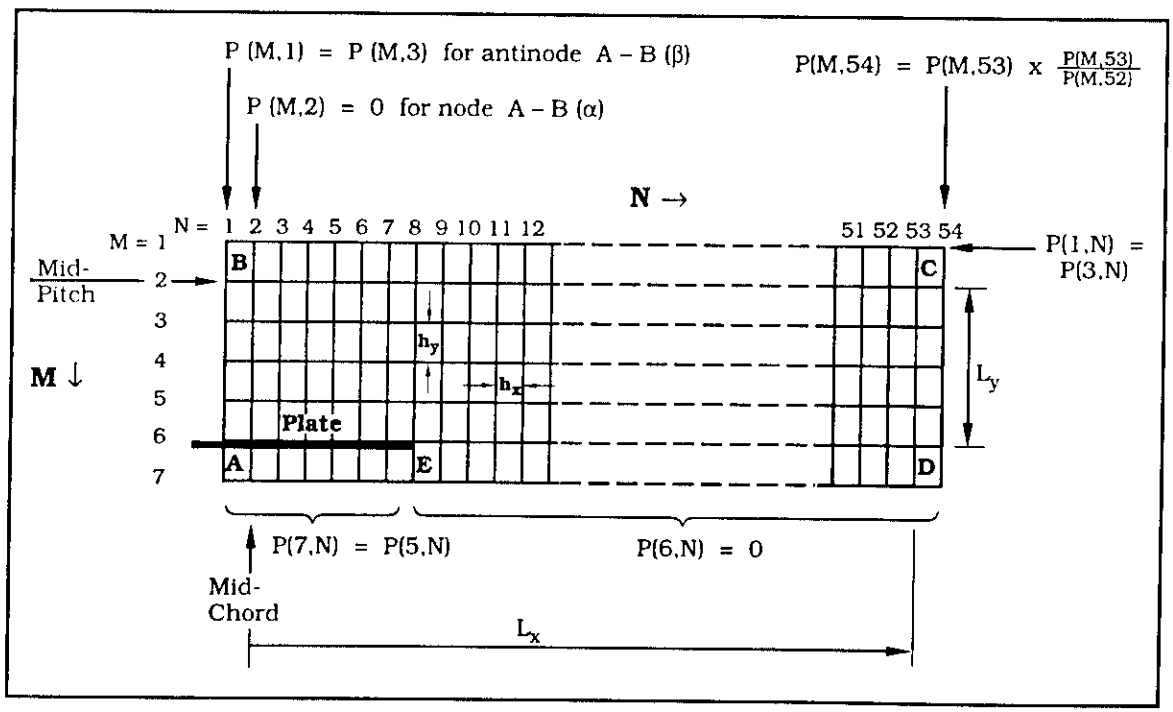

Figure 6-3. Network of Finite Elements Used to Represent α , β Modes of Cascade System. (Reproduced from Parker.[2])

Boundary conditions are specified on this diagram for two different types of modes (see Figure 6-2 a, b). For the α modes, there is an anti-node (pressure maximum) along the mid-cord centerline, and the corresponding boundary condition along this line is that the pressures at points on either side in the x-direction [designated by P(M,1) and P(M,3)] are equal, signifying a pressure maximum and zero particle velocity along the line (M,2). For the β mode, the pressure is zero along this mid-cord node line or $P(M,2) = 0$. For both of the modes, there is also an anti-node along the mid-pitch line (2,N) so that the pressures on either side, P(1,N) and P(3,N) are equal.

Two more boundary conditions are needed. One is along the line corresponding to one plane of the cascade plate structure. In this case, along that portion of the line coincident with the solid boundary of the plate, the condition for a zero pressure gradient (i.e., zero particle velocity) is again invoked; that is, $P(7,N) = P(5,N)$ for $N = 2$ to 7 where $N = 7$ at the point just before the end of the plate. For the rest of this line, which falls in the open, unconfined area of the cascade duct (starting at the edge [N = 8] of the plate itself), the pressure is assumed to be 0 or $P(6,N) = 0$ for $N = 8$ to 54. Finally, at the right side of the rectangle, along the line CD, a new type of boundary condition is invoked – namely, that the pressure gradient in the x-direction be a constant along this line. This is imposed as a necessary and sufficient constraint on the pressure field in this area to accommodate the fact that the field is unbounded in this direction and, for this case, it can be shown[2] that the pressure field is expected to decay exponentially with x.

For rectilinear two-dimensional sound fields such as designated in Figure 6-3, the Helmholtz equation corresponding to Equation (6-8) is given by

$$\frac{d^2 P'(x,y)}{dx^2} + \frac{d^2 P'(x,y)}{dy^2} + P(x,y) = 0. \qquad (6\text{-}23)$$

Using a heuristic analysis, Parker[2] predicts that the corresponding mode shape for the general case of an axial flow system without hard boundaries at the inlet and outlet of the cascade would be expected to have the form

$$P(x,y) = P_o \cos(k_c y) \exp\left[-k_c x \sqrt{1 - (f/f_c)^2}\right] \qquad (6\text{-}24)$$

where $k_c = 2\pi f_c/c$, the wave number at the "between plates" plane wave resonance frequency f_c in the duct,

f_c = c/2s for the α, β modes and c/s for the γ, δ modes (Figure 6-2),

s = pitch spacing of the cascade plates,

f = the frequency of the acoustic field corresponding to the vortex shedding frequency,

and $f < f_c$.

However, this analytical definition for the mode shape in the cascade system can be validated by solving Equation (6-23) numerically with the relaxation process using the boundary conditions specified earlier. It is only necessary to specify a finite difference approximation for each of the second derivatives in Equation (6-23). Allowing for rectangular cell dimensions h_X and h_Y , it can be shown that this is given by the sum of two finite difference approximations – one for each direction – in the form of Equation (6-6). The result is

$$\frac{d^2 P'(x,y)}{dx^2} + \frac{d^2 P'(x,y)}{dy^2} \approx FDA_x + FDA_y = FDA(x,y)$$

where

$$FDA(x_i,y_j) = \frac{P'(x_{i-1}, y_j) + P'(x_{i+1}, y_j) - 2P'(x_i, y_j)}{h_x^2}$$

$$+ \frac{P'(x_i, y_{j-1}) + P'(x_i, y_{j+1}) - 2P'(x_j, y_j)}{h_y^2} \qquad (6\text{-}25)$$

$$= \frac{\{\Sigma P'(x_{i\pm1}, y_j) + (h_x/h_y)^2 \Sigma P'(x_i, y_{j\pm1}) - 2[1 + (h_x/h_y)^2] P'(x_i, y_j)\}}{h_x^2}.$$

Thus the corresponding expression for the residual error for the Modal Intensification method at the point x_i, y_j will be

$$F_{i,j} = FDA(x_i, y_j) + P(x_i, y_j) \qquad (6\text{-}26)$$

where it is understood that $FDA(x_i, y_j)$ applies to the unknown modal pressures, $P'(x_i, y_j)$. This equation is directly analogous to the one-dimensional version given by Equation (6-11).

Finally, the corresponding expression for the Rayleigh quotient is given by

$$(kL)^2 = - \frac{\Sigma P(x_i, y_j) \; FDA (x_i, y_j)}{h_x^2 \quad \Sigma P^2(x_i, y_j)} \; . \qquad (6\text{-}27)$$

Note that for these last two expressions, only the ratio of the (non-dimensional) values of h_x and h_y is required for Equation (6-26), i.e., h_x can be set to unity in the denominator of FDA(x,y) for Equation (6-26) since only relative values of P(x,y) are needed at this point. However, the true absolute (non-dimensional) value of h_x and the ratio h_x/h_y is required for Equation (6-27).

Given these basic tools, the computational steps involved for application of the Modal Intensification relaxation process can be summarized in Section 6.2.7.

6.2.7 Computational Steps for the Modal Intensification Relaxation Method

The relaxation process using the Modal Intensification method is carried out in the following steps for any system.

1. The boundary conditions are established, using either $P'(x_i, y_j) = 0$ when the point x_i, y_j falls on a pressure node line, or $P'(x_{i-1}, y_j) = P'(x_{i+1}, y_j)$ when the point x_i, y_j falls on a pressure anti-node line (in the x-direction) such as at a rigid surface.

2. An initial estimate is made of the values for $P(x_i, y_j)$, the variable on the right side of Equation (6-26), at each point. Although a rough estimate of the expected final shape helps to speed up the iteration process, this initial guess can be quite arbitrary – a constant value of 100 is often used.

3. The initial values for the unknown (modal) pressures $P'(x_i, y_j)$ are assumed to be zero.

4. The corresponding values for the error terms, $F_{i,j}$, are computed at each point from expressions like Equations (6-26). For the first iteration, these initial values of $F_{i,j}$ are the same as the initial estimates of $P(x_i, y_j)$ since, from Equation (6-23), with $P'(x_i, y_j) = 0$, then $FDA (x_i, y_j) = 0$ and $F_{i,j} = P(x_i, y_j)$.

5. Using these values for $F_{i,j}$, a single, constant incremental change $\delta P'$ is computed using a Block relaxation step. The value for this initial constant increment applied to *all* points is equal to

$$\delta P' = \frac{-\sum F_{i,j}}{\sum F_{i,j} \text{ for } P'(x_i, y_j) = 1} \qquad (6\text{-}28)$$

where the numerator $\sum F_{i,j}$ is the sum of the residual error terms computed from Step 4, and the denominator $[\sum F_{i,j}$ for $P'(x_i, y_j) = 1]$ is the sum of all the residual error terms when a unit change is made to the pressure $P'(x_i, y_j)$ of each point. This quantity can be obtained from the equivalent of the operations table (Table 6-1). For example, for the case of a closed two-dimensional cavity with rigid walls on all sides that is divided up into M x N cells, the value of this denominator is equal to $-4\,[(M + N)/2 - 1]$.

6. The new value for $P'(x_i, y_j)$ is computed as the sum of the previous value plus the incremental change $\delta P'$. The first time this new value of $P'(x_i, y_j)$ is computed, it is the same as the increment $\delta P'$ at all points since the initial value for $P'(x_i, y_j)$ was zero from Step 3.

7. New values for the residual error terms, $F_{i,j}$, are computed following the procedures of Step 4.

8. For this step, it is most efficient to employ a Multiple Point Relaxation procedure where an increment $\delta P'_{(i,j)}$ is computed for each point x_i, y_j which has a residual error within a range of 25 to 100 percent of the maximum value found from Step 7.

9. Steps 6 to 8 are again repeated as necessary until a stable value for the modal amplitudes $P'(x_i, y_j)$ are obtained – that is, until the change from one step to another is very small relative to the overall magnitude. However, if the initial mode shape $P(x_i, y_j)$ was assumed to be a constant value (say, 100) at all points, then a more efficient iteration process involves use of a Block Relaxation step after several applications of the Multiple Point relaxation procedure.

Figure 6-4 illustrates how the error in eigenfrequency and mode shape decreases with the number of iterations for the case of a rectangular two-dimensional cavity with hard walls broken down into four equal quadrants, each made up of 6 x 4 cells. Figure 6-4a shows that the mode shape error decreases at a *relative* rate comparable to that for the eigenfrequency but that the absolute error for the latter is about 10 times less. For this figure, the 17 initial mode shapes, $P(x_i, y_j)$, are estimated by a very simple algorithm indicating an amplitude for the fundamental mode within each quadrant proportional to the quantity $[(i/N)\ (j/M)]^{1/2}$. This provided the correct trend in slope for the mode shape.

Figure 6-4b shows how the error in eigenfrequency decreases with the number of iterations when the initial modal amplitude was assumed to be a constant but using three different strategies for the number of Multiple Point relaxations employed before a Block relaxation was employed. (For the figure legend, application of each Block relaxation was considered as one step.) It is apparent that for almost any one of these techniques, the final error in eigen-frequency is less than 2 percent after about 20 iterations whereas this accuracy was achieved after only about 8 iterations when the more accurate estimate was made for the initial mode shape.

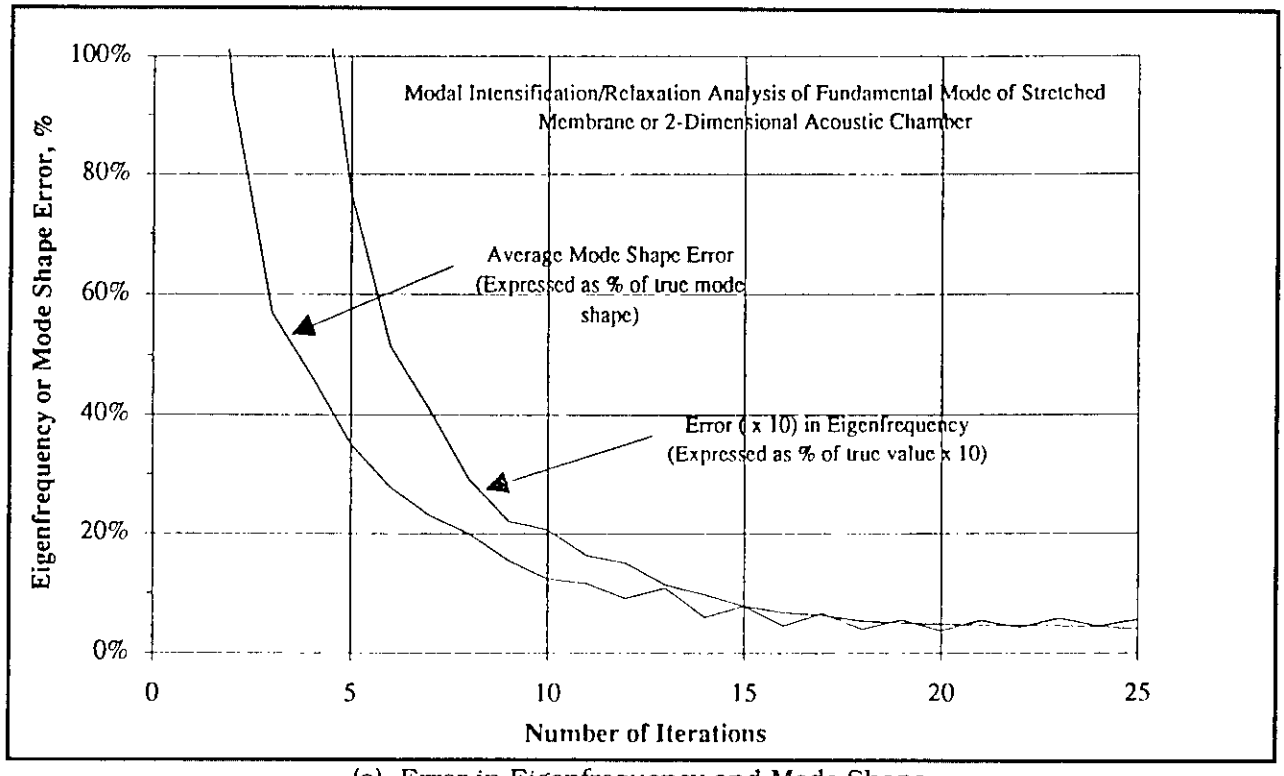

(a) Error in Eigenfrequency and Mode Shape.

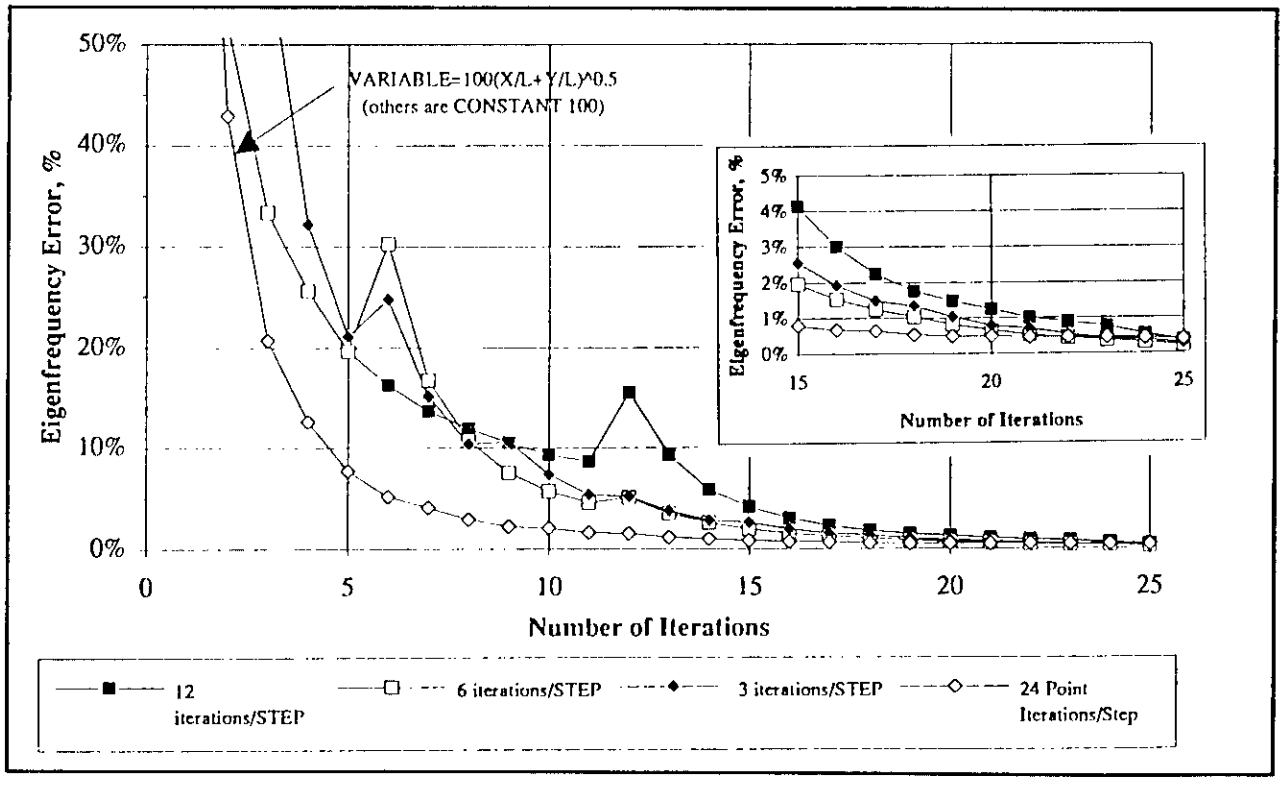

(b) Comparison of Different Multi-Point Relaxation Strategies.

Figure 6-4. Influence of Number of Iterations on Errors in Eigenfrequency and Mode Shape for Fundamental Mode of Two-Dimensional Rectangular Acoustic "Chamber" Using Modal Intensification Method.

6.3 Application of the Relaxation Method to Cylindrical Coordinates

For systems involving axial symmetry, such as axial flow compressors, etc., the Helmholtz equation to be used for analysis of acoustic resonance frequencies is given in two-dimensional cylindrical coordinates in the radial, r , and axial, z , directions by the following equation (the coordinates r and z are non-dimensional values having been normalized by a characteristic radius R)

$$\frac{d^2 P(r,z)}{dr^2} + \frac{1}{r}\frac{dP(r,z)}{dr} + \frac{d^2 P(r,z)}{dz^2} + (kR)^2 P(r,z) = 0 . \qquad (6\text{-}29)$$

Since this expression describes the two-dimensional field in the cylinder in a plane which contains the cylinder axis and any radius, this two-dimensional model of the cylindrical sound field can be broken down (for the most general case) into a network of rectangular finite element cells with dimensions $h_r \times h_z$. Then the FDA for the first three terms in this equation, at the point r_i, z_j , are given by the sum of approximations for the second and first derivatives in r plus an approximation for the second derivative in z or

$$FDA(r_i, z_j) = \left\{ \sum P(r_{i\pm1}, z_j) + (h_r/h_z)^2 \sum P(r_i, z_{j\pm1}) - 2\left[1 + (h_r/h_z)^2\right] P(r_i, z_j) \right.$$

$$\left. + (h_r/2r_i)\left[P(r_{i+1}, z_j) - P(r_{i-1}, z_j)\right] \right\} / h_r^2 \qquad (6\text{-}30)$$

where the designation $FDA(r_i, z_j)$ is used here to distinguish the FDA from the value for a rectilinear system. Note that this expression is essentially the same as Equation (6-25) for the rectilinear two-dimensional system except for the added approximation for the first derivative. Also, in this case, the actual values of h_r and h_z , non-dimensionalized by R , must be used since they do not appear to the same power in this equation.

To apply this expression to the Modal Intensification relaxation method, Equation (6-30) is used in Equations (6-26) and (6-27) in place of the $FDA(x_i, y_j)$ term for the residual error $F_{i,j}$ (for the i,j'th point) and for the eigenvalue, $(kR)^2$, respectively. The pressures $P'(x_i, y_j)$ and $P(x_i, y_j)$ are, of course, also changed to $P'(r_i, z_j)$ and $P(r_i, z_j)$.

6.4 Acoustic Resonances in Rectilinear and Cylindrical Cascades

With this general background on computation of acoustic resonance frequencies in any system, consider, now, some of the results of the experimental studies of the effect of these resonances on fluctuating pressures and structural vibration in cascade systems. The following summary statements are drawn from the conclusions stated in many of the papers listed in the references at the end of this chapter.

1. Acoustic resonances in cascades can be excited by wake shedding at frequencies for which the modal spacing is greater than the plate pitch as well as at modes for which the modes have node lines in the planes of the cascade plates.[5]

2. The lowest resonance frequency is controlled by the plate chord and the velocity of propagation along the cascade is approximately the velocity of sound.[5]

3. At higher resonance frequencies, the wavelength decreases faster than the increase in frequency indicating that the velocity of propagation along the cascade falls below the velocity of sound.[5]

4. In axial-flow compressors or fans with cylindrical geometry, the same sort of cascade resonance effects can occur in the annulus areas around the blades due to vortex shedding from the blades. The resonance frequencies may correspond to an integral number of wavelengths circumferentially around the annulus but may not relate to the number of blades. However, they are only excited if the acoustic resonance frequency is less than the value that would exist in the absence of any blades.[6] There is a well-defined minimum number of circumferential waves, for any given geometry, which propagate at approximately the speed of sound, but as the number of waves increases for higher-order modes, they can occur at nearly the same frequency leading to beating between closely adjacent modes.[7]

5. Resonances in axial flow compressors are more likely to occur in any one stage when there is a high temperature rise (corresponding to energy input) in that stage.[8]

6. Rotor blades can excite waves traveling backwards or forwards relative to the blade rotation but backward waves tend to dominate. Stationary blades can excite waves of the same frequency but traveling in opposite directions around the annulus.[7] A subsequent, more detailed study indicates a complex pattern for the type, predominance, and sensitivity to flow of different circumferential modes in an annular cascade.[6]

7. For an axial flow compressor with large spacing between blades, spinning acoustic modes can be generated by vortex shedding from stationary blades. The direction of spinning can be forward or backward (relative to the direction of the rotor) but for the system tested, higher sound levels occurred over a wide flow-velocity range for higher order forward-spinning modes (many wavelengths around the annulus). The relationship between acoustic resonance frequency and flow velocity was not significantly affected by rotor speed. Although significant rotor blade vibration did <u>not</u> occur at the structural resonance frequencies of the blades for the configuration tested, significant forced blade vibration did occur at frequencies given by $\omega_r = \omega_a - N\,\Omega$ where ω_a is the acoustic resonance frequency, N is the mode number, and Ω is the angular rotor speed.[9]

8. For axial flow compressors with multi-stage blading, the highest acoustic pressures occurred when the axial blade row spacing resulted in excitation at the same frequency as the vortex shedding frequency of the upstream blade row.[10]

9. Blades with thick trailing edges can excite resonances with peak pressures of the order of two times the dynamic pressure or $(0.5\rho V^2)$ where V is the *relative* flow velocity.[7] However, when compared to rounded trailing edges, blunt trailing edges exhibit a lower resonant response and a narrower range of velocities over which such resonances occur.[6]

10. Another study of resonance effects on aerofoils with blunt trailing edges indicates that predictions of unsteady aerofoil theory may help explain why such shapes can result in higher acoustic resonance responses (i.e., higher fluctuating pressures). This study also showed that a cavity

at the base of this trailing edge shape could minimize the resonance buildup by momentarily trapping each vortex and forcing some of the vorticity into the opposite shear layer where it is dissipated, thus reducing the energy input to the acoustic system.[11]

11. In certain ranges for the flow velocity in a cascade, the vortex shedding frequency will become synchronized with, or lock onto, the acoustic resonance frequency. This range is a function, among other things, of the trailing edge profile of the cascade plates or blades. A plate with a semi-circular trailing edge was found to result in the vortex shedding "locking on" to an acoustic resonance frequency that was either above or below the nominal vortex shedding frequency in the absence of the plates. For plates with a blunt trailing edge, the vortex shedding frequency only "locked up" to a higher acoustic resonance frequency. It was also observed that for semi-circular trailing edges, the shed vortex was less intense but this condition corresponded to more intense acoustic pressures at resonance.[12]

12. Vortex shedding from cascade blades occurs at all flow speeds with a frequency given approximately by a Strouhal Number of 0.2. However, the shedding is well correlated across the span of the trailing edge of the blade and hence can act as a strong source of sound or structural vibration only when the shedding frequency is close to an acoustic resonance frequency. The resonance amplification factor or "Q" of such resonances was observed to be of the order of 40 for one particular configuration. The resonance amplification was reduced by nearly a factor of 10 (or 19 dB) by adding small strips with a thickness about 20 percent of the blade thickness in a wavy pattern at the blade trailing wedge.[13] It can be expected that this behavior and the resonant Q will vary significantly with the geometry of the cascade system.

6.5 Quantitative Results for Analysis of Acoustic Resonances in Cascades

Parker[2.14] has shown that the acoustic resonance frequencies measured in rectilinear cascades corresponding to a finite stack of parallel plates are bounded by two curves as shown in Figure 6-5 for the first two modes for the type of cascade system illustrated earlier in Figure 6-1. The two classes of modes are designated by the mode numbers, (0,n) or (1,n). The first index, 0 or 1, represents the number of half-wavelengths in the acoustic field parallel to the flow along each plate. The second index, n, represents the number of waves in the direction normal to the flow. The curves are derived from analyses of resonances for an infinite stack of plates with a finite spacing. The upper bound for each pair is derived with the Modal Intensification method for the case of finite values for the plate spacing s . The lower bound is derived analytically for this ideal case when the stack spacing reduces to zero.[14] The experimental data points[15] fall between the two curves. The analytical expression which defines the lower bound curve in Figure 6-5 is[14]

$$C/(\lambda) = \left(\frac{f_c}{f}\right)\left\{\frac{m}{2} + \left(\frac{1}{\pi}\right)\arctan\left(\left[\left(\frac{f_c}{f}\right)^2 - 1\right]^{1/2}\right)\right\} \qquad (6\text{-}31)$$

where C = Chord length;
f = Resonance frequency = c/λ;
f_c = Plane wave resonance frequency = $c/2s$;
s = Plate spacing;
m = 0,1 for modes corresponding to β or α modes, respectively; and
c = Speed of sound.

As suggested in Item 11 in Section 6.4, the vortex-shedding frequency in a cascade is strongly influenced by the acoustic resonance frequency. The complex pattern for this behavior is shown in Figure 6-6 for several different conditions. For example, Figure 6-6a shows how the shedding frequency follows the expected Strouhal number relationship until this flow-induced frequency approaches the nominally fixed acoustic resonance frequency. Then the former "locks on" to the latter but increases slightly as flow velocity increases over a substantial range. Then, as flow velocity increases further, the shedding frequency may "jump" to the next higher acoustic resonance frequency (Figure 6-6b). Note that the slight increase in the vortex shedding frequency while it is "locked on" to the acoustic

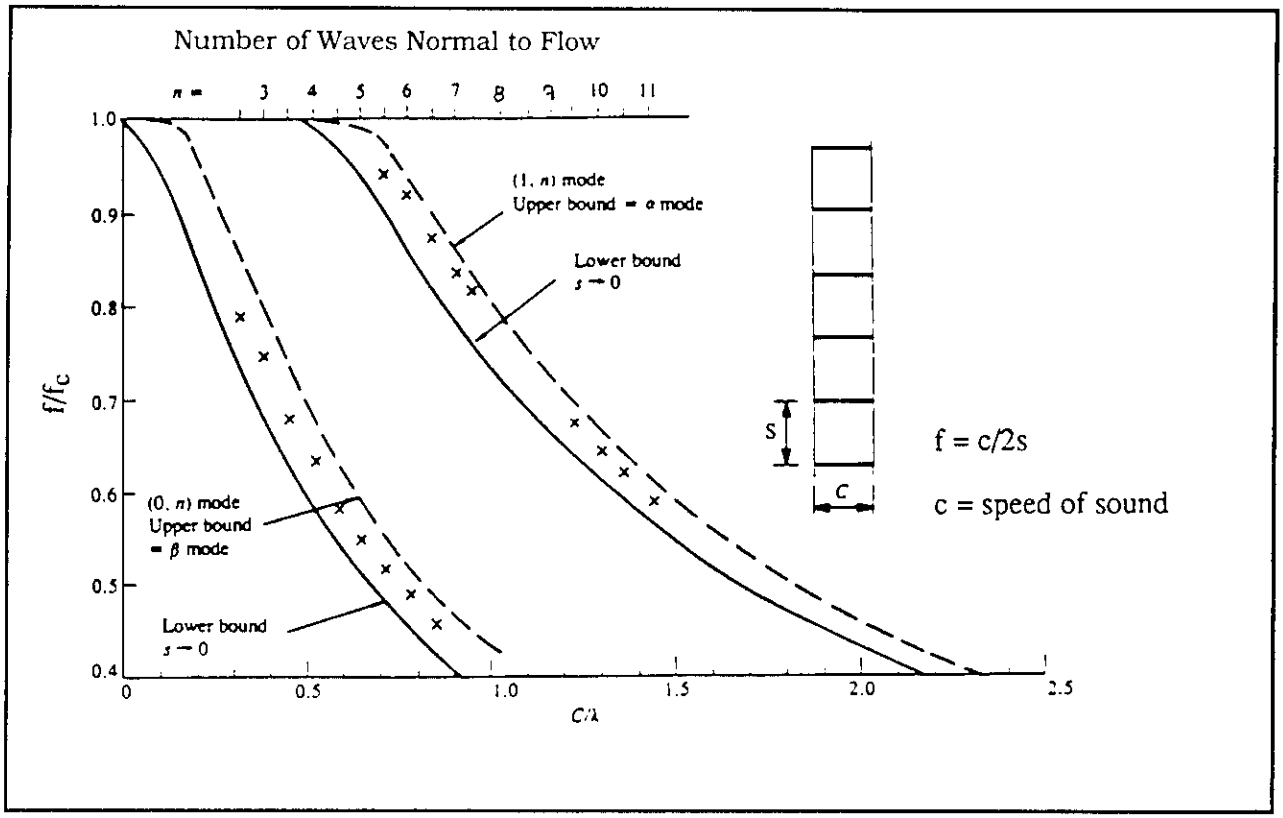

Figure 6-5. Frequency Ratios for the First Two Acoustic Models (α, β) of Flat Plate Cascades (x are points from Parker and Llewellyn,[15] figure from Parker and Stoneman[1]).

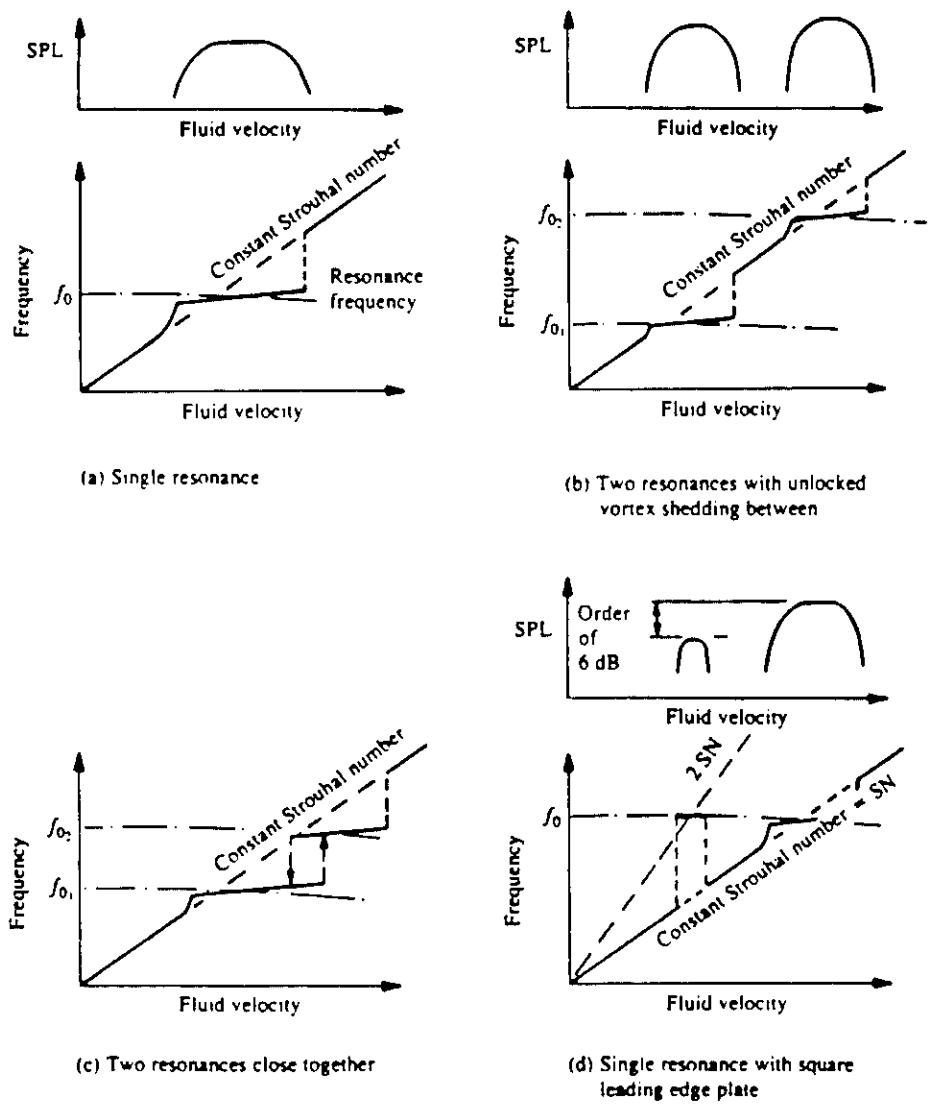

Figure 6-6. Typical Frequency/Amplitude/Velocity Relationship for Flow-Excited Resonances. (Reproduced from Parker and Stoneman.[1])

resonance frequency may simply reflect the expected increase in the latter as the effective speed of sound (equal to static sound speed plus flow velocity) increases with flow velocity. The other parts of Figure 6-6 show a similar behavior for other flow and vortex shedding conditions.

6.6 Structural Vibration Responses in Cascade Systems

Whenever significant structural vibration occurs in a cascade system, there are two resonance frequencies for each acoustic mode. The situation is illustrated by the computed results in Figure 6-7 for the case of a plate with zero damping. This figure and the following discussion are drawn from the summary in Parker and Stoneman.[1] The key parameters in the figure are: $\omega = 2\pi f$, the angular frequency of the actual vibroacoustic response; ω_p, the mechanical resonance frequency of the plate in a vacuum; ω_a, the acoustic resonance frequency with the plate replaced by a rigid boundary; and the resonance frequency, Ω, of the duct with the same axial acoustic modal distribution as in the regions upstream and downstream of the plate but with the plate removed (i.e., the empty duct frequency).

For the example in Figure 6-7, only one plate is involved and its cord length is assumed to be the same as the duct width. To illustrate how changes in the mechanical resonance frequency, ω_p, of the plate interact with the acoustic resonances, the former frequency was allowed to increase (representing an assumed increase in plate stiffness) to give a range for the ratio ω_p/Ω of 0.36 to 1.0.

Two conditions are considered to illustrate the general behavior: (1) $\omega_p < \Omega$, and (2) $\omega_p > \Omega$. For condition (1), if the flow velocity is such that vortex shedding excitation is just slightly below the plate natural frequency (i.e., Point 1 in the figure), the plate vibration is very strong because the plate and acoustic velocities are out of phase which results in a stronger, span-wise, more coherent vortex shedding process. In fact, for any significant vibration to occur in a cascade plate, the vortex shedding from the plate must be well correlated along its span. Thus this is the most critical condition to be avoided in a cascade system. On the other hand, for the same value of ω_p/Ω, if the vortex shedding excitation occurs at the acoustic resonance frequency ($\omega \approx \omega_a$), while strong acoustic pressures may occur, they will not be accompanied by large structural vibration responses of the plate.

For condition (2), with $\omega_p > \Omega$, structural vibration tends to be weakest if the vortex shedding excitation frequency is close to the plate resonance frequency but well above the acoustic modal frequency or $\omega_p > \omega_a$. (This is indicated as Region B in the figure.) On the other hand, stronger plate vibration may occur, along with a higher acoustic pressures if the vortex excitation frequency is close to the acoustic resonance frequency, or $\omega_a \approx \omega$ corresponding to Region D in the figure. However, this response decreases as the ratio ω_p/Ω approaches 1.0.

In the ω_p to ω_a transition region, where the absolute value of the difference $| \omega_p - \omega_a |$ is small, both the acoustic and structural responses tend to be large.

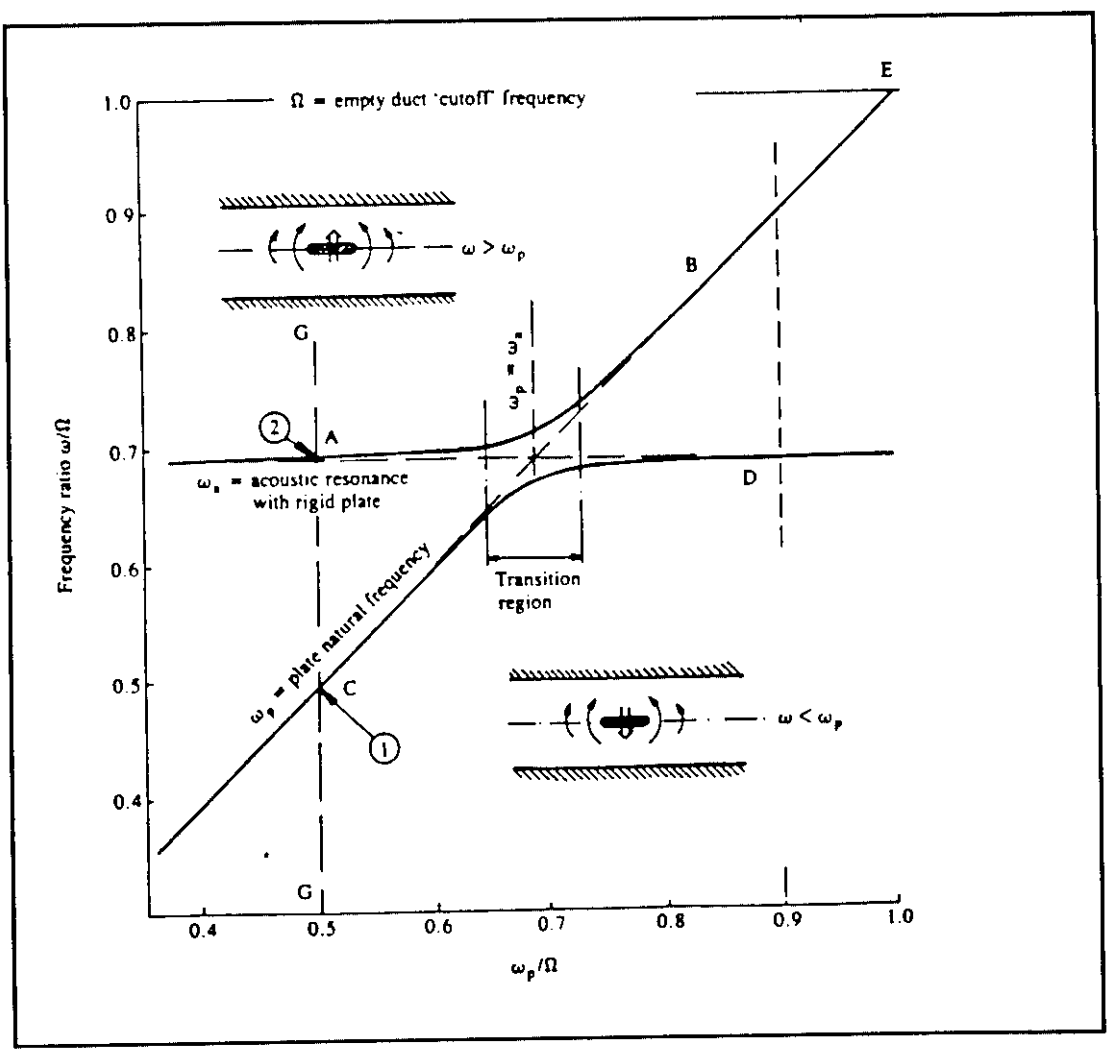

Figure 6-7. Frequencies of Acoustic Mode Combined With Plate Vibration – Single Plate Between Parallel Walls. (Reproduced from Parker and Stoneman.[1])

REFERENCES FOR CHAPTER SIX

1. Parker, R., and Stoneman, S.A.T., "The Excitation and Consequences of Acoustic Resonances in Enclosed Fluid Flow Around Solid Bodies," *Proc. Inst. Mech. Eng., 203*, March 1989.

2. Parker, R., "Resonant Effects in Wake Shedding From Parallel Plates: Calculation of Resonant Frequencies," *J. Sound Vib., 5*, 330-343, 1967.

3. Allen, D.N. deG., *Relaxation Methods*, McGraw Hill Book Co., London, 1954. LOC Cat.No 52-12349.

4. Kinsler, L.E., Frey, A.R., Coppens, A.B., and Sanders, J.V., *Fundamentals of Acoustics*, 3rd Edition, John Wiley and Sons, New York, 1982.

5. Parker, R., and Griffiths, W.M., "Low-Frequency Resonance Effects in Wake Shedding From Parallel Plates," *J. Sound Vib., 7*, 371-379, 1968.

6. Parker, R., and Pryce, D.C., "Wake-Excited Resonances in an Annular Cascade: An Experimental Investigation," *J. Sound Vib., 37*, 247-343, 1974.

7. Parker, R., "An Investigation of Acoustic Resonance Effects in an Axial Compressor Stage," *J. Sound Vib., 8*, 281-297, 1968.

8. Parker, R., "Acoustic Resonances and Blade Vibration in Axial Flow Compressors," *J. Sound Vib., 92*, 529-539, 1984.

9. Parker, R., and Stoneman, S.A.T., "An Experimental Investigation of the Generation and Consequences of Acoustic Waves in an Axial Flow Compressor: Large Axial Spacings Between Blade Rows," *J. Sound Vib., 99*, 169-192, 1985.

10. Parker, R., and Stoneman, S.A.T., "An Experimental Investigation of the Generation and Consequences of Acoustic Waves in an Axial Flow Compressor: The Effect of Variations in the Axial Spacings Between Blade Rows," *J. Sound Vib., 116*, 509-525, 1987.

11. Wood, C.J., "The Effect of Lateral Vibrations on Vortex Shedding From Blunt-Based Aerofoils," *J. Sound Vib.*, 91-102, 1971.

12. Welsh, M.C., Stokes, A.N., and Parker, R., "Flow-Resonant Sound Interaction in a Duct Containing a Plate: Part I, Semicircular Leading Edge," *J. Sound Vib., 95*, 305-323, 1984.

13. Cumpsty,. N.A., and Whitehead, D.S., "The Excitation of Acoustic Resonances by Vortex Shedding," *J. Sound Vib., 18*, 353-369, 1971.

14. Parker, R., "A Note on Frequency Ratios for Acoustic Resonances of Flat Plate Cascades With Plate Spacing Less Than Half the Longitudinal Wavelength," *J. Sound Vib., 86*, 594-596, 10 1983.

15. Parker, R., and Llewelyn, D., "Flow-Induced Vibration of Cantilever-Mounted Flat Plates in an Enclosed Passage: Experimental Investigation," *J. Sound Vib., 25*, 451-463, 1972.

PART II

FLOW-INDUCED EXCITATION MODELING

CHAPTER 7

STABILITY OF FREE SHEAR LAYERS

by Michael J. Lucas
Wyle Laboratories

Stability can be defined as the fluid quality of being immune to small disturbances in a flow. The decay of a disturbance – whether it is the subject of a mechanical, electrical, or hydrodynamic system – is the necessary condition for stability. Implicit to any of these systems is the amplification factor, the value of which determines the rate at which an infinitesimally small disturbance introduced will amplify or decay.

The basic equations used to examine the stability of fluid flows are a perturbed form of the Navier-Stokes equations. Since these equations take the form of non-linear partial differential equations, linearized approximations are made to reduce the system of equations so that progress towards understanding flow stability can be realized. The derivation and solutions of these equations are the subject of this chapter.

The importance of linear stability theory lies in the ability to predict the most unstable frequency of the disturbance. This frequency dominates the transition region between laminar and turbulent flow. The disturbance amplification rate, the respective wave number, and the Reynolds number at which the flow first becomes unstable are also determined using this technique.

A disturbance in an unstable flow may be represented in the form of a velocity, vorticity, or pressure fluctuation. In the initial stages, the disturbance grows with periodicity and amplification rate that often agrees well with linear stability theory. When the amplitude of the disturbance becomes sufficiently large, the flow deviates from purely two-dimensional form. In this region, the frequency content of the fluctuations may still exhibit a pronounced component at the most unstable frequency predicted on the basis of linear stability theory. Farther downstream, the eddies become increasingly more three-dimensional until they become random fluctuations and the flow is fully turbulent.

This chapter describes the basic mathematical formulations for stability theory, with emphasis on predicting wavelength between eddies and frequency of

production. Section 7.1 derives the equations for a disturbance in a flow field. These equations are the linearized form of the Bernoulli equation, the Orr-Sommerfield equation, and the Rayleigh equation. Section 7.2 presents the numerical solutions to the Rayleigh equations with emphasis on velocity profiles common to plane parallel mixing layers, jets, and wakes.

7.1 Stability of Two Parallel Streams

7.1.1 Linearized Bernoulli Equation

Shown in Figure 7-1 are two fluid streams, one beneath the other, having densities ρ_1 and ρ_2, moving parallel with flow velocities U_1 and U_2. The surface common to both fluids is plane and horizontal when undisturbed. The intermediate region between the streams is assumed to be infinitesimally thin.

The interest in this problem is to determine the conditions when the boundary separating the two fluids becomes unstable. This will be accomplished by superimposing a small oscillatory flow disturbance on the mean component of velocity which will allow the flow constituents such as velocity, pressure, and density to be decomposed into mean and fluctuating components.

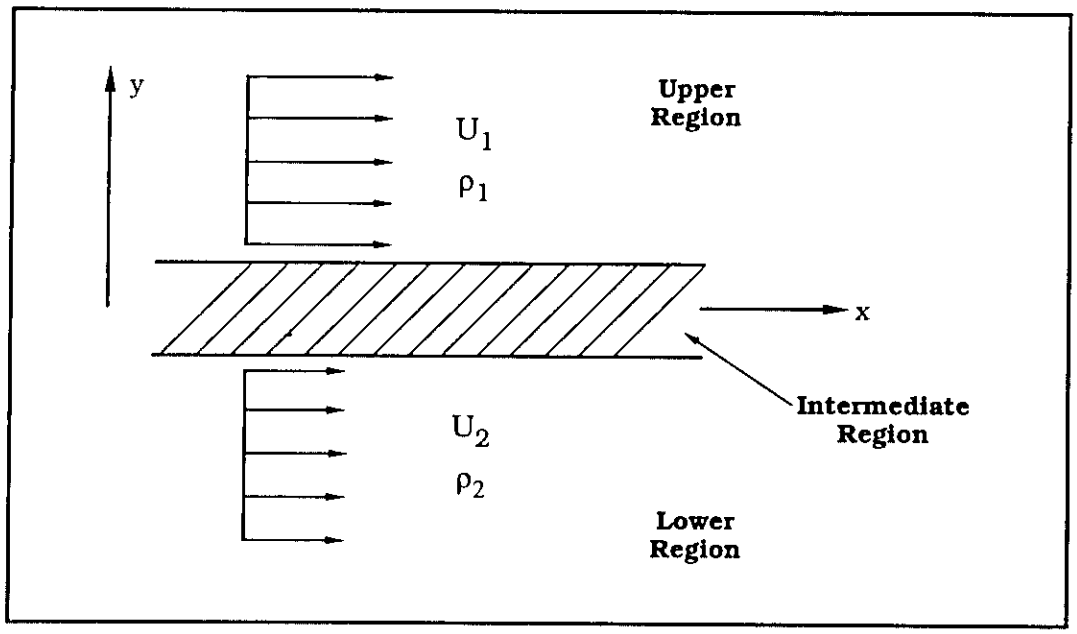

Figure 7-1. Two Adjacent Uniform Streams Moving in the Same Direction.

The general form of the unsteady Bernoulli equation is

$$\frac{p}{\rho} = \frac{\partial \phi}{\partial t} - \frac{q^2}{2} - g\,y, \tag{7-1}$$

where $q^2/2$ is the kinetic energy, $\phi\,(x,y,t)$ is the velocity potential, and g is the acceleration due to gravity. The horizontal and vertical components of the velocity potential are given by $u = \frac{\partial \phi}{\partial x}$ and $v = \frac{\partial \phi}{\partial y}$, respectively. This relationship holds throughout the entire field of irrotational flow of an incompressible fluid. Assuming parallel mean flows, the velocity potential and its components, the pressure, and the displacement can be expressed in terms of mean and fluctuating components as

$$\begin{aligned}
\phi\,(x,y,t) &= \bar{\phi}\,(x,y) + \tilde{\phi}\,(x,y,t), \\
u\,(x,y,t) &= \bar{U}\,(y) + \tilde{u}\,(x,y,t), \\
v\,(x,y,t) &= \tilde{v}\,(x,y,t), \\
p\,(x,y,t) &= \bar{P}\,(y) + \tilde{p}\,(x,y,t), \\
y &= \bar{y} + \tilde{y}.
\end{aligned} \tag{7-2}$$

The tilde, $(\tilde{})$, denotes the fluctuating component, and the bar, $(\bar{})$, signifies the mean quantity. Substituting these expressions for u, v, p into the Bernoulli equation; neglecting, by virtue of their smallness, higher-order terms such as $\tilde{u}^2$ or $\tilde{v}^2$; and subtracting the mean Bernoulli equation, the linearized Bernoulli equation

$$\frac{\tilde{p}}{\rho} = \frac{\partial \tilde{\phi}}{\partial t} + \bar{U}\,\frac{\partial \tilde{\phi}}{\partial x} - g\,\tilde{y} \tag{7-3}$$

is obtained. Referring to Figure 7-1, the fluctuating pressures at the top and bottom of the interface are equal, so that

$$\rho_1 \left\{ \frac{\partial \tilde{\phi}_1}{\partial t} + \bar{U}_1 \frac{\partial \tilde{\phi}_1}{\partial x} - g\,\tilde{h} \right\} = \rho_2 \left\{ \frac{\partial \tilde{\phi}_2}{\partial t} + \bar{U}_2 \frac{\partial \tilde{\phi}_2}{\partial x} - g\,\tilde{h} \right\}. \tag{7-4}$$

A second condition applied across the parallel stream interface is shown in Figure 7-2. V_n, is the velocity normal to the stream interface and can be described as

$$\theta = \tan^{-1} \left\{ \frac{\partial h}{\partial x} \right\}, \tag{7-5}$$

$$V_n = v \cos\theta - u \sin\theta, \tag{7-6}$$

$$\tilde{V} = \tilde{v} \cos\theta - (\bar{U} + \tilde{u}) \sin\theta, \tag{7-7}$$

where h is the interface vertical displacement. For small oscillations about a steady motion, θ is small and from Equation (7-7), $\tilde{V} \sim \tilde{v}$. The relationship between displacement and velocity at the upper and lower sides of the interface becomes

$$\tilde{v}_1 = \frac{\partial \tilde{h}}{\partial t} + \bar{U}_1 \frac{\partial \tilde{h}}{\partial x}, \tag{7-8a}$$

$$\tilde{v}_2 = \frac{\partial \tilde{h}}{\partial t} + \bar{U}_2 \frac{\partial \tilde{h}}{\partial x}, \tag{7-8b}$$

where $\tilde{h}(x,t)$ is the fluctuating amplitude of the displacement of the shear layer, and the fluctuating velocity is given by $\tilde{v}_1 = \frac{\partial \tilde{\phi}_1}{\partial y}$ and $\tilde{v}_2 = \frac{\partial \tilde{\phi}_2}{\partial y}$. The system of partial differential equations (Equations (7-4) and (7-8)) can be simplified by seeking a solution in terms of complex functions:

$$\tilde{h}(x,t) = \mathbf{h}\, e^{i\alpha(x-ct)}, \tag{7-9a}$$

$$\tilde{\phi}(x,y,t) = \phi(y)\, e^{i\alpha(x-ct)}, \tag{7-9b}$$

$$\phi_1(y) = \mathbf{A}_1\, e^{-\alpha y}, \tag{7-9c}$$

$$\phi_2(y) = \mathbf{A}_2\, e^{\alpha y}. \tag{7-9d}$$

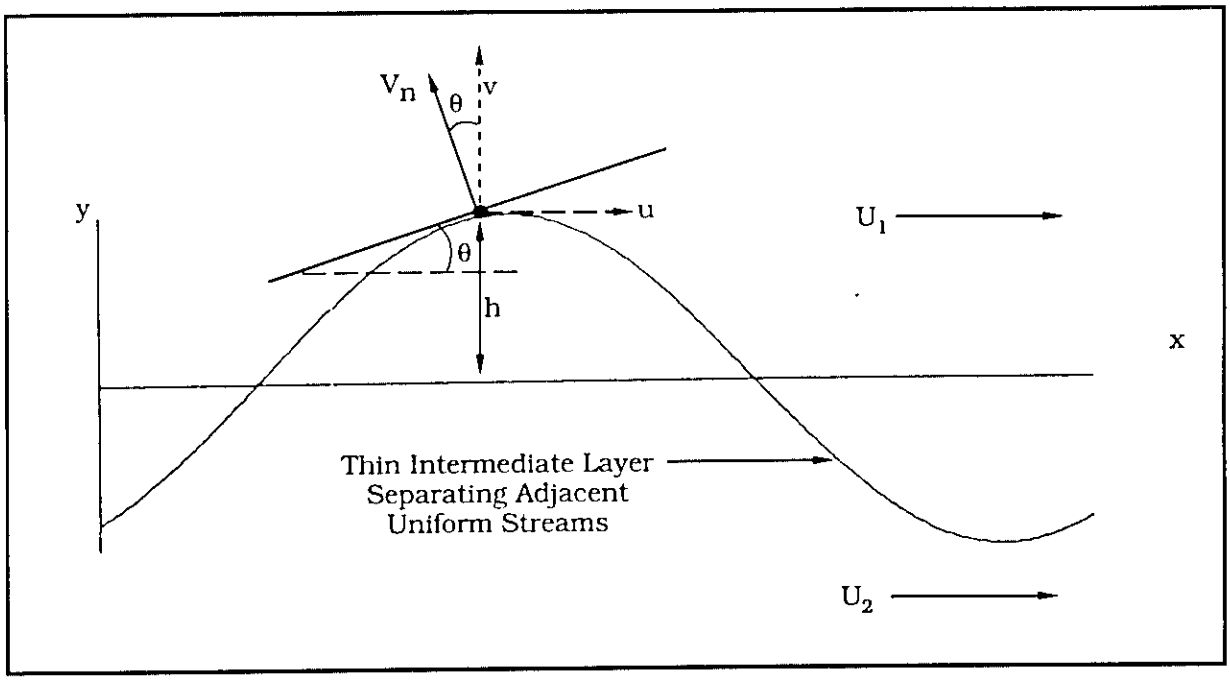

Figure 7-2. Consideration of Velocities Normal to the Interface.

The amplitude and phase information are the eigenvalues for this system. Here, ϕ, **h**, and **A** are complex amplitudes; α is the wave number and is equal to $2\pi/\lambda$. $\tilde{\phi}$ is the perturbation potential; $\tilde{\phi}_1$ and $\tilde{\phi}_2$ are the perturbation potential for the upper and lower streams, respectively. The quantity c is the speed at which the wave is moving in the x-direction

$$c = c_r + i\, c_i \tag{7-10}$$

where c_r is the wave speed of the oscillation and is directly related to the real part of the complex angular frequency, $\beta = \beta_r + i\,\beta_i$, through the wave number

$$\beta_r = 2\pi f = \alpha\, c_r . \tag{7-11}$$

The quantity c_i is called the disturbance amplification factor. The disturbance amplification depends on the values of c_i as follows:

$c_i < 0$ Disturbance Damped

$c_i = 0$ Neutral Disturbance

$c_i > 0$ Disturbance Amplified.

Substituting Equations (7-9) into Equations (7-4) and (7-8), after eliminating the complex amplitudes $\mathbf{h}$, $\boldsymbol{\phi}$, and $\mathbf{A}$, the complex velocity

$$c = \frac{\rho_1 \overline{U}_1 + \rho_2 \overline{U}_2}{\rho_1 + \rho_2} \pm \left[\frac{g}{\alpha} \frac{\rho_1 - \rho_2}{\rho_1 + \rho_2} - \frac{\rho_1 \rho_2}{(\rho_1 + \rho_2)^2} (\overline{U}_1 - \overline{U}_2)^2 \right]^{1/2} \tag{7-12}$$

is obtained. The first term on the right of the equal sign is the mean velocity of the two currents. The second term may be either real or imaginary. When the second term is real it represents the speed with which the wave is traveling relative to the mean velocity. This term is imaginary if

$$(\overline{U}_1 - \overline{U}_2)^2 > \frac{g}{\alpha} \frac{\rho_1^2 - \rho_2^2}{\rho_1 \rho_2}. \tag{7-13}$$

The stream interface stability is therefore dependent on the fluid velocities and the densities. If $\rho_1 = \rho_2$, Equation (7-12) reduces to

$$c = \frac{\overline{U}_1 + \overline{U}_2}{2} \pm i \left[\frac{\overline{U}_1 - \overline{U}_2}{2} \right] \tag{7-14}$$

and may be expressed as $c = c_r + i\, c_i$ where

$$c_r = \frac{\overline{U}_1 + \overline{U}_2}{2} \qquad \text{and} \qquad c_i = \pm \frac{\overline{U}_1 - \overline{U}_2}{2}. \tag{7-15}$$

7.1.2 Orr–Sommerfeld Equation

In the previous section a linearized form of the Bernoulli equation was solved to show the hydrodynamic instability of two uniform streams. The analysis disregarded details of the intermediate region between the streams, where rotational aspects must be considered. The discussion that follows treats this intermediate region in detail by basing unsteadiness predictions on the velocity profiles in the intermediate region.

The derivation begins with the Navier–Stokes equations for two-dimensional incompressible flow

$$\frac{\partial u}{\partial x} + \frac{\partial v}{\partial y} = 0, \tag{7-16}$$

$$\frac{\partial u}{\partial t} + u \frac{\partial u}{\partial x} + v \frac{\partial u}{\partial y} + \frac{1}{\rho} \frac{\partial p}{\partial x} = \nu \left\{ \frac{\partial^2 u}{\partial x^2} + \frac{\partial^2 u}{\partial y^2} \right\}, \tag{7-17}$$

$$\frac{\partial v}{\partial t} + u \frac{\partial v}{\partial x} + v \frac{\partial v}{\partial y} + \frac{1}{\rho} \frac{\partial p}{\partial y} = \nu \left\{ \frac{\partial^2 v}{\partial x^2} + \frac{\partial^2 v}{\partial y^2} \right\}, \tag{7-18}$$

where ν is the kinematic viscosity.

Consider, as before, a mean parallel flow in the x direction. A tilde is used to denote the fluctuating components and a bar signifies the steady mean quantity. For purposes of simplification, the mean component of u will be restricted to vary only with y and the mean component of p to vary only with x. This may be written as

$$u(x,y,t) = \overline{U}(y) + \tilde{u}(x,y,t), \tag{7-19}$$

$$v(x,y,t) = \tilde{v}(x,y,t), \tag{7-20}$$

$$p(x,y,t) = \overline{P}(x) + \tilde{p}(x,y,t). \tag{7-21}$$

Introducing these equations into the Navier–Stokes equations, the linearized equations for the disturbance become

$$\frac{\partial \tilde{u}}{\partial x} + \frac{\partial \tilde{v}}{\partial y} = 0, \tag{7-22}$$

$$\frac{\partial \tilde{u}}{\partial t} + \overline{U}\frac{\partial \tilde{u}}{\partial x} + \tilde{v}\frac{\partial \overline{U}}{\partial y} + \frac{1}{\rho}\frac{\partial \tilde{p}}{\partial x} = \nu \nabla^2 \tilde{u}, \tag{7-23}$$

$$\frac{\partial \tilde{v}}{\partial t} + \overline{U}\frac{\partial \tilde{v}}{\partial x} + \frac{1}{\rho}\frac{\partial \tilde{p}}{\partial y} = \nu \nabla^2 \tilde{v}. \tag{7-24}$$

These three equations have three unknowns: $\tilde{u}$, $\tilde{v}$, $\tilde{p}$. Pressure can be eliminated by subtracting Equation (7-23) from Equation (7-24), leaving two equations for $\tilde{u}$ and $\tilde{v}$. These two equations are reduced to an ordinary differential equation by seeking solutions of the type

$$\psi(x,y,t) = \Phi(y)\, e^{i\alpha(x-ct)} \tag{7-25}$$

where ψ is a complex stream function; Φ is a complex amplitude function that is assumed to depend only on y; and, as before, α and c are the wave number and wave speed, respectively. The stream function ψ represents an arbitrary two-dimensional disturbance that is a Fourier decomposition of partial oscillations.

Calculating the fluctuating velocity components $\tilde{u}$ and $\tilde{v}$ from the stream function

$$\tilde{u} = \frac{\partial \psi}{\partial y} = \frac{\partial\, \Phi(y)}{\partial y}\, e^{i\alpha(x-ct)}, \tag{7-26a}$$

$$\tilde{v} = -\frac{\partial \psi}{\partial x} = -i\alpha\, \Phi(y)\, e^{i\alpha(x-ct)}. \tag{7-26b}$$

Introducing these components into the linearized equations of motion, a fourth-order differential equation in terms of the amplitude, $\Phi(y)$ is derived

$$(\overline{U} - c)\ (\Phi'' - \alpha^2 \Phi)\ -\ \overline{U}''\ \Phi\ =\ -\frac{i}{\alpha\, Re}\ (\Phi'''' - 2\ \alpha^2\ \Phi'' + \alpha^4\ \Phi). \qquad (7\text{-}27)$$

Equation (7-27) is known as the Orr–Sommerfeld equation. The left-hand side of the equation contains the inertia terms, while the right-hand side contains the viscous terms.

The equation has been non-dimensionalized. All length dimensions have been divided by the boundary layer thickness, δ, or the momentum thickness, θ. The velocities have been divided by the maximum velocity U_m. The primes denote differentiation with respect to a dimensionless coordinate y/δ or y/θ, and

$$Re\ =\ \frac{\overline{U}_m\,\delta}{\nu} \qquad \text{or} \qquad Re\ =\ \frac{\overline{U}_m\,\theta}{\nu} \qquad (7\text{-}28)$$

are expressions for the Reynolds number.

7.1.3 Rayleigh's Equation

Since most applications in turbomachinery, the value of the Reynolds number is expected to be large, the right-hand side of Equation (7-27) can be omitted because of the smallness of the coefficient $1/Re$. In this case, the disturbance amplification is dominated by inviscid effects, and only the inertia terms on the left side of Equation (7-27) need to be considered. Equation (7-27) reduces to

$$\Phi''\ =\ \left(\frac{\overline{U}''}{\overline{U} - c}\ +\ \alpha^2\right)\Phi. \qquad (7\text{-}29)$$

This important equation governs the stability of parallel inviscid flows and was first obtained by Rayleigh. It is a drastic simplification from the Orr–Sommerfeld equation being a second-order ordinary differential equation as opposed to a fourth. To solve the Rayleigh equation, the mean velocity profile $\overline{U}(y)$ must be specified along with the appropriate boundary conditions. Numerical methods are normally used to determine the dependence of the eigenvalues, α and c, on the eigenfunction $\Phi(y)$.

7.1.4 General Properties of the Stability Equations

7.1.4.1 *Temporal and Spatial Stability*

The Orr-Sommerfield and the Rayleigh equations are both eigenvalue problems. Their solution requires specifying the mean velocity profile and the boundary conditions. When these conditions are furnished, the solution gives one eigenfunction $\Phi(y)$ and one complex eigenvalue α for each pair of values c and Re. These equations may also be solved to given one eigenfunction $\Phi(y)$ and one complex eigenvalue c for each pair of values α and Re.

Before proceeding with the solution, it must first be decided whether the growth of the disturbance will be followed as a function of time (see Figure 7-3) or space (see Figure 7-4). When c is complex and α is real, the growth of the disturbance is time dependent; when α is complex and c is real, the growth of the disturbance is spatially dependent. The simple relationships that hold for temporal and spatial systems are as follows.

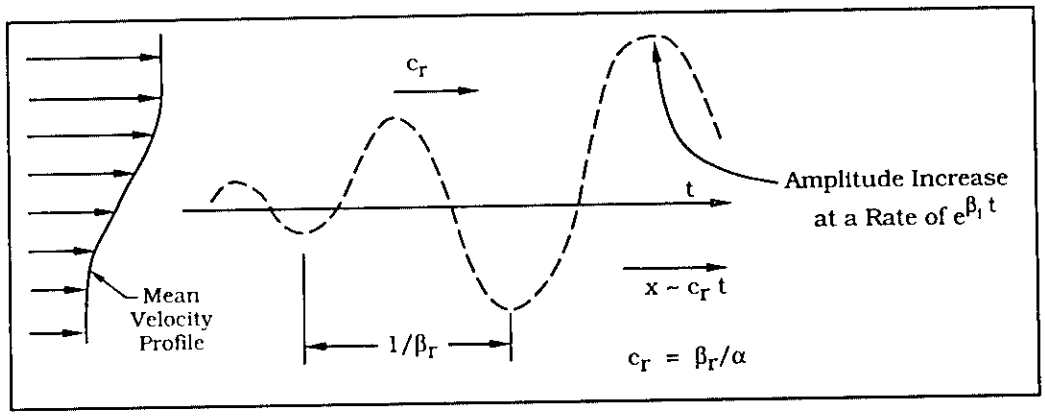

Figure 7-3. Illustration of Wave That Grows With Time.

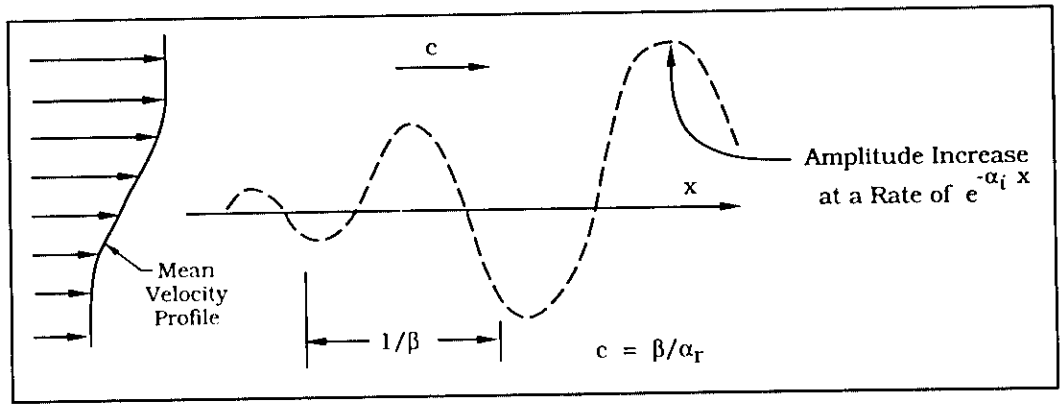

Figure 7-4. Illustration of Wave That Grows With Spatial Position.

If c is complex and α is real,

$$\psi(x, y, t) = \Phi(y)\ e^{i\alpha(x-ct)}, \tag{7-30a}$$

$$\psi(x, y, t) = \Phi(y)\ e^{(i\alpha x - i\alpha\, c_r\, t - i^2\, \alpha\, c_i\, t)}, \tag{7-30b}$$

$$\psi(x, y, t) = \Phi(y)\ e^{\alpha\, c_i\, t}\ e^{i\,(\alpha x - \alpha\, c_r\, t)}, \tag{7-30c}$$

where $(\ )_r$ and $(\ )_i$ denote real and imaginary parts, respectively. If $\beta = \alpha c$, then

$$\psi(x, y, t) = \Phi\,(y)\ e^{\beta_i\, t}\ \ e^{i\,(\alpha x - \beta_r\, t)}, \tag{7-30d}$$

the real part of which is

$$\psi_r = e^{\beta_i\, t}\ [\,\Phi_r\,(y)\ \cos\,(\alpha\, x - \beta_r\, t)\ -\ \Phi_i\,(y)\ \sin\,(\alpha\, x - \beta_r\, t)\,]\ . \tag{7-31}$$

For spatial amplification:

$$\psi(x, y, t) = \Phi(y)\ e^{(i\,\alpha_r\, x\, +\, i^2\,\alpha_i\, x\, -\, i\beta t)}, \tag{7-32a}$$

$$\psi(x, y, t) = \Phi(y)\ e^{-\alpha_i\, x}\ \ e^{i\,(\,\alpha_r\, x\, -\, \beta t)}, \tag{7-32b}$$

the real part of which is

$$\psi_r = e^{-\alpha_i\, x}\,[\Phi_r\,(y)\ \cos\,(\alpha_r\, x - \beta t)\ -\ \Phi_i\,(y)\ \sin\,(\alpha_r\, x - \beta t)]\ . \tag{7-33}$$

In the temporal description the wave travels in the x-direction with a speed c_r and grows with time in accordance with the amplification rate of $\beta_i > 0$. In the spatial description, the wave grows with x and it is amplified when $\alpha_i < 0$.

Gaster[1] made theoretical comparisons between temporal and spatial theory. His findings showed that the two viewpoints are not identical. However, for weak amplification rates, when

$$c_i \ll c_r \qquad \text{or} \qquad \alpha_i \ll \alpha_r$$

a transformation is possible by the group velocity

$$\frac{\alpha_r\, c_i\,(T)}{U_{Group}\,(T)} = \alpha_i\,(S)\ . \tag{7-34}$$

Here the real and imaginary parts are denoted by the subscripts r and i while the spatial and temporal parameters are symbolized using an S and T. U_{Group} is the speed at which wave packets travel and is defined as

$$U_{Group} = \partial\, \beta_r\ /\ \partial\alpha_r \tag{7-35}$$

This transformation is often used to make comparisons between temporal and spatial calculations, but it is limited to small amplifications. In the case of parallel flows, where there are large disturbances, Gaster demonstrated that spatial stability theory more accurately represents the disturbance amplification in a flow. Consequently, when comparing theoretical versus experimental disturbance growth rates, favorable agreement is obtained with spatial stability predictions.

7.1.4.2 *Streamwise Amplification and Frequency Selection*

Figure 7-5 illustrates the basic features of turbulent transition for a plane mixing layer. Figure 7-5(a) shows two parallel streams of unequal velocity that are brought together to form a thin shear layer. As shown in the figure, the shear layer undergoes vertical undulations that are characterized initially by an exponential amplification of the fundamental frequency component β_0 along streamwise coordinates. This rapid amplified growth is shown on Figure 7-5(b) as a straight line on a semi-log coordinate graph. The exponential growth in the disturbance was shown previously via stability theory to grow either in space or time and had a corresponding slope of either β_i or α_i.

As the disturbance continues to amplify in the streamwise direction, the amplitude increases until there is a departure from the linear growth. This departure is seen in Figure 7-5(b) as a decrease in amplitude in the streamwise direction. The deviation from linear growth occurs when the disturbance amplitude is approximately 0.2 to 0.3 of the free-stream velocity. The transition region that follows is highly non-linear; successive vortices coalesce with one another or divide into smaller vortical structures. The spectral content of the non-linear region shows an energy exchange occurring between the fundamental component and its harmonics.

For any unstable shear layer there is a non-linear growth region where the growth of the fundamental disturbance component has saturated, and harmonics of the fundamental evolve at a linear rate (Figure 7-5(b)). At a distance well into the non-linear region, the disturbance amplitude of these harmonic components increases to a point where they dominate, thereby transferring the energy from the fundamental to its harmonics. If the fundamental frequency is β_0, then in these types of problems there is often a subharmonic frequency $\beta_0/2$ that is directly related to the coalescence of two vortical pairs. This half tone might hypothetically add or subtract to integer harmonics to produce a frequency spectrum that looks like Figure 7-5(c).

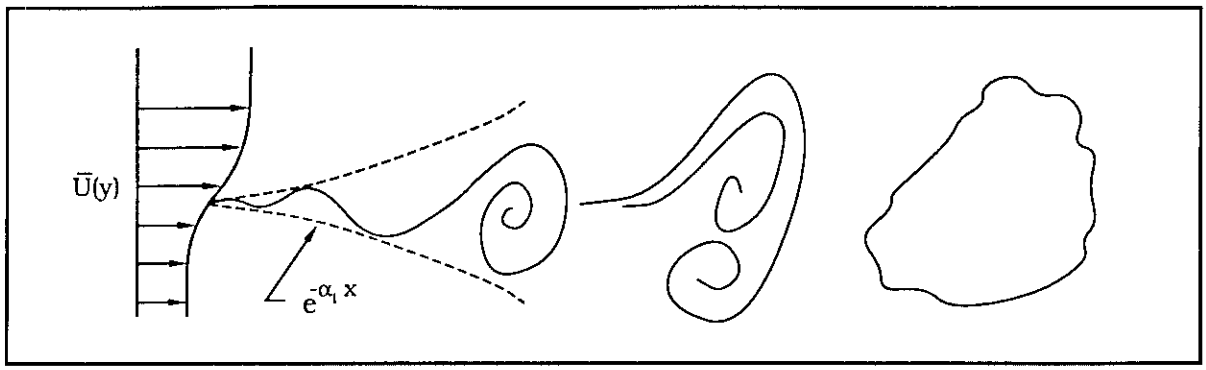

(a) Schematic Illustrating Essential Features.

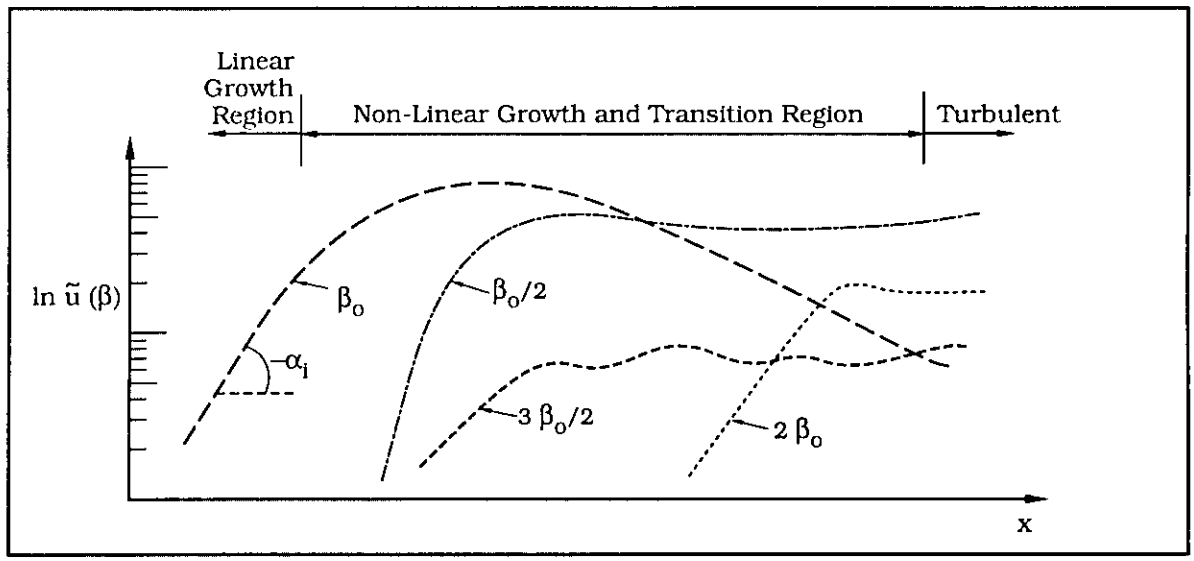

(b) Streamwise Disturbance Growth Rates.

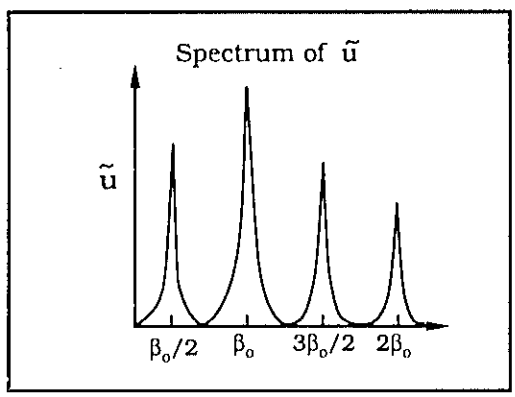

(c) Frequency Spectra.

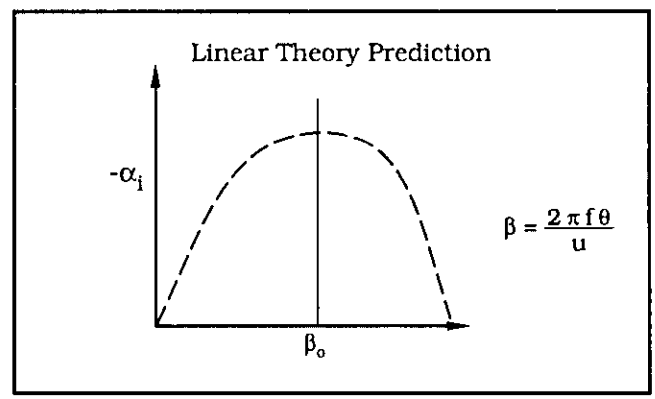

(d) Amplification Features as Predicted by Stability Theory (Rayleigh Equation).

Figure 7-5. Plane Mixing Layer.

The frequency which will produce the most rapid amplified disturbance is the primary disturbance frequency β_0. This is determined by solving the Rayleigh equation for a specified velocity distribution. Solutions to the Rayleigh equation (Figure 7-5(d)) show the dependence of disturbance amplification rate versus non-dimensional frequency. Our interest in this figure is the disturbance frequency that corresponds to the largest amplification factor.

The most unstable frequency of a free shear layer is dependent upon two parameters: the mean velocity distribution, $\bar{U}(y)$, and the momentum thickness θ. The mean velocity profile experiences substantial changes from the point at which two parallel streams meet, to the point at which the flow is fully turbulent. It is traditional when making linear stability calculations to base the mean velocity profile on one which is fully developed. A fully developed profile corresponds to a point far enough downstream that linear growth has ended. The validity of this approximation rests on the fact that the downstream unsteadiness in a shear layer acts as a dominant upstream influence in the sensitive region at separation where initial unsteadiness begins. Frequency selection at the point of separation is then coupled by a pressure feedback to downstream unsteadiness.

The momentum thickness, θ, is normally estimated based on the local shear layer thickness at some representative location downstream of the separation point. The proper choice of the momentum thickness is often unclear and presents difficulties when making predictions of the fundamental frequency using stability theory.

Consider, for example, a splitter plate or nozzle. At distances sufficiently far downstream, the momentum thickness of a wake or fully developed jet remains constant. This can be verified using simple control volume theory. In the region immediately downstream of the nozzle edge, however, where the mean streamlines are not straight and parallel, and/or the jet has a top-hat velocity distribution with thin shear layers, the momentum thickness will tend to increase, perhaps 20 to 30 percent, or more, to its equilibrium, fully established value. On the other hand, for the case of mixing layer, there is no equivalent conservation concept and the momentum thickness increases continuously in the downstream direction. When applying these concepts, the momentum thickness of a jet is typically based on the orifice half-width; while for a free shear layer the momentum thickness is calculated at the midpoint in the linear growth region.

7.2 Predictions for Free Shear Layers

Not until the early 1960s was it possible, through the use of digital computers, to economically evaluate the eigenvalues and eigenfunctions from the linearized stability equations for realistic mean velocity profiles. Michalke[2] was one of the first to demonstrate the power of using instability analysis for predicting the disturbance growth rates in mixing layer types of flows.

Shortly thereafter, linear stability calculations were made for other parallel flow problems. Most of these works fall into three main categories: mixing layers, jets, and wakes. This section describes the most notable solutions and shows how these calculations can be used in predicting the fundamental disturbance frequency to a free shear layer.

Table 7-1 is a collection of solutions to the Rayleigh equation. The left column shows the mean velocity profiles U(y) used to solve the Rayleigh equation. The right column shows the corresponding eigenvalue solutions. The solutions to the first two profiles assume temporal instability, whereas the remaining profiles use a spatial stability approach. The remainder of this chapter, Sections 7.2.1 through 7.2.4, address each of the velocity profiles shown in Table 7-1.

7.2.1 Discontinuous and Piecewise Linear Profiles

The discontinuous profile shown in Table 7-1(a) was described by Helmholtz in 1868.[3] The two streams are parallel and are considered to be separated by a vortex sheet of zero thickness. In the adjoining figure, an infinitesimal disturbance α grows at the rate $e^{\alpha c_i t}$. The stability criteria derived in Section 7.1.1 and included in the table show that when the density of the fluids is the same, the shear layer is unstable at all wavelengths.

The piecewise linear profile shown in Table 7-1(b) is closer to the smooth profile to be expected in an actual fully developed shear flow. Rayleigh[4] calculated the growth rate of the amplified disturbance as a function of the disturbance wave number. This shear layer is most sensitive to disturbance amplification when $\alpha = 0.4$.

Table 7-1

Solutions to the Rayleigh Equation for Six Mean Velocity Profiles

Mean Velocity Profile	Solution to the Rayleigh Equation
(a) Discontinuous (Reference 5) 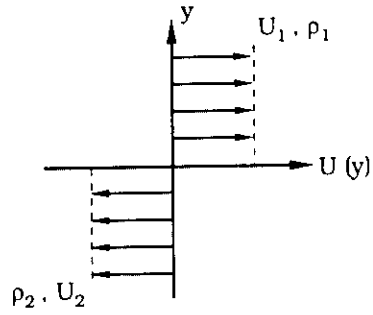	$y \geq 0 \quad u = U_1$ $y < 0 \quad u = U_2$ 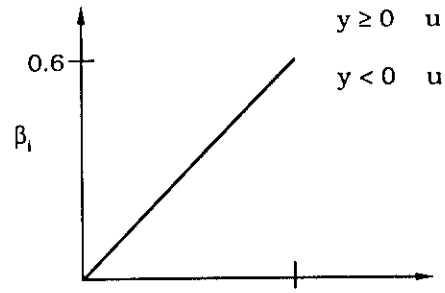 $\alpha = \frac{2\pi\theta}{\lambda}$
(b) Piecewise Linear (Reference 5) 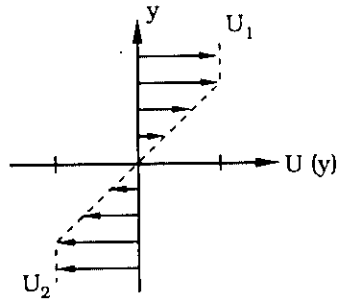	$y > 1 \quad u = U$ $1 \leq y \leq -1 \quad u = Uy$ $y < 1 \quad u = -U$ 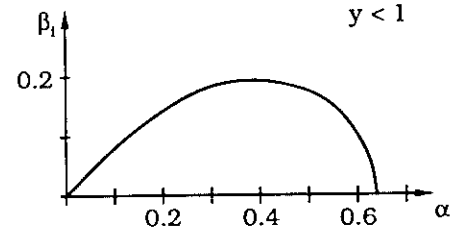 $\alpha = \frac{2\pi\theta}{\lambda}$
(c) Hyperbolic Tangent (Reference 7) 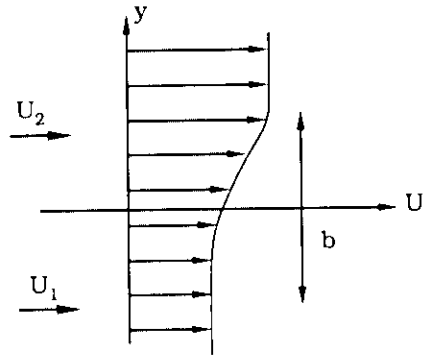	$\Delta = \frac{U_1 - U_2}{U_1 + U_2}$ $U(y, \Delta) = 1 + \Delta \tanh(y/2)$ 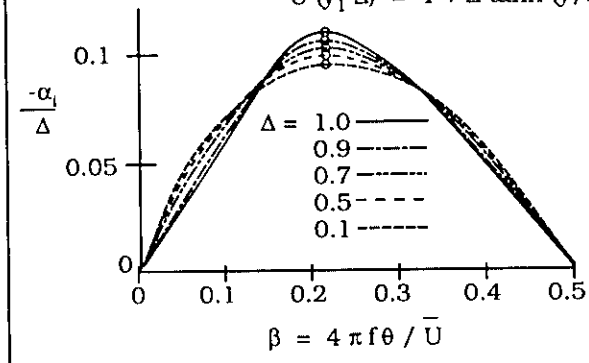

Table 7-1 (Continued)

Mean Velocity Profile	Linear Stability Theory
(d) Jet, Planar (Reference 10) 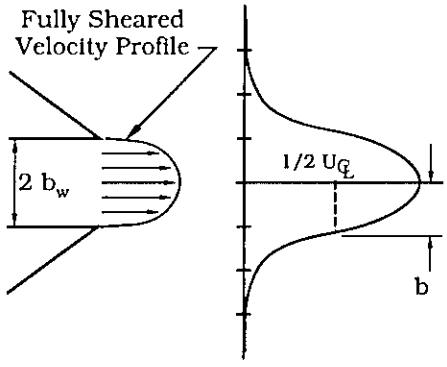 $b \simeq b_w$	$U(y) = \left[1 + sk_1 y^2 \left(\frac{2 - y^2 - y^4}{1 + k_1 y^6} \right) \right] \text{sech}^2 (ay)$ 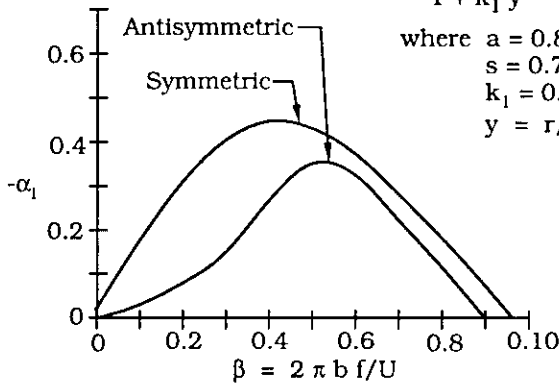 where a = 0.88136, s = 0.70, k_1 = 0.1977, and y = r/b_w
(e) Jet, Axisymmetric (Refs. 11,12) 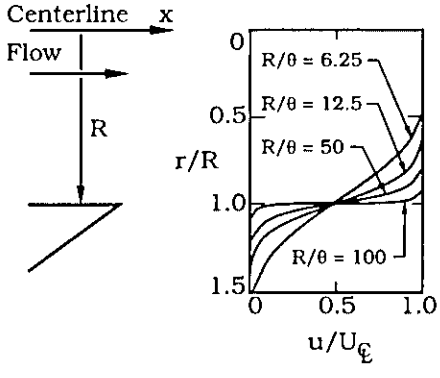	Axisymmetric Mode Lowest Order $U(r) = 0.5 \{ 1 + \tanh [b_2 (R/r - r/R)] \}$, where $b_2 = 0.25\ R/\theta$. 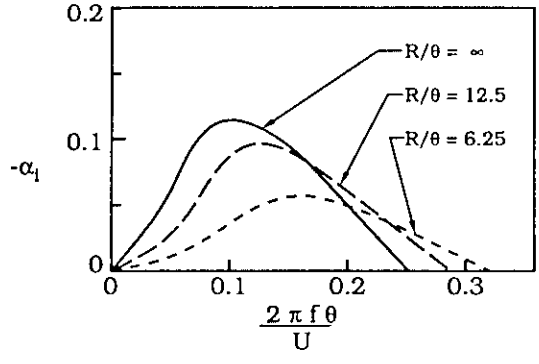
(f) Wake (Reference 13) 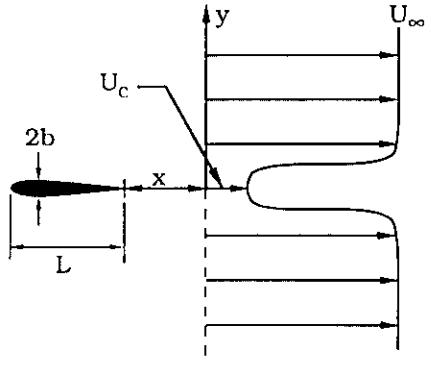	$\frac{U - U_\infty}{U_c - U_\infty} = \text{sech}^2 (\sigma Y)$ $Y = y/\beta$ $\beta_r = \frac{2 \pi f b}{U_\infty}$

	x/L	0.003	0.02	0.05	0.15	0.30
	U_c/U_∞	0.0012	0.0532	0.1290	0.308	0.440
Sym-metric	$-\alpha_i$	0.700	1.000	0.411	0.202	0.130
	α_r	1.090	1.000	0.994	0.900	0.887
	β	0.492	0.520	0.550	0.600	0.650
Anti-Sym-metric	$-\alpha_i$	0.110	0.095	0.078	0.049	0.034
	α_r	0.398	0.399	0.406	0.447	0.459
	β	0.110	0.125	0.150	0.225	0.275

7.2.2 Hyperbolic Tangent Profile

In the case of a hyperbolic tangent profile, the amplification factor predicted by spatial stability theory is based upon the dimensionless velocity ratio $\Delta = (U_1 - U_2)/(U_2 + U_1)$ across the two flows. When $\Delta = 0$, the upper and lower velocity are equal and there is no shear, the flow reduces to a wake. If $\Delta = 1$, there is shear due to the movement of the upper stream against a stationary lower stream.

The amplification factor $-\alpha_i$ versus normalized frequency is plotted for selected values of Δ in Table 7-1(c). The circles indicate the point on the curve where there is maximum amplification. It is seen here that for all values of Δ, the value of β ranges between $0.21 \leq \beta \leq 0.225$ for maximum amplification. The maximum amplification rate increases approximately linearly with Δ, and the associated phase velocity is equal to the average velocity of the two streams.

Many flow geometries can be modeled using a hyperbolic tangent profile. The three most common are backward facing steps, cavities, and jets. In real flow situations it is difficult to estimate the shear layer momentum thickness. Ideally the momentum thickness is measured at a distance downstream from the point of separation which corresponds to the middle of the linear growth region. This is often approximated for these geometries by computing the momentum thickness at the point of separation based on the boundary layer profile. Figure 8-4 in Chapter 8 suggests a technique to predict the spreading rate and, in turn, the momentum thickness for a plane mixing layer. These techniques are useful when estimating the frequency shifting that will occur when vortices pair and merge.

As an example, consider flow over a cavity for which the value for Δ is equal to 1. From Table 7-1(c), the non-dimensional frequency corresponding to the maximum amplification rate is

$$\beta = \frac{4\pi\theta f}{\overline{U}} = 0.21 \tag{7-36}$$

so that the Strouhal number is

$$St = \frac{f\theta}{\overline{U}} = 0.017 \tag{7-37}$$

This can be compared to the experimental work of DeMetz and Farabee,[6] who determined that, for a laminar boundary layer preceding a cavity, the resonance frequency corresponds to St = 0.022 which was valid for circular and rectangular openings.

7.2.3 Jet Profiles

In the case of jets, two kinds of instabilities exist: one that is associated with the thin shear layer lip instability and the other that is associated with the efflux as a whole. The former is termed the shear layer mode, and the latter is commonly referred to as the preferred mode. The emphasis in this section is on the shear layer lip instability. Table 7-2 summarizes the different methods used to estimate the shear layer modes. For a discussion on the preferred mode of instability, see Section 8.1 or Reference 8.

Table 7-2

Jet Matrix, A Survey Using
Methods Derived From Linear Stability Theory

Jet Type	**Flow Velocity Profile**	
	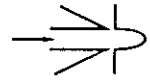 **Fully Developed**	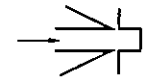 **Top-Hat Shaped**
Planar	**Table 7-1(d)**	**Table 7-1(c)**
Axisymmetric	**Table 7-1(e)**	**Table 7-1(e)**

7.2.3.1 *Planar Jet Profiles*

Shown in Table 7-1(d) are the results to Sato's velocity profile[9] for a plane parallel jet profile. The solution assumes the flow is "quasi-parallel", which means that the ratio of the axial component of velocity is much greater than its vertical component. The non-dimensional frequency appearing in the figure is based on the shear layer half-width, b, which often is approximated using the nozzle half-width, b_w.

The two curves drawn in the figure illustrate, for the symmetric and anti-symmetric disturbances, the variation of the disturbance growth rate as a function of non-dimensional frequency. Symmetric disturbances are often called varicose instabilities and antisymmetric disturbances are called sinuous instabilities. Anti-symmetric disturbances occur in most practical situations and have a distinctive sinuous or sinewave-like form. The antisymmetric disturbance has a non-dimensional frequency of 0.52 at maximum amplification.

When the jet stream near the nozzle exit is top-hat shaped with thin shear layers, the frequency of the lip instability can be estimated using the results from a mixing layer (see Table 7-1 c). In such a situation, the streamlines are no longer parallel. The shape of the instability wave and the mean velocity profile will vary with streamwise distance. The momentum thickness, θ, will increase by 20 to 30 percent, or perhaps even more, until it reaches its equilibrium, fully established value. The momentum thickness used in these cases is determined at the point of separation from the nozzle lip. This value can be estimated by performing a boundary layer calculation that begins at the entrance to the nozzle. The momentum thickness is evaluated at the point where the boundary layer separates from the nozzle lip.

7.2.3.2 *Axisymmetric Jets*

Experimental measurements made in circular jets indicate that the vortices generated near the nozzle exit are initially axisymmetric, but that the disturbance of higher-order helical modes increases significantly farther downstream. Shown in Table 7-1(e) are solutions to the axisymmetric mode made by Michalke for the circular jet. This is the lowest-order mode. To the left of the figure are the velocity profiles for selected R/θ coditions. θ is the initial momentum thickness and is evaluated at the nozzle exit. The ratio of R/θ is a measure of the radius of

the nozzle relative to the boundary layer thickness and its value determines the maximum amplification frequency. For example, when the velocity profile is a thin shear layer, R/θ is infinite. From Table 7-1(e) it is found that the Strouhal number ($f\theta/U$) has a value of 0.017. This value is identical to the mixing layer when $\Delta = 1$.

When the velocity profile is fully developed, such as downstream from the potential core, the jet stream can only support higher-order spinning modes. Results to higher-order modes can be found in References 11 and 12.

The effect of compressibility in a circular jet is shown in Figure 7-6. The stability equation is solved for two profiles: $R/\theta = 100$ and $R/\theta = 6.25$. It is seen here that irrespective of the jet mode, compressibility has the effect of lowering the most unstable frequency and amplification factor with increasing Mach number. The shifting effect just described is not nearly as severe for $R/\theta = 100$ as it is when $R/\theta = 6.25$.

7.2.4 Wake Profiles

There are two classes of wake flows: those from thin, streamlined, trailing-edges and those from bluff bodies. In the former case, the disturbances grow in a fashion similar to mixing layers and jets. The growth of the instability is due to the inflection points in the mean velocity profile that are characteristic to thin shear layers. In the latter case, the mean velocity profile has a very deep deficit that may even be reversed in the near wake region. There will be large-scale separations behind the bluff body for which a classical example is the flow behind a circular cylinder. However, farther downstream from a bluff body, the mean velocity profile has a form similar to the thin trailing edge and one can apply the techniques which are to be described herein.

A major share of wake flows encountered inside turbomachinery will be of bluff body types. In turbomachinery, turbine blades tend to be relatively thick and have been observed to produce a von Karman vortex sheet, even at extremely high Reynolds numbers. Fan blades from a compressor or supercharger are relatively thin and will produce wakes that are more typical of those from streamlined bodies. In this section, results from Mattingly and Criminale[13] are presented for streamlined bodies. Chapter 9 describes techniques to estimate the frequency from bluff bodies of different geometries and from tube banks.

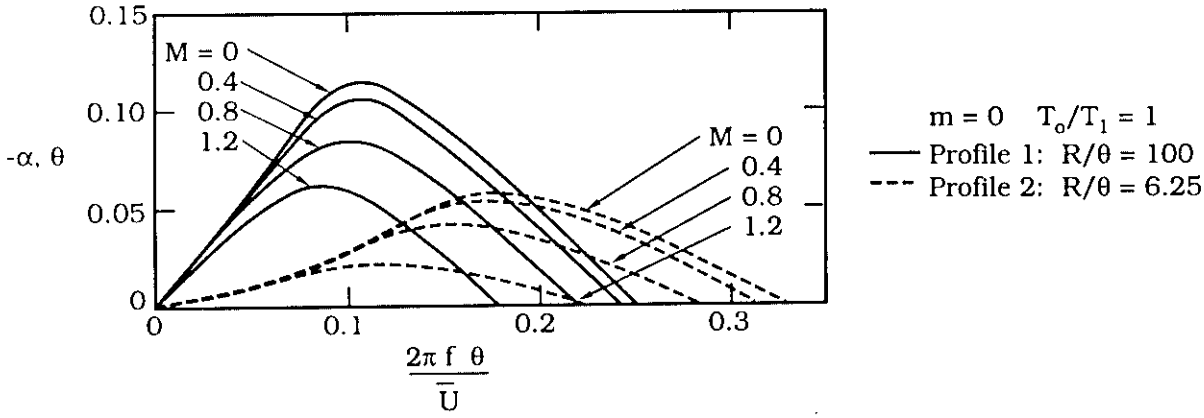

(a) Axisymmetric Mode

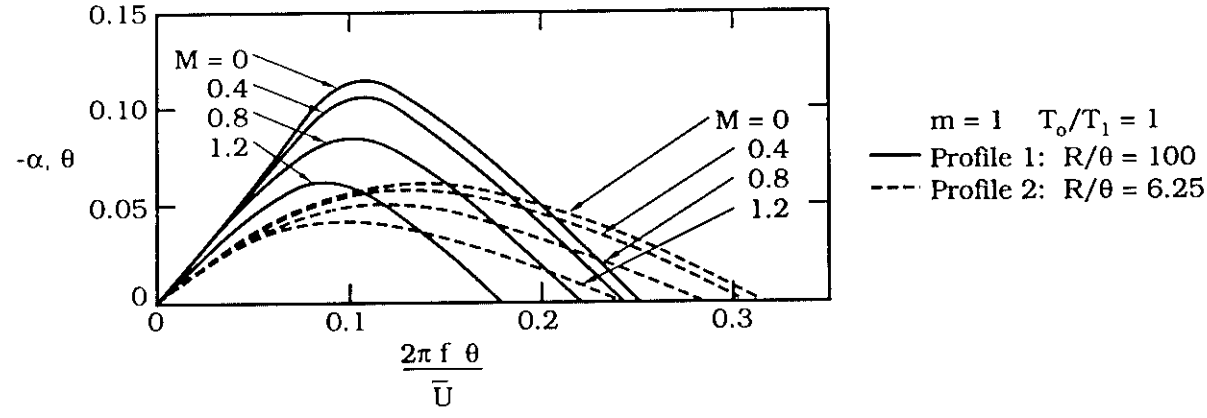

(b) First Azimuthal Mode, Helical Instabilities

Figure 7-6. The Effect of Compressibility in a Circular Jet.
(Reproduced from Michalke.[11])

The results of Mattingly and Criminale[13] are shown in Table 7-1(f). Their wake was generated using a NACA 0003 symmetric airfoil having a cord length denoted by L and a thickness of 2b. The velocity profile has been non-dimensionalized with respect to the centerline velocity and is shown to collapse at selected downstream coordinates onto itself. Knowing the dependence of the centerline velocity on downstream coordinates, successive calculations may be made using different mean velocity profiles to determine the variation of the eigenfunction and eigenvalues with downstream coordinates. This procedure is necessary to account for the continuous changes of the mean velocity profile in the formation region.

The wake may operate either as a symmetric or antisymmetric disturbance. The two disturbance modes are treated in the solution through the boundary conditions for the vertical component of velocity along the wake centerline. Experimental measurements show that naturally amplified disturbances in the wake are of the symmetric kind.

Table 7-1(f) lists the eigenvalue results at successive wake stations. It is seen in the table that the frequency monotonically increases with downstream coordinates for both disturbance types. The amplification factor for all wake stations is consistently larger for the symmetrical disturbances than for the anti-symmetric disturbance. Thus the symmetrical disturbances are the most highly amplified according to the linearized stability analysis. Averaging over the wake region investigated and accounting for a wave propagation phenomenon that produces a frequency shift in the eigenvalues, the maximum spatial amplification is one for which

$$\beta = \frac{2\pi fb}{U_\infty} = 0.55 \quad \text{and} \quad \alpha_r = \frac{2\pi\theta}{\lambda} = 0.994\,. \tag{7-38}$$

As an example, the non-dimensional frequency for a wake behind a cylinder is

$$\beta = \frac{2\pi f(D/2)}{U} = 0.55\,, \tag{7-39}$$

with a corresponding Strouhal number of

$$St = \frac{f2b}{U} = \frac{\beta}{\pi} = 0.18. \tag{7-40}$$

In Chapter 9 it is shown experimentally that when the distance between the shear layers, measured at the end of the formation region, is used to calculate the Strouhal number, the Strouhal number equals 0.18 and is independent of the body shape.

REFERENCES FOR CHAPTER 7

1. Gaster, M., "A Note on the Relation Between Temporally Increasing and Spatially Increasing Disturbances in Hydrodynamic Stability", *J. Fluid Mech., 14*, 1962, 222-224.

2. Michalke, A., "On the Inviscid Instability of the Hyperbolic Tangent Velocity Profile", *J. Fluid Mech., 19*, 1964, 543-556.

3. Helmholtz, H., "Monatsbericht, Königl. Akad. Wiss.", Berlin, pp. 215-228. See also, Helmholtz, H., l.c. ante, p. 22.

4. Rayleigh, L., "On the Stability of Certain Fluid Motions", *Proc. Math. Soc. London, 11*, 1880, 57, and *19*, 1987, 67. See also, "On the Stability and Instability of Certain Fluid Motions", *Scientific Papers*, Cambridge University Press, Vol. I, 1880, p. 474-487; "On the Stability and Instability of Certain Fluid Motions, Part II", *Scientific Papers*, Cambridge University Press, Vol. III, p. 2-23; "On the Stability and Instability of Certain Fluid Motions, Part III", *Scientific Papers*, Cambridge University Press, Vol. IV, 1895, p. 203-209; "On the Stability of the Laminar Motion of an Inviscid Fluid", *Scientific Papers*, Cambridge University Press, Vol. VI, 1813, 197-204; and "Further Remarks on the Stability of Viscous Fluid Motion", *Scientific Papers*, Cambridge University Press, Vol. VI, 1914, p. 266-275.

5. Esch, R., "The Instability of a Shear Layer Between Two Parallel Streams", *J. Fluid Mech., 3*, 1957, 289-303.

6. DeMetz, F.C., and Farabee, T.M., "Laminar and Turbulent Shear Flow-Induced Cavity Resonances", AIAA Paper 77-1293, 1977.

7. Monewitz, P.A., and Huerre, P., "Influence of the Velocity Ratio on the Spatial Instability of Mixing Layers", American Institute of Physics, *Physics of Fluids*, 25 (7), July 1982, 1137-1143.

8. Ho, C., and Huerre, P., "Perturbed Free-Shear Layers", *Annual Review of Fluid Mechanics*, 1984, 365-424.

9. Sato, H., "The Stability and Transition of a Two-Dimensional Jet", *J. Fluid Mech., 7*, 1960, 53-80.

10. Baja, A.K., and Gary, V.K., "Linear Stability of Jet Flows", Transactions of the ASME, *J. Applied Mech., 44*, 378-384.

11. Michalke, A., "Instabilität eines Kompressiblen runden Freistrahls unter Berücksichtigung des Einflosses der Strahlgrenzschichtdicke", *Z. Flugwiss, 19*, 1971, 319-328.

12. Michalke, A., "Survey on Jet Instability Theory", *Prog. Aerospace Sci., 21*, 159-199.

13. Mattingly, G.E., and Criminale, W.O., "The Stability of an Incompressible Two-Dimensional Wake", *J. Fluid Mech., 51*, 1972, 233-272.

CHAPTER 8

JETS

by Michael J. Lucas
Wyle Laboratories

The two basic forms of a nozzle are circular and planar. Nozzles can be either long and smoothly tapered or short in length, possibly terminated with a knife-edge orifice. A nozzle that is well formed to avoid flow separation from inside the nozzle may have a velocity profile at the exit that is fully sheared, while a short nozzle with an abrupt termination may have a thin shear velocity profile that is fully turbulent. The shape of the nozzle ultimately determines the character of the mean velocity profile at the nozzle exit, the downstream development of vortex structure, and the amount of flow noise generated.

In this chapter, procedures to predict the most amplified frequencies are described for the circular and rectangular jets. In most situations, turbomachinery jet nozzles are <u>not</u> well formed and have large Reynolds numbers, producing a velocity profile at the nozzle exit that is thin shear. For this reason, this chapter appropriately limits the discussion to thin shear velocity profiles.

Section 8.1 describes the procedures for estimating the most amplified frequencies in a planar and axisymmetric jet. Sections 8.2 and 8.3 contain relationships for sizing the jet potential core and for calculating the vortex merging locations. In some cases, the jet stream inside turbomachinery will interact with other engine components. The procedure described in Sections 8.2 and 8.3 are used for evaluating this condition. Section 8.4 contains a sample calculation.

8.1 Shear Layer and Preferred Instability Modes

Thin shear layers originating from the nozzle lips form an instability wave that rolls up into coherent structures that merge and are convected downstream. The process of successive vortex merging leads to the shear layer spreading and lowering of the vortex passage frequency. Several vortex mergings occur between the nozzle and the end of the potential core. Farther downstream, these vortices become large-scale structures producing perturbations that can feedback to the trailing edge. It is these large-scale vortex structures that are characteristic of

the *column mode* of instability f_p. The vortices that roll up at the nozzle lip are characteristic of the *shear layer mode* f_n.

The *shear layer mode* with instability frequencies designated as f_n has a length scale of θ which denotes the thickness of the shear layer. The *preferred mode* or *column mode* with instability frequencies f_p has a length scale of D or w which denotes the diameter of the axisymmetric nozzle or the width of the planar nozzle, respectively.

To estimate f_n for a thin shear velocity profile, use the following Strouhal number

$$St = \frac{f_n \theta}{U_m} = 0.017, \tag{8-1}$$

where f_n is the most amplified frequency and is sometimes called the shear layer mode frequency, θ is the initial momentum thickness, and U_m is the mean velocity measured at the jet exit. The initial momentum thickness θ is proportional to $U_m^{-1/2}$ and hence

$$f_n \propto U_m^{3/2}. \tag{8-2}$$

Measurements of unsteady velocity (see Table 8-1) at the nozzle exit confirmed the 3/2 power dependence of shear layer mode on free-stream velocity but indicated a stepwise variation of the frequency with the jet exit velocity. The initial Strouhal number derived from these experiments showed some degree of scatter. Possible causes for the scatter are probe interference, the level of turbulence contaminating the air supply, and the jet nozzle configuration.

The preferred mode measured for a circular jet in air is shown in Table 8-2. The dimensionless frequency for the preferred mode is found to vary between 0.25 and 0.5, depending on the experiment. More recent experiments have shown that the preferred Strouhal number is dependent on the initial momentum thickness at low jet velocities, as shown in Figure 8-1 for both circular and planar jets. For high flow rates, the Strouhal number for the circular jet becomes constant and equal to 0.44 and for the planar jet equal to 0.25. Presently, there is no satisfactory explanation for the Strouhal number remaining constant above a critical value. The important feature to realize is the preferred mode is present even though the boundary layer from the nozzle lip may be turbulent at separation and is incapable of undergoing successive vortex merging characteristics of the thin shear layer.

Table 8-1

Shear Layer Mode Measured For Planar and Circular Jet in Air
(Reproduced from Gutmark and Ho[12])

Authors	Jet Type	$St = f_n \theta / U_m$
Sato[1]	Planar	0.012–0.017
Michalke[2]	Theoretical Prediction Planar	0.0165
Browand[3]	Planar	0.013
Miksad[4]	Planar	0.017
Pfisenmaier[5]	Planar	0.0128
Hussain and Zaman[6]	Planar	0.012
Freymuth[7]	Axisymmetric	0.018
Michalke[8]	Axisymmetric	0.009
Davies and Baxter[9]	Axisymmetric	0.014
Husain and Hussain[10]	Axisymmetric	0.017
Drubka[11]	Axisymmetric	0.013

Table 8-2

Preferred Mode Measured for Circular Jet in Air
(Reproduced from Gutmark and Ho[12])

Authors	D_j (cm)	U_m (m/sec)	Mach Number, M	$St = f_p D_j / U_m$	Probe Location, X/D_j	Re x 10^4
Bechert & Pfizenmaier[13]	4.0	204	0.6	0.48	Far Field	50
Chen[14]	5.7	67	0.2	0.35	3.3	26
Crowe & Champagne[15]	5.0	31	0.09	0.3	4.0	10
Fuchs[16]	10.0	40	0.12	0.5	3.0	24
Ko & Davies[17]	2.5 & 5.0	6 to 100	0.02 to 0.3	0.3 to 0.5	1.5 & 4.0	3 to 30
Moore[18]	0.39	102 to 307	0.2 to 0.9	0.35 to 0.5	Far Field	25 to 75
Peterson[19]	2.5	30	0.09	0.25 to 0.4	4.0	5
Yule[20]	5	2 to 64	0.01 to 0.18	0.3 to 0.45	4.0	0.7 to 20

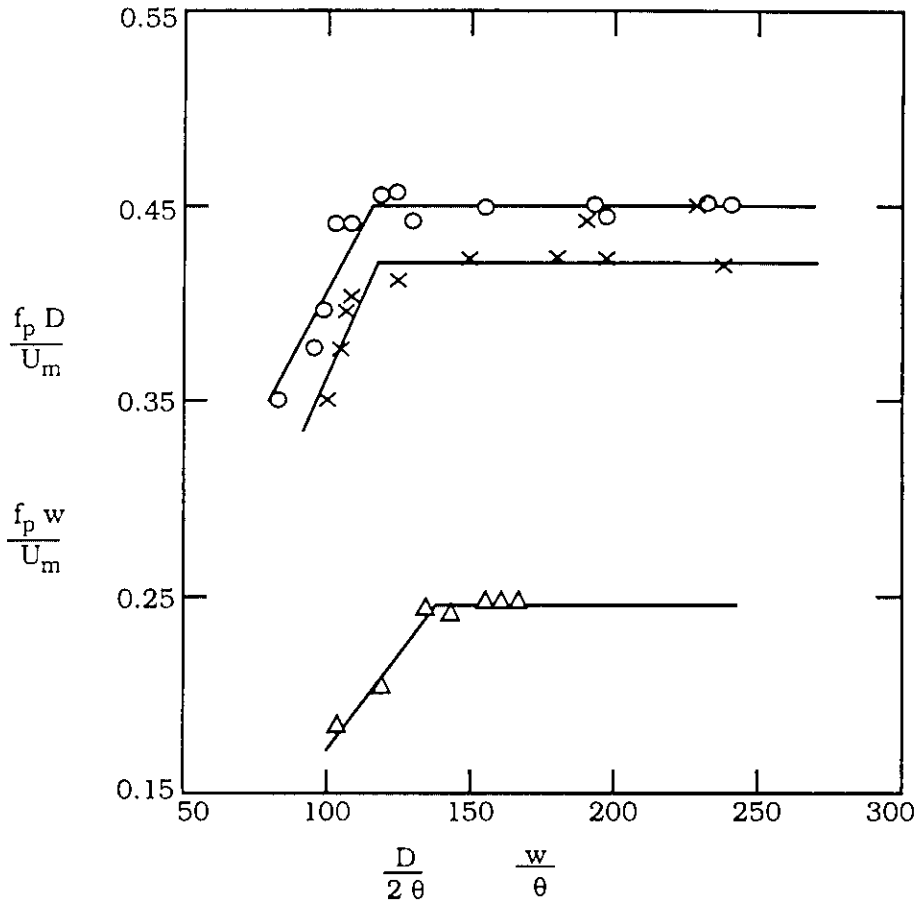

Figure 8-1. Strouhal Number of Preferred Mode in Jets Versus Characteristic Length Ratio.

Axisymmetric Jets: ○ Kibens[21] (1981);
× Drubka[22] (1981);
Planar Jets: △ Ho & Hsiao[23] (1983).

(Reproduced From Ho & Huerre.[24])

Figure 8-2 shows the range of Strouhal numbers obtainable from an axisymmetric jet. The shaded region, as before, represents the preferred mode. The curve $St = 0.0156 \sqrt{Re}$ shows the expected vortex formation frequency due to the shear layer mode. It represents the upper limit in Strouhal numbers and corresponds to the shortest wavelength of the jet. Thus the region bounded by the shear layer mode and the preferred mode forms an envelope of possible Strouhal numbers for a circular jet.

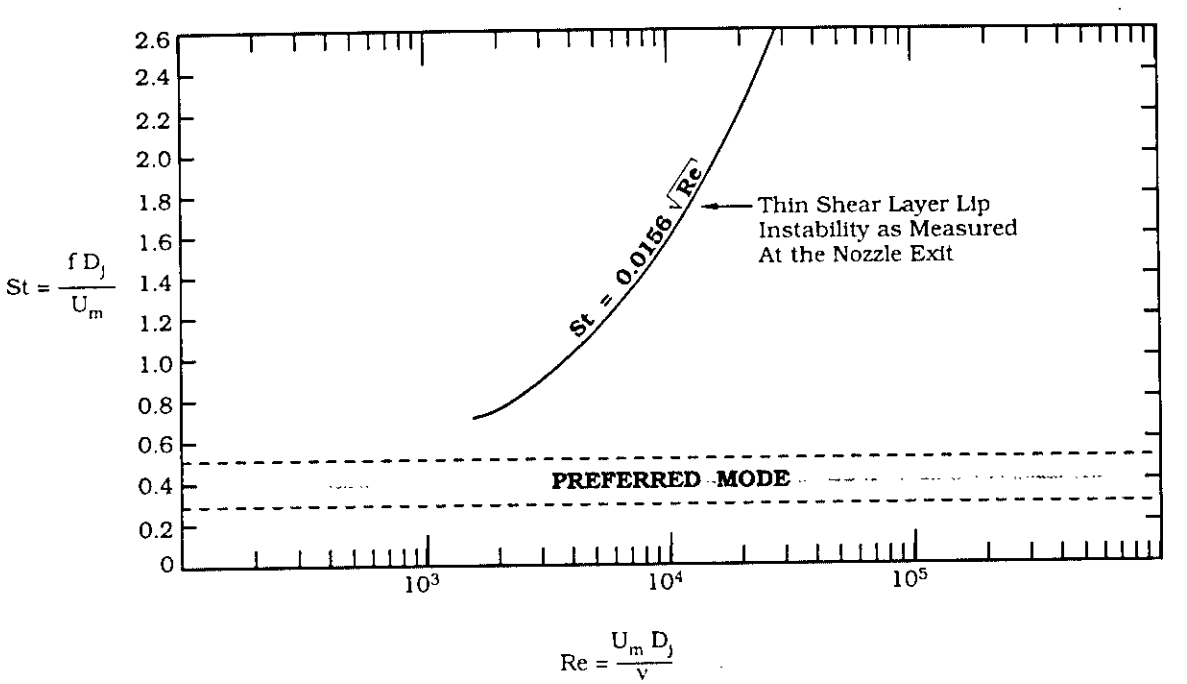

Figure 8-2. Strouhal Numbers in an Axisymmetric Jet.
(Reproduced from Blake.[25])

8.2 Potential Core Dimensions

Depicted in Figure 8-3 is a turbulent jet spreading in a medium that has a free-stream velocity. The two fluids are assumed parallel and the boundary layer thickness at the nozzle exit is assumed negligible in comparison to the orifice diameter D_j. The jet is shown here to have a uniform velocity U_1 that expands into an adjoining media with a free-stream velocity of U_2. Using nomenclature consistent with Abramovich,[26] the ratio of U_2 to U_1 is

$$m = U_2/U_1 . \tag{8-3}$$

When $m = 0$ the jet expands into a medium that is at rest.

In Figure 8-3b, Lines 01 are a boundary that defines the region of constant longitudinal velocity U_1. This region is the potential core. Inside the core there is no transverse component of velocity. Line 02 defines the line of constant longitudinal velocity, U_2. The mixing layer (hyperbolic tangent) velocity profile, discussed earlier in Chapter 7, is bounded between lines 01 and 02.

The shear layer thickness, b, increases proportionally with the location of the free-stream along the x-direction, X, beginning at the nozzle lip, i.e.,

$$b = \pm \tau X \left(\frac{1-m}{1+m}\right). \tag{8-4}$$

The proportionality factor τ is an experimental constant that varies between the limits of 0.15 and 0.3; smaller values of τ are used when U_1 and U_2 are moving in the same direction. Larger values of τ are used when U_1 and U_2 move in opposite directions.

Equation (8-4) may be written as

$$b = \pm \tau X \Delta , \tag{8-5}$$

where Δ is the dimensionless velocity ratio

$$\Delta = \frac{U_1 - U_2}{U_1 + U_2}. \tag{8-6}$$

The minus sign in Equations (8-4) and (8-5) is used when the free-stream velocity is greater than the jet velocity ($m > 1$). For a hyperbolic tangent profile, the momentum thickness θ is exactly equal to one-fourth the shear layer thickness ($b = 4\theta$). Thus the value of θ, like b, increases linearly with x. From Equation (8-5), θ can then be expressed as

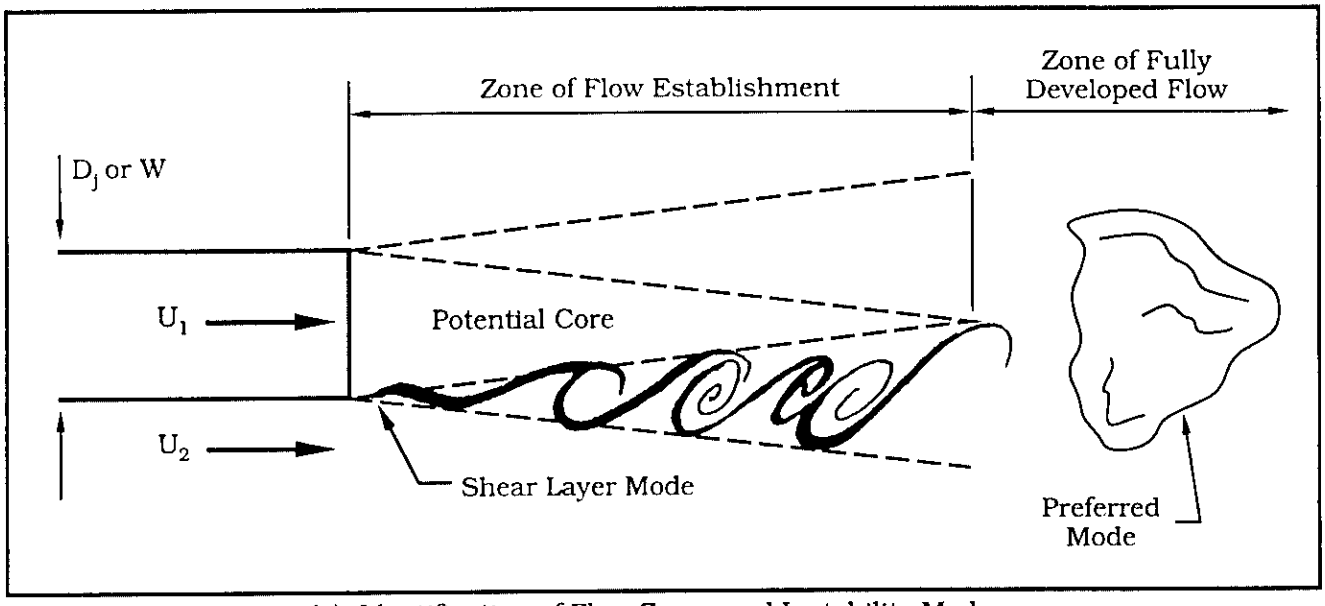

(a) Identification of Flow Zones and Instability Modes.

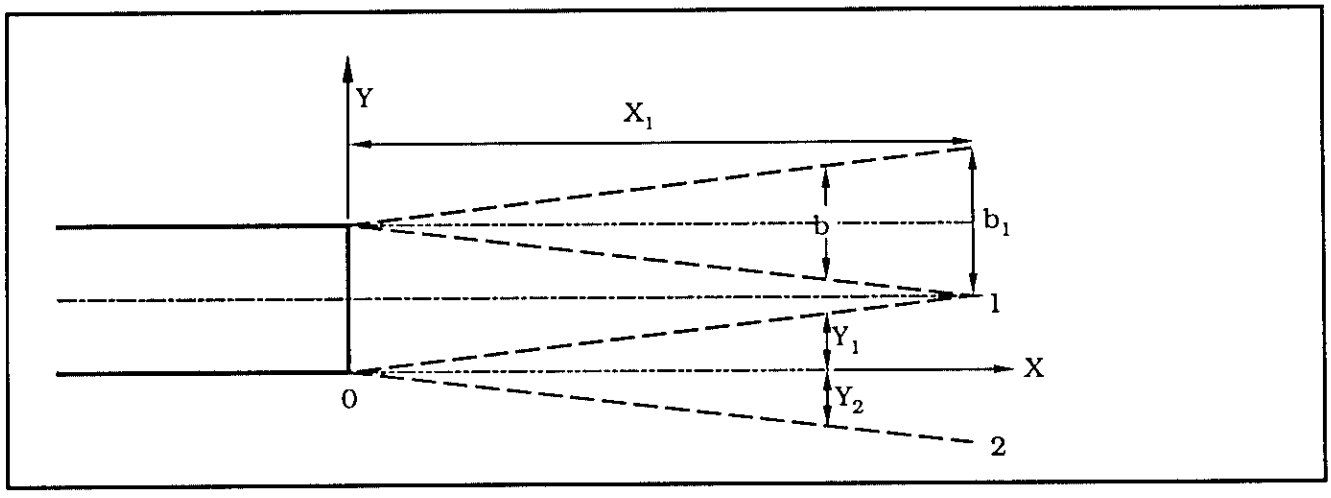

(b) Potential Core Dimensions

Figure 8-3. Initial Region of the Jet.

$$\theta = \pm \tau X \Delta/4 , \tag{8-7}$$

and derivatives of the shear-layer and momentum thicknesses, respectively, are

$$db/dx = \tau \Delta \quad \text{and} \quad d\theta/dx = \tau \Delta/4 . \tag{8-8}$$

Figure 8-4 shows the spreading rate of the turbulent plane mixing layer as a function of Δ. The slope of the lines are values of τ. The divergence of the straight lines increases with Δ and the scatter of the data is due in part to differences in the experimental configurations. According to Abramovich, when $\Delta = 1$ (i.e., $U_2 = 0$), $\tau = 0.27$ for a planar and axisymmetric jet.

Referring to Figure 8-3, the widths of the shear layers, Y_1 and Y_2, are given by

$$\frac{Y_1}{b} = 0.416 + 0.134\ m \tag{8-9a}$$

and

$$\frac{Y_2}{b} = -0.584 + 0.134\ m. \tag{8-9b}$$

Equations (8-9) are for a planar jet but are approximately correct for an axisymmetric jet. It is assumed here that the momentum thickness at the exit is very small in comparison to the nozzle width ($\theta \ll D_j/2$).

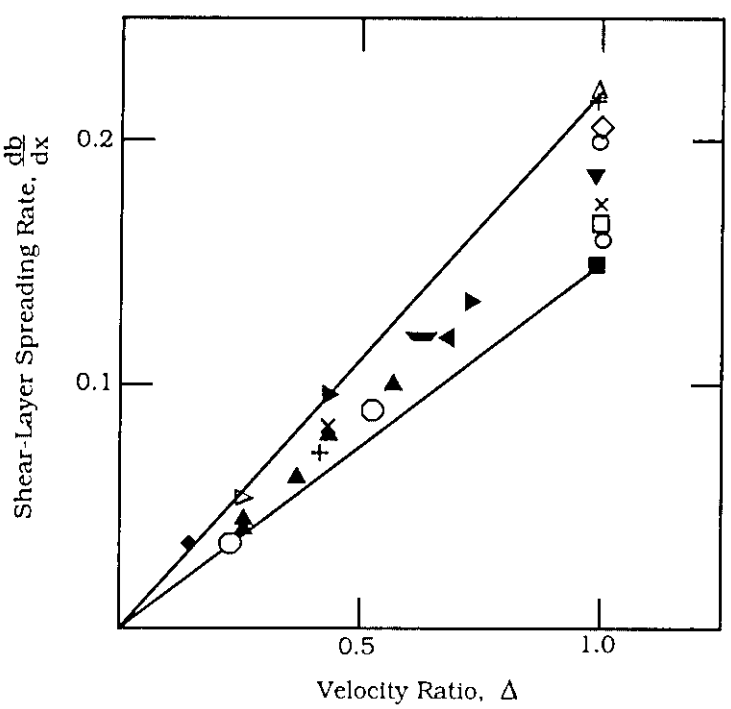

Figure 8-4. Variation of Shear Layer Spreading Rate db/dx With Velocity Ratio Δ For a Turbulent Mixing Layer. (Reproduced from Oster and Wygnanski.[27])

When the free-stream velocity is greater than the jet velocity ($m > 1$), the external edge (line 02 in Figure 8-3b) of the shear layer may intersect the centerline of the jet. In this situation the jet efflux will be strongly warped. Depending on the value of m, there may no longer be a positive pressure gradient along the jet centerline and the formation of a circulation region near the jet centerline is likely.

The thickness of the shear layer at the end of the potential core, b, is given by

$$\frac{b}{(W \text{ or } D_j)} = \frac{1}{2\,(0.416 + 0.134\,m)} \qquad (8\text{-}10)$$

and from Equation (8-5) the length of the potential core, X_1, for a planar jet is

$$\frac{X_1}{(W \text{ or } D_j)} = \pm \frac{(1 + m)}{2\,\tau\,(1 - m)\;(0.416 + 0.134\,m)} \qquad (8\text{-}11)$$

Figure 8-5 shows the variation in length of the potential core as a function of the velocity ratio m. It is seen here that the lengths of the potential cores for planar and axisymmetric jets are approximately the same.

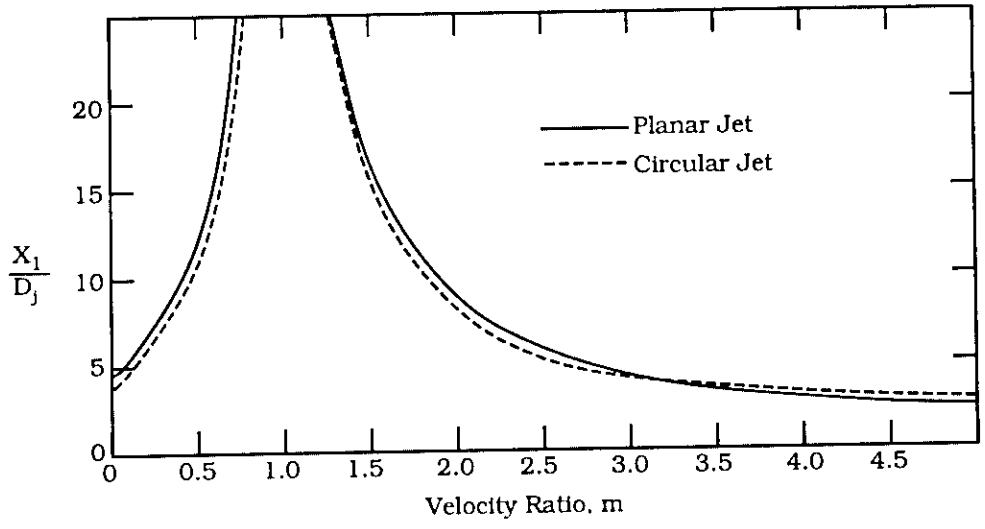

Figure 8-5. The Potential Core Length (X_1) as a Function of the Velocity Ratio (m). (Reproduced from Abramovich.[26])

8.3 Vortex Merging in a Jet

The shear layer growth is attributed to the development of a single vortex that merges with successive vortices. The vortex merging creates pressure waves which propagate upstream that may influence the development of the shear layer. The time required for a vortex to reach a pairing location and the time needed for a pressure signal at the point of merging to propagate upstream is equal to an integer multiple of the period, i.e.,

$$X_i \left(\frac{1}{U_c} + \frac{1}{c} \right) = \frac{n}{f_i} \tag{8-12}$$

where X_i is the distance from the trailing edge to the i'th vortex merging location, f_i is the frequency after the i'th merging, U_c is the convective speed of the vortex, c is the speed of sound, and n is an integer. The experimental value for n is approximately 2. The measured streamwise convective velocity U_c of the flow disturbance is approximately $U_c \approx 1/2\ (U_1 + U_2)$ where U_1 and U_2 are defined in Figure 8-3. At low subsonic speeds, $1/c$ term can be neglected. Equation (8-12) then becomes

$$f_i\ X_i / U_c = n \tag{8-13}$$

and

$$f_i = f_n / 2^i \tag{8-14}$$

where f_n designates the shear layer mode. Substituting Equation (8-14) into Equation (8-13), the merging location of the i'th vortex

$$X_i = 2^i\ n\ U_c / f_n \tag{8-15}$$

can now be predicted. This formulation has been verified with experimental data.[12]

8.4 Example Calculation

As an example, consider an axisymmetric air jet that has a nozzle diameter of 5 cm and mean flow velocities of 3 m/sec, 5 m/sec, and 8 m/sec. The Reynolds number is calculated to be as shown in Table 8-3,

Table 8-3

Sample Jet Reynolds Number

U_m (m/sec)	Re
3	1.1×10^4
5	1.8×10^4
8	2.8×10^4

where $Re = U_m D_j / \nu$. The minimum Reynolds number of all three velocities is greater than 10^4, therefore the mean exit velocity profile will be thin shear.

Next, calculate from the Strouhal number the frequency associated with the preferred mode of the jet column. In this situation the Strouhal number can vary between $0.3 < St_D < 0.5$, and the frequency (see Table 8-4) is found to vary between 18 Hz and 80 Hz.

Table 8-4

Sample Jet Preferred Modes

U_m (m/sec)	Freq. (sec^{-1}) at $St_D = 0.3$	Freq. (sec^{-1}) at $St_D = 0.5$
3	18	30
5	30	50
8	48	80

Finally, calculate the thin shear layer instability as measured at the nozzle exit. Using Figure 8-2 to deduce the Strouhal numbers, the shear layer mode (see Table 8-5) varies between 96 Hz and 416 Hz.

Table 8-5

Sample Jet Shear Layer Modes

U_m (m/sec)	St_D	Freq (sec^{-1})
3	1.6	96
5	2.1	210
8	2.6	416

Measurements made by Cohen and Wygnaski[28] of a 5 cm air jet are shown in Figures 8-6 and 8-7. In this study, Cohen and Wygnanski are able to determine a number of quantities in the jet including the momentum thickness and unsteady velocity near the exit where the shear-layer mode dominates. In the remainder of this example, the shear-layer modes are calculated using Equation (8-1) and compared with the velocity spectra measured near the jet exit.

In Figure 8-6a the dependence of momentum thickness on the jet velocity is shown. These measurements were made at $x/D = 0.25$, near the end of the linear growth region. The solid curve drawn indicates a $U^{-1/2}$ dependence.

In Figure 8-6b, the momentum thickness and the mean centerline velocity are plotted as a function of streamwise coordinates. It is seen here that the momentum thickness at the nozzle has an initial value of approximately 0.34 mm, then increases linearly in the x direction. The mean velocity depicted in Figure 8-7b has a constant value until $x/D = 3.5$; at this point the velocity linearly decreases. The deviation of the centerline velocity from its initial value marks the end of the potential core.

Using the momentum thickness from Figure 8-7a, the thin shear layer lip instability is determined from Equation (8-1). The frequencies become as shown in Table 8-6.

Table 8-6

Shear-Layer Modes Calculated Using Momentum Thickness

U_m (m/sec)	f (sec^{-1})
3	95
5	208
8	411

Figure 8-7 shows spectra measured at two centerline locations from the nozzle exit. The broken line indicates measurements made at $x/D = 0$ and the solid line measurements were made at $x/D = 0.25$. Also drawn in the figure (lower part) are the disturbance amplification rates as predicted by linear stability theory for a thin shear layer. Comparison between Tables 8-5 and 8-6 with Figure 8-7 shows favorable agreement.

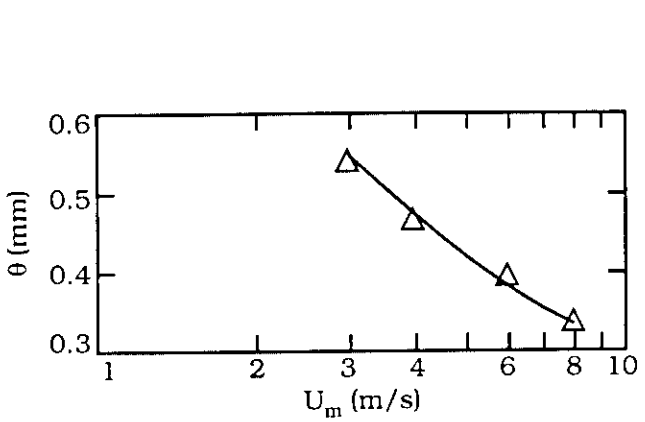

(a) Variation of Momentum Thickness With Jet Exit Velocity Measurements Made at x/D = 0.25. Curve Represents Relation $\theta \propto U^{-1/2}$.

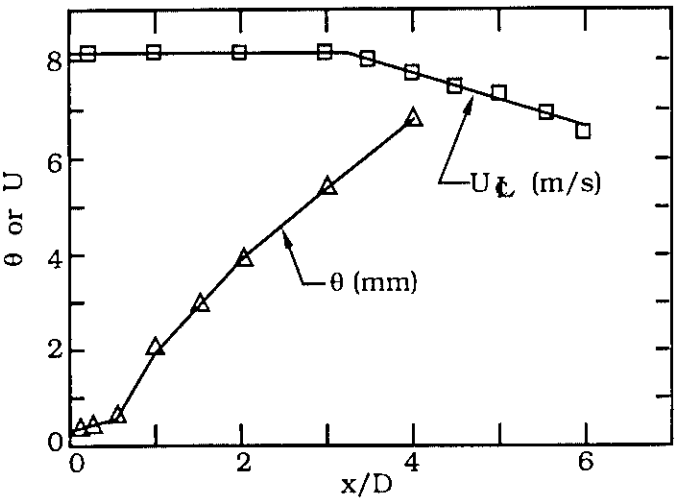

(b) Streamwise Variation of Planar Momentum Thickness Δ and Mean Velocity □.

Figure 8-6. Measurements of a 5 cm Air Jet.
(Reproduced from Cohen and Wygnanski.[29])

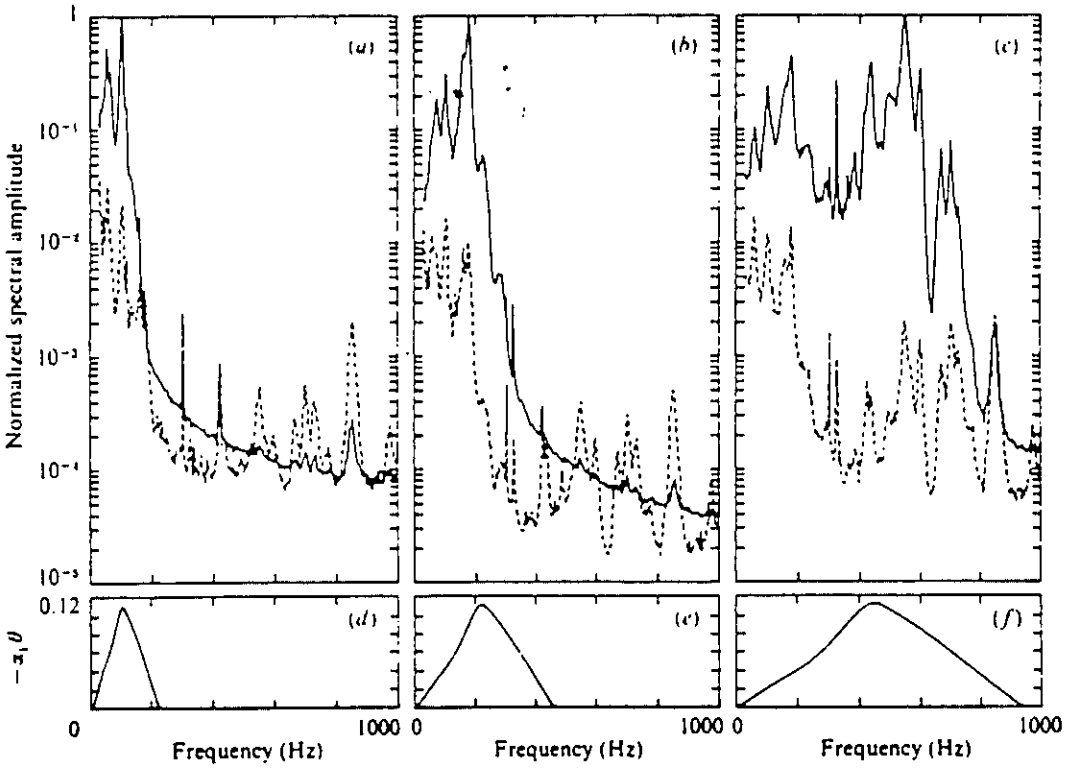

(a) 3m/sec (b) 5m/sec (c) 8m/sec

Figure 8-7. Normalized Power Spectra and Calculated Spatial Growth Measured at Nozzle Exit for Three Jet Velocities. Broken line x/D = 0.0, Solid Line x/D = 0.25 for
(Reproduced from Cohen and Wzgnanski.[28])

REFERENCES FOR CHAPTER 8

1. Sato, H., "The Stability and Transition of a Two-Dimensional Jet", *J. Fluid Mech.*, 7, 1960, 53-80.

2. Michalke, A., "On Spatially Growing Disturbances in an Inviscid Shear Layer", *J. Fluid Mech.*, *23*, 1965, 521-544.

3. Broward, F.K., "An Experimental Investigation of the Instability of an Incompressible Separated Shear Layer", *J. Fluid Mech.*, *26*, 1966, 281-307.

4. Miksad, R.W., "Experiments on the Nonlinear Stages of Free Shear Layer Transition", *J. Fluid Mech.*, *56*, 1972, 695-719.

5. Pfizenmaer, E., Doktor-Ingenieur thesis, Technische Universitat Berlin, 1973.

6. Hussain, A.K.M.F., and Zaman, K.B.M.Q., *J. Fluid Mech.*, *87*, 1978, 349.

7. Freymuth, P., "On Transition in a Separated Laminar Boundary Layer", *J. Fluid Mech.*, *25*, 1966, 683-704.

8. Michalke, A., "The Instability of Free Shear Layers", *Prog. Aerosp. Sci.*, *12*, 1972, 213-239.

9. Davies, P.O.A.L., and Baxter, D.R.J., *Lecture Notes in Physics*, *75*, Fiedler, H. (Ed.), Springer, Berlin, 1978, 125.

10. Husain, Z.D., and Hussain, A.K.M.F., *AIAA J.*, *17*, 1979, 48.

11. Drubka, R.E., Ph.D. thesis, Illinois Institute of Technology, 1981.

12. Gutmark, E., and Ho, C., "Preferred Modes and the Spreading Rates of Jets", *Physics of Fluids*, *26* (10), October 1983, 2932-2938.

13. Bechert, D., and Pfizenmaier, E., "On the Amplification of Broad Jet Noise by a Pure-Tone Excitation", *J. Sound Vib.*, *43*, (3), 581-587.

14. Chen, Y.Y., "Spatial Waves In Turbulent Jets", *Physics of Fluids*, *17*, 46-53.

15. Crow, S.C., and Champagne F.W., "Orderly Structure in Jet Turbulence", *J. Fluid Mech.*, *48* part 3, 1971, 547-591.

16. Fuchs, H.V., "Measurements of Pressure Fluctuations Within Subsonic Turbulent Jets", *J. Sound Vib.*, *22* (3), 1972, 361-378.

17. Ko, N.W.M., and Davies, P.O.A.L., "The Near Field Within the Potential Core of Subsonic Cold Jets", *J. Fluid Mech.*, *50*, Part 1, 1971, 49-78.

18. Moore, C.J., "The Role of Shear-Layer Instability Waves in Jet Exhaust Noise", *J. Fluid Mech.*, *80*, Part 2, 321-367.

19. Petersen, R.A., "Influences of Wave Dispersion on Vortex Pairing in a Jet", *J. Fluid Mech., 89*, Part 3, 1987, 469-495.

20. Yule, A.J., "Large-Scale Structure in the Mixing Layer of a Round Jet", *J. Fluid Mech., 89*, Part 3, 1978, 413-432.

21. Kibens, V., "The Limit of Initial Shear Layer Influence on Jet Development", AIAA Paper No. 81-1960, 1981.

22. Drubka, R.E., "Instabilities in Near Field of Turbulent Jets and Their Dependence on Initial Conditions and Reynolds Number", Ph.D. thesis, Illinois Institute of Technology, 1981.

23. Ho. C.M., and Hsiao, F.B., "Evolution of Coherent Structures in a Lip Jet", *Structure of Complex Turbulent Shear Layers*, Dumas, R., and Fulachier, L. (Eds.), Berlin/Heidelberg/New York, Springer, 1983, 121-136.

24. Ho. C.M., and Huerre, P., "Perturbed Free Shear Layers", *Annual Review of Fluid Mech., 16*, 1984, 365-424.

25. Blake, W., "Mechanics Flow-Induced Sound And Vibration, Volume I, General Concepts And Elementary Sources", *Applied Math. & Mech., 17-1*, Academic Press, 1986.

26. Abramovich, G.N., *The Theory of Turbulent Jets*, The M.I.T. Press, 1963.

27. Oster, D., and Wygnanski, I., "The Forced Mixing Layer Between Parallel Streams", *J. Fluid Mech., 123*, 1982, 91-130.

28. Cohen, J., and Wygnanski, I., "The Evolution of the Instabilities in the Axisymmetric Jet. Part 1. The Linear Growth of the Disturbance Near the Nozzle", *J. Fluid Mech., 176*, 1987, 191-219.

CHAPTER 9

VORTEX SHEDDING FROM BLUFF BODIES

by Michael J. Lucas
Wyle Laboratories

The interest in vortex shedding from bluff bodies, in relation to turbomachinery, stems from the fact that this phenomenon may result in acoustic coupling inside turbomachinery. If the natural acoustic frequency of a standing wave in a duct or enclosure coincides with the shedding frequency from a bluff body, then there will be an energy transfer between the mean flow and the acoustic wave, producing sound amplification. Acoustic coupling will also lead to highly amplified vortex shedding that may in turn result in structural failure of the body itself.

Three geometries common to turbomachinery lend themselves to a bluff body flow instability analysis: instrument probes, struts, and heat exchangers. Instrument probes might be a gas temperature thermocouple or a pitot pressure tube that is mounted to a cylindrical rod which in turn is fastened to the engine housing. Example struts are turning vanes and nozzles; both of these components are prevalent throughout an engine. Heat exchangers are used in turbomachinery to preheat gases prior to combustion. In the SSME the liquid oxygen injector posts are an example of such a heat exchanger.

In this chapter the dependence of non-dimensional frequency (Strouhal number) on Reynolds number will be presented for selected geometries. The Reynolds number range applicable to turbomachinery problems is between 10^4 and 10^7; thus the data will be appropriately limited to this range of Reynolds numbers.

Section 9.1 describes the mechanisms and respective regimes for vortex generation from solitary cylinders in a cross-flow, Section 9.2 presents comparable data for other bluff bodies, and Section 9.3 shows methods used to predict the Strouhal number for tube bundles in cross-flow for various tube configurations.

9.1 Vortex Formation From a Cylinder

The basic mechanism that determines the frequency of vortex shedding behind any bluff body is the distance separating the two shear layers. As the shear layers are brought closer together, their interaction is facilitated and the shedding frequency increased. In the case of the cylinder there is no single point along the surface of the cylinder that promotes boundary layer separation. The lack of a clearly definable separation point on the surface of the cylinder makes the azimuth for a separating boundary layer more sensitive to the Reynolds number than other geometries in cross-flow might be, such as a square or a triangle. This in turn impacts the distance separating the two shear layers and their shedding frequency.

The role of Reynolds number on the flow structure interaction in the wake of a cylinder is depicted in Figure 9-1. These figures were adapted from a review article by Morkovin[1] that shows how the underlying flow field characteristics change with Reynolds number. The regimes and terminology described herein are consistent with the literature.

The Reynolds number range is divided into five regimes. The concerns of this chapter are the so-called subcritical, supercritical, and transcritical regimes. Each of the regimes shown in Figure 9-1 is described below.

Vortex shedding is considered to be subcritical when the attached flow near the surface of the cylinder is laminar to and past the point of separation. The boundary layer separates from the cylinder at an angle of approximately $\theta = \pm 80°$ from the forward stagnation point.

The subcritical regime extends from the pure Karman range up to a Reynolds number of 2×10^5. The Karman range is where unsteadiness sets in (Re ~ 40) and where well-defined vortex shedding persists (up to Re ~ 300). In the subcritical regime there exists an underlying organization in the vortex shedding; vortices are shed in a clearly definable alternating pattern. The generally accepted value for the Strouhal number in this range is 0.21. This value is accurate to within 5 percent.

When the Reynolds number is increased beyond 2×10^5 the laminar boundary layer separates, quickly experiences a transition to the turbulent state, reattaches on the surface of the cylinder, then separates again farther along the

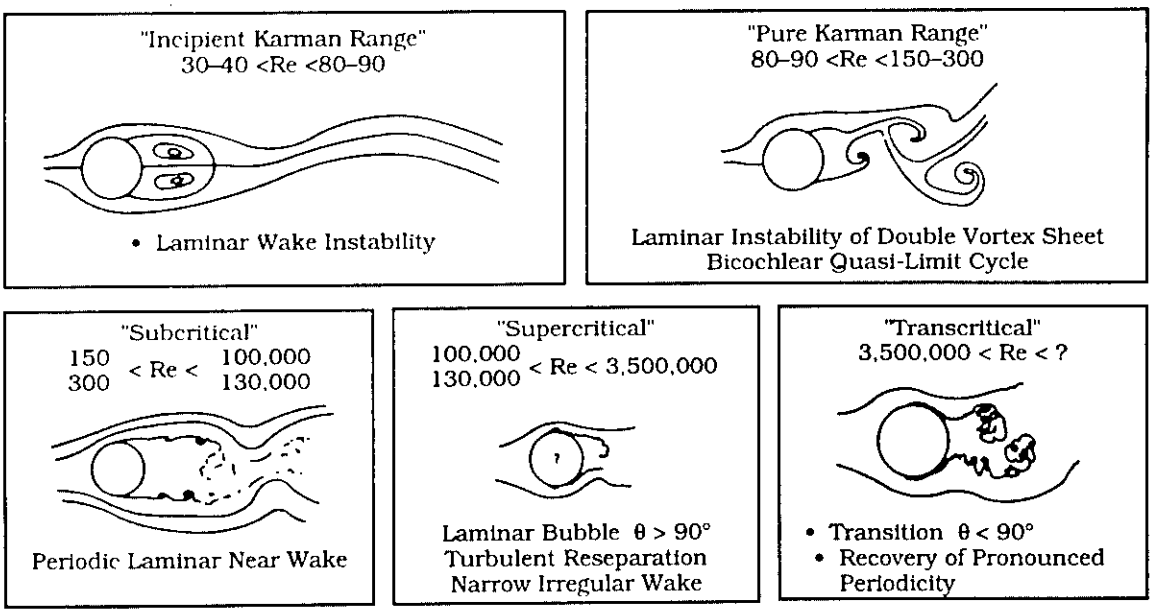

(a) Flow Regimes.

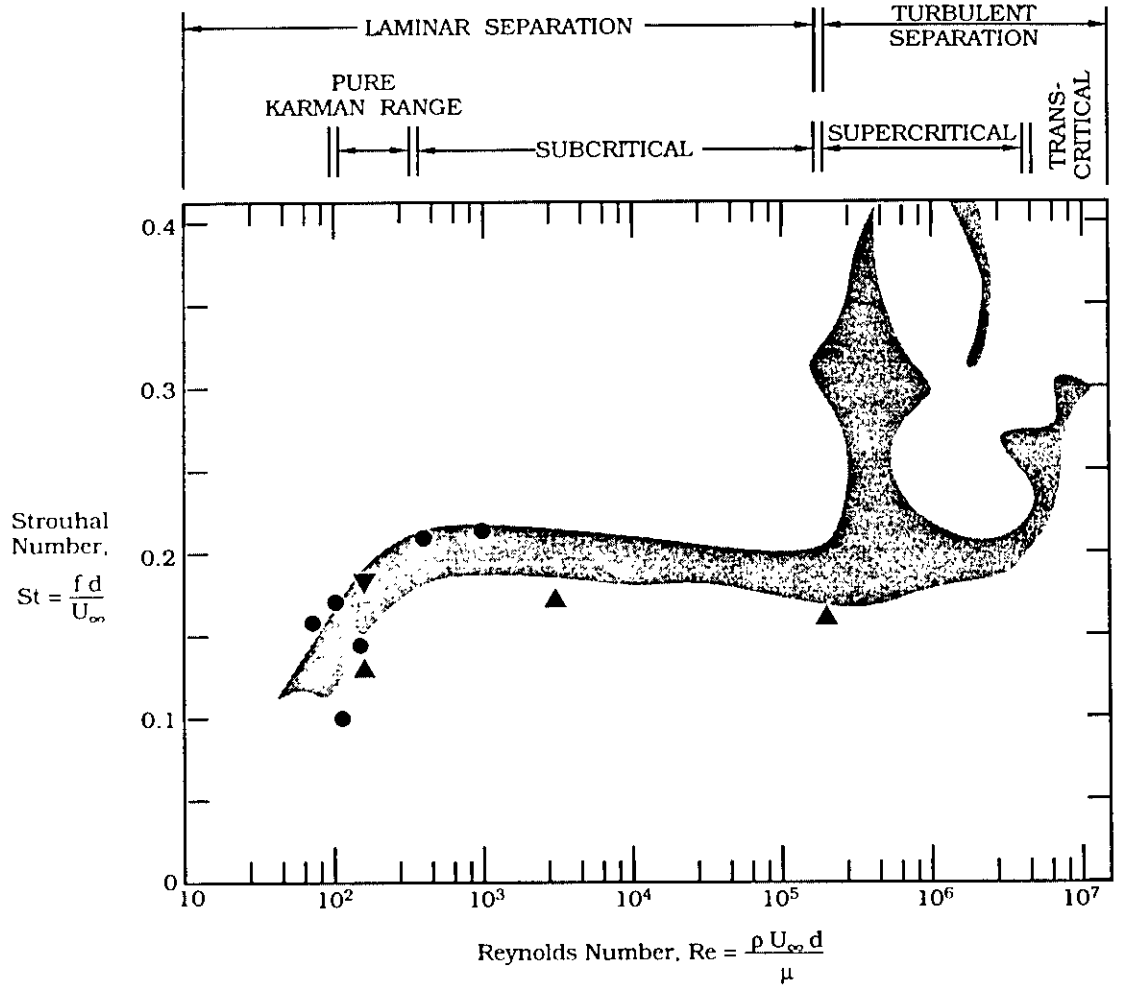

(b) Strouhal Number Versus Reynolds Number.

Figure 9-1. Characteristics of the Wake From a Circular Cylinder. (Reproduced from Morkovin.[1])

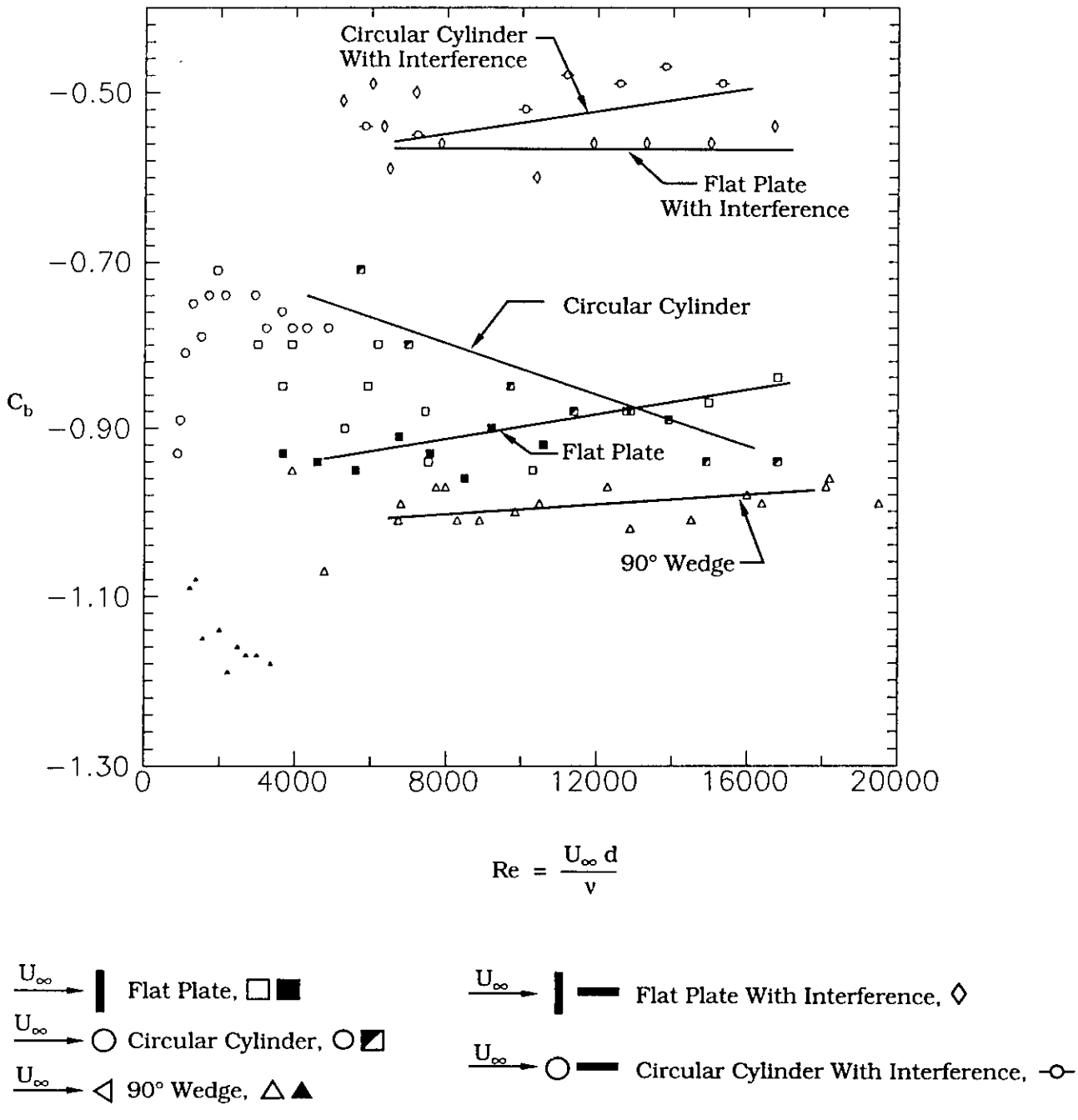

Figure 9-2. Base Pressure Coefficient for Two-Dimensional Bluff Bodies. (Reproduced from Roshko.[2])

cylinder. In the supercritical regime, the flow structure on the rear half of the cylinder is dramatically different from the subcritical regime and the pressure redistributes causing a well-known decrease in the mean drag coefficient. The highly coherent periodic shedding ceases. However, there still remains a wake oscillation that has an underlying coherence, though the spectra are wideband as opposed to periodic. Investigators[1] have reported, in the supercritical regime, Strouhal numbers that vary between 0.17 to 0.45. The Strouhal number about which the wake will operate is dependent upon the free-stream turbulence and the cylinder surface roughness condition.

When the Reynolds number exceeds 3×10^6 the boundary layer undergoes turbulent transition prior to separation. This regime is known as the transcritical regime. If the cylinder has a rough surface or if there is some degree of free-stream turbulence, then the transition to the transcritical regime will occur at a lower Reynolds number. Transition can be tripped by a ridge on the surface of the cylinder. The turbulent boundary layer separates from the cylinder at an angle of approximately $\theta = \pm 120°$ measured from the forward stagnation point. The flow exhibits a return to a coherent periodicity. The Strouhal number becomes $St \sim 0.3$ when $Re \gtrsim 10^7$.

In summary, flow past cylinders with Reynolds numbers in the subcritical and transcritical regimes are likely to reinforce large amplitude acoustic or body oscillations. Both these regimes are predictable with a high degree of confidence. The supercritical regime ($2 \times 10^5 < Re < 3 \times 10^6$) does have some coherent alternating vortex shedding pattern but the oscillation is mostly broadband. The supercritical regime suffers a degree of uncertainty when predicting the modes of oscillation; this is an artifact of the flow being transitional and thereby highly dependent on free-stream conditions and cylinder roughness.

9.2 Vortex Formation From Other Bodies

Different bluff bodies are known to shed similarly structured wakes. In all cases a shear layer separates from both sides of the body. The shear layer rolls up, producing alternating vortices. The region behind the body in which this occurs extends several body widths downstream. This region plays an important role in the strength of the vortices and the frequency at which they are shed.

The basic parameters that control the vortex shedding process are the magnitude of the negative base pressure coefficient, C_b, and the distance between the shear layers, d'. The base pressure coefficient is defined as

$$C_b = \frac{P_b - P_\infty}{0.5\ \rho_\infty\ U_\infty^2} \qquad (9\text{-}1)$$

where P_b = the base pressure, the pressure immediately downstream of the bluff body,

P_∞ = the pressure in the undisturbed flow,

U_∞ = the free stream velocity, and

ρ_∞ = the density of the fluid.

The free-stream Reynolds number and Figure 9-2 can be used to determine C_b for various geometries. By applying Bernoulli's equation at the separation point just outside the boundary layer, the wake velocity

$$U_s = (1 - C_b)^{1/2}\ U_\infty \qquad (9\text{-}2)$$

is obtained. The quantity $(1 - C_b)^{1/2}$ is usually replaced by K such that

$$U_s = K\ U_\infty \qquad (9\text{-}3)$$

where K is called the base pressure parameter.

The distance separating the shear layers or wake width d' as depicted in Figure 9-3 is the characteristic length that is common to all bluff bodies. It is a universal measure of the "bluffness" of the body in that "bluffer" bodies produce more severe distortion of the flow in the streamwise direction. Figure 9-4 shows the wake width as a function of the base pressure parameter.

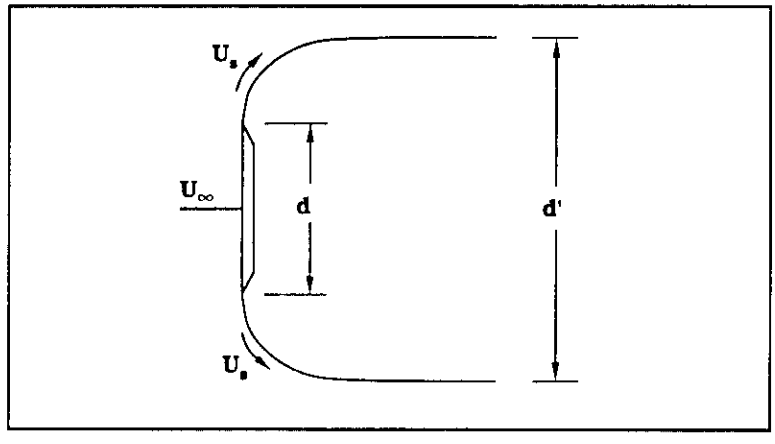

Figure 9-3. Wake Structure of a Bluff Body.

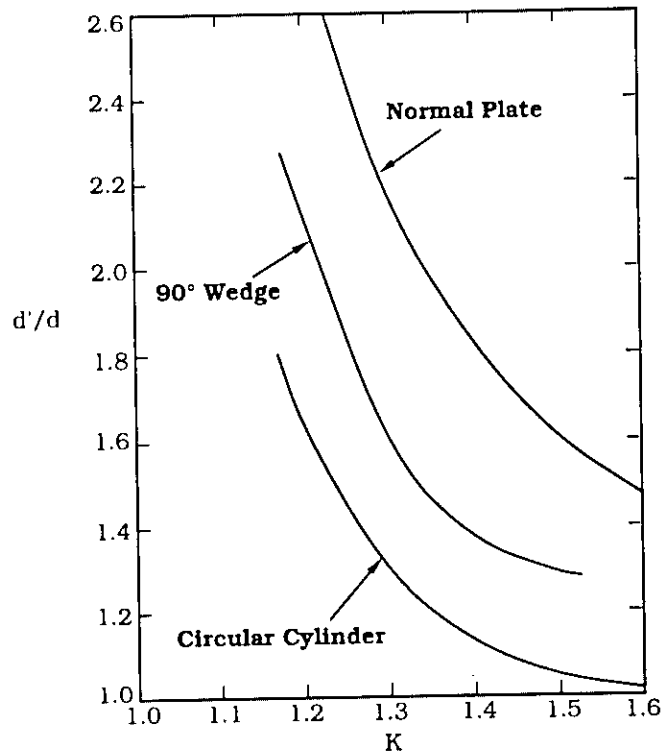

Figure 9-4. Wake Width for Two-Dimensional Bluff Bodies. (Reproduced from Roshko.[2])

If the free-stream velocity, U_∞, remains unchanged while the body width dimensions are increased, it seems intuitive that the distance separating the shear layers d' will increase and so will the base pressure coefficient C_b. Since the base pressure coefficient is simply related to the wake velocity, it follows that a wake Strouhal number is appropriately defined as

$$St^* = \frac{f\,d'}{U_s}. \qquad (9\text{-}4)$$

Roshko[2] has developed a relationship between St^* and K that collapses measurements from a cylinder, a normal flat plate, and a 90-degree wedge over a range of Reynolds numbers. These results were later supported by Bearman[3] who transcribed the work of Roshko and other investigators onto a single plot, reproduced here as Figure 9-5.

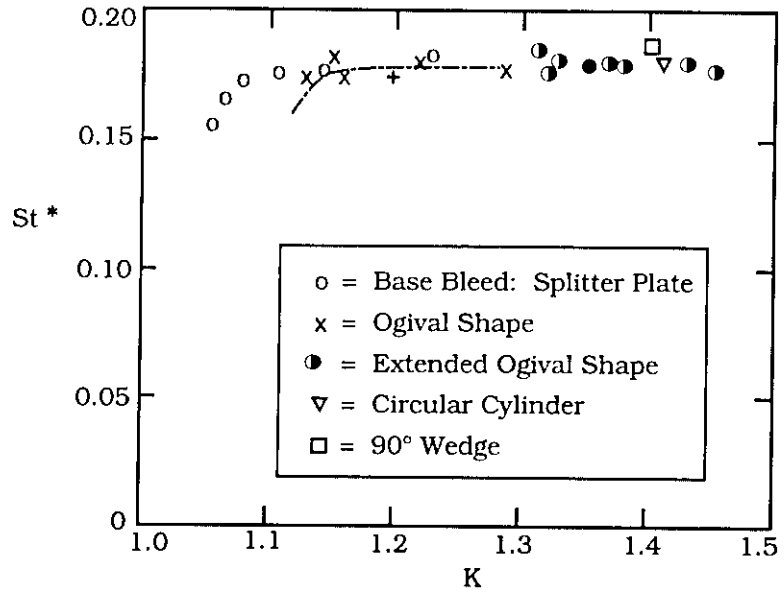

Figure 9-5. Universal Strouhal Number Versus Base Parameter Coefficient K for a Variety of Bodies.

It is evident from Figure 9-5 that $St^* \cong 0.18$ is a universal Strouhal number that spans a range of base pressure coefficients. A departure from $St^* = 0.18$ is observed at pressure coefficients below 1.1. This universal Strouhal number may be successfully applied over a range of base pressure coefficients, Cb . In Figure 9-5 the Reynolds number is mostly contained within the subcritical regime.

A procedure for calculating the wake Strouhal number for a bluff body is as follows:

1. Estimate the value of K from Figure 9-2.

$$K = (1 - C_b)^{1/2}$$

2. Use this value and Figure 9-4 to determine $\dot{d}'$.
3. Calculate U_s from Equation (9-3).
4. Calculate the shedding frequency using Equation (9-4).

9.3 Prediction of Strouhal Number for Tube Banks In Cross-Flow

9.3.1 Overview

A heat exchanger is a device that is widely used in turbomachinery to transfer thermal energy between two or more fluids. The type of heat exchanger most commonly found in turbomachinery is the cross-flow heat exchanger. In this exchanger design, gas or fluid is forced across a tube bundle, while another fluid is used inside the tubes for heating or cooling purposes. The tube banks are a vibration concern when the cross-flow fluid velocity is high or the design contains long tubes with small diameters. The tubes may fail either due to fatigue or collision with neighboring tubes. To identify when such failures will occur, an analysis is made that considers four important factors affecting vibration: (1) vortex shedding, (2) turbulent buffeting, (3) acoustic resonances, and (4) fluid-elastic whirling referenced to the tube natural frequency.

Figure 9-6 shows a cross-section of a heat exchanger tube bundle. The emphasis of most theories used to evaluate the potential for vibration problems is on tube geometrics having in-line and staggered tube arrays.

Consider a tube array exposed to a gradually increasing cross-flow velocity. The instability shedding excitation frequency, f_e, increases with a constant Strouhal number, until the natural frequency of the tube, f_n, or the acoustic resonance mode of the enclosure, f_a, is reached. When f_e approaches f_n or f_a, the vortex shedding becomes regular and highly correlated along the spans of tubes. This so-called "locking-in" condition can be maintained over a considerable velocity range such that the Strouhal number is no longer considered to be constant. With a further increase in the velocity, the shedding frequency suddenly increases to a Strouhal number given by its original value prior to the locking condition.

The occurrence of a "locking-in" condition inside heat exchangers is a well-known problem and has led to the formulation of a design methodology. The accuracy of the technique will vary depending on the heat exchanger geometry and flow conditions. For example, the flow in a heat exchanger is usually never entirely perpendicular to the tubes nor is the flow uniform through the tube bundle. Sections 9.3.2 and 9.3.3 will discuss the methods to determine the frequencies for the factors which influence tube vibration.

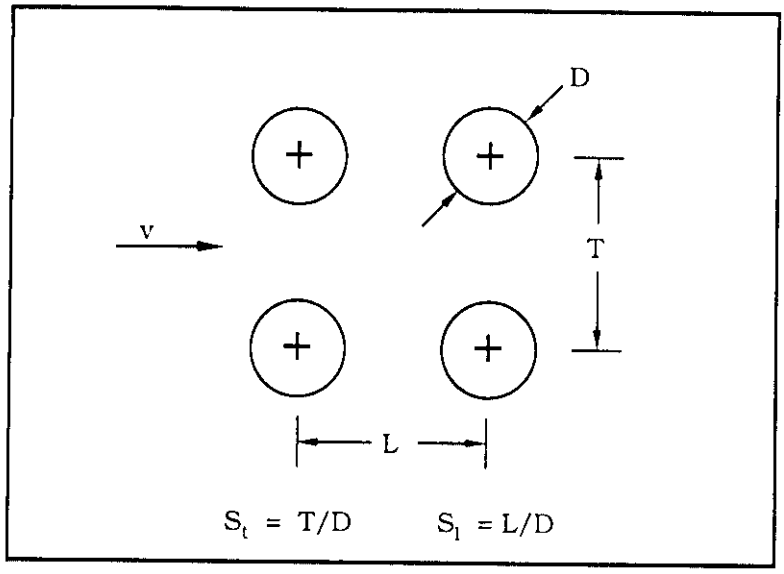

(a) Geometry of In-Line Tube Array.

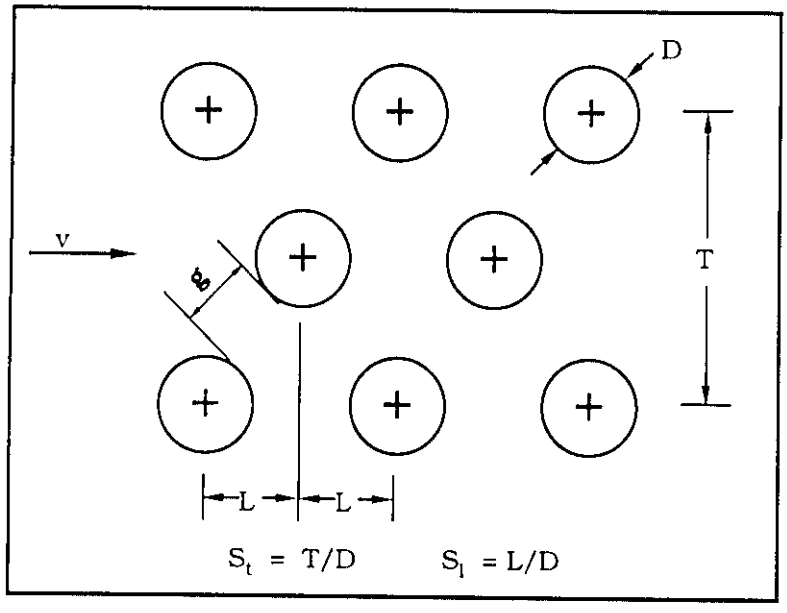

(b) Geometry of Staggered Tube Array.

Figure 9-6. Tube Layout Basic Parameters.

9.3.2 Vortex Shedding Excitation Frequency, f_e

Vortex shedding excitation in a tube bank is similar to the shedding process of a solitary cylinder. However, identifiable vortex shedding is often limited to the first few rows of a tube bank. These rows have an incident flow with the least amount of contaminating turbulence. Grover and Weaver[4] have reported the existence of organized periodic shedding up to the first 15 rows of a tube array. The periodicity is, of course, greatly enhanced if the shedding instability frequency coincides with an acoustic resonant mode or a fluidelastic/whirling instability.

Experimental measurements made by Fitz-Hugh[5] and Chen[6] are shown in Figure 9-7. The independent variable St characterizes the tube layout as shown previously in Figure 9-6.

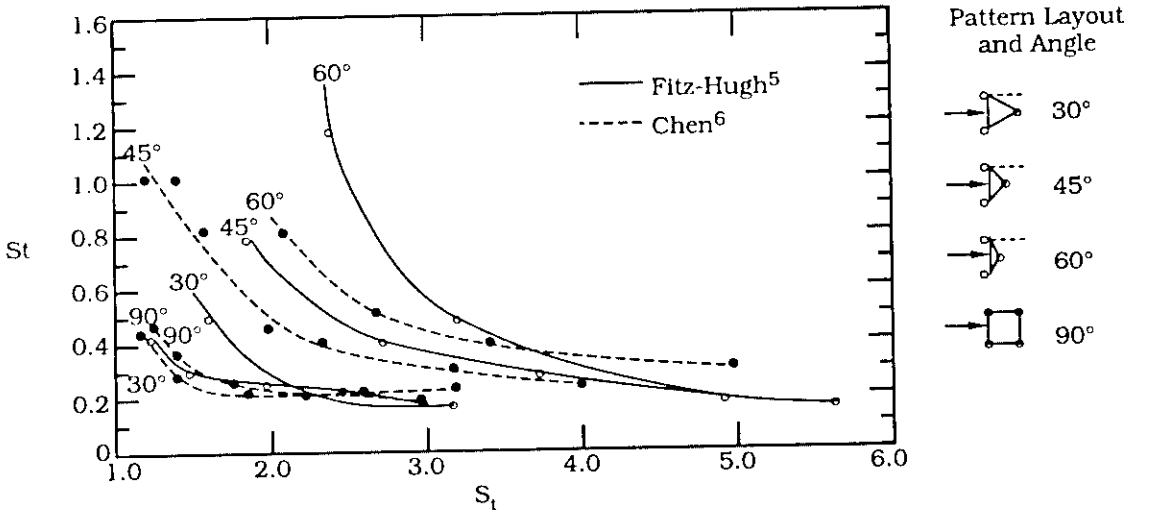

Figure 9-7. Strouhal Number (St) Versus S_t for Tube Banks in Cross-Flow (see Figure 9-6 for definition of S_t).

Shown in Figure 9-8 is Fitz-Hugh's[5] collection of the experimental measurements made by a number of investigators collapsed onto a single diagram. Either Figure 9-7 or 9-8 may be used to estimate the Strouhal number for a tube bank.

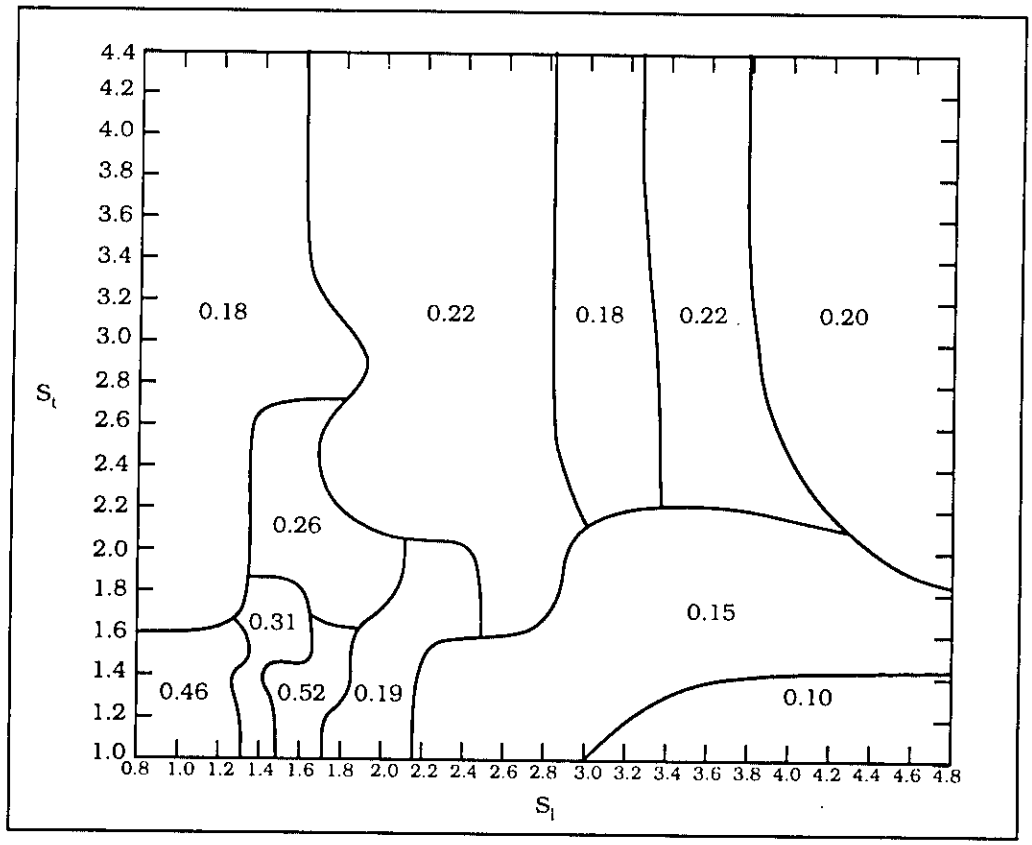

(a) S_t Versus S_l for In-Line Tube Arrays.

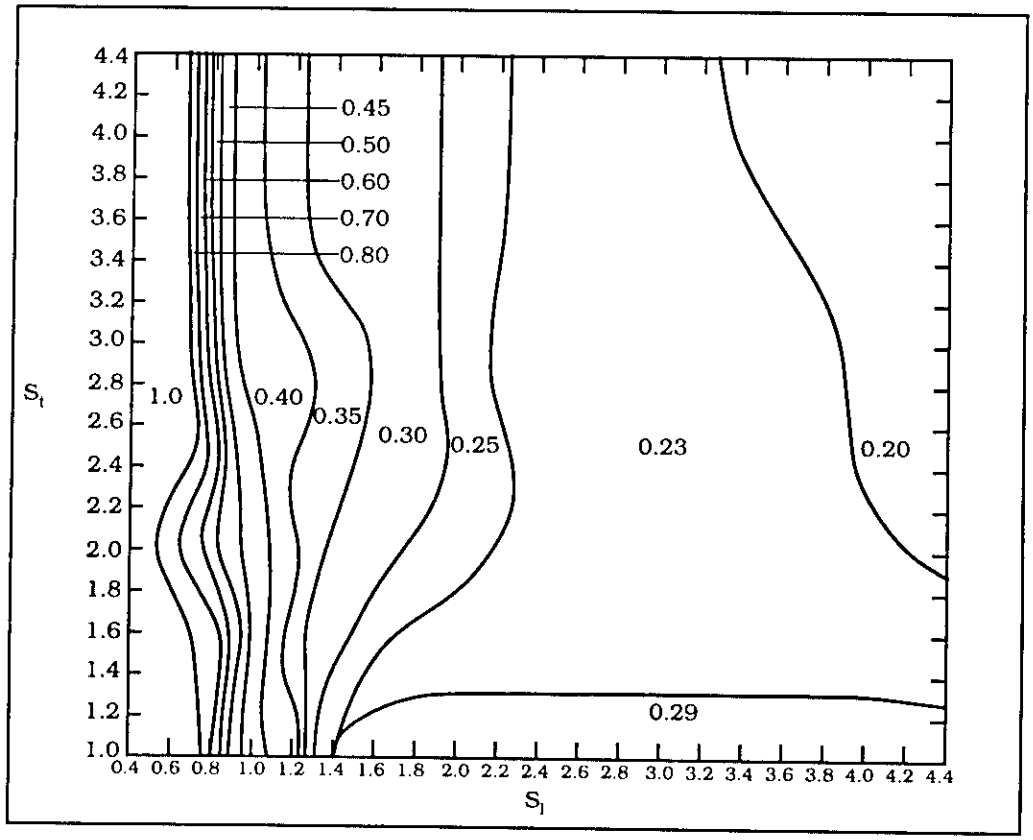

(b) S_t Versus S_l for Staggered Tube Arrays.

Figure 9-8. Values of Strouhal Number for Tube Arrays.
(Reproduced from Fitz-Hugh[5] and Paidoussis.[8])

9.3.3 Turbulent Buffeting Excitation, f_{tb}

Deep inside a tube bank, it may be assumed that the flow incident on a row of tubes is non-uniform. This type of flow is known as turbulent buffeting and is characterized by a spectrum of frequencies distributed about a dominant frequency. Owen[7] developed the following relationship to predict the predominant frequency f of this spectra

$$St = (f_{tb}\, D/U) \quad S_l\, S_t = 3.05\,(1 - 1/S_t)^2 + 0.28 \qquad (9\text{-}5)$$

where the velocity U is the average flow velocity at the minimum cross-section between the tubes, $U = U_\infty\, T/(T - D)$; U_∞ is the free-stream velocity; and S_l and S_t are the spacing parameters as depicted in Figure 9-6. Equation (9-5) only applies to gases. Data or equations are not yet available for turbulent buffeting frequencies for liquids.

The physical reasoning behind Equation (9-5) rests in the fact that buffeting is the source of excitation. This equation has been shown by Paidoussis[8] to agree with similar vortex shedding models, suggesting that the predominant peak may be due to either vortex shedding or buffeting.

9.3.4 Flow-Acoustic Coupling in Tube Arrays

When the frequency of flow periodicity inside the duct coincides with the acoustic modes of the duct, acoustical coupling may produce pressure amplitudes as high as 175 dB. However, such resonances will not materialize if the acoustic damping capacity of the system is sufficient to preclude resonances – the acoustic damping capacity being traceable to the vortex shedding pattern and its compatibility to the duct acoustic modes.[9]

To determine if the conditions inside the heat exchanger are favorable for the establishment of transverse acoustical resonances, Ziada *et al.*[10] developed a resonance parameter that is suitable for in-line and stagger tube arrays. The principal parameters used in the criterion are: the critical Reynolds number based on the gap velocity, the spacing parameters, and the acoustical Reynolds number based on an effective speed of sound, c_{eff}. For in-line and staggered tube arrays, respectively, the resonance parameters are

$$G_i = \sqrt{Re}\; S_T \left(\frac{\nu}{c_{eff}\, D} \right), \qquad (9\text{-}6)$$

$$G_s = \sqrt{Re}\left[\frac{\sqrt{2\,S_l(S_T-1)}}{(2\,S_l-1)}\right]\left(\frac{\nu}{c_{eff}\,D}\right), \qquad (9\text{-}7)$$

where Re = Reynolds number,

U = average flow velocity at the minimum cross-section between tubes,

c_{eff} = effective speed of sound which has been shown by Parker[11] to be equal to $\frac{c_{eff}}{c} \approx (1+\sigma)^{-1/2}$,

c = speed of sound,

σ = solidity ratio, fraction of space occupied by solid bodies such as tubes,

D = tube diameter,

ν = kinematic viscosity, and

S_t , S_l = spacing parameters.

Ziadia *et al.* use a critical Reynolds number based on the maximum gap speed, since resonance is most likely to occur at the highest speeds.

The dependence of the resonance parameters G_i and G_s on S_l^2 and 2 L/h are shown in Figure 9-9. The parameter 2 L/h , appearing for the staggered array, represents the ratio between the jet winding around the tubes (2 L) and the minimum thickness h .

$$h = \begin{cases} t/2 = (T-D)/2, & t/2 < g \\ g, & t/2 > g \end{cases} \qquad (9\text{-}8)$$

As the packing density is decreased, 2 L/h increases, and the heat exchanger becomes more susceptible to resonances. This behavior is clearly depicted in Figure 9-9.

9.3.5 Tube Natural Frequency, f_n

Since there are usually many uncertainties such as the vibration characteristics of the tube baffle supports and the longitudinal tube stresses associated with heat exchangers, a precise calculation of the tube's natural frequency is usually

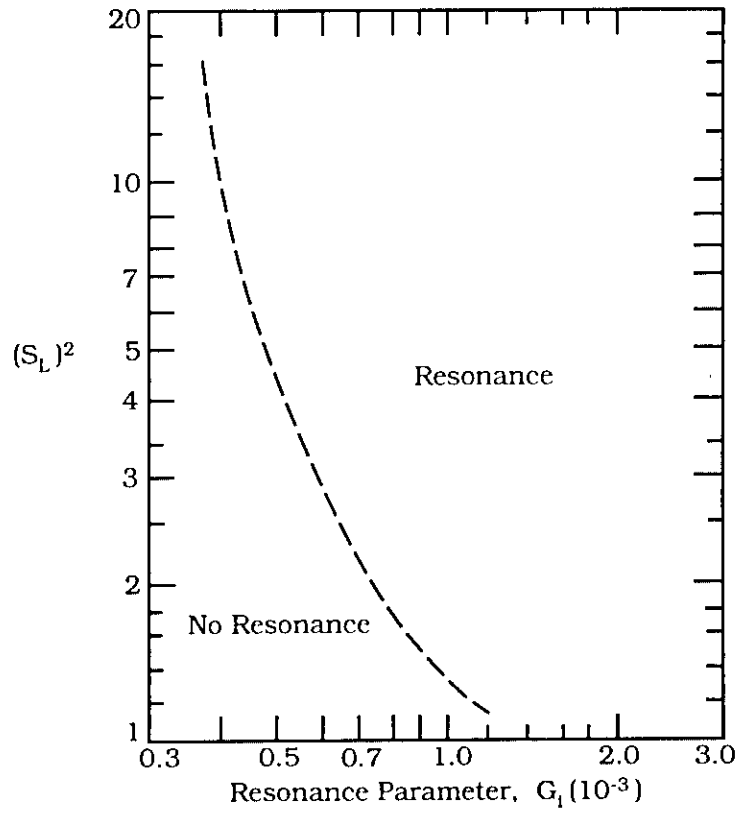

(a) In-Line Tube Bank

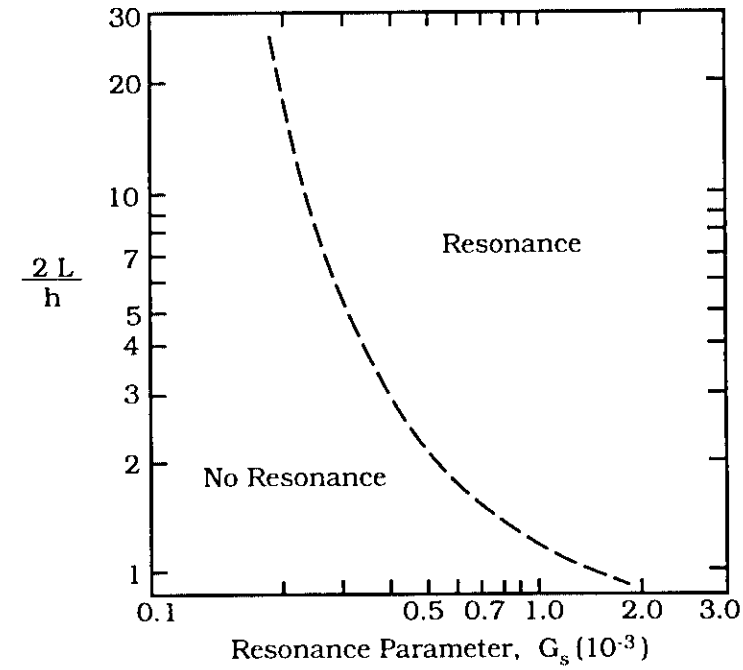

(b) Staggered Tube Bank

Figure 9-9. Resonance Parameters for an In-Line and Staggered Tube Array. (Reproduced from Ziada *et al.*[10])

not feasible. However, an adequate model used to estimate the tube's natural frequency assumes the tubes are continuous beams that are supported by intermediate baffles. The baffles provide some degree of damping resulting in a natural frequency

$$f_n = \frac{D}{2\pi}\sqrt{\frac{E\,I\,g}{W_e\,L^4}} \qquad (9\text{-}9)$$

where D = frequency constant (see Table 9-1),

E = modulus of elasticity of tube material,

I = sectional moment of inertia,

$= \pi\,\frac{d_o^4 - d_i^4}{64}$,

g = gravitational constant,

L = length of the span, and

W_e = effective weight per unit tube length.

Table 9-1

Values of Frequency Constant, D
(Reproduced from Fitz-Hugh[5])

End Support Conditions	Mode				
	1st	2nd	3rd	4th	5th
Both Clamped	22.4	61.7	120.9	199.9	298.6
One Clamped, One Hinged	15.4	50.0	104.2	178.3	272.0
Both Hinged	9.9	39.5	88.8	157.9	246.7

W_e includes the weight of the tube material, W_t, the weight of the fluid within the tube, W_i, and the weight of the fluid that oscillates with the tube, W_o. The effective weight is calculated as

$$W_e = W_t + W_i + W_o \qquad (9\text{-}10)$$

where W_t = weight of the tube material per unit length,

$W_i = \rho_i \frac{\pi d_i^2}{4}$, weight of the fluid within the tube per unit length,

$W_o = k \rho_o \frac{\pi d_o^2}{4}$, weight of the fluid that oscillates with the tube per unit length,

d_i = inside tube diameter, and

d_o = outside tube diameter

The value of k in W_o is determined using Figure 9-10. Fitz-Hugh[5] used a value of 1.0 when estimating k.

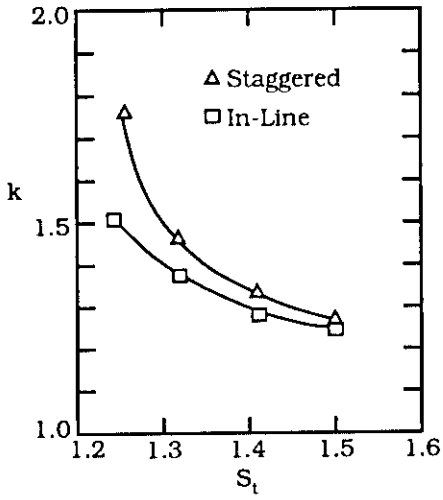

Figure 9-10. Experimental Measurement of Hydrodynamic Inertia Constant. (Reproduced from Chenoweth.[12])

It is a common occurrence in heat exchangers for the span length to vary between the tube bundles. In the SSME combustion chamber, the injector posts in the inner rows of the bundle are shorter than those in the outside row. The value of f_n should be calculated for each different span length, using the appropriate end conditions.

The axial stress of a tube may alter the natural frequency. The correction is[13]

$$f_n' = f_n \sqrt{1 + \frac{P L^2}{E I \pi^2}} \qquad (9\text{-}11)$$

where f_n' = stressed frequency,

f_n = unstressed frequency,

L = length of spa,

P = axial load, negative if compressed, positive if tensile,

$P = S \bullet A$,

S = axial stress, and

A = cross-section area of the tube, metal only.

The axial stress depends on the construction and installation of the tubes.

For heat exchangers that have a U-bend, the longest bend length should be used for L in Equation (9-9). The natural frequency should then be adjusted for in- and out-of-plane frequencies as follows:[13]

$$\text{In Plane} \quad f_i = 1.985\, f_n \tag{9-12a}$$

$$\text{Out Plane} \quad f_o = 0.829\, f_n \tag{9-12b}$$

These equations assume no intermediate supports.

The natural frequency for finned tube array heat exchangers similar to the one sketched in Figure 9-11 is obtained by using Equation (9-9) and making the following substitutions

$$I = \pi \frac{d_e^4 - d_{if}^4}{64} \tag{9-13}$$

where:

$$d_e = d_o + 1.08\,(d_{fo} - d_{if}) \tag{9-14}$$

and d_{fo} = tube diameter at root of fin,

d_{if} = tube inside diameter under finned section, and

d_o = tube outside diameter.

The actual weight of the tube, shown in Figure 9-11, should be used for the weight of the tube material, W_t. A value of k equal to 1.0 and the overall fin diameter should be used when calculating W_o.

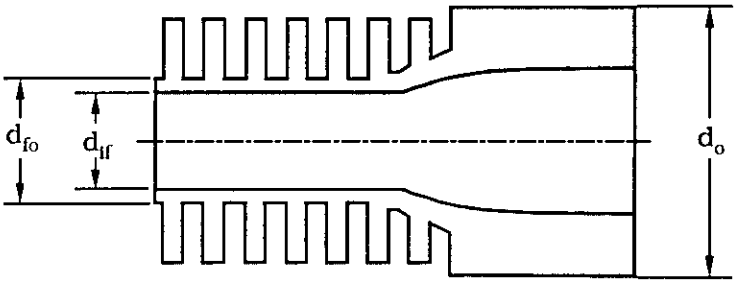

Figure 9-11. Tube Nomenclature.

9.3.6 Fluid-Elastic Instabilities in Tube Arrays

In a tube bank there are flow mechanisms, in conjunction with the elastic vibration of tubes, that are unrelated to the instabilities occurring in tube banks having ridge tubes. These mechanisms, commonly referred to as fluid-elastic instabilities, have amplitudes large enough to cause tubes crashing into one another. The basic objective is to predict the critical flow velocity for this type of instability.

There are many models that may be used to predict the onset velocity of fluid-elastic instabilities and a discussion of these theories, as well as a classification of the more recent works, is found in Chen[14] and Paidoussis.[15] In a more recent article by Paidoussis and Price,[16] a discussion on the mechanisms and how they may be synthesized into two broad categories may be found. In their article, Paidoussis and Price describe this mechanism as involving negative damping and a wake flutter mechanism. Paidoussis and Price predictions can be made of the critical velocity for the onset of fluid elasticity inside a tube row by synthesizing these two basic mechanisms. The onset condition is expressed in terms of the dimensionless parameter $U_{crit}/f_n D$ in which U_{crit} is the value of the flow velocity at which the array goes unstable, f_n is the natural frequency of the tube in vacuum, and D is the tube diameter. The fluid-elasticity is then controlled by the damping forces, and is shown to be expressed in terms of $m\delta$, where δ is the in-vacuum logarithmic decrement of damping and m is the tube mass.

9.3.7 Heat Exchanger Tube Bundle Vibration Prediction Procedure

The following procedure compares the fluid dynamic forcing frequencies to that of the acoustic resonator modes of the enclosure and the natural frequency of the tubes. Similar procedures have successfully predicted 80 percent[16] of the existing heat exchanger flow-induced vibrations. The steps are as follows:

1. Calculate the acoustic resonances of the enclosure, as described in Chapter 4 of this handbook. The simplest calculation that may apply is

$$f_a = \frac{n\, c_{eff}}{4\, L_{eff}} \qquad (9\text{-}15)$$

where f_a = acoustic frequency,

n = mode number, and

$\frac{c_{eff}}{c} = (1 + \sigma)^{-1/2}$.

c = speed of sound,

σ = fraction of space occupied by solid bodies, and

L_{eff} = effective heat exchanger enclosure dimension.

2. Estimate the resonance parameter G_i or G_s. Use 1.2 times the maximum projected flow speed as an average flow speed between the tubes. If the resonance parameter lies in a non-resonant region (see Figure 9-9), resonance will not occur at any of the lower speeds. Otherwise, compute the ratios of vortex shedding and turbulent buffeting frequencies to the acoustic frequency. If the fluid excitation frequency falls within the following limits, then the acoustic resonance may enhance fluid unsteadiness.

$$0.8 < \frac{f_e}{f_a} < 1.2 \qquad (9\text{-}16a)$$

$$0.8 < \frac{f_{tb}}{f_a} < 1.2 \qquad (9\text{-}16b)$$

3. Compute the ratio of the fluid excitation frequency to the natural frequency of the tube. If either of the following conditions is satisfied, the fluid unsteadiness may cause the tubes to undergo fluid–elastic vibration.

$$0.5 < \frac{f_e}{f_n} < 1.5 \qquad (9\text{-}17a)$$

$$0.5 < \frac{f_{tb}}{f_n} < 1.5 \qquad (9\text{-}17b)$$

REFERENCES FOR CHAPTER 9

1. Morkovin, M.V., "Flow Around a Circular Cylinder – A Kaleidoscope of Challenging Fluid Phenomena", *Symposium on Fully Separated Flows*, Hansen, A.G. (Ed.), ASME, New York, 1964, 102-108.

2. Roshko, A., "On the Drag and Shedding Frequency of Two-Dimensional Bluff Bodies", National Advisory Committee for Aeronautics, Technical Note 3169.

3. Bearman, P.W., "On Vortex Street Wakes", *J. Fluid Mech., 28*, Part 4, 1967, 625-641.

4. Grover, X., and Weaver, X., "Cross-Flow Induced Vibrations in a Tube Bank–Vortex Shedding", *J. Sound Vib., 59*, 1978, 263-276.

5. Fitz-Hugh, J.S., "Flow-Induced Vibration in Heat Exchangers", Paper 427, International Symposium on Vibration Problems in Industry, Keswick, 1973.

6. Chen, Y.N., "The Sensitive Tube Spacing Region of Tube Bank Heat Exchangers for Fluid–Elastic Coupling in Cross-Flow", *Fluid–Structure Interaction Phenomena in Pressure Vessel and Piping Systems*, Au-Yang, M.K., and Brown, S.J. (Ed.), ASME, 1977.

7. Owen, P.R., "Buffeting Excitation of Boiler Tube Vibration", *J. Mech. Eng. Science, 7* (4), 1965, 431-439.

8. Paidoussis, M.P., "Flow-Induced Vibration in Nuclear Reactors and Heat Exchangers", "Practical Experiences With Flow-Induced Vibration", Naudascher, E., and Rockwell, D. (Ed.), IAHR/UTAM Symposium, Karlsruhe, 1979.

9. Ziada, S., Oengoren, A., and Buehlmann, E.T., "On Acoustical Resonance in Tube Arrays. Part i: Experiments", *J. Fluids Struct., 3* (3), 1989, 292-314.

10. Ziada, S., Oengonen, A., and Buhlmann, E.T., "On Acoustical Resonance in Tube Arrays, Part I: Damping Criteria", *J. Fluids Structs., 3* (3), 1989, 315-324.

11. Parker, R., "Acoustic Resonances in Passages Containing Banks of Heat Exchanger Tubes", *J. Sound Vib., 57*, 1978, 245-260.

12. Chenowath, J.M., "Flow-Induced Vibrations in Shell-and-Tube Heat Exchangers", Final Report on Contract No. EY-76-C-03-1273, for Division of Conservation and Technology of ERDA, SAN/1273-1, UC-93, February 1977.

13. Rohsenow, W.M., Hartnett, J.P., and Ganic, E.N., *Handbook of Heat Transfer Applications*, 2nd Ed., McGraw-Hill Book Company.

14. Chen, S.S., *J. Fluids Struct., 1*, 1987, 35.

15. Paidoussis, M.P., *Appl. Mech. Reviews, 40*, 1987, 163.

16. Paidoussis, M.P., and Price, S.J., "The Mechanisms Underlying Flow-Induced Stabilities of Cylinder/Arrays in Cross-Flow", *J. Fluid Mech., 187*, 1988, 45-59.

CHAPTER 10

SWIRLING FLOWS

by Michael J. Lucas
Wyle Laboratories

There are a wide variety of configurations of flow machinery that generate internal swirling flows, and the instabilities of these flows are of considerable practical importance. These flows are possible whenever there is a combination of an axial (streamwise) and radial component of velocity. Engine components that are known to inject a swirl into the streamwise axial component of flow are pump inlet and exit chambers, cooling air cavities, combustion chambers, and sharp radial turns in the plumbing. A problem inherent in the design of these components is collecting the axial flow and redirecting it from or towards the main rotor axis. This action can introduce a swirling vortex that at some location downstream causes a transition or breakdown into a new flow state. The instabilities present in a swirling flow and the vortex breakdown phenomenon are of central importance in turbomachinery.

Section 10.1 introduces the basic aspects of vortex breakdown. Sections 10.2 through 10.4 contain a discussion on the behavior of swirling flows in various practical devices. The devices described in these sections are a vortex whistle, a vortex tube, and a ring inlet and exit chamber. The important feature common to all of these configurations is the dependence of pure-tone noise on flow rate.

10.1 Vortex Breakdown

Swirling flow is susceptible to a process known in the literature as vortex breakdown. This involves the rapid transformation of the flow from a highly organized, undisturbed state of swirl to a large-scale, highly turbulent flow region. It is important to realize that the transition process can lead to surges or large-scale fluctuations in the downstream tube. Also, this process of vortex breakdown can occur irrespective of the type of inlet and outlet flow restrictions.

A number of laboratory tests[1] on vortex flows have found that the predominant parameter responsible for determining the onset of vortex breakdown is the ratio of the swirl velocity V_θ to the axial velocity u. Although the swirl and

axial velocity distribution vary with radius, representative values of each of these velocities over the cross-section of the vortex are typically chosen to characterize the flow. In essence, when the value of the characteristic swirl velocity becomes sufficiently large relative to the characteristic axial velocity, then the flow undergoes vortex breakdown. Upstream of the location of vortex breakdown, the distribution of axial streamwise velocity is a jet-like distribution, whereas downstream of the vortex breakdown the distribution of axial velocity takes on a wave-like form. In the region of vortex breakdown, both organized and broadband fluctuations are in the form of a helical instability similar to that observed for the higher order (m = 1, 2, . . .) modes of a jet. Thus the possibility exists for vortex breakdown to excite the resonant acoustic modes of a flow system and produce vibrations on the structural components.

Although the flow downstream of vortex breakdown can exhibit unstable and turbulent behavior, the mechanism for producing the onset of breakdown is still a source of controversy. There are two basic views: the first is that breakdown involves a phenomenon similar to a hydraulic jump, involving the abrupt transformation from a supercritical to a subcritical condition; the second view is that it is driven by a phenomenon of hydrodynamic instability. In general, the former explanation seems to have wider acceptance.

Overviews and assessments of the mechanisms leading to vortex breakdown, both for external and internal flow configurations, are given in the reviews of Leibovich[2] and Escudier.[1,3] This chapter reviews the different flow devices used to study swirling flows and vortex breakdown. Where possible, prediction schemes are provided for estimating the resonance frequencies inside these geometries.

10.2 Vortex Whistles

Using a device resembling a whistle, Vonnegut[4] produced a pure-tone noise from a swirling flow. The whistle, as sketched in Figure 10-1a, has a tangential inlet swirl generator whose diameter, D, is greater than the inlet diameter, d_i, and greater than the exit tube diameter, d_o. Flow through the tangential inlet generated a pure-tone noise whose frequency increased proportionally with the flow rate.

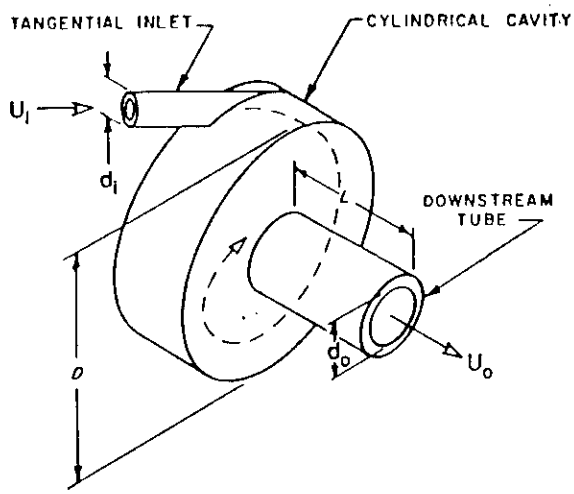

(a) Vortex Whistle

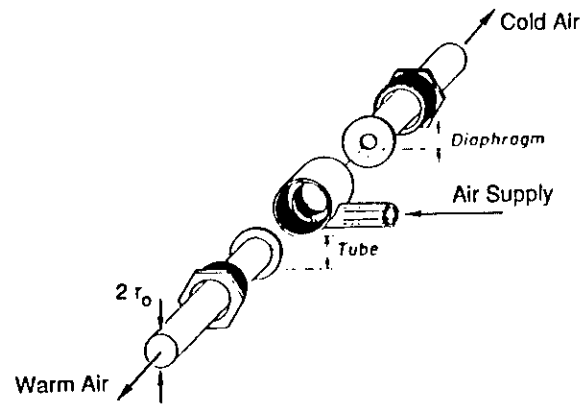

(b) Vortex Tube

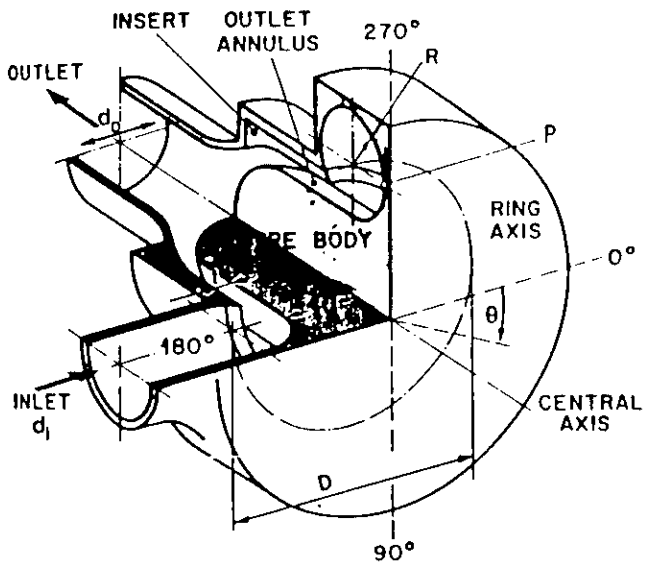

(c) Ring Inlet Chamber

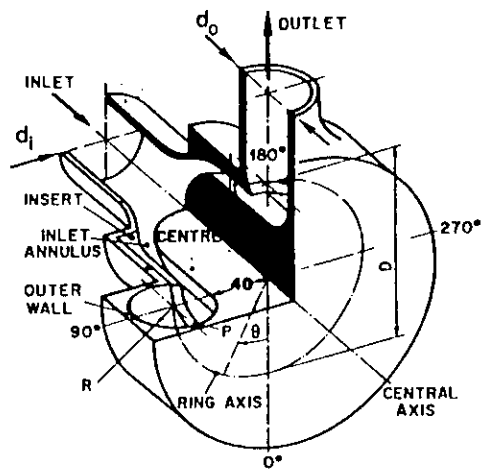

(d) Ring Exit Chamber

Figure 10-1. Basic Swirl Generators.

Measurements of frequency of Vonnegut's whistle are plotted against flow rate in Figure 10-2. In Figure 10-3, the frequency is plotted against the quantity $[(P_1 - P_2) / P_2]^{1/2}$, where P_1 is the entering pressure and P_2 is the exhaust pressure. The relationship to estimate the frequency is given by

$$f = \alpha \frac{c}{\pi D} \left[\frac{P_1 - P_2}{P_1}\right]^{1/2} \qquad (10\text{-}1)$$

where c = speed of sound,
D = diameter of vortex whistle,
P_1 = entering pressure, and
P_2 = exhaust pressure.

The value of α is a constant less than one. This factor accounts for frictional losses. If the fluid can be assumed inviscid, as in air at a sufficiently high Reynolds number, a value of one should be used for α.

A comparison of data taken by Vonnegut[4] and Channuad[5,6] for selected values of L/d is shown in Figure 10-4. The parameters used to characterize the whistle are the mean exit velocity U, the mean diameter of the downstream tube d, and the frequency of oscillation f. Vonnegut's measurements were made for an L/d ratio of 2.2 and a Reynolds number range of 6,000 to 25,000. His results, calculated from Figure 10-2, are shown in the figure as the shaded area. Channuad measurements were made in air for a Reynolds number range of 2,000 to 7,000. The whistle constructed by Channuad has a downstream tube that could be varied both in tube length L and diameter d.

The measurements made by Vonnegut show only fair agreement with those of Channuad. The Strouhal number reported by Vonnegut for air is between 1.2 and 1.5, while the measurements made by Channuad indicate a higher value. The decrease in Strouhal number with increasing L/d ratio, reported by Channuad, indicate a viscous drag reduction in the downstream tube and possibly related to the variable α reported by Vonnegut in Equation (10-1).

Both Vonnegut and Chanaud observed that when water is injected into the whistle, air bubbles in the water spiral around the exit tube axis at about the same frequency as that of the sound frequency. These observations suggest that a central mechanism responsible for the sound generation is the vortex breakdown

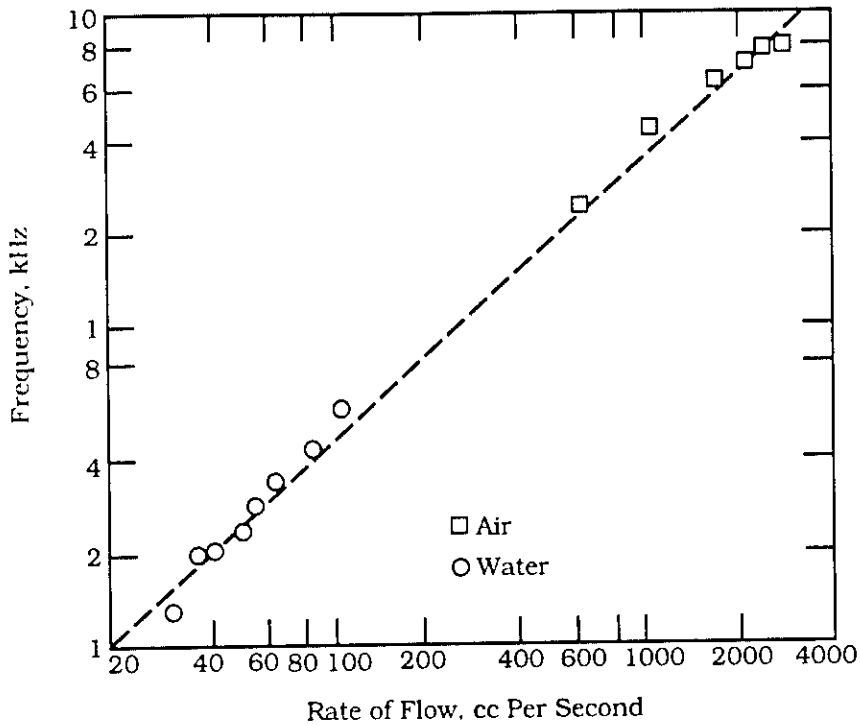

Figure 10-2. Frequency as a Function of Flow Rate of Air and Water for Vortex Whistle. (Reproduced from Vonnegut.[4])

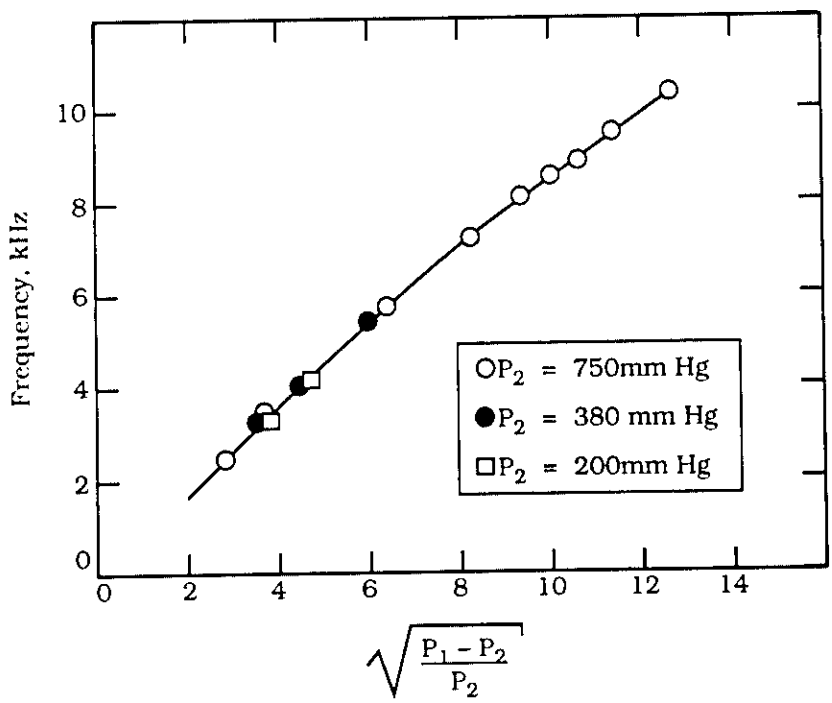

Figure 10-3. Frequency as a Function of Pressure of Incoming and Outgoing Air for Vortex Whistle (Reproduced from Vonnegut[4]).

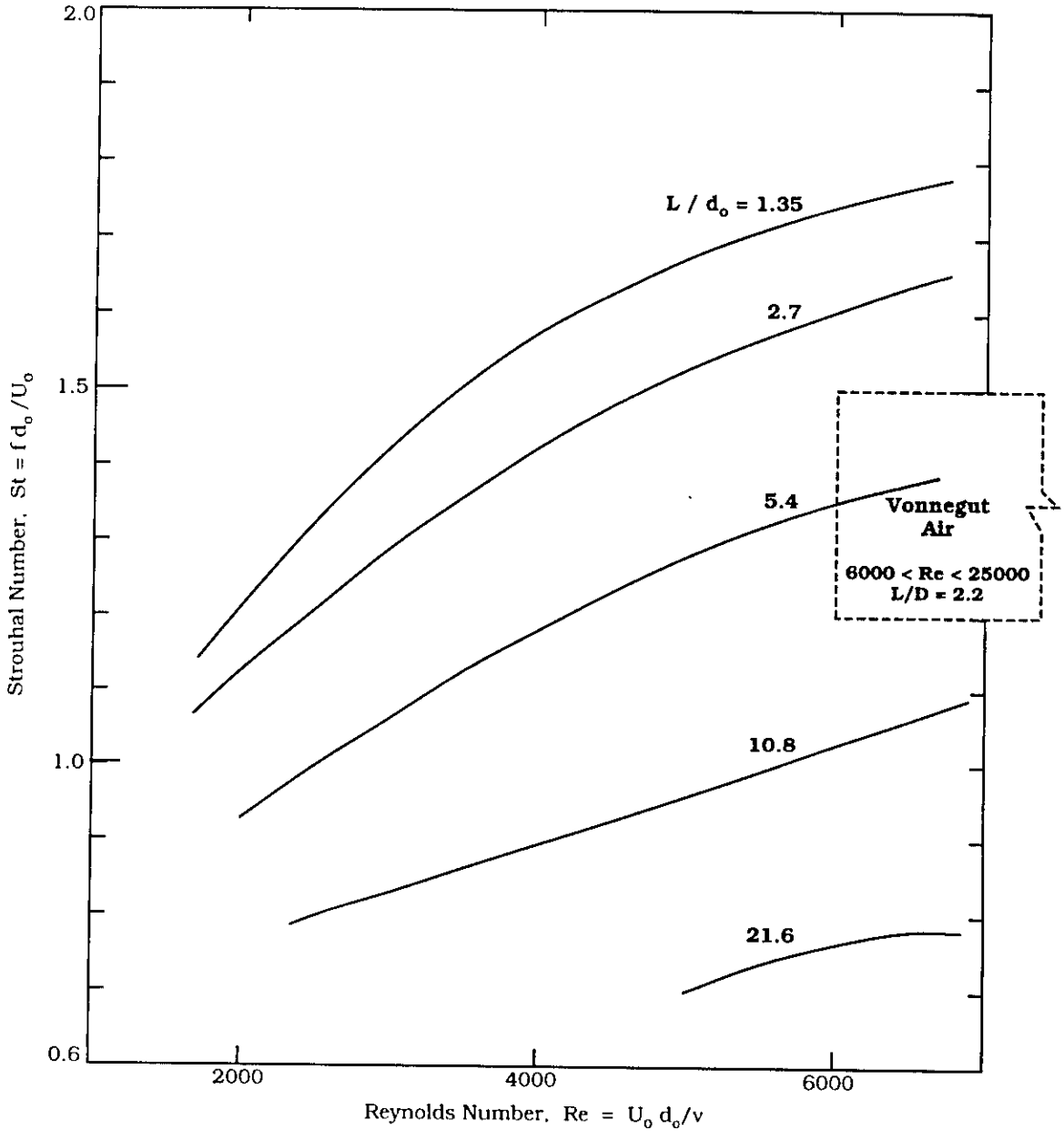

Figure 10-4. Comparison of Chanaud's[5] Vortex Whistle Air Experiment to Vonnegut's[4] Air and Water Experiment. Shaded region indicates range of Strouhal numbers for Vonnegut's experiment.

in the downstream tube. If the sound frequency is simply related to the fluid angular velocity, then the Strouhal number represents the ratio of the swirl velocity to the axial velocity

$$St = \frac{f\, d_o}{U_o} = \frac{\omega\, r_o}{\pi\, U_o} = \frac{V_\theta}{\pi\, U_o} \qquad (10\text{-}2)$$

where $r_o = d_o/2$, and

V_θ = fluid angular velocity.

This simple relationship to estimate the sound frequency was shown to provide a reasonable estimate, provided L/d_o is less than 2.

10.3 Vortex Tubes

Figure 10-1b shows a sketch of a vortex tube. This device is similar to the vortex whistle in that when air is injected through the tangential tube into a cylindrical container a pure-tone noise is emitted whose frequency is proportional to the flow rate of the swirl. The presence of the diaphragm shown in the figure separates the air flow into two streams. The colder air escapes through the hole in the diaphragm, while the hotter air is exhausted through the other end of the tube.

The discovery of the vortex tube led to numerous experimental investigations by Ranque,[7] Hilsch,[8] and others to evaluate the nature of an observed total temperature separation that occurred inside the cylindrical tube. At one time it was thought that the vortex tube might be used as an efficient cooling device. In fact, Vonnegut[4] was led to his findings on the vortex whistle while working on the application of the Ranque–Hilsch vortex tube effect. Vonnegut observed temperature differences as high as 50°C between the center of the vortex core and the outer rotational fluid.

Kurosaka[9] suggested that it is acoustic streaming by the vortex whistle which produces the Ranque–Hilsch effect. Acoustic streaming is the mean motion in a fluid generated by sound. It is forced by the Reynolds stresses, defined as the mean momentum flux due to the acoustic waves.[10] Kurosaka explains that when the whistle is inaudible, the steady-state tangential velocity distribution in the radial direction is in the form of a free vortex and the steady-state temperature is

uniform. But when the whistle is audible, the velocity profile transforms to that of a forced vortex and the temperature distribution spontaneously separates into a hotter stream near the outer wall and a colder stream near the axial centerline.

Kurosaka[9] developed a frequency swirl relationship from which the first harmonic of the vortex whistle is determined

$$f = \frac{\omega}{2\pi} = \frac{\Gamma}{2\pi r_o^2} = \frac{1}{\pi D}\frac{\Gamma}{r_o}. \qquad (10\text{-}3)$$

In this equation, Γ is the circulation of the forced vortex and may be estimated by assuming that the value of the circulation around the tube periphery is equal to that around the circumference at the exit of the swirl generator; r_o is the radius of the tube from which the hot air is expelled. Figure 10-5 shows the calculated frequency together with the measured values. This analysis shows that the frequency of the swirling fluid is the first harmonic of the vortex whistle. The disagreement between the measured values and those predicted are explained by viscous losses in the cylindrical tube.

10.4 Ring Inlet and Exit Chambers

Merkli and Escudier[11] developed a simplified axial flow model to simulate the behavior of flow instabilities inside axial compressors, annular cascades, and turbine inlets. Figure 10-1c shows a sketch of a ring inlet chamber. Ring inlet chambers are used to distribute the flow from an inlet duct or pipe onto the first blade row of a compressor or turbine.

The geometry shown in Figure 10-1c is idealized; in practice the ring cross-section may be non-circular and the axial flow complicated by blading in the annular passage. These flow devices can be expected to induce turbulences that may affect the nature of the unsteadiness inside the ring chamber and the frequency of oscillation. With the exception of the presence of the center body (see Figure 10-1c), the inlet-chamber arrangement is quite similar to the vortex whistle (see Figure 10-1a).

Figure 10-6a shows the variation of Strouhal number with Reynolds number for a ring inlet chamber. Above a critical Reynolds number of 1.2×10^5, the frequency spectrum was observed to increase steadily with mass flow rate. As

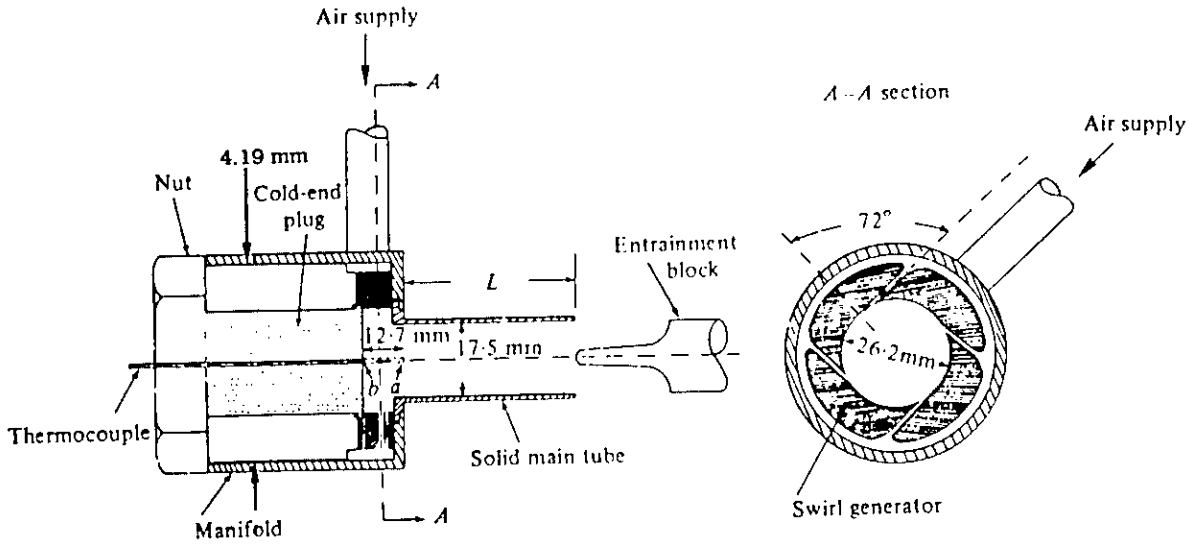

$$f = \left({}^{1}/_{\pi D}\right) \qquad V_o = \left({}^{1}/_{\pi (0.017m)}\right) \qquad V_o = \left(18\ {}^{1}/_{m}\right) V_o$$

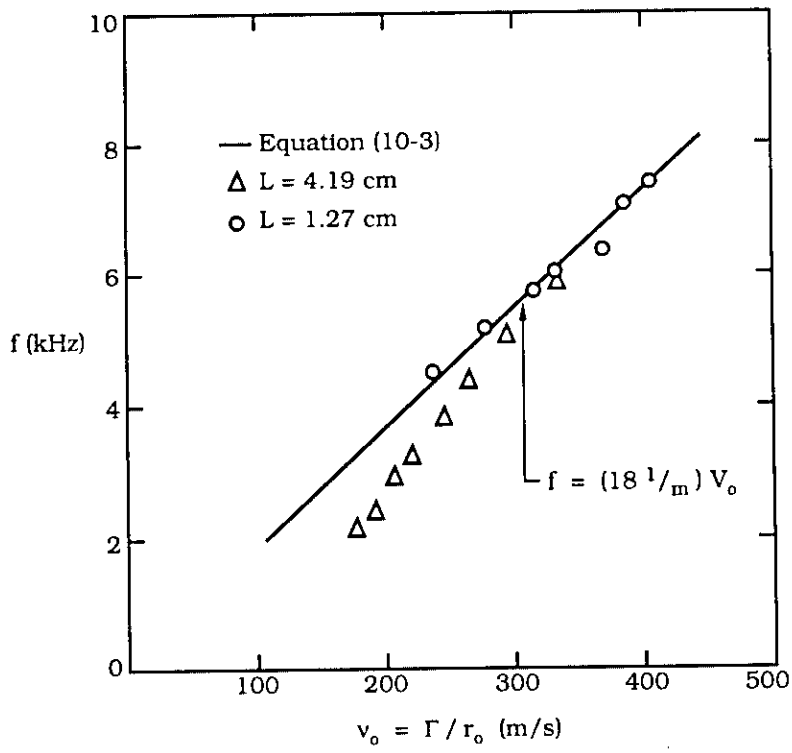

Figure 10-5. Comparison of Calculated and Measured Frequencies for a Vortex Tube. (Reproduced from Kurosaka.[9])

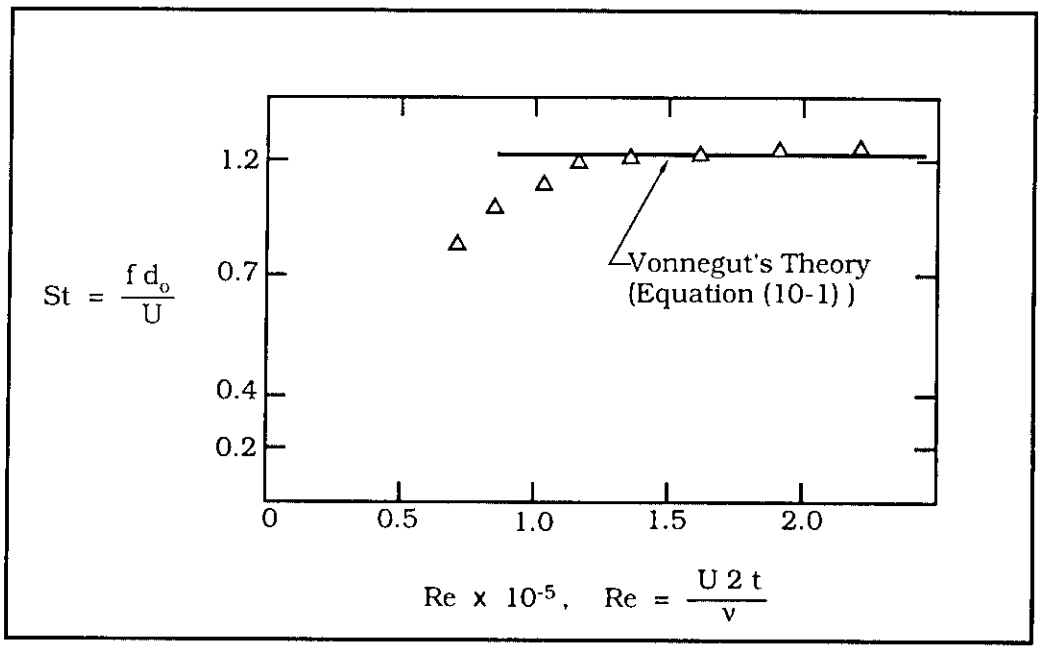

(a) Ring Inlet Chamber.

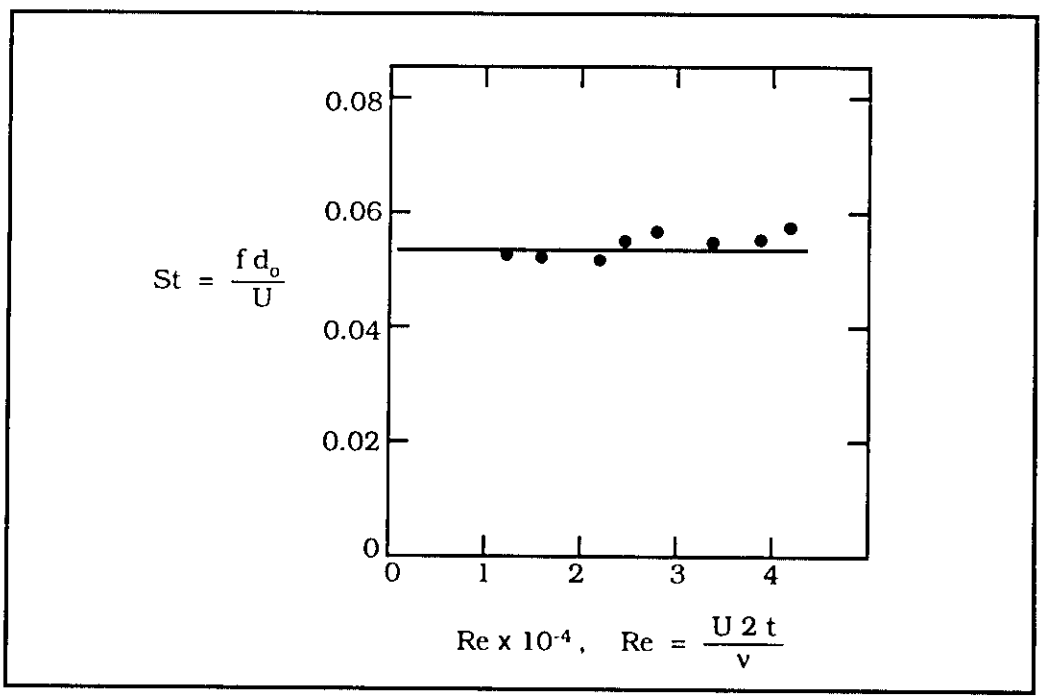

(b) Ring Exit Chamber.

Figure 10-6. Variation of Strouhal Number With Reynolds Number for Ring Chamber Inlet (a) and Exit (b). (Reproduced from Escudier and Merkli.[11,12])

shown in the figure, the Strouhal number ($St = \frac{f d_o}{U}$) has a constant value of 1.2 over the Reynolds number range of $1.2 \times 10^5 < Re < 2.25 \times 10^5$. At lower values of Reynolds number, the Strouhal number was observed to steadily decrease as Reynolds number decreased. Merkli used $Re = 2t\,U/\nu$ to define Reynolds number, where t is the annulus width and U is the average velocity in the annulus.

Merkli and Escudier observed that the ring chamber had two entirely different flow regimes. At flow rates below a critical Reynolds number the incoming flow splits symmetrically into two branches, which explains the observed decrease in Strouhal number below $Re = 1.2 \times 10^5$. At flow rates above the critical Reynolds number, the flow exhibited a swirling motion and in many respects showed similar features to the vortex whistle.

A cut-away diagram of the ring exit chamber model used by Merkli and Escudier is shown in Figure 10-1d.[12] These experiments were carried out for values of t/R varying from 0.16 to 0.58 and a Reynolds number between 1×10^4 and 6×10^4.

Flow visualization of the ring exit chamber revealed the existence of a strong vortex. The spatial structure resembled that of a helix wrapped around the ring axis. The helix shape is a result of the coriolis forces induced in the swirl as it bends around the ring. The two ends of the vortex core do not join; rather both ends turn into the end of the exit tube, as shown in Figure 10-7. This fact was confirmed by pressure measurements made at the chamber exit. The vortex is not stable but oscillates periodically about the central axis of the ring chamber.

Figure 10-6b shows the variation of Strouhal number with Reynolds number for the ring exit chamber. When the Reynolds number exceeds 10^5, the Strouhal number ($St = \frac{f d_o}{U}$) is equal to 0.052, is independent of the t/R ratio, and is only weakly dependent on the Reynolds number. The frequency of oscillation is unaffected with variations in the annulus width. The most notable change in the flow structure is that the amplitude of the helix increases or decreases depending upon the selection of t/R. Also, the first harmonic is very well defined and harmonics up to the sixth order are detectable.

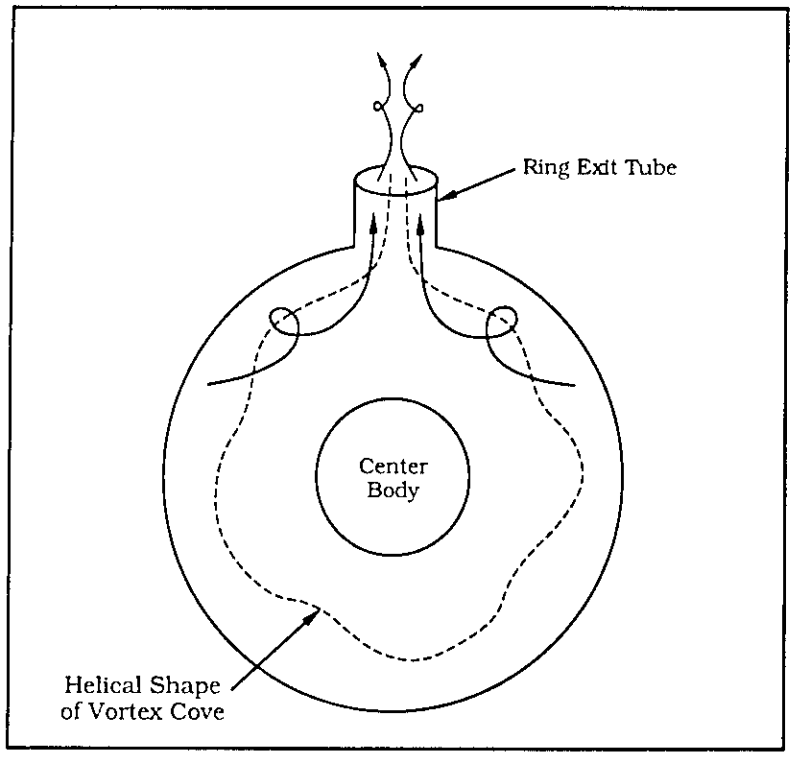

Figure 10-7. Axial View of Vortex Core in Ring Exit Chamber.

Example Calculation

As an example, consider the model of a ring exit chamber investigated by Merkli and Escudier.[11,12,13] The diameter of the model, D, is reported to be 135 mm. The inlet and outlet pipes have a diameter, d_o, of 55 mm. Suppose the ring chamber and the exit tube are represented by a T-tube with the two top branches wrapped around a cylinder and joined together at the two ends. Using the geometric data from the Merkli and Escudier model, the T-tube dimensions become l_o = 209 mm, L_o = 185 mm, and r = 27.5 mm (see Figure 4-2). The value of L_o is determined assuming 2 (L_o + r) = πD.

From the previous section, it was shown that the Strouhal number for a ring exit chamber is equal to 0.052. Assuming the speed of sound in the gas is 341 m/sec, the frequency for flow instabilities is

$$f = 322 \times (\text{Mach number}) \qquad (10\text{-}4)$$

To calculate the acoustic resonance inside the T-tube, use Equations (4-12a) and (4-23). The effective lengths appearing in these equations are calculated from Equations (4-19), (4-20), and (4-24). Table 10-1 shows the results from these calculations.

A comparison of measured pressure spectra at different mass flow rates appears in Figure 10-8. The pressure spectra contain pressure peaks due to the flow instability and peaks due to the acoustic resonance characteristics of the model. The pressure peaks due to flow instabilities increase in frequency with flow rate and are in agreement with Equation (10-4). The calculated acoustic resonance frequencies, drawn in the figure, were determined by Merkli and are in good agreement with the resonance frequencies presented in Table 10-1.

Table 10-1

Calculated Resonance Frequencies
For the Ring Exit Chamber

Top of T-Tube Equation (4-12a)	**Stem Equation (4-23)**
1382	146
2304	591
	902
	1315
	1671
	2033
	2441
	2755

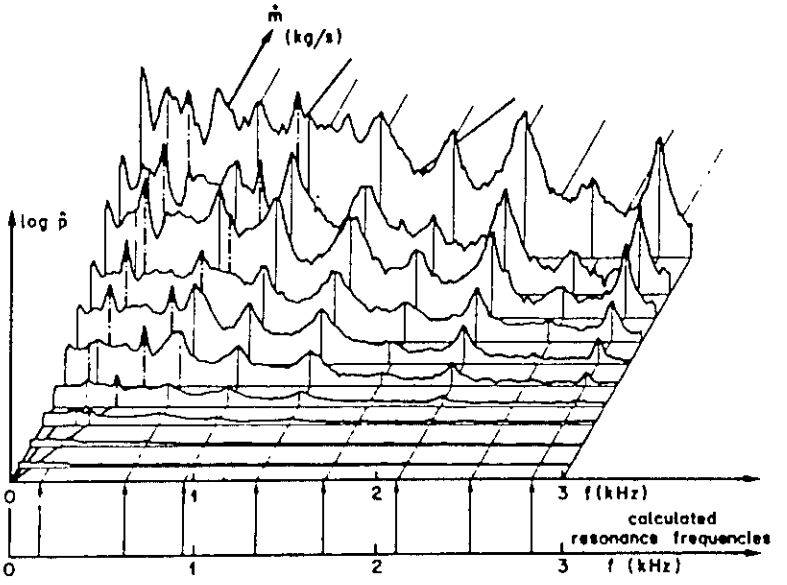

Figure 10-8. Frequency Spectra of Fluctuating Pressure at $\theta = 5$ deg for Model With Disk, Together With Calculated Acoustic Eigenfrequencies ($t/R = 0.16$).
(Reproduced from Escudier and Merkli.[11])

REFERENCES FOR CHAPTER 10

1. Escudier, M.P., "Confined Vortices in Flow Machinery", *Annual Rev. Fluid Mech., 19*, 1987, 27-52.

2. Leibovich, S., "Vortex Stability and Breakdown: Survey and Extension", *AIAA Journal, 22* (9), 1984, 1192-1206.

3. Escudier, M.P., "Vortex Breakdown: Observations and Explanations", *Prog. Aerosp. Sciences, 25*, 1988, 189-229.

4. Vonnegut, B., "A Vortex Whistle", *J. Acoust. Soc. Am., 26* (1), 18-20.

5. Chanaud, R.C., "Experiments Concerning the Vortex Whistle", *J. Acoust. Soc. Am., 35*, 1963, 953-960.

6. Chanaud, R.C., "Observations of Oscillatory Motion in Certain Swirling Flows", *J. Fluid Mech., 21*, 1965, Part 1, 111-127.

7. Kurosaka, M., "Acoustic Streaming in Swirling Flow and the Ranque-Hilsch (Vortex-Tube) Effect", *J. Fluid Mech., 124*, 139-172.

8. Ranque, M.G., *J .de. Phys.* et rad [7],4,112 (1933)

9. Hilsch, R. "The Use of the Expansion of Gases in a Centrifugal Field as Cooling Process", *The Review Of Scientific Instruments, 18* (2), February 1947, 108-113.

10. Lighthill, M.J., "Acoustic Streaming", *J. Sound Vib., 61* (3), 1978, 391-418.

11. Merkli, P., and Escudier, M.P., "Observations of Flow in a Ring Inlet Chamber", *J. Fluid Eng., 101*,, March 1979, 135-142.

12. Escudier, M.P., and Merkli, P., "Observations of the Oscillatory Behavior of a Confined Ring Vortex", *AIAA Journal, 17* (3), March 1979, 253-260.

13. Merkli, P., "Acoustic Resonance Frequencies for a T-Tube", *J. Applied Math. and Physics (ZAMP), 29*, 1978, 486-498.

CHAPTER 11

IMPINGING SHEAR LAYERS

by Michael J. Lucas
Wyle Laboratories

The consequence of a shear layer impinging on a downstream obstacle or edge can be the generation of a highly coherent disturbance. Impinging shear layers are recognized as a primary cause of unsteady pressure loading and noise radiation inside turbomachinery. Flow paths inside turbomachinery associated with this type of noise production include: the flow exchange between nozzles and turbines; the flow exchange between impellers and diffusers; the movement of fuel or lubricant over engine cavities; and the impinging wake generated by flow past bluff bodies as from struts and turning vanes on downstream obstacles.

In this chapter, the problem of a shear layer impinging on a downstream surface or edge will be presented for selected geometries. Section 11.1 provides an overview of the flow mechanics for basic shear layer impingement geometries. Section 11.2 describes the models for estimating the most highly amplified disturbance frequencies for a jet stream impinging on: an edge (classical edgetones), a perpendicular flat plate, and a perpendicular flat plate with a hole in its center. Section 11.3 contains acoustic and hydrodynamic models for estimating the disturbance frequency generated from cavity oscillations.

11.1 Overview

A summary of the types of shear layer impingement as categorized by Rockwell and Naudascher[1] is shown in Figure 11-1. The figure illustrates a dozen examples, classified by shear layer type. The three categories are planar jets, axisymmetric jets, and planar and axisymmetric mixing layers. The feature common to all of these is the pressure-phase relationship between the disturbance generated by the organized vorticity impinging on a downstream surface or edge, and its pressure convergence upstream in the vicinity of the separation edge. This pressure feedback selectively amplifies the shear layer, causing the flow fluctuations to occur within a narrowband of frequencies, that produce preferred "stages" or modes of oscillation.

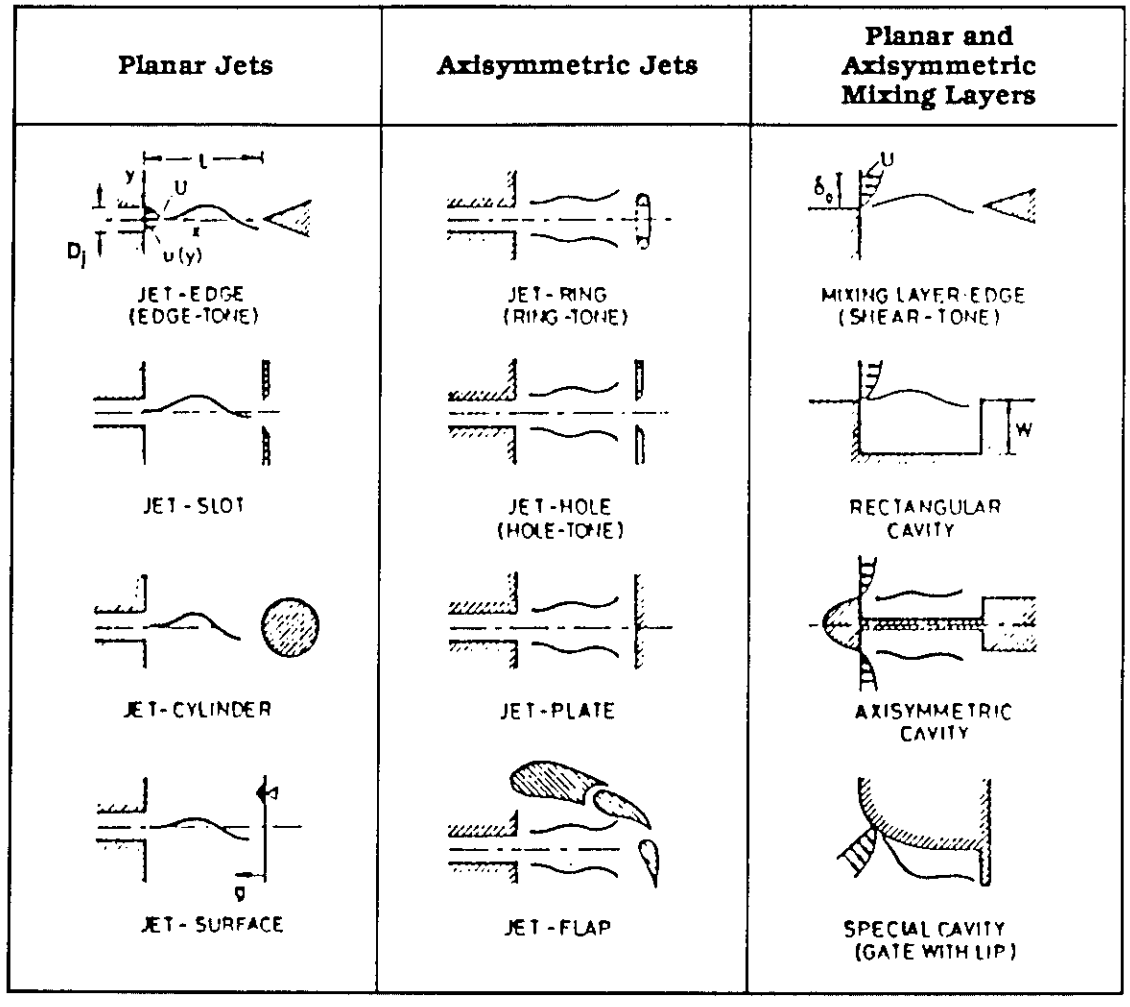

Figure 11-1. Basic Configuration of Shear-Layer and Impingment-Edge Geometries That Produce Self-Sustained Oscillations. (Reproduced from Rockwell and Naudascher.[1])

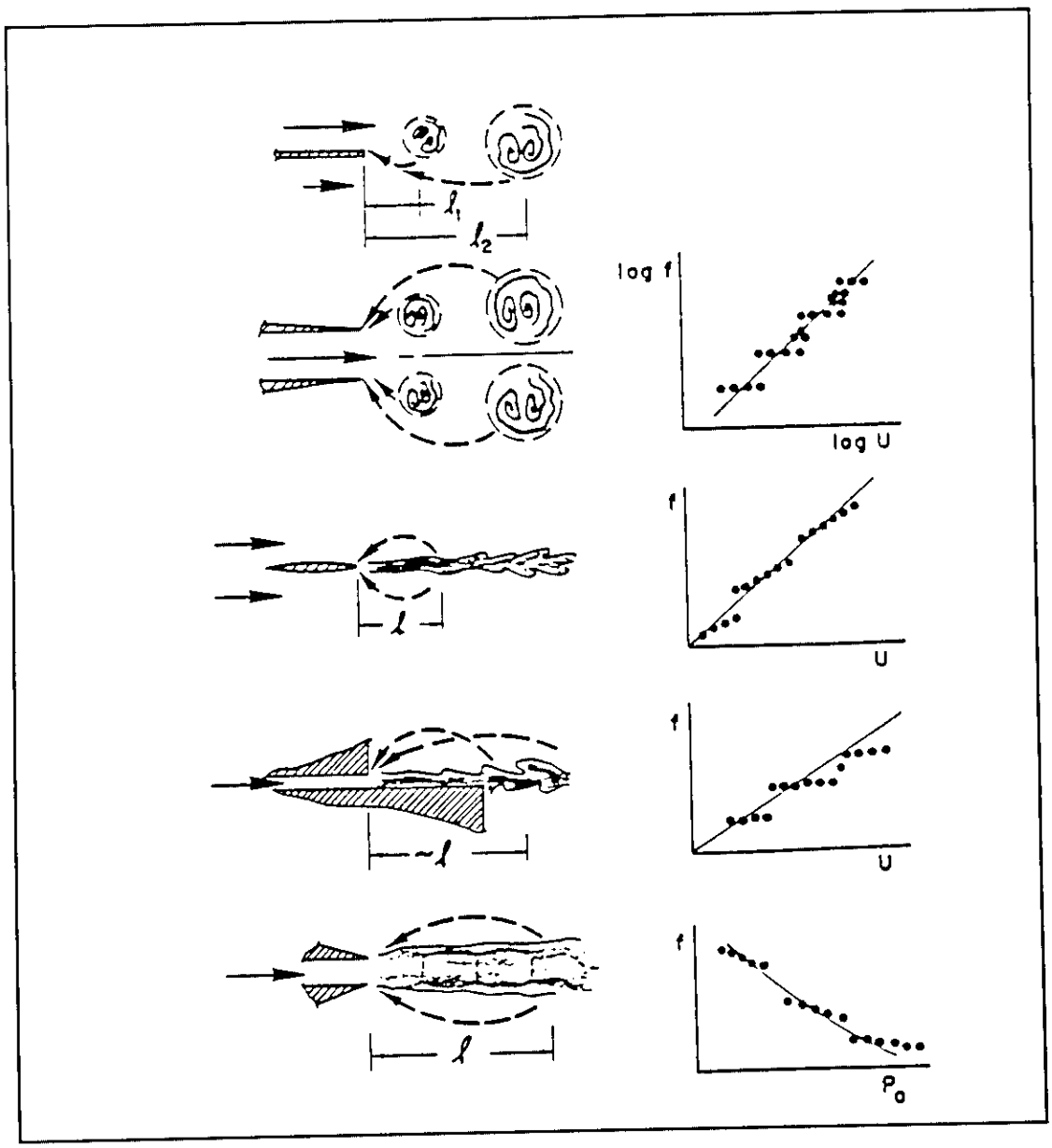

Figure 11-2. Apparent Streamwise Length Scales for a Variety of Non-Impinging Flows, and Typical Variation of Frequency (f) Versus Velocity (U). (Reproduced from Rockwell.[2])

Without the edge, the flows shown in Figure 11-1 may still exhibit a natural feedback process during vortex breakdown as shown in Figure 11-2. In a non-impinging flow, the downstream unsteadiness acts as an origin of upstream influences. An "apparent" length scale l is used to relate the vortex formation and pairing in a free shear layer. In a typical shear layer there might be a number of values for l. The consequence of the apparent length scale is the ladder-like change in the frequency (see Figure 11-2) that is observed when the velocity is increased. The mathematical description of this frequency-controlled behavior is

$$\frac{l}{U_c} + \frac{l}{c} = \frac{n}{f} \qquad (11\text{-}1)$$

where l = apparent length scale,

U_c = phase speed of the disturbance,

c = speed of sound,

f = frequency, and

n = stage of oscillation.

The stage of oscillation, represented by n/f in Equation (11-1), is the period of shear-layer oscillation or vortex shedding. The successive ladder-like jumps shown in Figure 11-2 are accounted for by higher values of n.

The events that lead to the establishment of a highly amplified disturbance from an impinging shear layer are described in the context of the edgetone generator. The essential features of an edgetone generator are shown in Figure 11-3. The feedback process is explained as: (1) the initiation, at the jet exit, of a disturbance wave; (2) the growth and propagation of the disturbance in the streamwise direction; (3) the impingement of the oscillating jet on an edge; and (4) the subsequent generation near the impingement point of an acoustic disturbance which is fed back to the sensitive region of the jet near the exit.

At low Mach numbers, nearly all flows of interest satisfy the criteria that the impingement distance, L, divided by the acoustic wavelength, λ_a, is much less than unity ($L/\lambda_a \ll 1$). This means that the upstream source lies in the non-propagating region. That is, the disturbances arising from the impingement edge are instantaneously felt at all upstream locations. For nearly all conditions in liquids, the condition $L/\lambda_a \ll 1$ is satisfied and the propagation of the disturbance is purely hydrodynamic.

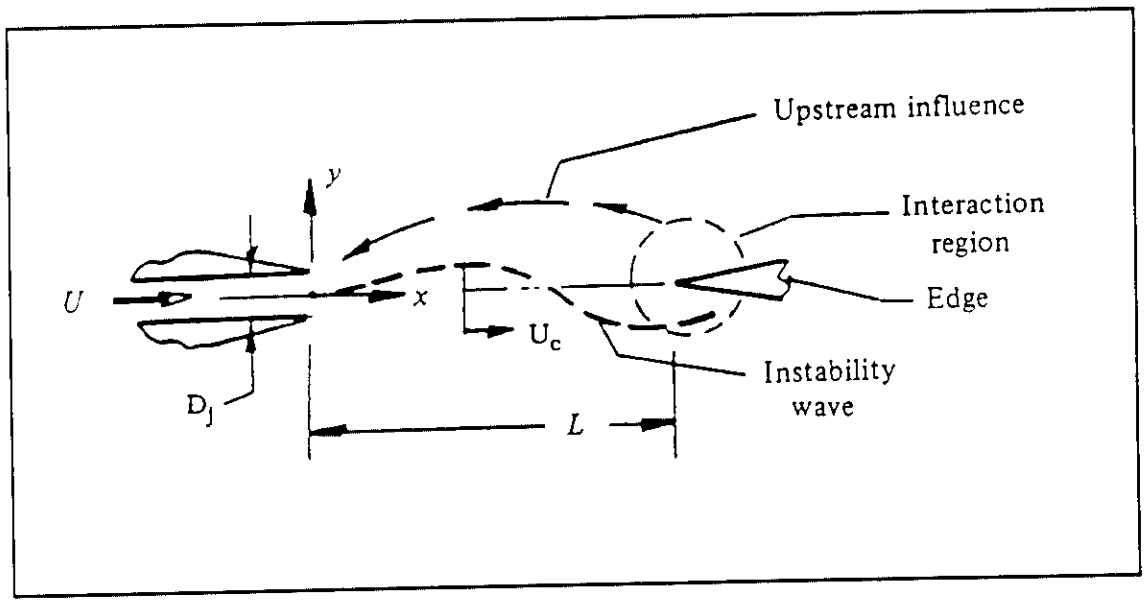

Figure 11-3. Features of an Edgetone Generator.

In the case of higher speed flows, for which the acoustical wavelength is relatively short, the upstream region can lie in the propagating region of the feedback disturbance. In this situation, the acoustic speeds become important when evaluating the delay time between impingement and the location of the shear-layer separation. Also, under these conditions the strength of the upstream influence is considerably larger than the case where the acoustic wavelength is very long.

In the case of an impinging flow, Blake[3] makes the following elementary description which applies to most of the frequency prediction models found in the literature. Consider the motion of a free shear layer. As described in Chapter 7, the fluctuating component of velocity for a spatially growing disturbance can be written as

$$\tilde{v}(x) = \tilde{v}\, e^{\alpha_i x}\, e^{i(\alpha_r x - \omega t)}, \quad 0 \le y \le L \tag{11-2}$$

where $\tilde{v}$ = fluctuating component of vertical velocity;

α_i = imaginary part of wave number (amplification factor); and

α_r = real part of wave number (equal to ω/c).

At the downstream edge the vertical component of velocity becomes

$$\tilde{v}(L) = \tilde{v}\, e^{\alpha_i L}\, e^{i(\alpha_r L - \omega t)}. \qquad (11\text{-}3)$$

Coupling is optimum when the downstream hydrodynamic disturbance wavelength is $\pi/2$ out of phase with the upstream edge. The phase relationship may be written as

$$\alpha_r L = 2n\pi - \pi/2\ , \quad n = 1, 2, 3, \ldots \qquad (11\text{-}4)$$

By substituting $\alpha_r = 2\pi f/U_c$ into the above expression, the preferred frequencies

$$f_n = \frac{U_c}{L}\left(n - \frac{1}{4}\right), \quad n = 1, 2, 3, \ldots \qquad (11\text{-}5)$$

are derived. In Equation (11-5), n is an integer and is sometimes referred to as the mode or stage of oscillation. This simple model ignores frequency synchronization that may arise from other acoustic resonators.

This relationship is sometimes modified to account for a phase lag that can occur between the encounter of the vortex sheet with the edge and its pressure response to the edge. The lag in phase is denoted by ϕ and is potentially significant for compressible flows. The incompressible limit is $\phi = 0$. The general expression for this condition may be written as

$$\alpha_r L + \phi = 2\pi\left(n \pm \frac{1}{4}\right), \quad n = 1, 2, 3, \ldots \qquad (11\text{-}6)$$

Blake shows that this relationship written in terms of a Strouhal number is

$$\frac{f_n L}{U_m} = \frac{U_c}{U_m}\left(n - \frac{1}{4} - \frac{\phi}{2\pi}\right), \quad n = 1, 2, 3, \ldots \qquad (11\text{-}7)$$

where L is the impingement length scale, U_m is mean speed of the flow, and U_c is the phase speed of the disturbance.

11.2 Impinging Flows From Jets

This section contains a discussion on the models that may be used to predict the most highly amplified disturbances for a jet stream that impinges on an edge, Section 11.2.1; a plate, Section 11.2.2; and a plate with a hole in its center, Section 11.2.3.

11.2.1 Jet-Edge Configuration

Sound levels produced by a jet-edge configuration, referred to hereafter as "edgetone", was first recorded by Sondhaus[4] in 1854. Many investigations and theories have been proposed to explain the cause of this sound. Powell[5] provided the first rigorous theoretical explanation on the nature of edgetone sound production. He demonstrated that the leading edge can be treated as an acoustic dipole source which disturbs the jet and that the instability characteristics are dependent on the Reynolds number, the Strouhal number, and the jet-to-edge separation distance.

Oscillations inside organ pipes and wind instruments have long been associated with the phenomenon of edgetones. This association is not entirely correct since jet edge interactions and their resultant forces are not essential to the production of sound. The oscillation in an organ pipe, for instance, is due to the modulation of the jet-profile caused by a feedback from the standing wave field inside the pipe. In contrast, the jet-edge interactions are known to play a major role when the jet-to-resonator coupling is weak.

The non-dimensional variables important to the edgetone phenomenon are: (1) the Reynolds number, $Re = U_m D_j/\nu$, based on U_m, the mean velocity in the nozzle; (2) the Strouhal number, $St = f D_j/\nu$, that introduces the frequency f; (3) the distance separating the jet nozzle and the leading edge divided by the nozzle width, L/D_j; (4) the disturbance amplitudes, such as $\tilde{u}$ and $\tilde{v}$, which are expressed in some suitable non-dimensional form; and (5) the velocity profile at the jet exit.

The frequency dependence on jet efflux speed and impingement length of an edgetone generator are shown in Figure 11-4. The frequency increases when either the velocity of the jet is increased or the distance separating the jet exit and the leading edge is decreased.

Jumps in frequency separate the stages in an edgetone generator. Figure 11-4a shows that as the frequency progressively increases with increasing Reynolds number, a critical Reynolds number is reached where the frequency jumps up from the original operation curve, referred to as stage 1, to a new curve, stage 2. As the Reynolds number is subsequently reduced, the downward frequency jumps from stage 2 to stage 1 with the transition occurring at a lower

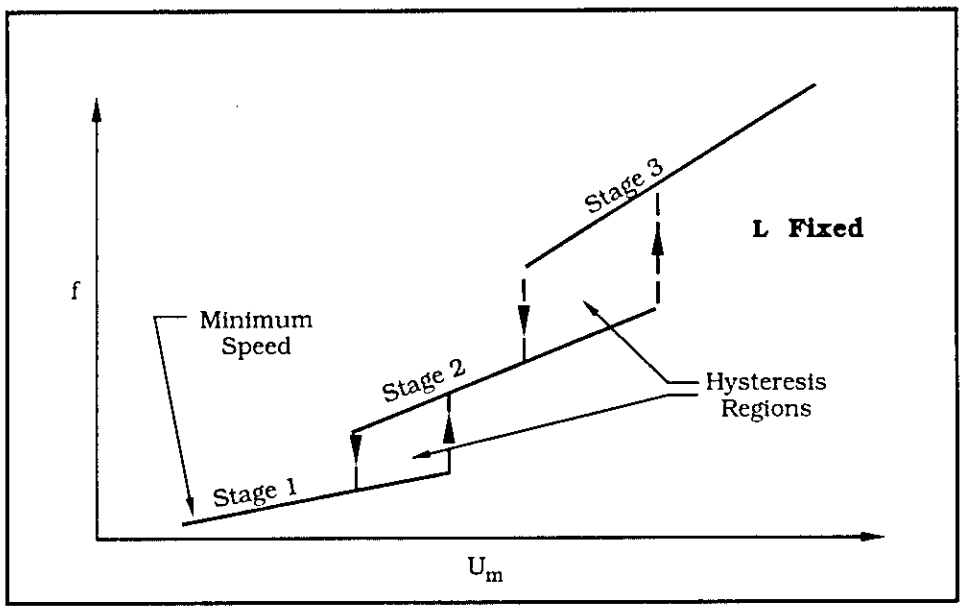

(a) Jet Efflux Speed, U_m .

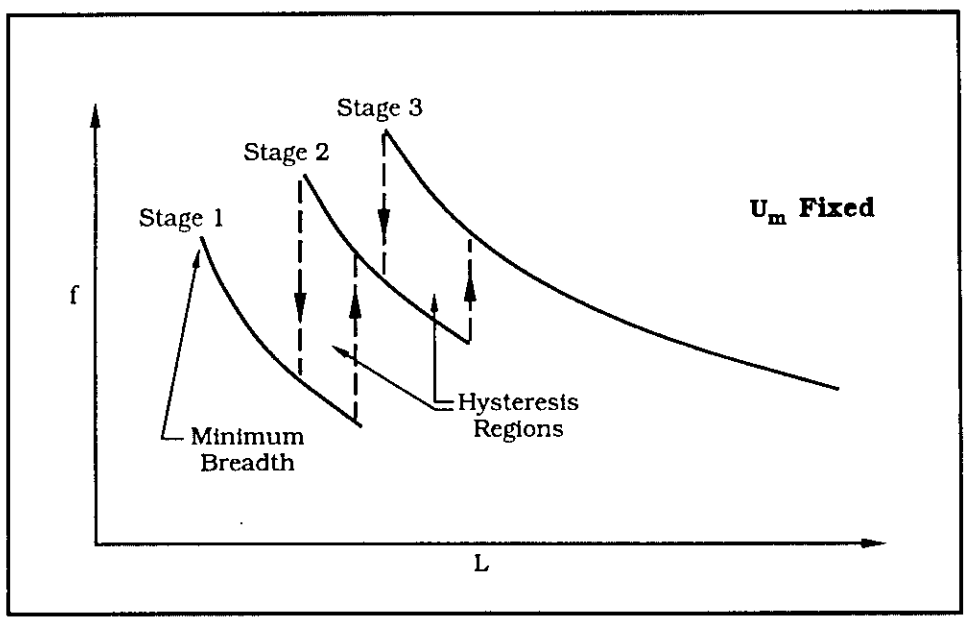

(b) Impingement Length, L .

Figure 11-4. Variation of Edgetone Frequency With Jet Efflux Speed and Impingement Length. (Reproduced from Karamcheti *et al.*[6])

Reynolds number than the jump-up. This results in a hysteresis region being formed. Figure 11-4b shows a similar trend in frequency as the impingement length is increased and decreased.

At a fixed edge distance there is a minimum Reynolds number below which edgetones disappear. Conversely, at a fixed Reynolds number there is a minimum slit-to-edge distance at which sound production begins. These minima are indicated on Figure 11-4.

11.2.1.1 *Survey of Experimental Investigations*

A survey of experimental edgetone measurements with planar and axi-symmetric jets is shown in Table 11-1. Most of the measurements have been made for planar jets in air with a nozzle width of 1 mm. The impingement edge for most of the studies has been a wedge; in a few instances a cylinder was substituted for the wedge. In many of the lower Reynolds number studies (Re < 2000), the velocity profile at the nozzle exit is fully developed and parabolic in shape. These profiles are very similar to the ones modeled by Bickley[7] and Sato,[8] which were discussed in Chapter 7.

Figure 11-5 shows curves of neutral stability that were developed by Powell and Unfried.[18] The region of edgetone activity lies below the neutral stability curves. It appears from the figure that edgetones would not exist for a Reynolds number below 50 and above 3000. In practice, the creation of edgetones for Reynolds below 50 and above 3000 are not always feasible. An extensive review article by Powell[19] describes the instabilities associated with higher Reynolds number jets. Recently, Umeda *et al.*[9] and Krothapalli and Horne[14] measured high-speed edgetones at Mach numbers ranging between 0.2 and 0.8 both in an axisymmetric and a planar jet.

Figure 11-6 shows measurements made by Powell[5] of Strouhal number versus Reynolds number of a planar jet with a nozzle width of 1 mm. In this figure the velocity is the mean velocity of the jet and the wedge has an included angle of 30 degrees. Lucas and Rockwell[16] showed that due to the rapid non-linear distortion of the shear layer the Strouhal number will retain a primary frequency of β and will exhibit as many as seven components that are sums and differences of β and $1/3\ \beta$. Possible relationships are

Table 11-1

Summary of Edge Tone Experiments With Planar and Axisymmetric Jets

Author	Year	Dia/Wd	Planar or Axisymm.	Air or Water	Re Range		St Range		L/D_j Range	
					Min.	Max.	Min.	Max.	Min.	Max.
Umeda, Maeda, Ishii[9]	1986	0.3937	A	A	1×10^5	1.6×10^5	0.29	1.65	0.5	8
Stegen & Karamehet[10]	1970	0.0642	P	A	580	580	0.08	0.1	5.58	5.58
Brown[11]	1935	0.039	P	A	1,050	1,050	0.02	0.198	3	16
Coltman[12]	1976	0.062	P	A	377	1,416	0.069	0.076	4.4	4.4
Lenlham & Richardson[13]	1940	0.0748	P	A	1,000	1,500	0.333	0.84	1.6	5.6
Powell[5]	1961	0.039	P	A	100	2,500	0.01	0.3	5	10
Krothapalli & Horine[14]	1988	0.118	P	A	3×10^4	5×10^4	---	---	6.25	6.5
Gross[15]	1959	0.012–0.034	P	W	50	150	0.005	0.04	17	62
Rockwell & Lucas[16]	1984	0.5	P	W	250	900	0.04	0.3	7.5	7.5
Rockwell[17]	1972	0.77	P	W	600	7,000	0.03	0.2	2.5	10.8

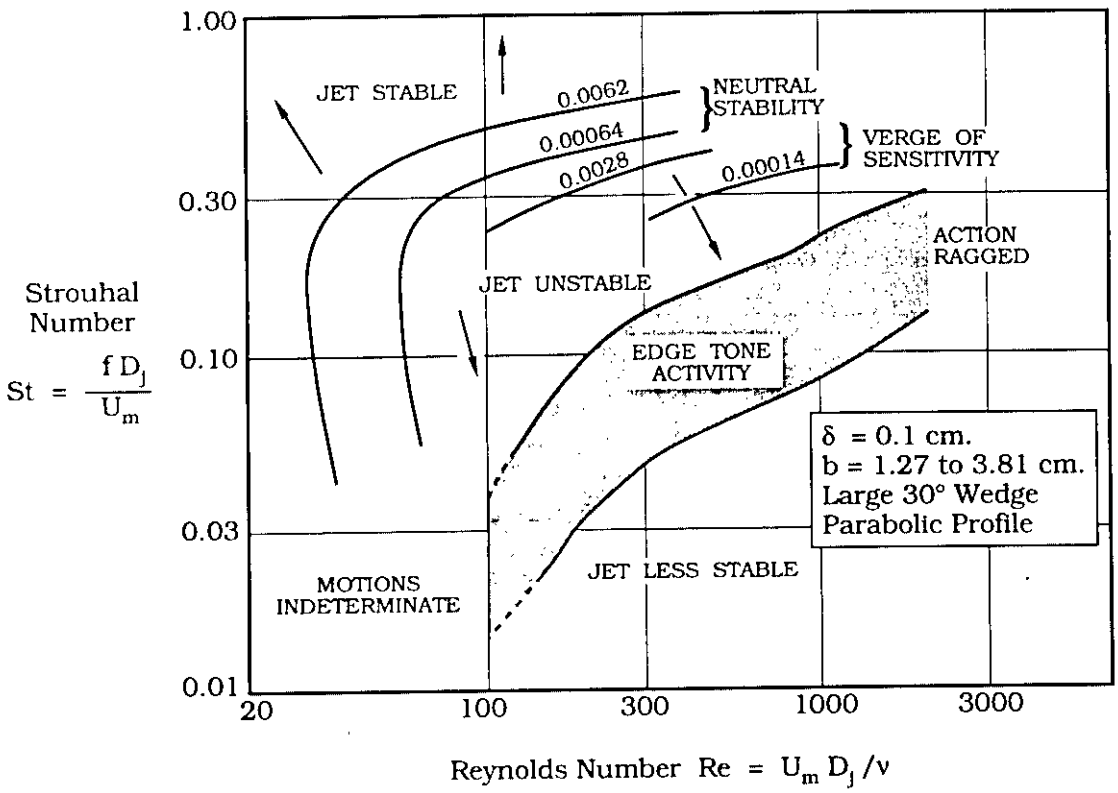

Figure 11-5. Neutral Stability Curves and Regions of Jet Instability and Edgetone Action.
(Reproduced from Powell and Unfried.[18])

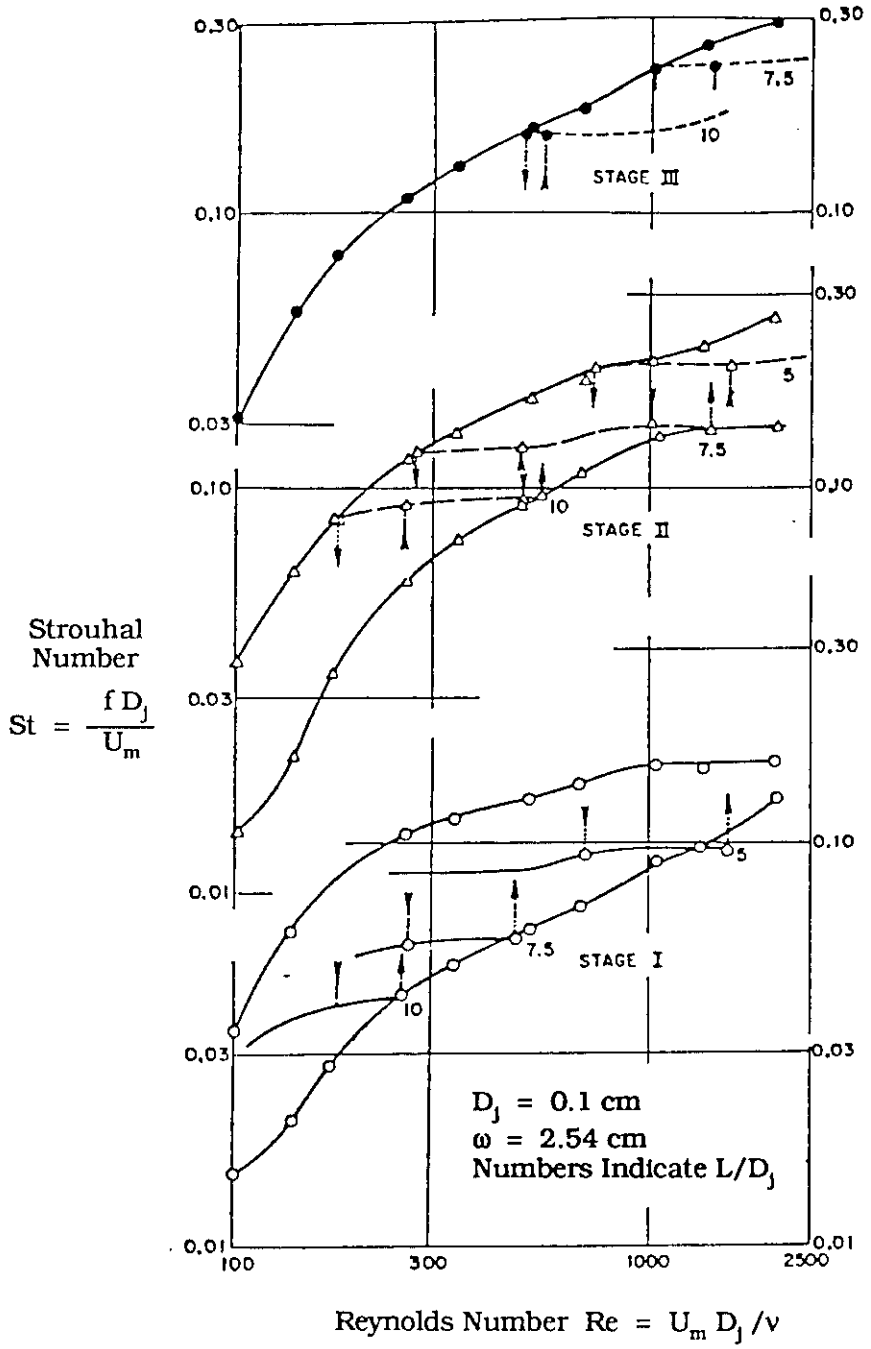

Figure 11-6. Regions of Activity for Three Individual Stages of Instability in a Planar Jet. (Reproduced from Powell.[5])

$$\frac{1}{3}\beta,$$

$$\frac{2}{3}\beta = \frac{1}{3}\beta + \frac{1}{3}\beta,$$

$$\frac{3}{3}\beta = \beta,$$

$$\frac{4}{3}\beta = \beta + \frac{1}{3}\beta, \qquad (11\text{-}8)$$

$$\frac{5}{3}\beta = \beta + \frac{2}{3}\beta,$$

$$\frac{6}{3}\beta = \beta + \beta,$$

$$\frac{7}{3}\beta = 2\beta + \frac{3}{3}\beta$$

11.2.1.2 *Survey of Edgetone Frequency Prediction Models*

Brown[20] made experimental measurements of a 1 mm orifice width planar jet impinging on a wedge with an included angle of 20 degrees. Brown suggested the relationship

$$f = 0.466\ \alpha\ (U_m - 40)\ (1/L - 0.07) \qquad (11\text{-}9)$$

where U_m = mean velocity in the nozzle;
L = distance from the slit to the edge of the wedge; and
α = 1.0, 2.3, 3.8, and 5.4 for stages 1, 2, 3, and 4, respectively.

Equation (11-9) assumes cgs units and is limited to the range of Strouhal numbers

$$0.035 < fL/U < 0.15 \qquad (11\text{-}10)$$

Lenihan and Richardson[13] later revised this formula using a 1.9 mm width jet impinging on a cylinder 0.47 mm in diameter. Their formula is

$$f = 0.466\ \alpha\ U_m\ (1/L - 0.07) \qquad (11\text{-}11)$$

where α = 1.0, 2.7, 3.8, 5.4, 7.2, and 9.2 for stages 1 through 6, respectively. In Equation (11-11), the values of α remain the same as in Equation (11-9), except that two additional values for α (7.2 and 9.2) have been added to the series given by Brown. Also, Lenihan and Richardson suggest the value of 2.7, instead of 2.3, for the value of α in the second stage.

Curle[21] developed a semi-empirical theory based on the growth of discrete vortices on either side of a planar jet. From Brown's flow visualization[20] Curle deduced the ratio of the impingement length, L, to wavelength is equal to

$(n + 1/4)$, where n is an integer. Next, Curle combined the expression for the convective velocity from Savic[22] with the experimental results of Brown to form the relationship

$$f = 0.5\ U_m \left(\frac{n+1/4}{L} - \frac{1}{30D} \right) \qquad (11\text{-}12)$$

which is valid only when L/D_j is ≥ 10. Curle's observation that the wavelength is one-quarter out of phase with the vortices shed from the nozzle lip incorporated the overall concept of disturbance feedback.

Nyborg[23] cast the equation of motion for a line of unconnected particles traveling in a jet-edge system. He considered the jet to be infinitesimally thin and the shape of the jet centerline to be

$$y(t) = \int_{t-\delta_o}^{t} (t - \tau)\ g[L - x(\tau)]\ \phi[y(\tau)]\, d\tau \qquad (11\text{-}13)$$

where δ_o = the time required for a particle to travel from the nozzle to the edge,

x = particle horizontal distance measured from the nozzle,

y = vertical distance of the thin jet stream as measured from the jet centerline,

t = time,

$(t-\tau)$ = time particle left orifice and is at distance x,

g = function that describes the dependence on distance from particle to edge,

ϕ = instantaneous vertical displacement y of the free end, and

L = distance from the slit to the edge of the wedge.

Nyborg's theory states that the particles move in the thin jet stream from the nozzle to the edge with a prescribed velocity $u(x)$. While the vertical acceleration of the particle is dependent upon two quantities: $g[L - x]$ and $\phi[y]$, Nyborg assumed an elementary form for g and ϕ to be

$$g[L - x] = 1, \quad 0 < (L - x) < L \qquad (11\text{-}14)$$

$$\phi[y] = \begin{cases} B, & y < 0 \\ -B, & y > 0 \end{cases}$$

In Equation (11-14), g represents the vertical force acting on the jet at any instant and is the same at all points in the region $0 < x < L$. ϕ is equal to B, the shear layer amplitude, whenever y is negative; and -B when y is positive. Substitution of these

functions into Nyborg's integral equation gives for the shear-layer frequency the relationship

$$f_m = \frac{1}{2\,\delta_o}\,[n\,(n+1)]^{1/2}\,, \quad n = 1, 3, 5, \ldots \qquad (11\text{-}15)$$

where the value of n is an odd integer. The determination of the value of δ_o requires knowledge of u(x), which is generally not available.

Tabulated in Table 11-2 are the ratios of frequencies between stages. Since the ratios between frequencies of the different stages are independent of u(x), Nyborg's and Brown's predictions are shown in the table for comparison. The values of n used for Nyborg's formula 1, 3, 5, and 7 for the observed stages of 1, 2, 3, and 4.

Table 11-2

Shear Layer Frequencies for Nyborg[23] and Brown[20] Models

Stage Number m	n	Nyborg f_m/f_1	Brown f_n/f_1	Percent Difference
1	1	1.00	1.0	0%
2	3	2.44	2.3	5.7%
3	5	3.86	3.8	1.6%
4	7	5.29	5.4	2.1%

Powell[5] expressed Lighthill's equation for aerodynamic sound production in a form in which the edge is represented as a distribution of dipole sources and the acoustic pressure field surrounding the edge is directly related to the distribution of sources. Powell's formula is suitable for estimating the strength of the pressure and velocity. First, the pressure in the field surrounding the edge at a distance x is given by

$$p(x) = -\frac{1}{4\pi}\,\frac{i\,\omega\,F_o}{x\,a_o}\,\frac{1+2\pi\,i\,x/\lambda}{2\pi\,i\,x/\lambda}\,\cos\theta\,\exp\left[i\,(\omega t - kx)\right] \qquad (11\text{-}16)$$

where the value of θ is the angle between the plane perpendicular to the jet stream and the point of observation. F_o is the amplitude of the fluctuating lift force at the edge. An upper limit for this force is given by Powell to be

$$F_o = 5\,\rho_o\,U_m^2\,b\,D_j \qquad (11\text{-}17)$$

where D_j is the thickness of the jet at the nozzle exit and b is the width of the jet.

When the distance between the nozzle and the edge considerably exceeds the greater dimension (b) of the rectangular orifice ($L/b \gg 1$), the induced velocity field at the orifice, due to the vortex action near the wedge, is given by Powell as

$$U_o = \frac{1}{4\pi}\left(\frac{F_o\, e^{i\omega t}}{i\,\omega\,\rho_o\, L^3}\right). \qquad (11\text{-}18)$$

It is this situation for which the action at the orifice is like that of a point force, even though the nozzle is in the hydrodynamic near field ($L/\lambda \ll 1$).

If, on the other hand, the edge is very close to the nozzle, then the action at the nozzle is more like that of a line dipole of force per unit length. In this case the induced velocity becomes

$$U_o = \frac{1}{2\pi}\left(\frac{F_o\, e^{i\omega t}}{i\,\omega\,\rho_o\, L^2\, b}\right). \qquad (11\text{-}19)$$

In both situations the separation region near the nozzle is the location at which control of the jet motion is established. The frequency at which this motion occurs has to be taken at the eigenvalues of $(n + 1/4)$ where n is the stage number in Brown's terminology. According to Powell, the time required to establish n cycles of motion between the nozzle and the edge is

$$T = \frac{L}{U_c} \qquad (11\text{-}20)$$

where U_c is the hydrodynamic convective wave speed of the disturbance. The frequency then becomes

$$f = \frac{U_c}{L}\left(n + \frac{1}{4}\right). \qquad (11\text{-}21)$$

This may be cast in terms of the Strouhal number as

$$St = \left(\frac{U_c}{U_m}\right)\left(\frac{D_j}{L}\right)\left(n + \frac{1}{4}\right). \qquad (11\text{-}22)$$

11.2.2 Jet–Plate Configuration

This section describes for a jet-plate configuration: (1) the source of the pressure fluctuations, (2) the conditions under which a resonant impinging jet is capable of producing tonal noise, and (3) a prediction methodology which is suitable for estimating the frequency of the jet tone.

High levels of pure-tone noise can be generated when the flow of an axisymmetric jet impinges on a flat plate at a high subsonic speed. The nozzle-to-plate separation distance relates to the creation of a pressure disturbance upstream in the near field which forces, with sufficiently large amplitude, the growth of a shear layer at the nozzle exit. Under these conditions, the jet stream is in a resonant state because the upstream wave has become phased-locked with the wave traveling downstream. The turbulent nature of the jet becomes highly coherent and almost periodic. When the jet is in resonance, the jet stream will produce excessive pressure fluctuations at the surface of the plate. It will also produce a pressure disturbance that is capable of exciting acoustic resonances if the jet were enclosed in a cavity, as is often the situation inside turbomachinery.

The source of pressure loading on the plate is due to an instability process referred to as *collective interaction*.[24] Figure 11-7 illustrates the essential features of a collective interaction. The plate, not shown in the figure, is located downstream from the nozzle exit. The Mach number is greater than 0.7 and the L/D_j ratio is less than 0.75. Shear layer vortices emerge from the nozzle exit with a wavelength of a non-impinging jet. Farther downstream from the nozzle exit the shear layer vortices undergo rapid merging and large-scale coherent structures are created. The merging of the vortex structures is so rapid that it is not likely due to the vortex pairing process as observed in a free jet. The merging of coherent structures is attributed to collective interaction which is characterized by a sharp decrease in frequency and a rapid shear layer growth.

The evolution of the shear layer vortices from the nozzle exit is consistent with the prediction of a free jet. The vortex shedding frequency has a Strouhal number ($St = f D_j / U_m$) that ranges between 3 and 5 and is observed to increase with the square root of the Mach number. These observations agree with theoretical predictions made by Michalke[25] for the jet's initial instability frequencies.

Farther downstream from the nozzle exit, at 1.3 nozzle diameters, the jet transitions to a low-frequency disturbance. The range of Strouhal number of the large-scale structure is reduced to $0.3 < St < 0.4$, which is almost a tenfold decrease from the shear layer instability measured near the nozzle exit.

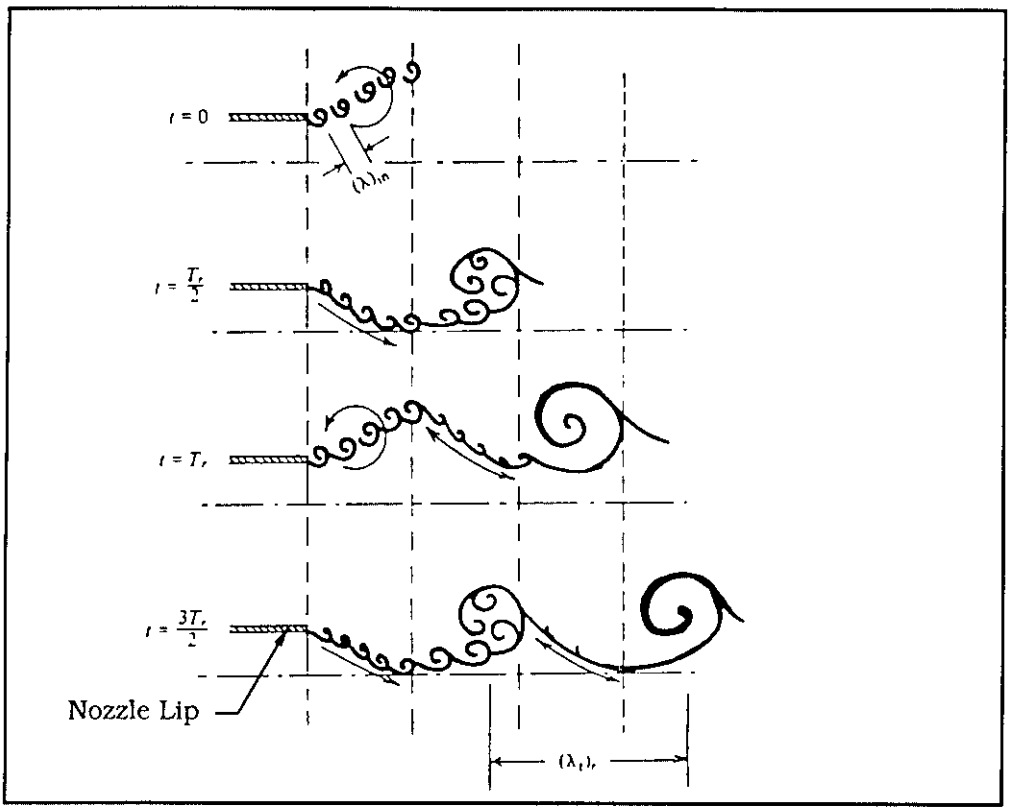

Figure 11-7. Collective Interaction. (Reproduced from Ho and Nosseir.[24])

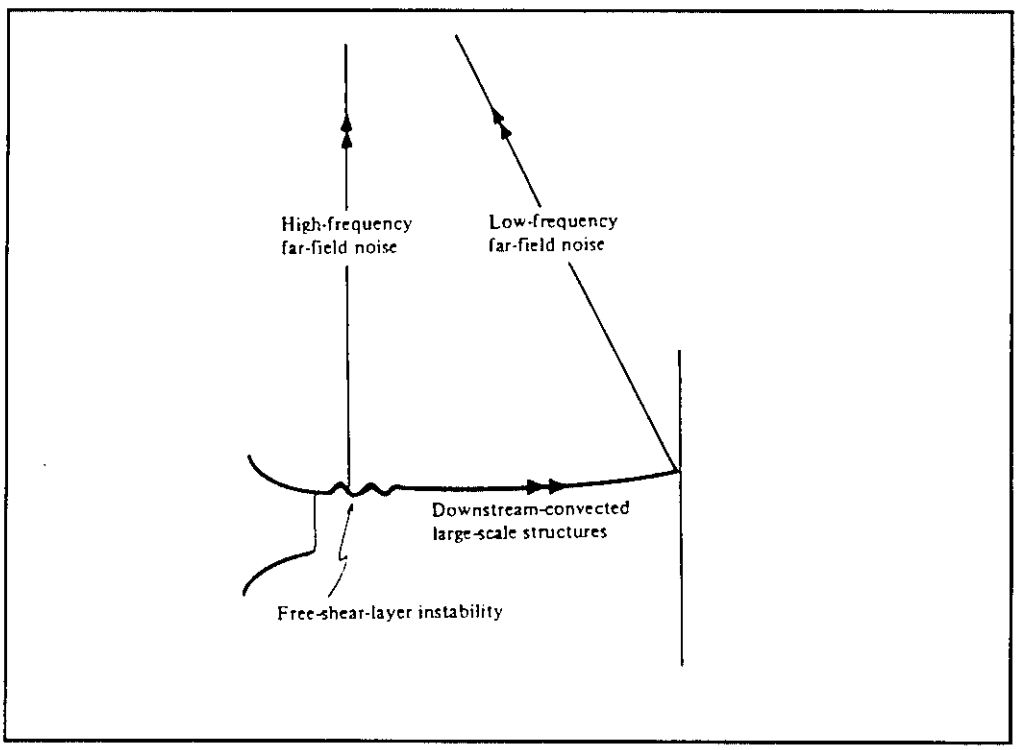

Figure 11-8. Noise-Generation Mechanisms in an Impinging Jet. (Reproduced from Nosseir and Ho.[26])

The high-frequency pressure disturbance associated with the jet instability cannot follow the same acoustic path to the far field as the large coherent structures simply because the instability waves have lost their identity before they have reached the plate. In fact, Nosseir and Ho[26] dentified two separate noise-generating mechanisms, shown in Figure 11-8, that propagate to the far field via two separate paths. One of the acoustic sources is due to vortex shedding, pairing, and their subsequent convection. The other acoustic source is caused by the impingement of the large-scale structures. Most of the far-field pressure disturbance is not attributed to the former acoustic source; rather the primary noise source is the noise generated by vortex impingement at the plate.

Figures 11-9a and 11-9b are the raw pressure signal and power spectrum measured at 0.13 and 1.31 diameters downstream from the exit of a resonating jet. It is seen here that the low-frequency pressure signal has a superimposed high-frequency shedding component. The low-frequency component that dominates the pressure signal illustrates the importance of the vortex impingement at the plate and its subsequent upstream influence.

Figure 11-9c compares far-field power spectrum measurements made at several nozzle-to-plate separation distances. These measurements were made by Marsh[27] using a circular air jet (1.5 inches diameter) with a Mach number of 0.66. From Figure 11-9, the following trends in the power spectrum are noted:

- The frequency of peak SPL decreases with increasing plate separation distance;
- The shape of the spectrum changes from a pronounced peak to a very broad peak with increasing plate separation distance; and
- The magnitude of the peak SPL decreases by 24 dB when the plate is removed.

Not shown in Figure 11-9 is the variation of the overall sound power level with separation distance. Marsh[27] observed that the sound power increased rapidly as the separation distance decreased. At a nozzle-to-plate distance of two diameters the overall sound power level was found to be 10 dB greater than that produced when the plate is removed.

The dependence of Strouhal number on Mach number for both an impinging jet and free jet is shown in Figure 11-10. It is seen here that near the

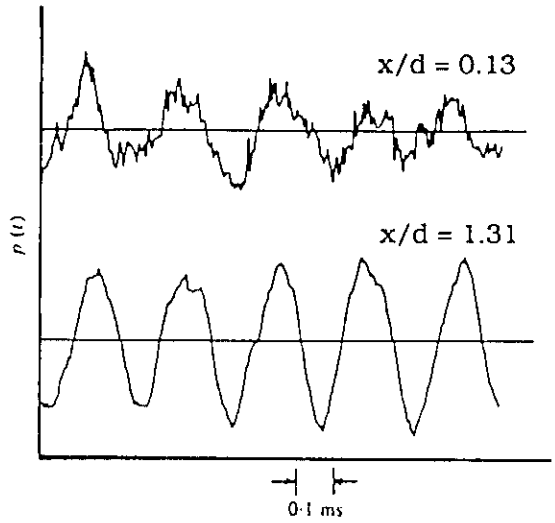

(a) Near-Field Pressure Signals.
M = 0.9 and L/D = 4.5. (Ho and Nosseir.[24])

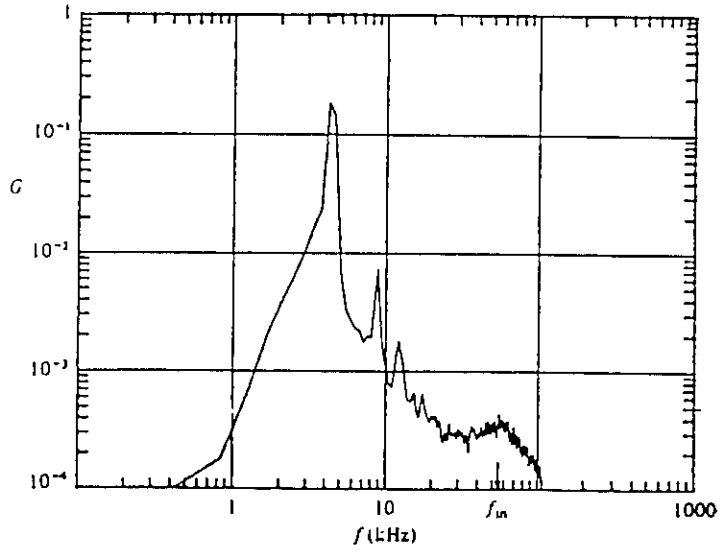

(b) Near-Field Power Spectrum.
M = 0.9, L/D = 4.5, Microphone at x/d = 0.13. (Ho and Nosseir.[24])

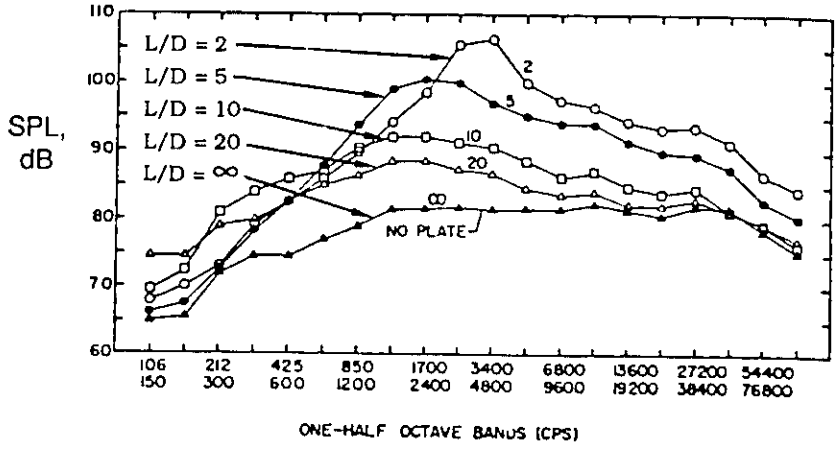

(c) Far-Field Power Spectrum
M = 0.66. (Marsh.[27])

Figure 11-9. Radiation From an Impinging Jet Operated in Resonance.

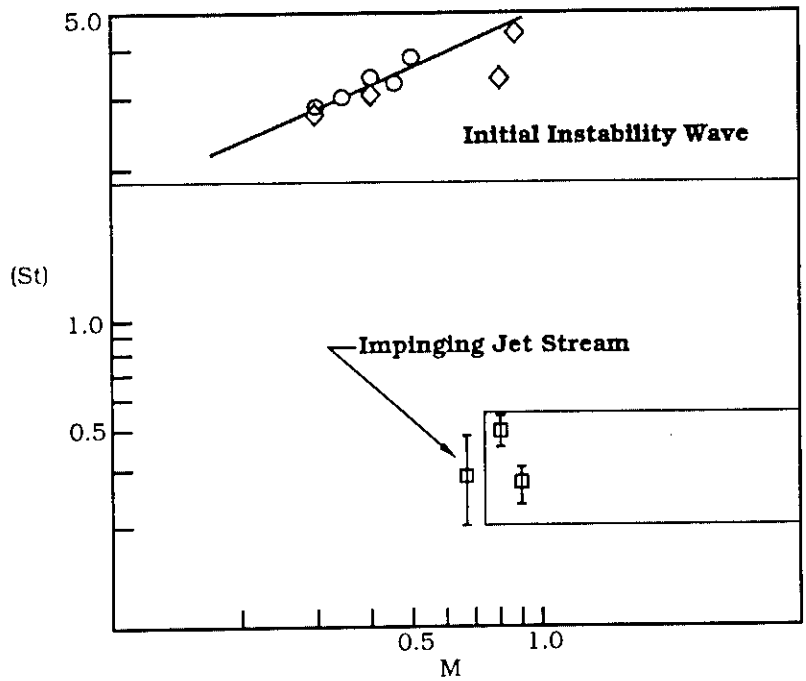

Figure 11-10. Instability and Resonant Strouhal Numbers for Free and Impinging Jets. (Reproduced from Ho and Nosseir.[24])

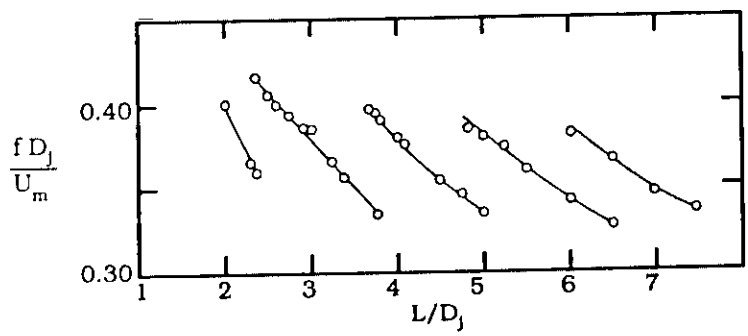

(a) Variations of the Non-Dimensional Resonant Frequency Parameter $\frac{f D_j}{U_m}$ With Plate Locations, M = 0.9.

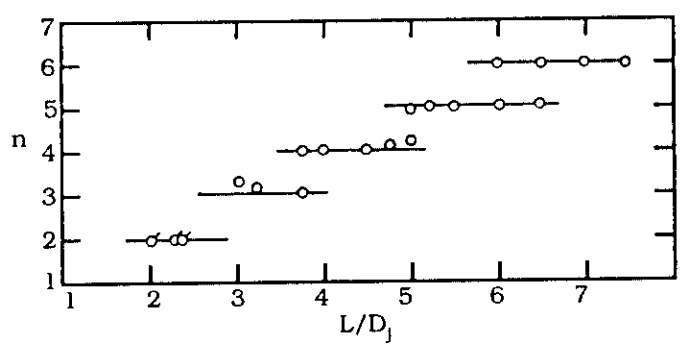

(b) Resonant Frequency Stages, $N = L/\lambda_1 + L/\lambda_2$.

Figure 11-11. Variation of Frequency and Stage Number With Plate Separation Distance. (Reproduced from Ho and Nosseir.[24])

nozzle exit at Mach numbers below 0.6 the Strouhal number wave ranges between 3 and 5 and the presence of the plate does not change the initial instability frequency. When the Mach number is increased, the impinging jet becomes resonant and exhibits large coherent structures with a Strouhal number between 0.3 and 0.4 as reported by Marsh[27] and Ho & Nosseir.[24] The vertical bars in Figure 11-10 represent the frequency variations observed with different plate locations. Finally, this figure illustrates that the upstream pressure feedback has sufficient intensity to impact the vortex shedding and interaction process only when the Mach number exceeds 0.6.

Figure 11-11a shows the variation of resonance frequency versus separation distance, and Figure 11-11b shows the same frequencies plotted according to their stage number. In Figure 11-11a the Strouhal number decreases with increasing nozzle-to-plate separation distance until it reaches a minimum value of approximately 0.33. This lower limit corresponds to the most unstable mode of free jet column buckling. With a further increase in the separation distance the Strouhal number changes abruptly to a higher value, then decreases again until the minimum value for Strouhal number is again achieved. Every step change in the Strouhal number involves a corresponding change in the mode number.

The presence of jet stages is not unfamiliar; most leading-edge interactions exhibit abrupt changes in frequency when the impinging length scale is increased. The Ho and Nosseir[24] model for predicting the variation of frequency with Mach number assumes that the phase difference between the downstream convective wave and the upstream acoustic wave is zero. If it is stipulated that resonance condition requires an integer number of waves to exist in the feedback loop, then

$$n = \frac{L}{\lambda_1(f)} + \frac{L}{\lambda_2(f)} \qquad (11\text{-}23)$$

where the value of n is an integer that corresponds to the number of waves in the feedback loop. λ_1 and λ_2 are the wavelengths for the downstream and upstream traveling waves, respectively.

$$\lambda_1 = \frac{0.62\, U_m}{f}\,, \qquad \lambda_2 = \frac{c}{\cos\theta_a}\,\frac{1}{f}\,. \qquad (11\text{-}24)$$

Equation (11-24) assumes the downstream traveling wave has a convective speed of $0.62\, U_m$ and the upstream traveling wave propagates upstream at the

speed of sound, c , in a direction making an angle of θ_a to the jet axis. Figure 11-12 shows the dependence of the wavefront angle θ_a with the separation distance. The figure indicates the direction of the wavefront propagation varies with the position of the plate and the resultant angle is approximately 30 degrees. Equations (11-23) and (11-24) are now rewritten in the form

$$n = St\left(\frac{L}{D_j}\right)\left[\frac{1}{0.62} + M\cos\theta_a\right] \qquad (11\text{-}25)$$

where $\theta_a = 30°$.

This formulation may be used to predict the Strouhal number given the Mach number and L/D_j ratio. Figures 11-10 and 11-11 also provide a suitable estimate of the Strouhal number.

In Table 11-3, a comparison is made between Equation (11-25) and the experimental results of Ho and Nossier.[24]. Tabulated are the nozzle-to-plate separation distances at which the jet transitions to a new stage. The predicted values are within 4 percent of the measured values.

Table 11-3

Comparison Between Predicted and Measured Values[24]
($M = 0.9$, $\theta_a = 25°$, $D_j = 2.54$ cm)

Frequency Stage n	L/D_j		Percent Difference
	From Equation (11-25)	Measured	
1	1.25	--	--
2	2.50	2.40	4%
3	3.74	3.75	0.3%
4	4.99	4.8–5.0	3.8%–0.2%
5	6.24	6.0–6.5	3.8%–4.2%
6	7.49	7.50	0.1%

11.2.3 Jet–Plate–Hole Configuration

A jet impinging on a plate with a hole through its center, referred to hereafter as a hole tone, is another example of a jet-driven mechanism that produces discrete tones.

Much of the work on hole tones is described in a paper by Chanaud and Powell.[28] Their measurements were made in air using an axisymmetric jet with a mean exit velocity profile having a top-hat shape. Exploratory experiments were

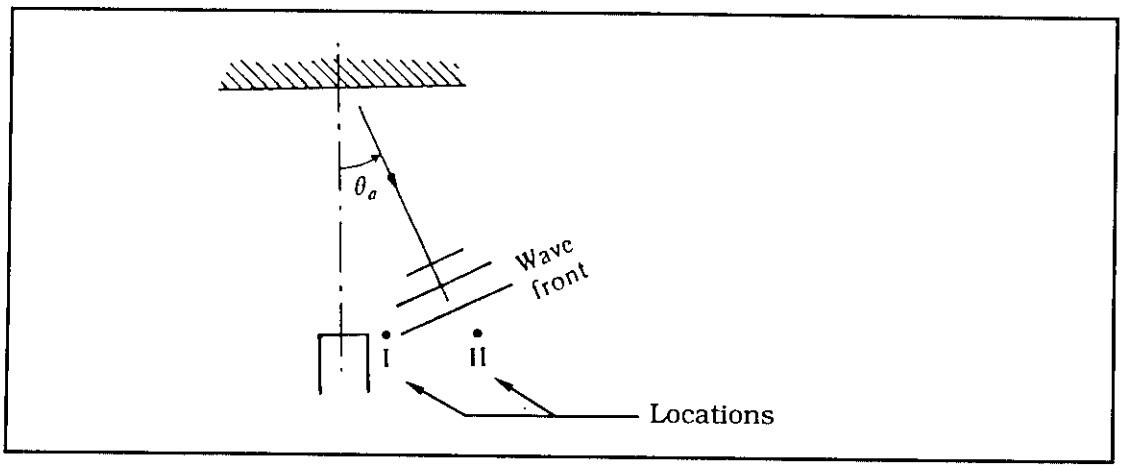

(a) Depiction of Wavefront Angle and Its Measurement Locations.

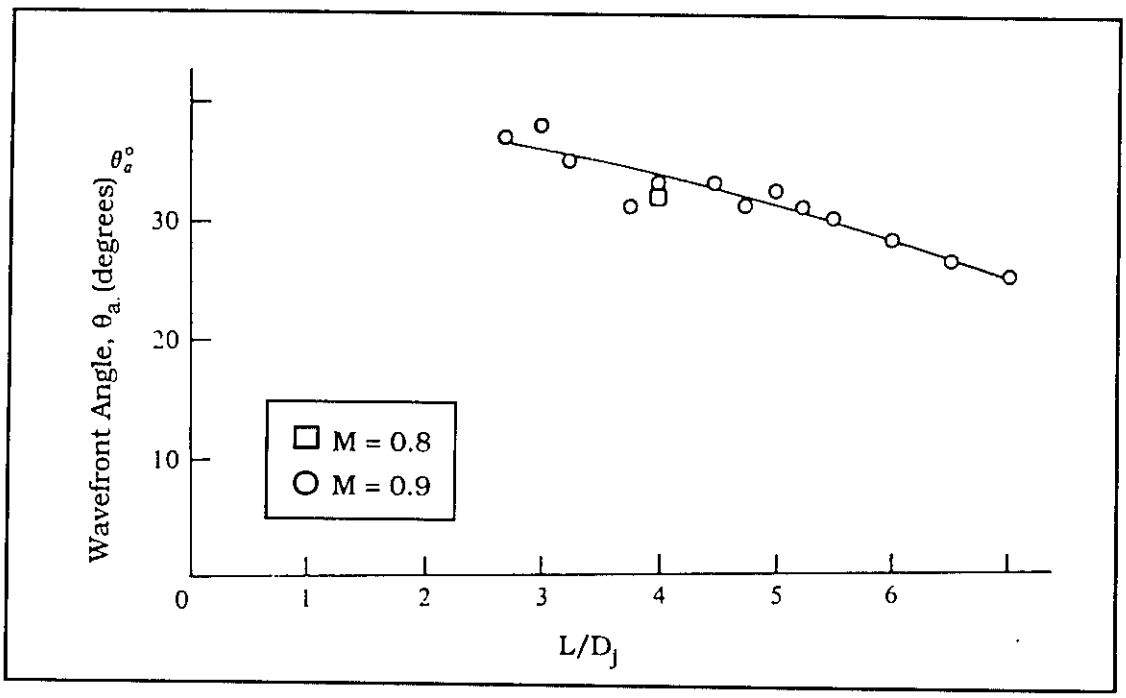

(b) Measured Angle Between the Upstream-Propagating Waves and the Jet Axis for Different Plate Locations.

Figure 11-12. Dependence of Wavefront Angle on Plate Separation Distance. (Reproduced from Ho and Nosseir.[24])

made using a nozzle that produced a parabolic velocity profile. This nozzle was discarded when it was discovered that the jet was relatively stable, producing tones only for a very limited Reynolds number range.

Chanaud and Powell observed that the test apparatus was extremely sensitive to a number of experimental conditions. For example, the location of the hole downstream from the nozzle exit was found to be critical for the jet to produce a discrete tone. Any slight misalignment of the test rig caused the jet to undergo changes in frequency and the production of higher harmonics.

Chanaud and Powell also discovered that the relative size of the hole as compared to the nozzle diameter was critical for tone production. If the hole in the plate was twice the size of the orifice diameter, the jet stream passed through the hole. The sound pressure level was so low that it was difficult to measure and it was presumed that the maximum velocity perturbation occurred within the vortex ring, which was now a greater distance from the edge of the hole.

Figure 11-13 shows the approximate wave speed as a function of streamwise coordinates from the nozzle exit. The plate used to complete these measurements was four diameters downstream with a hole diameter equal to the nozzle exit. The data shown here are compared to an edgetone experiment using a planar jet with a fully developed parabolic velocity profile. As compared to the edgetone, a higher convective wave speed ratio was obtained in the hole tone experimental arrangement.

Shown in Figure 11-14 is the dependence of the Strouhal number versus Reynolds number for hole tone systems . Depending on the Reynolds number, the Strouhal number ranged between 0.5 and 0.75. The concept of frequency stages (jumps) and hysteresis effects are once again demonstrated in these figures.

Blake[3] suggests as a frequency prediction model

$$St = \frac{fL}{U_m} = \frac{U_c}{U_m} \frac{(n - 1/4)}{2\pi(1 + M)} \qquad (11\text{-}26)$$

where the wave speed ratio (U_c / U_m) ranges between 0.5 and 0.9, and M_c is the convective Mach number.

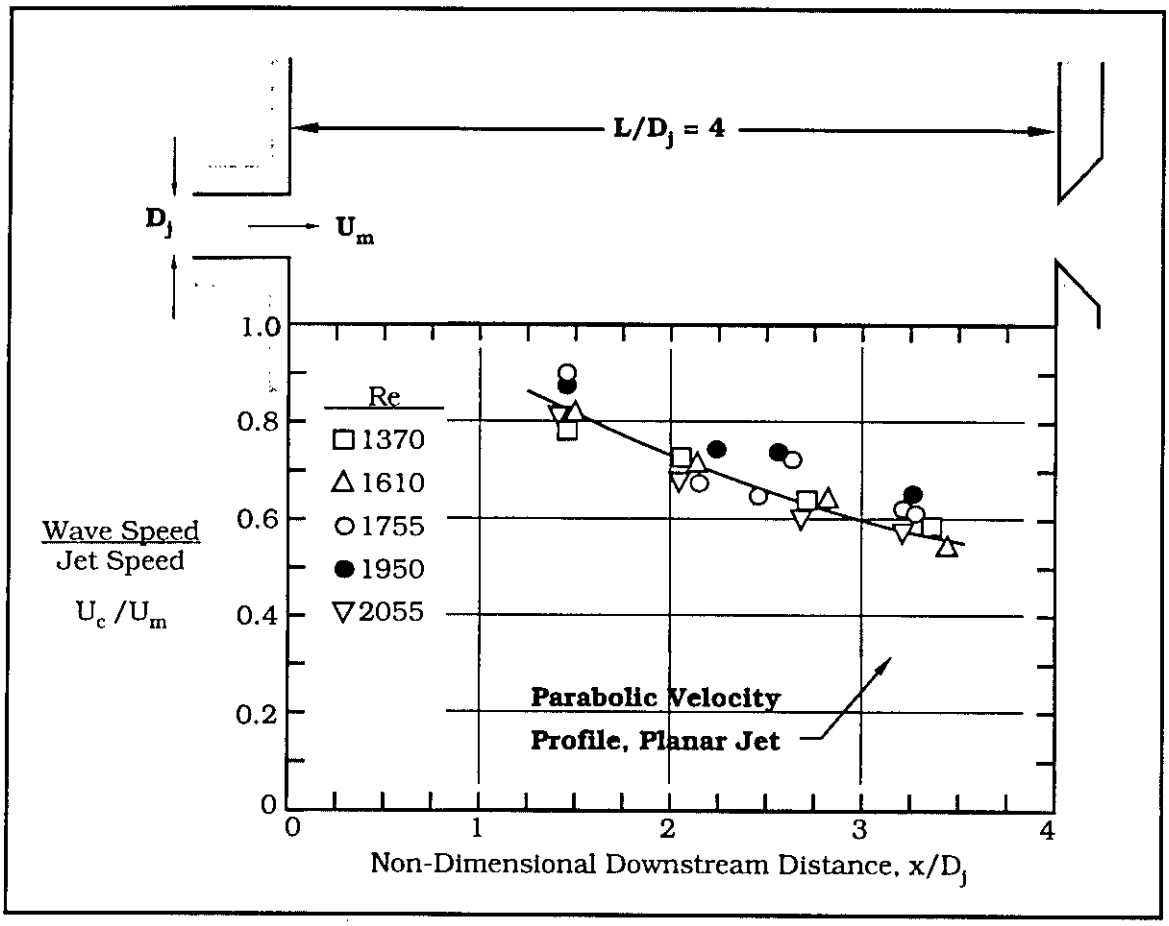

Figure 11-13. Approximate Wavespeed Profile of an Axisymmetric Jet As Compared to a Planar Jet. (Reproduced from Chanaud and Powell.[28])

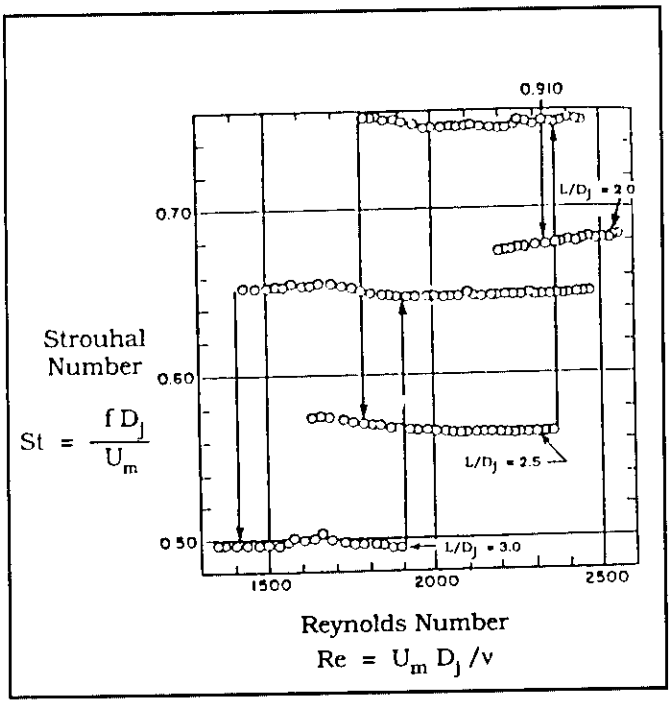

(a) Change From Stage I (Lower Contours) to Stage II for a Hole-Tone System With 6-Inch-Diam. Plates. The Dimensionless Distance Between Plates is Denoted by L/D_j .

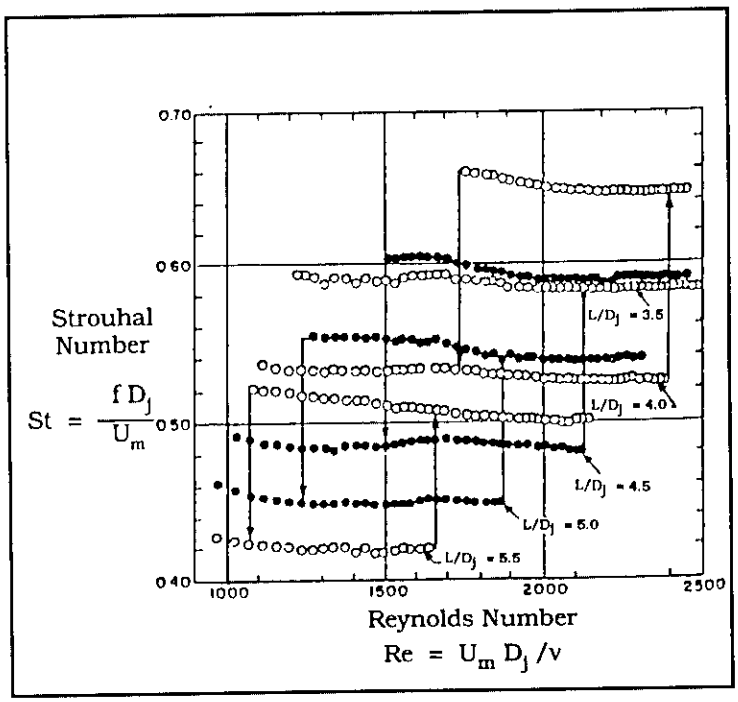

(b) Stage II and III of the Hole-Tone System.

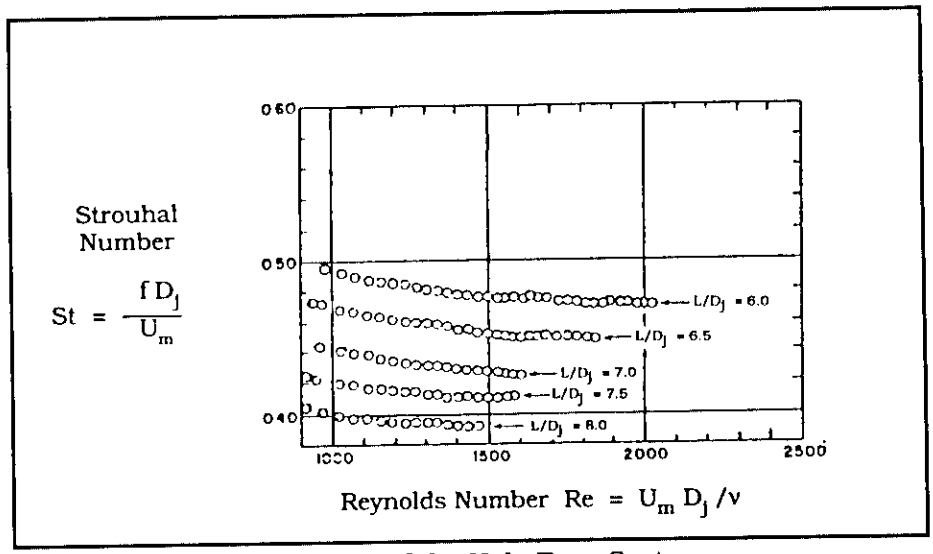

(c) Stage III of the Hole-Tone System.

Figure 11-14. Strouhal Number Versus Reynolds Number for a Hole-Tone System. (Reproduced from Chanaud and Powell.[28])

11.3 Flows Past Cavities

Flow past a rectangular or slotted cavity provides the basis not only for self-sustained oscillations of the purely hydrodynamic type, but also the potential for coupling of these basic instabilities with a resonant acoustic mode within the cavity or elastic characteristics of the cavity walls. Common to turbomachinery are the shear layer instability modes coupled to cavity acoustic resonance modes. This type of coupled oscillations is common because the speed of the gas flow is sufficiently high (typically $M > 0.2$) to cause the associated acoustic wavelength to be smaller than the dimensions of the cavity. Described in this section are several classes of oscillations, ranging from those that are purely hydrodynamic and uninfluenced by acoustics effects to those that are strongly influenced by acoustic resonant coupling.

11.3.1 Classification of Cavity Oscillations

A review of cavity oscillators developed by Rockwell and Naudascher[1] is shown in Figure 11-15. The cavity oscillators are organized into three basic types, as indicated in the first column of the figure. The second column shows the basic cavity geometry. Sketches of cavities in the third column depict variations from the basic model. The three types of cavity oscillations are:

Fluid-Dynamic Oscillations – Cavity oscillations that are driven solely by the inherent instability of the shear layer.

Fluid-Resonant Oscillations – Cavity oscillations that result from coupling of the inherent instability of the shear layer with one or more of the acoustic resonant modes of the cavity.

Fluid-Elastic Oscillations – Cavity oscillations that result from coupling of the inherent instability of the shear layer with elastic movement of a part or all of the cavity bounding walls.

In practice, the classification of cavity oscillations proposed by Rockwell and Naudascher may in fact occur simultaneously in nature. For instance, a cavity oscillation may be controlled simultaneously by fluid-dynamic, fluid-resonant, and fluid-elastic oscillations. Their matrix classification scheme is designed to help facilitate detailed analysis of the predominant hydrodynamic, acoustic, and structural features of a cavity oscillation. Sections 11.3.1.1, 11.3.1.2, and 11.3.1.3 address each type of classification shown in Figure 11-15, respectively.

Type	Basic Cavity	Variations of Basic Cavity
Fluid-Dynamic Shear Layer Instability	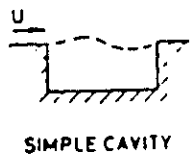	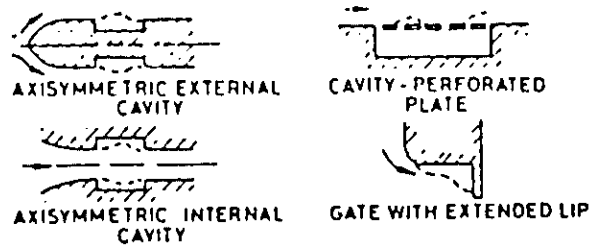
Fluid-Resonant Shear Layer Instability and Cavity Acoustic Resonances	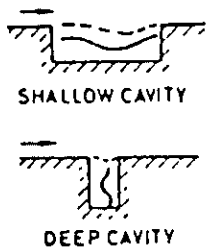	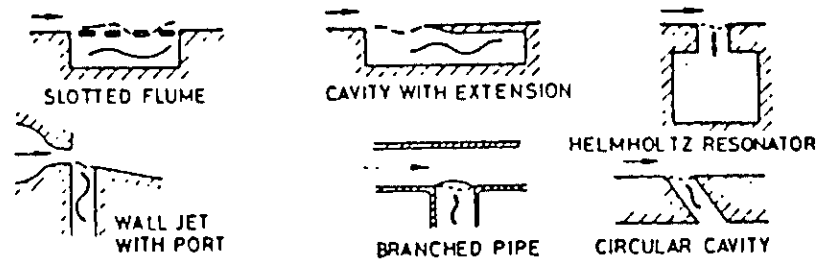
Fluid-Elastic Shear Layer Instability and Cavity Elastic Deformation	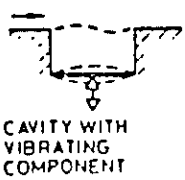	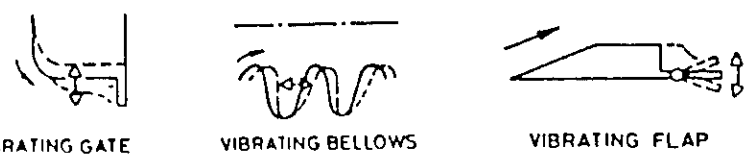

Figure 11-15. Classification of Cavity Oscillators.
(Reproduced from Rockwell and Naudascher.[1])

11.3.1.1 *Fluid-Dynamic Oscillations*

The purely fluid-dynamic oscillation is limited to the situation where the cavity length (or other dominant dimension) is less than one-fourth the acoustical wavelength of the disturbance. For this class of oscillations the acoustical wavelengths exceed the dimensions of the cavity, preventing the existence of standing waves and negating the effect of the cavity as a resonator.

The mechanism responsible for the self-sustained oscillations is the amplification of the unsteady shear layer which is strongly enhanced by the presence of the downstream leading edge. Fluid-dynamic oscillation can be expected to have features similar to the edgetone, suggesting a similar analytical approach. Flax[29] suggests a fluid-dynamic oscillator could be modeled with a fixed Strouhal number to determine the frequency of the cavity oscillation. Flax's suggestion does not rule out the possibility of selective amplification of the shear layer causing certain disturbances to be more amplified than others. Discontinuous frequency activity and hysteresis regions are possible because the downstream edge of the cavity provides the capability for a feedback mechanism that will result in preferred modes of oscillation.

11.3.1.2 *Fluid-Resonant Oscillations*

Fluid-resonant cavity oscillation occurs when the shedding frequencies are sufficiently high and the acoustic wavelengths sufficiently short so as to allow for standing waves inside the cavity.

Cavity behavior varies with depth as characterized by the length-to-depth ratio. If the cavity length-to-depth ratio is sufficiently large ($L/D > 1$), then longitudinal standing waves dominate and the cavity is termed shallow. Conversely, for a length-to-depth ratio that is small ($L/D < 1$), the cavity is denoted as a deep cavity and the acoustic waves are predominantly in the transverse direction.

Longitudinal wave resonance is possible when $\lambda_a \leq 2L$ and for the case of acoustic waves in the depth-wise mode, acoustic resonances will be observed when $\lambda_a \leq 4D$.

11.3.1.3 *Fluid-Elastic Oscillations*

Fluid-elastic cavity oscillations occur when one or more of the cavity walls undergoes a deformation that is large enough to control the shear layer perturbation. The frequency response of the system can therefore be represented by a diagram in which the lines of shear layer instability are drawn along with the lines of natural frequency for the elastic structure.

Fluid-elastic oscillations are more prone to occur in liquids where the incompressibility tends to make structural distortions to the cavity walls. Additional features and complications with liquids are the possibilities of cavitation, dead water regions, and entrapped gas – all of which will impact the compliance of the cavity volume.

11.3.2 Survey of Cavity Oscillation Models

The history of cavity oscillation models dates back to work originally done by Helmholtz[30] in 1868. Since that time, the interest in cavity oscillations remained largely confined to musical interest, until in the mid-1990s severe unsteady loads inside aircraft weapon bays and wheel wells were discovered. This problem led to an extensive number of articles on cavity oscillation models that apply different physical treatments to estimate the modes of oscillation. A literature review by Flax describes many of these models according to their common treatments. Contained in this section is a survey of only those models most applicable to turbomachinery applications.

In this section, two physical treatments are reviewed: (1) feedback transit time models, and (2) acoustic resonance models. Feedback transit time models sum the transit time for vortex sheets formed by fluid layers moving in the downstream direction to the transit time for an acoustic pressure disturbance traveling upstream from the cavity trailing edge. Similar approaches have been used by Powell[5] and others to explain a variety of self-sustained phenomena. Several transit time models have already been discussed in previous sections. Acoustic resonance models have the added criterion that a clearly identifiable acoustic mode or modes must be excited in the cavity. In accordance with the foregoing remarks, the cavity models are organized as follows:

1. Feedback Transit Time Models, Empirical Estimates – The leading edge of the cavity provides a complete feedback for a downstream disturbance. The sum of the transit times on both paths equals the period. The transit time frequency is the time required for a disturbance to travel downstream plus the time required for the disturbance to feed back to the sensitive region of the cavity lip. The transit times are estimated using empirical data.

2. Feedback Transit Time Models, Analytical Estimates – The transit time of the disturbance is estimated by making analytical estimates of the sum of the phase of a downstream-traveling wave and the phase of the upstream-traveling acoustic wave.

3. Feedback Transit Time Models and Cavity Resonance Model – The disturbance transit time is estimated using an approach similar to models 1 and 2, above. However, this approach requires the transit time frequency to be coincident with the cavity acoustic resonances.

In an early, highly successful study, Rossiter[31] estimated the excitation frequency using a transit time model. Rossiter recognized that the creation of a cavity tone requires the existence of a fluid-dynamic excitation having features similar to those described in Section 11.1 for the edgetone generator. He also showed that the cavity geometry serves to enhance tone generation, but the cavity need not be resonant for a tone to be generated. The formula developed by Rossiter is well supported with experimental data. But Rossiter's formula has received criticism because it does not predict whether a self-sustained oscillation will in fact occur. Specifying the turbulent characteristics of the separated shear layer near the cavity leading edge is necessary to predict instability characteristics. Such quantities are not required in Rossiter's model. As shown in Figure 11-16, the fluid velocity, the turbulent characteristics near the cavity opening, and the cavity dimensions all play a significant role in predicting the cavity tones.

11.3.2.1 *Feedback Transit Time Models, Empirical Estimates*

The problem of any cavity feedback transit model is to estimate the sum of the time required for the disturbance wave to cross the cavity opening and the

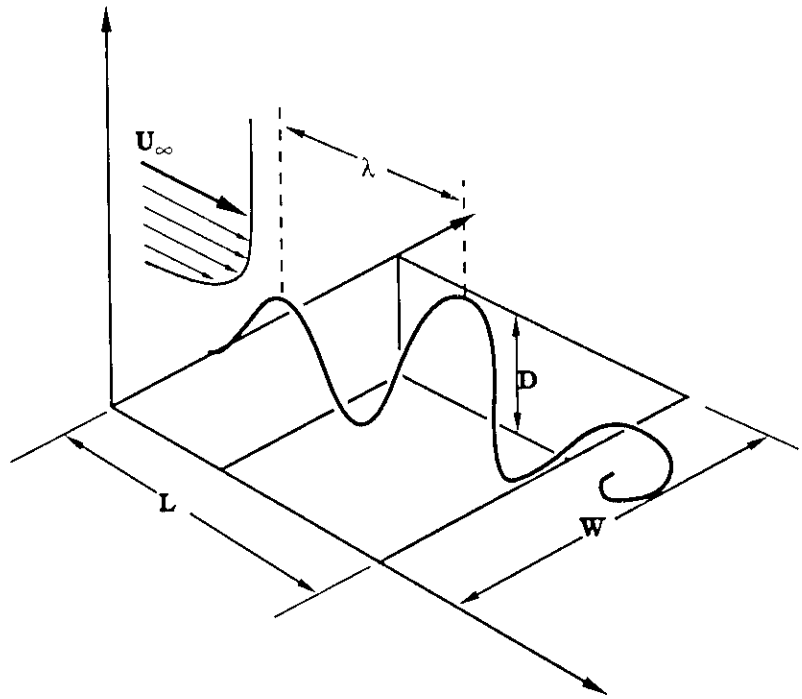

Shear Layer

λ – hydrodynamic wavelength

U_c – convective velocity

U_∞ – free-stream speed

f – shear-layer frequency

θ – momentum thickness

M – Mach number

Acoustic Radiation

λ_a – acoustic wavelength

c – speed of sound

f_a – acoustic frequency

P_b – RMS pressure at base of cavity

P_o – RMS pressure at cavity opening

Figure 11-16. Physical Dimensions and Flow Parameters for Cavity Oscillation Models.

time required for the acoustical wave to travel back upstream. The sum of these two events equals the period of the oscillation. Rossiter[31] formulated the following model

$$t_1 = \text{disturbance wave time} = \frac{L}{k_v U_\infty}$$

$$t_2 = \text{acoustic wave time} = \frac{L}{c}$$

$$T = t_1 + t_2 = \frac{L}{k_v U_\infty} + \frac{L}{c}$$

to derive

$$\frac{fL}{U_\infty} = \frac{m - \alpha}{M + 1/k_v} \qquad (11\text{-}27)$$

where $k_v = U_c / U_\infty$ = the ratio of shear layer velocity to free-stream velocity,
$m = 1, 2, 3 \ldots$ = mode number,
α = empirical constant,
L = cavity length, and
M = Mach number as measured in the free-stream.

Values of k_v and α are empirically determined; Rossiter obtained values of 0.57 and 0.25, respectively. α is a constant that accounts for the phase differences between (1) the upstream arrival of the acoustic wave and the subsequent vortex shedding, and (2) the downstream interaction with the leading edge and the subsequent acoustic radiation.

A refinement pertinent to high-speed flows is that of Heller *et al.*[32,33] The Rossiter model was found to predict frequencies consistent with experimental data provided the Mach number was below 1.5. At higher Mach numbers the Rossiter model underpredicted the Strouhal number.

Heller attributes the breakdown in the Rossiter model to the temperature difference inside the cavity as compared to the free-stream temperature. The speed of sound inside the cavity, c_a, may be determined by

$$c_a = c_\infty \left[1 + r\,(\lambda - 1/2)\,M^2\right]^{1/2} \qquad (11\text{-}28)$$

where c_∞ is the free-stream static sound speed, λ is the adiabatic exponent, and r is the temperature recovery factor

$$r = \frac{T_c - T_\infty}{T_0 - T_\infty} \qquad (11\text{-}29)$$

where T_∞ and T_o are the static and stagnation temperatures of the free stream and T_c is the average static temperature within the cavity.

The temperature recovery factor for compressible flows was found to be close to unity when the Mach number exceeds 1.5. Rossiter assumed the speed of sound in the cavity to be the free-stream speed of sound, thereby assuming a value of zero for the recovery factor. Using Equation (11-29), Heller obtained

$$\frac{f L}{U_\infty} = (m - \alpha) \Big/ \left\{ \frac{M}{\left[1 + (\gamma - 1) M^2/2\right]^{1/2}} + \frac{1}{k_v} \right\}, \quad m = 1, 2, 3, \ldots \qquad (11\text{-}30)$$

11.3.2.2 *Feedback Transit Time Models, Analytical Estimates*

Bilanin and Covert[34] calculate the transit time for the disturbance by introducing a monopole acoustic source at the downstream edge. This source represents pressure fluctuations due to the shear layer impingement. Two general solutions are derived. One models the shear layer displacement in the streamwise direction. The other general solution models the acoustic pressure field due to an acoustic monopole source at the impingement edge.

The phase relationship is derived by the summation of phase around the entire feedback loop, i.e., summation of the phase of the acoustic feedback pressure and the phase of the downstream vortex sheet. The phase of the acoustic feedback pressure field can be determined by inspecting the asymptotic formula for the potential of a cylindrical wave given by Rayleigh[35] as

$$\Phi = -\left(\frac{\pi}{2kr}\right)^{\frac{1}{2}} \cos k\left(ct - r - \frac{1}{8}\lambda\right) \left\{1 - \frac{1^2 \cdot 3^2}{1 \cdot 2 \cdot (8kr)^2} + \ldots\right\}$$
$$+ \left(\frac{\pi}{2kr}\right)^{\frac{1}{2}} \sin k\left(ct - r - \frac{1}{8}\lambda\right) \left\{\frac{1^2}{1 \cdot 8\,kr} - \frac{1^2 \cdot 3^2 \cdot 5^2}{1 \cdot 2 \cdot 3 \cdot (8kr)^2} + \ldots\right\} \qquad (11\text{-}31)$$

where $k = \omega/c$, and c is the speed of sound in the fluid media. The potential in Equation (11-31) has an acoustic pressure phase given by $kL - \pi/4$. The pressure has a phase difference of $\pi/2$ from the potential so that the acoustic pressure phase becomes $kL + \pi/4$.

The phase difference for the downstream-moving vortex sheet is determined from the general form for a perturbed shear layer. Bilanin and Covert show that the phase has two parts: the phase of the spatial frequency, $k_r L$, and the

phase, ϕ , due to the lag of the vortex sheet after forcing at x = 0. Added to these two terms is $\pi/2$ to account for a maximum pressure at the downstream edge when the shear layer displacement is at a minimum.

The resulting expression is obtained for the eigenvalue equation for excitation frequencies

$$k_r L + \phi + \frac{3\pi}{4} + \frac{\omega L}{c} = 2\pi n \qquad (11\text{-}32)$$

which becomes

$$\frac{fL}{U_\infty} = \frac{n - 3/8 - \phi/2\pi}{1/k_v + M\,(c_\infty/c_a)} \qquad (11\text{-}33)$$

where $k_v = \omega/k_r U_\infty$,

$\alpha = \phi/2\pi + 3/8$,

c_∞ = speed of sound in free-stream,

c_a = speed of sound inside cavity.

The form of Equation (11-33) is similar to that of Rossiter's formula.

In earlier work by Covert,[36,37] a hydrodynamic stability approach was taken to approximate which frequency of the shear layer is most susceptible to highly amplified growth. A set of linearized perturbation equations were written for the cavity's internal and external flows. At the cavity opening, the equations were bounded by the requirement of continuous pressure across the interface. The resulting equations were reduced to a single integral whose characteristic equation provides a relationship for the wave number and frequency. The relationship is only satisfied for certain values of frequency and is complex with the sign of the imaginary part governing the disturbance. When the imaginary part of the frequency is positive the disturbance grows; when it is negative the disturbance decays.

Figure 11-17 shows results of Covert's integral equation calculated for subsonic and supersonic flows. In the region where the damping factor is positive, the disturbance can be expected to grow with a frequency indicated by the Strouhal number. For incompressible flows (Mach number less than 0.25), the flow is unstable below a critical Strouhal number that is determined at the zero crossing. As the Mach number is increased, the behavior changes as the stability curves cross the zero axis twice. As shown in Figure 11-17b (M = 0.75), there are

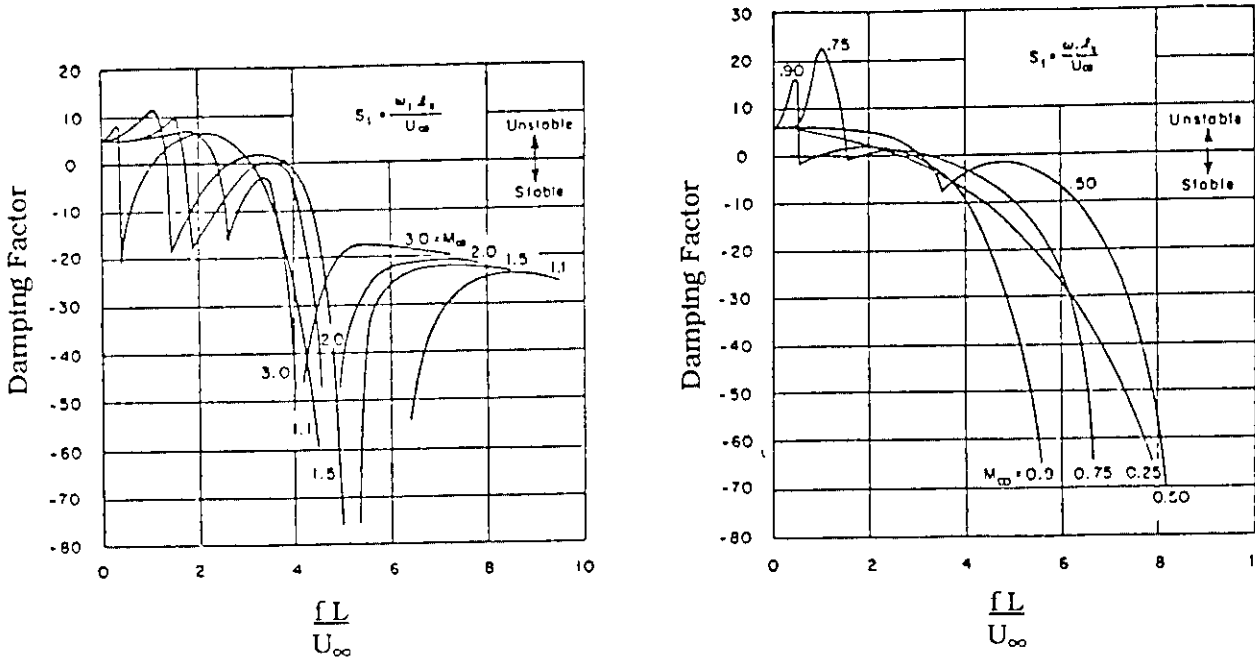

(a) M > 1.

(b) M < 1.

Figure 11-17. Damping as a Function of Strouhal Number. (Reproduced from Covert.[37])

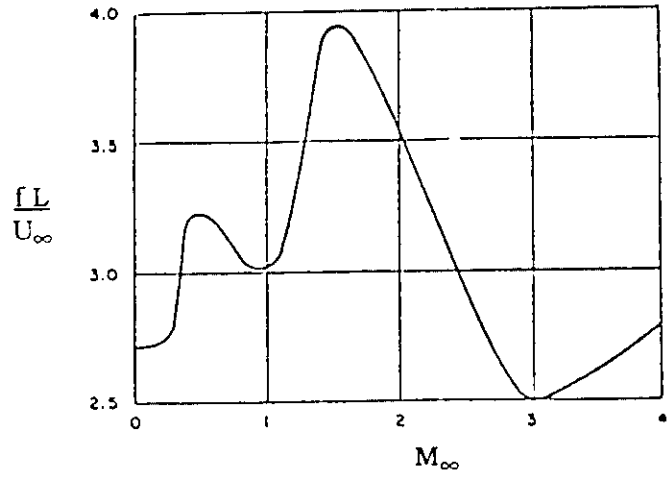

Figure 11-18. Variation of Strouhal Number Versus Mach Number for Neutral Stability. (Reproduced from Covert.[37])

two unstable regions separated by a stable region. At higher Mach numbers (M = 0.9), the stability curves return to crossing the horizontal neutral axis only once.

Figure 11-18 shows a plot of the Strouhal number as a function of Mach number constructed from the stability curves (shown in Figures 11-17a and b) and the points where they cross the horizontal axis. The only unknown quantity in Figure 11-18 is the freestream velocity, and its value defines when the disturbance is neutrally stable.

11.3.2.3 *Feedback Transit Time Models and Cavity Resonance Model*

Block[38] models the shear layer as an infinitesimally thin sheet and the acoustic disturbance at the cavity trailing edge as a simple acoustic point source. In an attempt to account for the acoustic resonance modes of the cavity, Block included the first image source at the trailing edge of the cavity to account for the effect of the acoustic wave reflected from the bottom of the cavity.

The acoustic field and the motion of the shear layer are matched at the leading and trailing edges to develop

$$\frac{fL}{U_\infty} = \frac{m}{\frac{1}{k_r} + M\left(1 + \frac{0.514}{L/D}\right)} \qquad (11\text{-}34)$$

where k_r = real part of wave number (use a value of 0.57), and
m = mode number, integer.

Equation (11-34) correctly accounts for the dependence of the Strouhal number on the L/D ratio as observed in experimental data. According to Block, this formula represents the lengthwise or vortical-acoustic modes of oscillation.

The depthwise standing wave-oscillations are calculated by using a relation developed by East:[39]

$$\frac{fL}{U_\infty} = \left(\frac{1}{M}\right)\left(\frac{L}{D}\right)\frac{1/4}{1 + A\,(L/D)^B}. \qquad (11\text{-}35)$$

East derived Equation (11-35) from Rayleigh's formula for an open circular pipe:

$$0.25 = \left(\frac{fD}{c}\right)\left[1 + A\,(L/D)^B\right] \qquad (11\text{-}36)$$

where A and B are empirical constants. Values of A = 0.65 and B = 0.75 give a curve that compares favorably with experimental and theoretical models.[39]

If Equations (11-34) and (11-35) are combined so that the frequency for the shallow acoustic waves coincides with the depthwise acoustic modes, the formula

$$M = \frac{(1/k_r)\ L/D}{4m\left[1 + A\,(L/D)^B\right] - [(L/D) + 0.514]} \qquad (11\text{-}37)$$

may be used to estimate the Mach number at which a cavity begins to oscillate in a given mode, m . Equation (11-37) was tested by Block[38] and shown to provide adequate agreement for a Mach number range of 0.1 to 0.5 and a cavity L/D ratio below 2.

11.3.4 Prediction Procedure

All of the models reviewed in the preceding section have been shown to correlate well with experimental data. Many of these models follow a phenomenological formulation similar to Rossiter's model. Yet all of these models are limited to a specific range of L/D and Mach number values. The success of correlating the models with experimental data is apparently due to a flow-induced oscillation that is strongly dependent on a few very dominating variables. These parameters include the Mach number, the cavity length-to-depth ratio, and the phase.

Plotted in Figure 11-19 is a comparison of the Mach numbers and L/D ratios for which these models have been shown to work. Included in the figure is an envelope illustrating the cavity conditions expected inside most turbomachinery. It is seen in Figure 11-20 that the models of Rossiter,[31] Block,[38] East,[39] and Plumblee[40] fall within the envelope drawn for turbomachinery cavities. The Rossiter and Block models estimate hydrodynamic/acoustic modes in the streamwise direction, while the East formulation is specifically for the depthwise cavity mode. The Plumblee model, which is purely an acoustical model, favors shallow and deep cavities alike.

Table 11-4 shows the Strouhal numbers calculated using the Rossiter, Block, and East models. The shading indicates values of L/D and Mach number that are not contained within the ranges shown in in Figure 11-19. The difference between Rossiter and Block models is an outcome of the first image

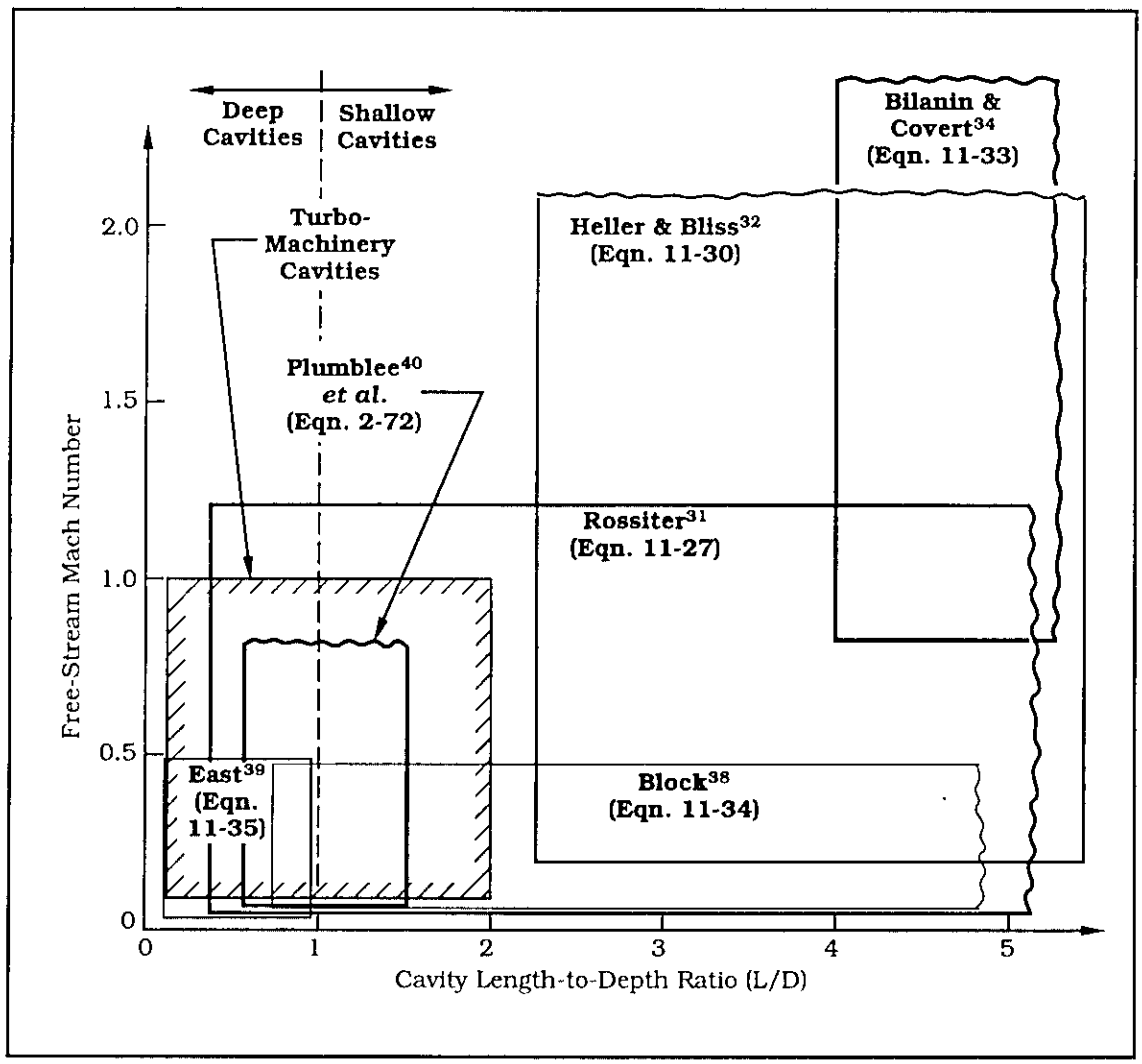

Figure 11-19. Range of Validity of Cavity Oscillation Models.

source that Block has included in her model; thus the L/D dependence is built into the Block model. Values for the East model are tabulated here for comparison.

When making predictions inside turbomachinery, use Block's formula for cavities having an L/D > 1. If the cavity has an L/D < 1, then use East's formula to determine the resonance of the depth mode and Rossiter's formula to determine the longitudinal resonance mode. The latter mode will be the weaker of the two modes in deep cavities.

Table 11-4

Comparison of Strouhal Numbers Calculated from the Rossiter, Block, and East Cavity Oscillation Models

L/D	Mach	Rossiter[31] (Eqn. 11-27)			Block[38] (Eqn. 11-34)			East[39] (Eqn. 11-35)
		m = 1	m = 2	m = 3	m = 1	m = 2	m = 3	
0.25	0.20	0.384	0.895	1.407	0.423	0.845	1.268	0.254
	0.40	0.348	0.812	1.276	0.336	0.672	1.008	0.127
	0.60	0.319	0.743	1.168	0.279	0.557	0.836	0.085
	0.80	0.294	0.685	1.077	0.238	0.476	0.714	0.064
	1.0	0.272	0.635	0.998	0.208	0.416	0.624	0.051
0.5	0.20	0.384	0.895	1.407	0.463	0.926	1.389	0.451
	0.40	0.348	0.812	1.276	0.390	0.780	1.169	0.225
	0.60	0.319	0.743	1.168	0.337	0.673	1.010	0.150
	0.80	0.294	0.685	1.077	0.296	0.592	0.888	0.113
	1.0	0.272	0.635	0.998	0.264	0.529	0.793	0.090
0.75	0.20	0.384	0.895	1.407	0.478	0.956	1.434	0.615
	0.40	0.348	0.812	1.276	0.412	0.824	1.235	0.308
	0.60	0.319	0.743	1.168	0.362	0.723	1.085	0.205
	0.80	0.294	0.685	1.077	0.322	0.645	0.967	0.154
	1.0	0.272	0.635	0.998	0.291	0.581	0.872	0.123
1.0	0.20	0.384	0.895	1.407	0.486	0.972	1.458	0.758
	0.40	0.348	0.812	1.276	0.424	0.847	1.271	0.379
	0.60	0.319	0.743	1.168	0.376	0.751	1.127	0.253
	0.80	0.294	0.685	1.077	0.337	0.674	1.012	0.189
	1.0	0.272	0.635	0.998	0.306	0.612	0.918	0.152
1.25	0.20	0.384	0.895	1.407	0.491	0.982	1.473	0.884
	0.40	0.348	0.812	1.276	0.431	0.862	1.294	0.442
	0.60	0.319	0.743	1.168	0.384	0.769	1.153	0.295
	0.80	0.294	0.685	1.077	0.347	0.694	1.040	0.221
	1.0	0.272	0.635	0.998	0.316	0.632	0.948	0.177
1.5	0.20	0.384	0.895	1.407	0.494	0.989	1.483	0.997
	0.40	0.348	0.812	1.276	0.436	0.873	1.309	0.498
	0.60	0.319	0.743	1.168	0.391	0.781	1.172	0.332
	0.80	0.294	0.685	1.077	0.354	0.707	1.061	0.249
	1.0	0.272	0.635	0.998	0.323	0.646	0.969	0.199

REFERENCES FOR CHAPTER 11

1. Rockwell, D., and Naudascher, E., "Self-Sustained Oscillations of Impinging Free Shear Layers", *Annual Rev. of Fluid Mech., 11*, 1979, 67-94.

2. Rockwell, D., "Oscillations Of Impinging Shear Layers", *AIAA Journal, 21* (5), 1983, 645-663.

3. Blake, "Mechanics of Flow-Induced Sound and Vibration," Academic Press, Inc., *Applied Mathematics and Mechanics, 17*, 1986.

4. Sondhaus, C., Ann Physik (Leipzig), *91*, 1854, 216.

5. Powell, A., "On The Edgetone", *J. Acoust. Soc. Am., 33* (4), 1961, 395-409.

6. Karamcheti, K., Bauer, A.B., Shields, W.L., Stegen, G.R., Woolley, J.P., "Some Features of an Edgetone Field", *Basic Aerodynamic Noise Research*, NASA SP-207, July 14-15, 1969, 275-303.

7. Bickley, W.G., *Phil. Mag., 7* (23), 727, 1937.

8. Sato, H., "The Stability of Transition of a Two-Dimensional Jet", *J. Fluid Mechanics, 7*, 53-80.

9. Umeda, Y., Maeda, H., and Ishii, R., "Frequency Characteristics of Discrete Tones Generated in a High Subsonic Jet", *AIAA Journal, 24* (4), 1986, 693-694.

10. Stegen, G.R., and Karamcheti, K., "Multiple Tone of Edgetones", *J. Sound Vib., 12*, 1970, 281-284.

11. Brown, G.B., "On Vortex Motion In Gaseous Jets and the Origin of Their Sensitivity to Sound," Proc. Physical Society (London), *47*, 1935, 703-732.

12. Coltman, J., "Jet Drive Mechanisms in Edge Tone and Organ Pipes", *J. Acoust. Soc. Am., 60* (3), 1976, 725-733.

13. Lenihan, J.M.A., and Richardson, E.G., "Observations on Edgetones," *Physi-ophical Magazine, 29*, 1940, 400-406.

14. Krothapalli, A., and Horne, W.C., "Observations on the Structure of an Edge-Tone Flowfield", *AIAA Journal, 24* (8), 1986, 1385-1388.

15. Gross, M.J., "Underwater Edge Tones", *Acustica, 9*, 1959, 164-172.

16. Rockwell, P., and Lucas, M.J., "Self-Excited Jet: Upstream Modulation and Multiple Frequencies", *J. Fluid Mech., 147*, 1984, 333-352.

17. Rockwell, D., "Transverse Oscillations of a Jet in a Jet-Splitter System", *ASME Trans., J. Basic Eng., 94*, 1972, 675-681.

18. Powell, A., and Unfried, H.H., "An Experimental Study of Low-Speed Edgetones", Defense Documentation Center Defense Supply Agency, AD 610 028, Report No. 64-49, Nov. 1964.

19. Powell, A., "The Sound-Producing Oscillations of Round Underexpanded Jets Impinging on Normal Plates", *J. Acoust. Soc. Am., 83* (2), February 1988, 515-533.

20. Brown, G.B., "The Vortex Motion Causing Edge Tones," Proc. Physical Society (London), 1937, Vol. 49, pp. 493-507.

21. Curle, N., "The Mechanics of Edge-Tones", *Proc. Royal Soc. London, 216A*, 1953, 412-424.

22. Savic, P., "On Acoustically Effective Vortex Motion in Gaseous Jets", *hil. Mag., 32*, 1941, 245.

23. Nyborg, W.L., "Self-Maintained Oscillations of the Jet in a Jet-Edge System", *J. Acoust. Soc. Am., 26*, 1954, 174.

24. Ho, C.M., and Nosseir N., "Dynamics of an Impinging Jet. Part 1. The Feedback Phenomenon", *J. Fluid Mech., 105*, 1981, 119-142.

25. Michalke, A., "Survey on Jet Instability Theory", *Prog. Aerospace Sci., 21*, 1984, 159-199.

26. Nosseir, N., and Ho, C.M., "Dynamics of an Impinging Jet. Part 2. The Noise Generation", *J. Fluid Mech., 116*, 1982, 379-391.

27. Marsh, A.H., "Noise Measurements Around a Subsonic Jet Impinging on a Plane, Ridge Surface", *J. Acoust. Soc. Am., 33* (8), 1961, 1065-1066.

28. Chanaud, R.C., and Powell, A., "Some Experiments Concerning the Hole and Ring Tone", *J. Acoust. Soc. Am., 37* (5), 1965, 902-911.

29. Flax, A.H., "A Note on the Oscillation of Cavities Coupled to Aerodynamic Flows", Institute for Defense Analysis, Report dated June 1982.

30. Helmholtz, 1868.

31. Rossiter, J.E., "Wind Tunnel Experiments on the Flow Over Rectangular Cavities at Subsonic and Transonic Speeds", *Royal Aircraft Establishment*, TR 64037, 1964.

32. Heller, H.H., and Bliss, D.B., "Flow-Induced Pressure Fluctuations in Cavities and Concepts for Their Suppression", Summerfield, M. (Series Ed.), *Progress in Astronautics and Aeronautics, 45*, 1976, 281-296. Also, AIAA Paper 75-491, presented at Second Aero-Acoustical Conference.

33. Heller, H.H., Holmes, G.D., and Covert, E.E., "Flow-Induced Pressure Oscillations in Shallow Cavities", USGDA-880 496/5, *Journal, 8009*, December 1970, TR-70-104; also *J. Sound Vib., 18* 94), 1971, 545-553.

34. Bilanin, A.J., and Covert, E.E., "Estimation of Possible Excitation Frequencies for Shallow Rectangular Cavities", *AIAA Journal, 11*, March 1973, 347-351.

35. Rayleigh, J.W.S., *The Theory of Sound*, New York Dover Publications, Second Edition, 1945, Vol. 2, Article 342.

36. Covert, E.E., "An Analytical Investigation of Cavity Oscillations, Cavities With Unobstructed Openings, and Discontinuous Velocity Profile", AD299218 MIT AL TR-38, October 1962.

37. Covert, E.E., "Approximate Calculation of the Onset Velocity of Cavity Oscillation", *AIAA Journal, 8* (12), December 1970, 2189-2194.

38. Block, P.J.W., "Noise Response of Cavities of Varying Dimensions at Subsonic Speeds", NASA–Langley Research Center Technical Paper D-8351, 1976.

39. East, L.F., "Aerodynamically Induced Resonance in Rectangular Cavities", *J. Sound Vib., 3* (3), 1966, 277-287.

40. Plumblee, H.E., Gibson, J.S., and Lassiter, L.W., "A Theoretical and Experimental Investigation of the Acoustic Response of Cavities in an Aerodynamic Flow", Flight Dynamics Laboratory, Aeronautical Systems Division, Air Force Systems Command, Wright-Patterson Air Force Base, WADD-TR-61-75, 1962.

☆U. S. GOVERNMENT PRINTING OFFICE 1995 633–109 / 20042

REPORT DOCUMENTATION PAGE

Form Approved
OMB No. 0704-0188

Public reporting burden for this collecton of information is estimated to average 1 hour per response, including the time for reviewing instructions, searching existing data sources, gathering and maintaining the data needed, and completing and reviewing the collection of information. Send comments regarding this burden estimate or any other aspect of this collection of information, including suggestions for reducing this burden, to Washington Headquarters Services, Directorate for Information Operations and Reports, 1215 Jefferson Davis Highway, Suite 1204, Arlington Va 22202-4302, and to the Office of Management and Budget, Paperwork Reduction Project (0704-0188), Washington, DC 20503.

1. AGENCY USE ONLY (Leave Blank)	2. REPORT DATE	3. REPORT TYPE AND DATES COVERED
	May 1995	Contractor Report (Final)

4. TITLE AND SUBTITLE

The Acoustic Characteristics of Turbomachinery Cavities

5. FUNDING NUMBERS

NAS8-37360

6. AUTHOR(S)

M. J. Lucas, R. Noreen, L. D. Southerland, J. Cole III, and M. Junger

7. PERFORMING ORGANIZATION NAME(S) AND ADDRESS(ES)

Wyle Research
2001 Jefferson Davis Highway, Suite 701
Arlington, VA 22202

8. PERFORMING ORGANIZATON REPORT NUMBERS

M-778

9. SPONSORING/MONITORING AGENCY NAME(S) AND ADDRESS(ES)

George C. Marshall Space Flight Center
Marshall Space Flight Center, Alabama 35812

10. SPONSORING/MONITORING AGENCY REPORT NUMBER

NASA CR-4671

11. SUPPLEMENTARY NOTES

Technical Monitor: Tomas E. Nesman, Structures and Dynamics Laboratory, Science and Engineering Directorate

12a. DISTRIBUTION/AVAILABILITY STATEMENT

Unclassified-Unlimited
Subject Category 02

12b. DISTRIBUTION CODE

13 ABSTRACT *(Maximum 200 words)*

Internal fluid flows are subject not only to self-sustained oscillations of the purely hydrodynamic type but also to the coupling of the instability with the acoustic mode of the surrounding cavity. This situation is common to turbomachinery, since flow instabilities are confined within a flow path where the acoustic wavelength is typically smaller than the dimensions of the cavity and flow speeds are low enough to allow resonances. When acoustic coupling occurs, the fluctuations can become so severe in amplitude that it may induce structural failure of engine components. The potential for catastrophic failure makes identifying flow-induced noise and vibration sources a priority. In view of the complexity of these types of flows, this report was written with the purpose of presenting many of the methods used to compute frequencies for self-sustained oscillations. The report also presents the engineering formulae needed to calculate the acoustic resonant modes for ducts and cavities. Although the report is not a replacement for more complex numerical or experimental modeling techniques, it is intended to be used on general types of flow configurations that are known to produce self-sustained oscillations. This report provides a complete collection of these models under one cover.

To obtain copies of the programs contact Tom Nesman at (205) 544-1546 or E-mail Tom.Nesman@msfc.nasa.gov.

14. SUBJECT TERMS	15. NUMBER OF PAGES
vortex shedding, edgetone, unsteady flow, acoustics, oscillation, flow instability, turbomachine, turbopump	317
	16. PRICE CODE A14

17. SECURITY CLASSIFICATION	18. SECURITY CLASSIFICATION OF THIS PAGE	19. SECURITY CLASSIFICATION OF ABSTRACT	20. LIMITATION OF ABSTRACT
Unclassified	Unclassified	Unclassified	